

FACULTÉ DES SCIENCES ET DE GÉNIE
FACULTY OF SCIENCE AND ENGINEERING

Am C

REPORT ON
REGENERATIVE TRANSPONDERS FOR MORE
EFFICIENT DIGITAL SATELLITE SYSTEMS
PHASE II

By: Dr. Kamilo FEHER
Principal Investigator
Department of Electrical Engineering
University of Ottawa
OTTAWA
For: DEPARTMENT OF COMMUNICATIONS
OTTAWA



IC

LKC
P
91
.C654
F43
1981

UNIVERSITÉ D'OTTAWA
UNIVERSITY OF OTTAWA

P
91
C654
F43
1981
S. 1000

REPORT ON
REGENERATIVE TRANSPONDERS FOR MORE
EFFICIENT DIGITAL SATELLITE SYSTEMS
PHASE II

By: Dr. Kamilo FEHER
Principal Investigator
Department of Electrical Engineering
University of Ottawa
OTTAWA
For: DEPARTMENT OF COMMUNICATIONS
OTTAWA

Industry Canada
Library - Queen

AOUT 14 2012
AUG

Industrie Canada
Bibliothèque - Queen

MARCH 27, 1981

REPORT ON
REGENERATIVE TRANSPONDERS FOR MORE EFFICIENT
DIGITAL SATELLITE SYSTEMS
PHASE II

FOR:

DEPARTMENT OF COMMUNICATIONS
COMMUNICATIONS RESEARCH CENTRE
Shirleys Bay
P.O. Box 11490
Station H
OTTAWA, Ontario
K2H 8S2

DSS File Number: 09SU.36⁰101-0-3212

Serial Number of Contract: OSU80-00197

PREPARED BY:

Dr. K. Feher
Principal Investigator

Dr. V. Arunachalam
Mr. M. Wachira
Mr. D. Prendergast
Mr. T. LeNgoc
Dr. J. Huang
Ms. P. Hill
Mr. P. Amlekar
Mr. H. Girard

Department of Electrical Engineering
University of Ottawa
Ottawa, Ontario
K1N 6N5

June 1980 to March 1981

REPORT ON
REGENERATIVE TRANSPONDERS FOR MORE
EFFICIENT DIGITAL SATELLITE SYSTEMS

PHASE II

BY: Dr. Kamilo FEHER
Principal Investigator
Department of Electrical Engineering
University of Ottawa
OTTAWA

FOR: DEPARTMENT OF COMMUNICATIONS
OTTAWA

UNDER: Department of Supply and Services
Contract Serial No: OSU80-00197

PERIOD: JUNE 1980 to MARCH 31, 1981

Submitted: MARCH 27, 1981

Regenerative Transponders For More Efficient
Digital Satellite Systems Phase II

Summary

The need for more efficient use of existing and future satellite facilities has led to the study of on-board satellite regenerative systems. The first phase of this study gave some preliminary results indicating advantages of regenerative over conventional satellites systems, for the QPSK modulation method. Here, ~~an in-depth~~^A study of regenerative satellites systems using compute simulation is carried out and compared to conventional satellite systems for different modulation methods. Refinements in the computer simulation programs including sampling instead of integrate sample and dump detection gives more confidence in the results obtained under bandlimited conditions. The effects of Amplitude and group delay distortions are also included. A 120 Mb/s satellite system having two cascaded nonlinearities, which include AM/AM and AM/PM is used for simulation. This system has characteristics that are specified for the Intelsat V satellite system. The examination of the performance of QPSK, O-QPSK and MSK in regenerative satellites reveals that QPSK performs better than the latter two schemes. ^(Intelsat V configuration) Further it is shown that regeneration yields from 2 to 5.7 dB gain in E_b/N_0 at a $P_e = 10^{-4}$ depending on the modulation method used.

120 MB/s

With regeneration at the satellite, the Intelsat V E_b/N_0 requirements are easily met; without regeneration they can only be met when the HPA is operated at a large input backoff. Regeneration can thus result in considerable power savings.

Preliminary results for DPSK and DQPSK are encouraging enough to merit further consideration especially since these modulation methods ensure reduced complexity at the satellite. Advanced modulation methods are studied and show promise in solving the problem of spectral spreading hence out-of-band emission. In particular, IJF-OKQPSK is shown to out perform QPSK and other common modulation techniques spectrally. NLA-16-QAM is also considered because of its improved power efficiency and spectral efficiency. It is shown that this modulation method might realize a 6 dB system gain over more conventional methods of non-linear amplification. The concept of IJF 64-state NLA QAM is also introduced.

TABLE OF CONTENTS

| | Page |
|---|-------|
| SUMMARY | iv |
| TABLE OF CONTENTS | vi |
| LIST OF FIGURES | x |
| LIST OF TABLES | xviii |
| 1 INTRODUCTION | 1 |
| REFERENCES | 7 |
| 2 COMPARISON OF RECEIVER STRUCTURES AND EFFECTS OF AMPLITUDE AND SLOPE DISTORTION ON BAND- LIMITED QPSK | 8 |
| 2.0.0 Introduction | 8 |
| 2.0.1 Model Description | 9 |
| 2.1.0 Simulation Model | 19 |
| 2.2.0 Numerical Results and Conclusions | 24 |
| 2.3.0 Amplitude and Slope Distortion Effects on QPSK | 34 |
| 2.3.1 Introduction | 34 |
| 2.3.2 Crosstalk | 45 |
| 2.3.3 Modelling Impairments for Computer Simulation | 47 |
| i) Amplitude Slope | 47 |
| ii) Group Delay Slope | 47 |
| 2.3.4 Numerical Results | 48 |
| Conclusion | 50 |
| REFERENCES | 67 |
| 3 PERFORMANCE COMPARISON OF REGENERATIVE AND CONVENTIONAL SATELLITE CHANNELS FOR QPSK | 68 |
| 3.1.1 Introduction | 68 |
| 3.1.2 System Models and Simulation | 70 |
| 3.1.3 Results | 81 |
| 3.1.4 Conclusion | 87 |

| | Page |
|---|--|
| 4 | SPECTRAL SPREADING IN REGENERATIVE SATELLITE SYSTEMS 90 |
| | 4.1.1 Introduction 90 |
| | 4.1.2 Computation of Power Spectrum 92 |
| | 4.1.3 Application to INTELSAT V Case 100 |
| | REFERENCES 101 |
| 5 | EVALUATION OF DPSK AND DQPSK SYSTEMS 102 |
| | 5.1.1 Introduction 102 |
| | 5.2.0 Computer Simulation Technique 104 |
| | 5.2.1 Generation of a DQPSK Signal 108 |
| | 5.2.2 Decoding of the DQPSK Signal 110 |
| | 5.2.3 DQPSK Simulation Results 113 |
| | REFERENCES 117 |
| 6 | A STUDY OF OKQPSK AND MSK MODULATION METHODS 118 |
| | 6.1.1 Introduction 118 |
| | 6.1.2 Bandlimiting and Hardlimiting of QPSK, OK-QPSK and MSK 120 |
| | 6.1.3 Effects of Filtering and Limiting on P_e versus S/N Performance 127 |
| | 6.1.4 Effects of Filtering and Limiting on Symbol Waveshapes 135 |
| | 6.1.5 Performance of OKQPSK and MSK in Conventional and Regenerative Systems 145 |
| | 6.1.6 Conclusions 156 |
| | REFERENCES 157 |
| 7 | NEW IJF-OQPSK MODULATION TECHNIQUE AND ITS APPLICATIONS TO ON-BOARD REGENERATIVE SATELLITE SYSTEMS 158 |
| | 7.1.1 Introduction 158 |
| | 7.1.2 Characteristics of IJF Baseband Signals ... 162 |
| | 7.1.3 Characteristics of IJF Quadrature Modulated Signals in Linear Channels 169 |
| | 7.1.4 Properties of IJF Quadrature Modulated Signals in a Hardlimited Channel 180 |
| | a. Properties of Hardlimited IJF-QPSK Signals 182 |
| | b. Properties of Harlimited IJF-Offset-Keyed OQPSK Signals 191 |

| | Page |
|--|------|
| 7.1.5 Potential Applications of the IJF-OQPSK Modulation Technique to Onboard Regenerative Satellite Systems | 210 |
| a. Spectral Spreading and P_e Performance of the IJF-OQPSK Modem in Conventional Cascaded Nonlinear Channels | 210 |
| i) Spectral Spreading | 214 |
| ii) P_e Performance | 215 |
| b. P_e Performance of the IJF-OQPSK Modem in a Regenerative Satellite Link | 218 |
| 7.1.6 Conclusion | 226 |
| REFERENCES | 227 |
| 7.2.0 NLA-16-QAM: A New Method for Generating High Power 16-QAM Signals Through Nonlinear Amplification | 228 |
| 7.2.1 Introduction | 228 |
| 7.2.2 Modulation Method for NLA-16-QAM | 231 |
| A. Modulator | 231 |
| B. Principle of Operation | 234 |
| C. Transmitter Output Power Comparison Between NLA-16-QAM and Conventional 16-QAM | 236 |
| 7.2.3 Demodulation and Probability of Error Performance | 240 |
| 7.2.4 A Generalized Technique for Nonlinear Amplifier QAM Signal Generation | 243 |
| 7.2.5 Conclusion | 245 |
| REFERENCES | 249 |
| 7.3.0 State NLA QAM: A Method for Generating 64-State QAM Signals Using Nonlinear Amplification | 250 |
| 7.3.1 Introduction | 250 |
| 7.3.2 Modulation Design | 250 |

| | Page |
|---|------|
| 7.3.4 Demodulation | 254 |
| 7.3.5 Principle of Operation | 254 |
| 7.3.3 IJF 64-state QAM: An Extension of 64-state QAM | 259 |
| 7.3.4 Introduction | 259 |
| 7.3.5 Principle of Operation | 259 |
| 7.3.7 Conclusion | 261 |
| REFERENCES | 262 |

LIST OF FIGURES

| Figure | | Page |
|--------|--|------|
| 2.0.1a | Block Diagram of QPSK | 10 |
| 2.0.1b | Data Stream for QPSK | 11 |
| 2.0.2 | Baseband Model for QPSK | 13 |
| 2.0.3a | Matched Filter for a Pulse Input | 14 |
| 2.0.3b | Matched Filter for a Rectangular Pulse Input | 14 |
| 2.0.4 | Gradual Symmetric Roll-off Filter | 16 |
| 2.0.5 | Raised Filter Frequency Response | 18 |
| 2.0.6 | Impulse Response for Various Roll-offs | 18 |
| 2.0.7 | Spectral Amplitude of Rectangular Pulse | 19 |
| 2.1.0 | Simulation Model | 20 |
| 2.2.0 | Scheme A, $\alpha=0.0$ | 25 |
| 2.2.1 | Scheme A, $\alpha=0.5$ | 26 |
| 2.2.2 | Scheme A, $\alpha=1.0$ | 27 |
| 2.2.3 | E_b/N_o vs P_e , Scheme A, $\alpha=0.0$ | 28 |
| 2.2.4 | E_b/N_o vs P_e , Scheme A, $\alpha=0.5$ | 29 |
| 2.2.5 | E_b/N_o vs P_e , Scheme A, $\alpha=1.0$ | 30 |
| 2.2.6 | Scheme B, $\alpha=0.0$ | 31 |
| 2.2.7 | Scheme B, $\alpha=0.5$ | 32 |
| 2.2.8 | Scheme B, $\alpha=1.0$ | 33 |
| 2.2.9 | E_b/N_o vs P_e , Scheme B, $\alpha=0.0$ | 36 |
| 2.2.10 | E_b/N_o vs P_e , Scheme B, $\alpha=0.5$ | 37 |
| 2.2.11 | E_b/N_o vs P_e , Scheme B, $\alpha=1.0$ | 38 |
| 2.2.12 | Scheme C, $\alpha=0.0$ | 39 |

| Figure | | Page |
|--------|---|------|
| 2.2.13 | Scheme C, $\alpha=0.5$ | 40 |
| 2.2.14 | Scheme C, $\alpha=1.0$ | 41 |
| 2.2.15 | E_b/N_o vs P_e , Scheme C, $\alpha=0.0$ | 42 |
| 2.2.16 | E_b/N_o vs P_e , Scheme C, $\alpha=0.5$ | 43 |
| 2.2.17 | E_b/N_o vs P_e , Scheme C, $\alpha=1.0$ | 44 |
| 2.3.0 | Simulation Model | 46 |
| 2.3.1 | Simulated Degradation in E_b/N_o due to Amplitude Slope for Various Roll-offs | 51 |
| 2.3.2 | Eye Diagram for $\alpha=0.5$ with Amplitude Slope = 0.035 dB/MHz | 52 |
| 2.3.3 | Eye Diagram for $\alpha=0.5$ with Amplitude Slope = 0.07 dB/MHz | 53 |
| 2.3.4 | Eye Diagram for $\alpha=0.5$ with Amplitude Slope = .105 dB/MHz | 54 |
| 2.3.5 | Eye Diagram for $\alpha=0.5$ with Amplitude Slope = 0.14 dB/MHz | 55 |
| 2.3.6 | Eye Diagram for $\alpha=0.5$ with Amplitude Slope = .175 dB/MHz | 56 |
| 2.3.7 | Eye Diagram for $\alpha=0.0$ with Amplitude Slope = .175 dB/MHz | 57 |
| 2.3.8 | Eye Diagram for $\alpha=1.0$ with Amplitude Slope = .175 dB/MHz | 58 |
| 2.3.9 | Simulated Degradation in E_b/N_o due to Delay Slope for Various Roll-offs | 59 |
| 2.3.10 | Eye Diagram for $\alpha=0.5$ with Delay Slope = 0.035 ns/MHz | 60 |
| 2.3.11 | Eye Diagram for $\alpha=0.5$ with Delay Slope = 0.07 ns/MHz | 61 |
| 2.3.12 | Eye Diagram for $\alpha=0.5$ with Delay Slope = 0.105 ns/MHz | 62 |

| Figure | | Page |
|--------|---|------|
| 2.3.13 | Eye Diagram for $\alpha=0.5$ with Delay Slope = 0.14 ns/MHz | 63 |
| 2.3.14 | Eye Diagram for $\alpha=0.5$ with Delay Slope = 0.175 ns/MHz | 64 |
| 2.3.15 | Eye Diagram for $\alpha=0.0$ with Delay Slope = 0.175 ns/MHz | 65 |
| 2.3.16 | Eye Diagram for $\alpha=1.0$ with Delay Slope = 0.175 ns/MHz | 66 |
| 3.1.1 | Conventional Communication Satellite System Model | 72 |
| 3.1.2 | Regenerative Satellite System Model | 72 |
| 3.1.3 | Modulator Filter (F_1) | 73 |
| 3.1.4 | Demodulator Filter (F_4) | 74 |
| 3.1.5 | Input MUX Filter (F_2) | 75 |
| 3.1.6 | Output MUX Filter (F_3) | 76 |
| 3.1.7 | AM/AM and AM/PM Characteristics of HPA and TWT Input Backoff (dB) | 79 |
| 3.1.8 | P(e) Performance of QPSK, Case 1 | 82 |
| 3.1.9 | P(e) Performance of QPSK - Worst Case Group Delay | 83 |
| 3.1.10 | Effect of Amplitude Variation in MUX Filters for QPSK | 85 |
| 3.1.11 | Effect of Different Filter Positioning on QPSK | 86 |
| 3.1.12 | Effect of Different Filter Positioning for QPSK | 88 |
| 4.1.1 | Flow Chart of Program to Compute the Power Spectra After a Nonlinearity and System Model Used | 93 |
| 4.1.2 | Input Backoff (dB) | 94 |
| 4.1.3 | Flow Chart of Power Spectrum Evaluation Algorithm | 96 |

| Figure | | Page |
|--------|--|------|
| 4.1.4 | Method of Modified Periodogramme (Parzen Window) | 98 |
| 4.1.5 | Method of Modified Periodogramme (Kayser Window) | 99 |
| 5.1.1 | Block Diagram of Computer Simulation of DPSK Regenerative Satellite Repeater | 105 |
| 5.1.2 | Signal Processing by Computer Simulation | 107 |
| 5.1.3 | DPSK Signal Space or Phasor Representation Showing the Effect of Additive Noise | 111 |
| 5.1.4 | Effect of ISI on DPSK Decision Regions | 114 |
| 5.1.5 | DQPSK BER Performance Through an INTELSAT V System | 115 |
| 6.1.1 | Equivalent Baseband Model of Digital Systems Studied | 121 |
| 6.1.2 | Computed Power Spectral Densities for QPSK | 123 |
| 6.1.3 | Computed Power Spectral Densities for Offset QPSK | 124 |
| 6.1.4 | Computed Power Spectral Densities for MSK | 125 |
| 6.1.5 | P_e Versus $(S/N_b)_{\text{rcvr.input}}$ for QPSK System Simulated | 128 |
| 6.1.6 | P_e Versus $(S/N_b)_{\text{rcvr.input}}$ for QPSK System Simulated | 129 |
| 6.1.7 | P_e Versus $(S/N_b)_{\text{rcvr.input}}$ for MSK System Simulated | 130 |
| 6.1.8 | Degradation, Due to Filtering then Limiting of $(S/N_b)_{\text{rcvr.input}}$ vs Normalized Prelimiter Filter Bandwidth | 134 |
| 6.1.9 | Effects of Filtering and Filtering then Limiting on QPSK Symbol Waveshapes | 136 |
| 6.1.10 | Simulated Eye Diagrams for QPSK | 138 |
| 6.1.11 | Effects of Filtering and Filtered then Limiting on Offset QPSK Symbol Waveshapes | 140 |

| Figure | | Page |
|--------|---|------|
| 6.1.12 | Simulated Eye Diagrams for Offset QPSK | 141 |
| 6.1.13 | Effects of Filtering and Filtering then Limiting on MSK Symbol Waveshapes | 142 |
| 6.1.14 | Simulated Eye Diagrams for MSK | 144 |
| 6.1.15 | OQPSK $P_{(e)}$ Performance-case 1 | 146 |
| 6.1.16 | OQPSK $P_{(e)}$ Performance-worst Case Group Delay | 147 |
| 6.1.17 | MSK $P_{(e)}$ Performance - Case 1 | 149 |
| 6.1.18 | MSK $P_{(e)}$ Performance - Worst Case Group Delay | 150 |
| 6.1.19 | Comparison of $P_{(e)}$ Performance for Regenerative Case | 151 |
| 6.1.20 | Comparison of $P_{(e)}$ With One Non-linearity (HPA) | 152 |
| 6.1.21 | Effect of Different Filter Positioning | 153 |
| 6.1.21 | ISD-BER Curves for Three Different Modulation Techniques | 154 |
| 7.1.1 | Block Diagram of the IJF Signal Encoder Using the NLSF Concept | 163 |
| 7.1.2 | An Example of an IJF Signal Encoding Using the NLSF Concept | 165 |
| 7.1.3 | Power Spectra of the NRZ and IJF Signals | 167 |
| 7.1.4 | Block Diagram of an IJF Quadrature Phase-Shift Keying Modem | 170 |
| 7.1.5 | Time Domain Representations of Some IJF Signals | 172 |
| 7.1.6 | Normalized Power Spectra of Some IJF Quadrature Modulated Signals | 173 |
| 7.1.7 | Normalized Out-of-band-to-total Energy Ratios of OQPSK (QPSK), MSK, IJF-OQPSK Signals | 174 |
| 7.1.8 | Envelope Fluctuation and Phase Transition of the IJF-QPSK Signal | 175 |
| 7.1.8c | Signal Space Diagram of the IJF-QPSK Signal | 176 |

| Figure | | Page |
|---------|---|------|
| 7.1.9 | An Example of the Amplitude Fluctuation and Phase Transition of the IJF-OQPSK Signal | 178 |
| 7.1.9c | Signal Space Diagram of the IJF-OQPSK Signal | 179 |
| 7.1.10a | Block Diagram of an IJF Quadrature Modulator Followed by a Hardlimiting HPA | 181 |
| 7.1.10b | Transfer Characteristics of the Ideal Hardlimiter | 181 |
| 7.1.11 | Effects of Hardlimiting on I and Q Equivalent Baseband Components of the IJF-QPSK Signal (dotted lines show $Y_I(t)$ and $Y_Q(t)$) | 184 |
| 7.1.12 | An Example of the Waveshapes $u_i(t)$, for $i=1, 2, \dots, 8$ | 185 |
| 7.1.13 | 8-state Transition Diagram of the Baseband Component of the Hardlimited IJF-QPSK | 189 |
| 7.1.14 | Effects of Hardlimiting on I and Q Equivalent Baseband Components of the IJF-OQPSK Signal (dotted lines show $Y_I(t)$, $Y_Q(t)$) | 192 |
| 7.1.15 | 8-state Transition Diagram of the Waveshapes $s'_i(t_n)$, $i=1, 2, \dots, 8$ | 194 |
| 7.1.16 | An Example of the Waveshapes $v_i(t_n)$, $i=1, 2, \dots, 16$ | 197 |
| 7.1.17 | 16-state transition Diagram of the Baseband Component of the Hardlimited IJF-OQPSK Signal | 202 |
| 7.1.19 | Computed Normalized Power Spectra of Hard-limited IJF-OQPSK (using Eq. 7.1.29b) | 205 |
| 7.1.20 | Measured Power Spectra of the Hardlimited IJF-OQPSK Signals (bit rate: 64 kb/s, carrier: 512 kHz) | 206 |
| 7.1.21 | Measured Power Spectra of Hardlimited IJF-QPSK, IJF-OQPSK, and Bandlimited QPSK, OQPSK, MSK | 207 |
| 7.1.22a | Model of IJF-OQPSK Modem in a Bandlimited AWGN Channel | 208 |

| Figure | | Page |
|---------|--|------|
| 7.1.22b | P_e Degradation of IJF-OQPSK Modem in A Hardlimited Channel versus α evaluated for a $P_e = 10^{-6}$ * (Relative to the Optimum Performance of QPSK in AWGN Linear Channel) | 209 |
| 7.1.23a | Computer Simulation Model of a Conventional Satellite Link Using IJF-OQPSK Modems | 211 |
| 7.1.23b | Computer Simulation Model of a Conventional Satellite Link with QPSK Modems | 212 |
| 7.1.24 | Nonlinear Characteristics of HPA and TWTA | 213 |
| 7.1.25 | Spectral Spreading of IJF-OQPSK and QPSK Signals (simulation results) | 216 |
| 7.1.26 | Performance of the IJF-OQPSK Modem in Cascaded Nonlinear Channels (solid lines) | 217 |
| 7.1.27 | Eye Diagrams of Received IJF-OQPSK Signals in Linear and Cascaded Nonlinear Channels | 219 |
| 7.1.28 | Model of a Regenerative Satellite Link | 220 |
| 7.1.29a | P_e Performance of Conventional and Regenerative Satellite Links Using IJF-OQPSK Modems | 221 |
| 7.1.29b | Performance of Hardlimited IJF-OQPSK Modems in Conventional and Regenerative Satellite Systems | 222 |
| 7.1.30 | Comparative Performance of Regenerative Satellite Systems Using IJF-OQPSK and QPSK Modems | 225 |
| 7.2.1 | 16 QAM System Representation | 230 |
| 7.2.2 | NLA-16-QAM Modulator | 232 |
| 7.2.3 | Single Input Modulator | 237 |
| 7.2.5 | NLA-64-QAM Modulator | 246 |
| 7.2.4 | NLA-4-QAM Modulator | 247 |

| Figure | | Page |
|--------|--|------|
| 7.3.1 | Conventional 64-state APK System | 251 |
| 7.3.2 | 64-state NLA QAM Modulator and Demodulator [2] | 253 |
| 7.3.3 | Table of Relative Amplitudes of $I(t)$ and 64-ary Signal Set Design | 256 |
| 7.3.4 | Symbol Error Probability Versus Average SNR for 64-ary Alphabets [1] | |

LIST OF TABLES

| Table | | Page |
|-------|---|----------|
| 2.2.1 | Degradation for $P_e = 10^{-4}$ and Noise Power for Schemes A, B, C | 35 35 |
| 5.1.1 | Generation of a DQPSK Signal | 109 |
| 7.2.1 | Code Levels and Amplitudes of Modulated Signal $Z_A(t)$ for Various Combinations of Values of $I_1(t)$ and $I_2(t)$ | 235 |

CHAPTER 1

INTRODUCTION

Digital transmission in conjunction with TDMA has been considered a means of achieving efficient, high-capacity, flexible communications [1]. TDMA derives its efficiency partly from the single-carrier-per-transponder operation, which reduces the effect of the Travelling Wave Tube Amplifier (TWT) nonlinearities by avoiding inter-modulation products [2].

The increase in the number of digital communication satellites and their increased capacity necessitates several considerations. One of the major items contributing to the cost of satellite systems is the generation of high power at the earth station and at the satellite. To achieve the required output power, large transmit and receive antennas are required to provide sufficient system gain. For a cost efficient system, it is necessary to operate the radio-frequency (RF) devices in a nonlinear mode. These nonlinearities degrade and limit the performance of spectrally efficient modulated signals.

In satellite systems, the nonlinear operation of the power amplifier spreads the spectrum of the previously filtered modulated signal. To reduce spillover into adjacent channels, an RF filter is required. This bandlimited AM/AM and AM/PM converted (distorted) signal is further degraded by the transponder input MUX filter, the satellite TWT, and

the satellite output MUX transmit filter. The main degradation in the satellite is caused by cascading two band-limited nonlinearities. The advent of inter-satellite links will result in systems with more than two cascaded nonlinearities, and more degradation will be expected. In a number of presently planned (conventional) systems, a very significant (5 to 10 dB) degradation from theoretical performance is allowed. This has a drastic economic impact if it is taken into account that a 1 dB loss could amount to a considerable expenditure for high bit rate spectrally efficient system.

To reduce the system cost, cheaper (smaller) earth stations will be demanded. Also, more bandwidth efficient modulation methods will be employed in order to better utilize the spectrum. These factors will aggravate the problem of uplink power. Spectrum conservation methods including frequency reuse and multiple spot-beam antennas [3] will be called for. Co-channel interference is thus envisioned to become an important performance-limiting factor [4].

A solution to this problem is the use of signal processing satellite repeaters instead of the conventional translating repeaters mostly in use these days [2-8]. This (signal processing) repeater is capable of demodulating the incoming uplink signals into baseband data and remodulating for retransmission in the downlink. By splitting the

satellite link into two distinct parts, on-board regeneration provides the desired performance while saving on the satellite and earth station power. It also allows capabilities beyond those achievable with simple translating satellites. These include considerable interference protection, and inter-connectivity between different types of terminals [5].

Regeneration prevents the accumulation of noise and co-channel interference. Any effect of noise or distortion in the uplink is removed at the satellite and only the errors in the bit stream are propagated on to the downlink, hence instead of the noise in the two links adding up, only the bit errors add up (double errors are assumed negligible).

$$P_{e_t} = P_{e_u} + P_{e_d}$$

where P_{e_u} , P_{e_d} and P_{e_t} are the uplink, downlink and total bit error rates respectively.

For identical uplink and downlink, an almost 2.8 dB gain results by using a regenerative repeater in a linear channel. In nonlinear channels, the regenerative satellite system may well offer more than 3 dB gain in E_b/N_0 over the conventional nonregenerative one. The isolation of uplink and downlinks leads to an efficient use of the available EIRP by allowing the optimization of each link separately. For instance each link may be separately equalized to reduce intersymbol interference (ISI). Different modulation

methods may be used for the two links.

Regeneration provides versatility in the system. It is for example compatible with the store-and-forward concept for use with a single antenna beam [3]. This facilitates bit rate conversion to take place at the satellite which might be called in for if there are different size antennas each using a different modulation method. The availability, at the satellite repeater, of the detected baseband data stream leads to a high degree of interconnectivity, and new conveniences to users such as insert and drop which are not now possible. Electronic switching with LSI ensures miniature and very light circuitry as opposed to the heavier microwave switches required if switching is to be done in conventional systems. In the more distant future, other signal processing such as DSI may be used to further increase the capacity of the satellite link.

On-board regeneration enables the possibility of derivation of a unique carrier for all the downlink signals and results in burst-to-burst carrier coherence.

In this report the advantages of using on-board regeneration is studied using computer simulation. An illustrative example of a 120 Mb/s system having cascaded nonlinearities, which include both AM/AM and AM/PM, is used. The system parameters are those suggested for INTELSAT V [9] as these parameters are illustrative of future generation satellite systems. In Chapter 2, the optimum receiver

derivation is recalled. Three receiver schemes are compared in a simulation study of a bandlimited QPSK signal signal in a linear channel. This comparison is performed because sub-optimum schemes are sometimes used in a practical environment. Also considered, are the amplitude and slope distortion effects on a bandlimited QPSK signal.

Chapter 3 compares the performance of QPSK in a conventional (cascade of two nonlinearities) and regenerative satellite systems using computer simulation. The model chosen for the study uses INTELSAT V specifications and a bit rate of 120 Mb/s.

Chapter 4 explores the problem of regeneration of the side lobes of the power spectrum when a signal is transmitted through a saturated TWT. The TWT specifications used are those of INTELSAT V. The evaluation is conducted for different values of input power back offs.

In Chapter 5, a study of Differential Phase Shift keying and Differential Quadrature Phase Shift Keying is conducted. These modulation methods are attractive because of their reduced complexity since the problem of synchronization is reduced.

Chapter 6 discussed the study of MSK and OK-QPSK for regenerative satellite systems. These systems are attractive because of low envelope fluctuation property. These modulation methods are compared for conventional and regenerative

cases. Also, the effects of hardlimiting is given in this chapter.

A discussion of advanced modulation methods is presented in Chapter 7. Highlighted is the study of intersymbol interference and jitter free nonlinearly switched filters (IJF-NLSF) which give encouraging results with respect to side lobe regeneration after nonlinear amplification. These filters are applied to quadrature and offset quadrature modulated systems and results are presented. Other advanced modulation methods namely nonlinearly amplified 16-QAM and IJF 14-state NLA QAM are also presented.

Finally, in Chapter 8 some concluding comments are made and recommendations for future research are presented.

REFERENCES

- [1] K. Feher, A. Guibord, M. Wachira and J. Huang, "Regenerative Transponders for More Efficient Satellite Systems", Report to Communications Research Centre, DOC., Ottawa, February 1980.
- [2] S.J. Campanella, F. Assal and A. Berman, "Onboard Regenerative Repeater," IEEE ICC-77, Chicago, June 1977, p. 6.2-121-6.2-125.
- [3] C. Cuccia, R. Davies and E. Mathews, "Baseline Considerations of Beam Switched SS-TDMA Satellites Using Baseband Matrix Switching," IEEE ICC'77, p. 6.3.126-6.3.131.
- [4] K. Koga, T. Muratani and A. Ogawa, "Onboard Regenerative Repeaters Applied to Digital Satellite Communications", Proc. IEEE, Vol. 65, No. 3, March 1977, p. 401-410.
- [5] L.S. Metzger, "On-board Satellite Signal Processing", IEEE NTC'78, p. 8.1.1-8.1.5, December 1978.
- [6] J.T. Chiao and F. Chetnik, "Satellite Regenerative Repeater Study", IEEE Canadian Comm. and Power Conference, p. 222-225, Montreal, October 1976.
- [7] Y.S. Lee, "Simulation Analysis for Differentially Coherent Quarterternary PSK Regenerative Repeater", COMSAT Tech. Review, Vol. 7, No. 2, Fall 1977, p. 447-474.
- [8] T.C. Huang, J.K. Omura and L. Biederman, "Comparison of Conventional and Regenerative Satellite Communication System Performance", ICC'79, p. 58.3.1-58.3.5, Boston, June 1979.
- [9] "INTELSAT TDMA/DSI Specifications", BG-42-6SE, June 1980.

CHAPTER 2

COMPARISON OF RECEIVER STRUCTURES AND EFFECTS OF AMPLITUDE AND SLOPE DISTORTION ON BAND-LIMITED QPSK

2.0.0 Introduction

The study in this chapter compares the performance of three receive configurations which can be used for the detection of band-limited QPSK (quadrature phase shift keying) modulated signals in a linear channel. Here, the output of the transmit filter has a raised cosine power spectrum, the choice of which will be explained later. The three structures of receiver used here are:

1. Root of raised cosine filter + sampler
2. Integrator + Sampler
3. Root of raised cosine filter + Integrator + Sampler

where the integrator has an impulse response of duration 'T'.

Even though the optimum receiver is known to be structure 1 for a band-limited linear channel, this study is conducted to compare with sub-optimum schemes sometimes used in practice. The optimum receiver derivation is recalled in the following section and the receive schemes are compared in terms of the increase necessary for E_b/N_0 with respect to theory (no bandlimiting in a white Gaussian

environment [1]) for a probability of error, $P_e = 10^{-4}$, as generated by simulation on the computer (IBM370).

2.0.1 Model Description

A model of QPSK system is shown in Fig. 2.0.1a. The input data stream is assumed to consist of full length rectangular pulses (NRZ, non-return to zero signal). That is,

$$x(t) = \sum_n a_n p(t - nT_b) \text{ where } a_n = \pm A \quad (2.0.1)$$

$$\begin{aligned} \text{and } p(t) &= 1 \quad 0 < t < T_b \\ &= 0 \quad |t| > T_b. \end{aligned}$$

This stream is converted by a serial to parallel converter into rectangular pulses ($I(t)$ and $Q(t)$ in Fig. 2.0.1b) with a symbol rate half that of the incoming bit rate ($T_s = 2T_b$). In other words,

$$x(t) = \sum_n \underbrace{a_n}_{I(t)} p(t - nT_s) + j \sum_n \underbrace{b_n}_{Q(t)} p(t - nT_s) \quad (2.0.2)$$

where $a_n = \pm A$ and $b_n = \pm A$. In Fig. 2.0.1a, the transmitter filtering may be a combination of identical base-band filtering to the streams $I(t)$ and $Q(t)$ and filtering to modulator output signal, $s(t)$. However, given that the modulation process is linear, filtering to $s(t)$ can be

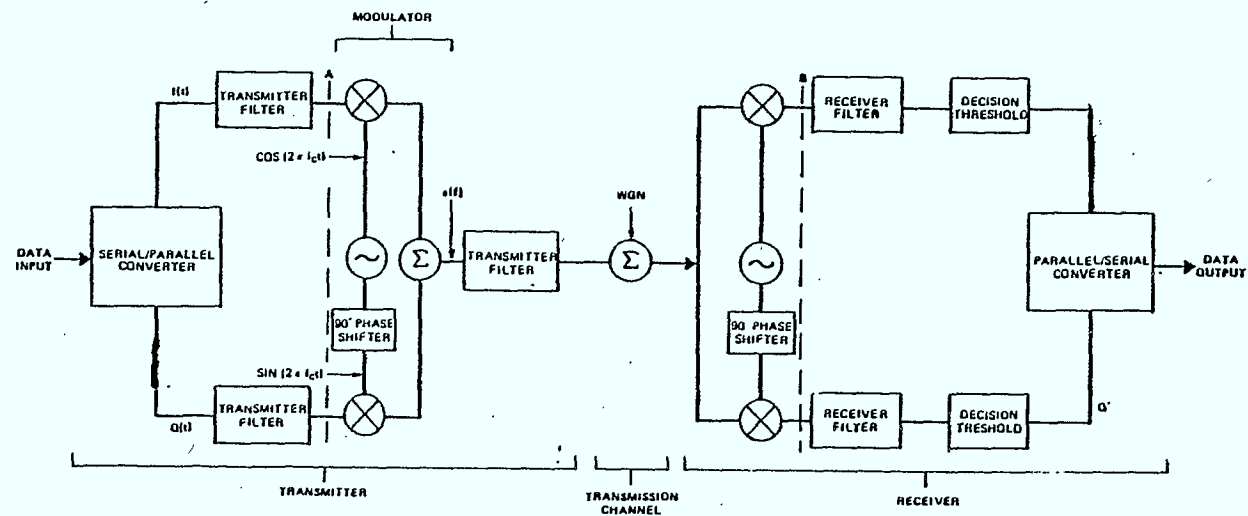


Figure 2.0.1a - Block Diagram of QPSK

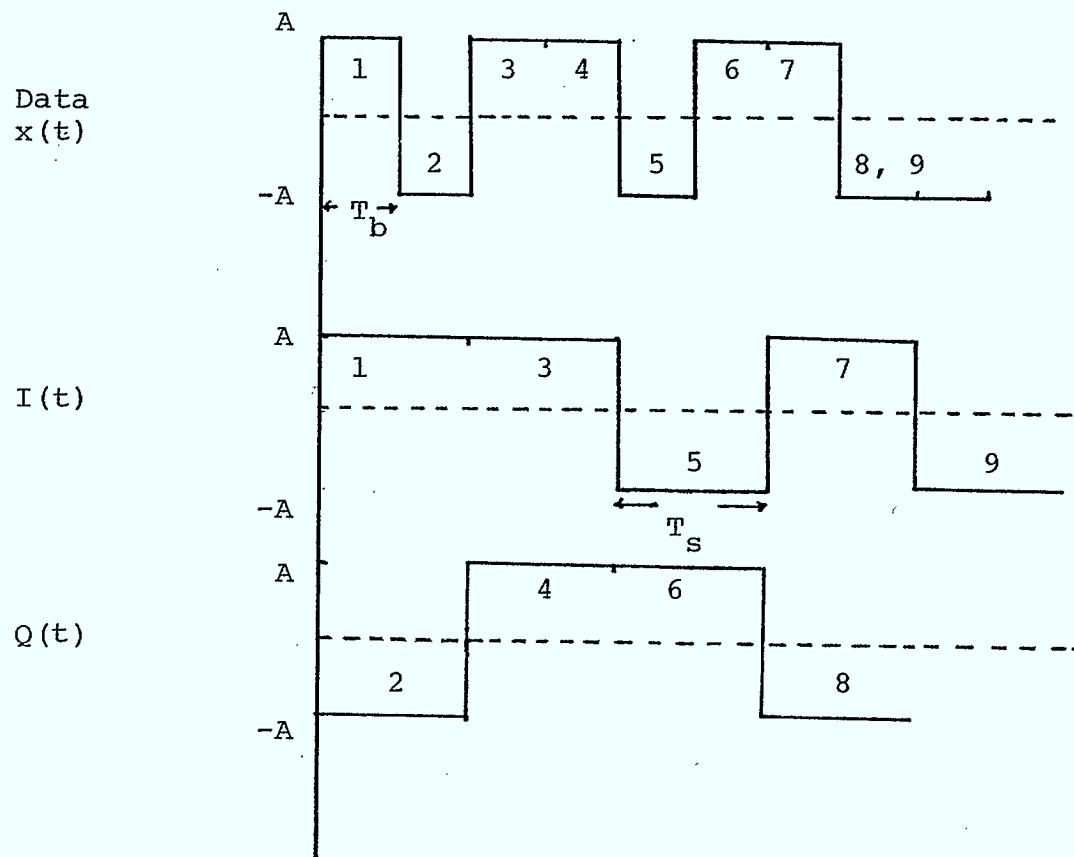


Figure 2.0.1b - Data Stream for QPSK

represented by its low-pass equivalent filtering to $I(t)$ and $Q(t)$ [2]. Hence, the information is represented by a complex baseband signal and the model for analysis is shown in Fig. 2.0.2. For our analysis we will consider all transmitter filtering, $T_x(f)$, to be in baseband and assume that the filtering of $S(t)$ is accounted for in this.

Before going through the description of the model in Fig. 2.0.2 the matched filter concept is introduced. For a single pulse, $p_1(t)$ in noise, the signal to noise ratio (SNR) at the output of the receive filter is maximum when the filter is matched to the pulse shape, that is, its impulse response is given by $p_1(T-t)$ where delay T is introduced for the system to be realizable (Fig. 2.0.3a). For the particular case of $p_1(t)$ being rectangular the matched filter impulse response again is a rectangular pulse (Fig. 2.0.3b) which is the finite time integrator where the sample at $t=T$ gives the maximum voltage value. This detector is sometimes referred to as an integrate sample and dump. For a pulse stream of "non-overlapping" rectangular pulses the matched filter is again an integrator. There we assume an infinite bandwidth system. For a band-limited system, the "non-overlapping" pulses (Fig. 2.0.2) get filtered by a transmit filter, $T_x(f)$. The output $x_t(t)$ now consists of "overlapping" pulses because $p_1(t)$ is no

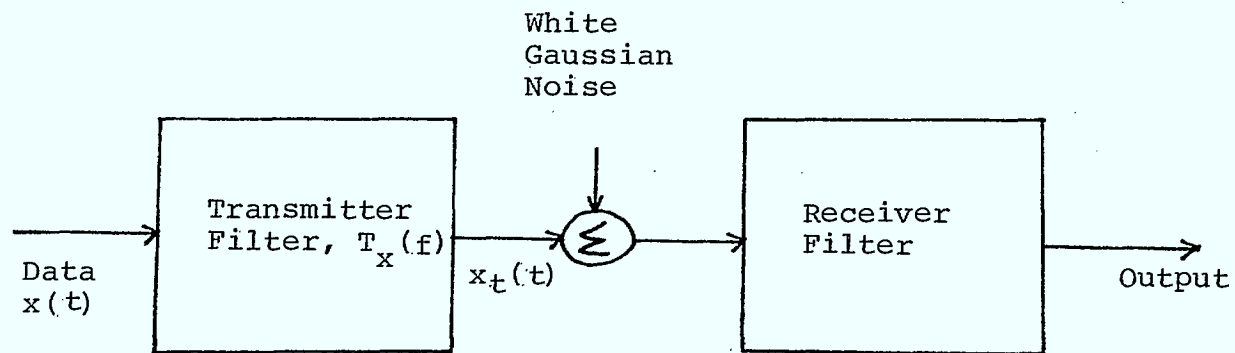


Figure 2.0.2 - Baseband Model for QPSK

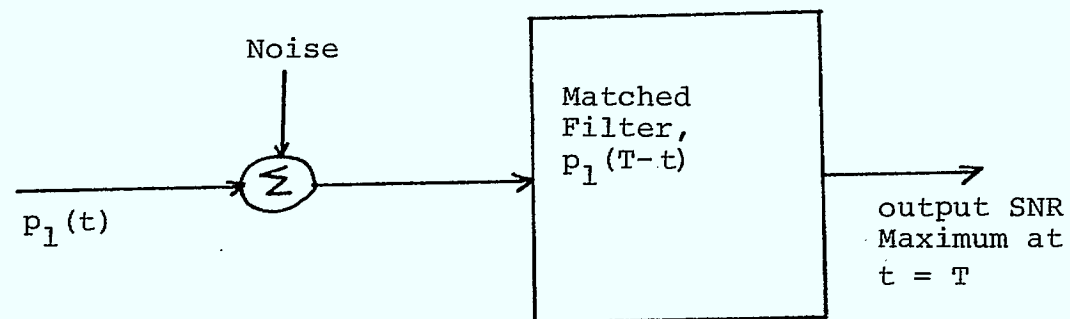


Figure 2.0.3(a) - Matched Filter for a Pulse Input

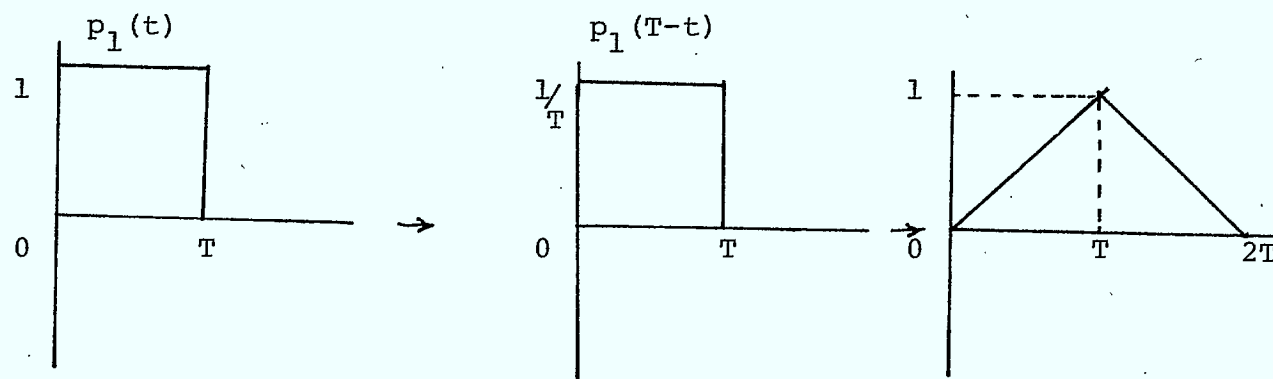


Figure 2.0.3(b) - Matched Filter for a Rectangular Pulse Input

longer time limited. The filter matched to this pulse shape will again give maximum SNR but with intersymbol interference (ISI) at the sampling instants which means degradation in probability of error, P_e . This calls for optimum filtering with maximum SNR and no ISI at the output.

The Nyquist theorem states that an impulse train of repetition rate $2f_1$ can be transmitted through a filter of bandwidth f_1 without interference between peaks of received pulses. This means that the filter's impulse response should pass through zero at regular 'T' intervals where $T = \frac{1}{2f_1}$. A filter which satisfies this criterion is the one with linear phase and amplitude characteristics of either low-pass or gradual symmetric roll-off as in Fig. 2.0.4.

The special case of the gradual roll-off filter that has been extensively used is the "raised-cosine" filter, the frequency response of which is shown in Fig. 2.0.5 can be mathematically represented as

$$\begin{aligned}
 &= 1 && 0 < f < f_1 - f_x \\
 A(f) &= \frac{1}{2} \left[1 - \sin \frac{\pi}{2\alpha} \left(\frac{f}{f_1} - 1 \right) \right] && f_1 - f_x < f < f_1 + f_x \\
 &= 0 && f > f_1 + f_x
 \end{aligned} \quad (2.0.3)$$

for the amplitude characteristic.

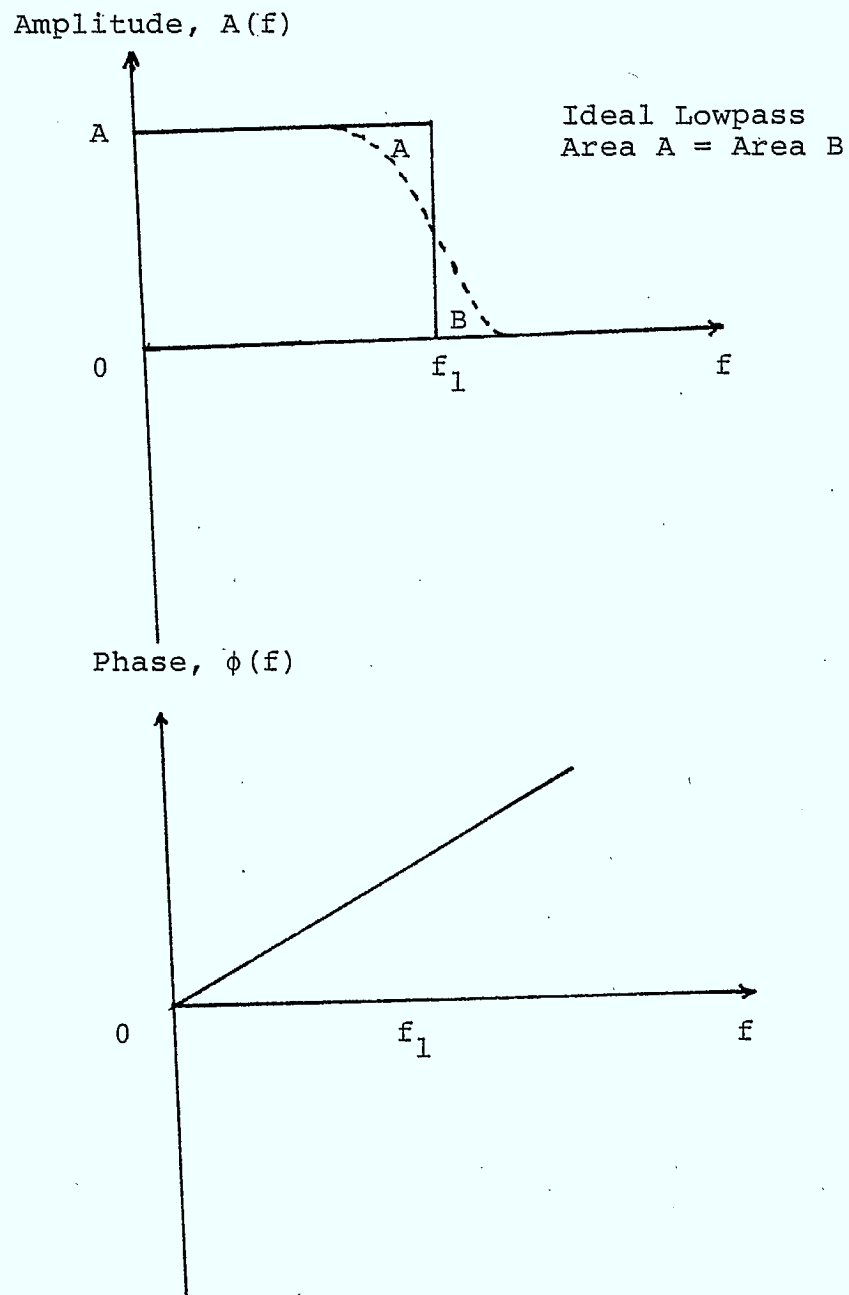


Figure 2.0.4 - Gradual Symmetric Roll-off Filter

The phase characteristic is given by

$$\phi(f) = Kf \quad 0 < f < f_1 + f_x, \quad K = \text{constant},$$

where α is the amount of bandwidth used in excess of minimum Nyquist bandwidth (f_1) divided by Nyquist bandwidth ($\alpha = f_x/f_1 = \text{roll-off factor}$). Thus an α of unity is referred to as 100% roll-off and means that the total bandwidth used is $2f_1$ while α of zero indicates that minimum bandwidth, f_1 is employed. The corresponding impulse response is shown in Fig .2.0.6. for various α 's. As can be seen zeros occur at sampling instants and hence there will be no ISI at the receiver output. Thus, if the overall spectrum $H(f) = T_x(f)R_x(f)$ is chosen to satisfy the Nyquist condition there will be no ISI at the sampling instant. This still leaves us with an arbitrary choice of transmit and receive filter since only their product, $H(f)$, has been specified by ISI removal conditions.

The problem now to be solved consists of finding the transmit and receive filters which minimize the error probability as a function of E_b/N_0 and with the constraint of no ISI at the sampling instants. Following the approach given in Reference[2] the results are

$$\text{Receiver filter} = R_x(f) = \frac{|H(f)|^{\frac{1}{2}}}{N^{\frac{1}{4}}(f)} \quad (2.0.5)$$

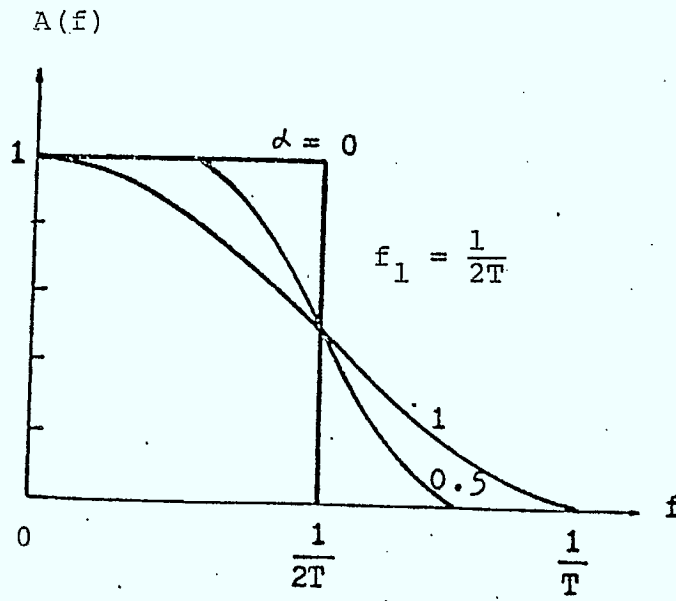


Figure 2.0.5 - Raised Cosine Filter Frequency Response

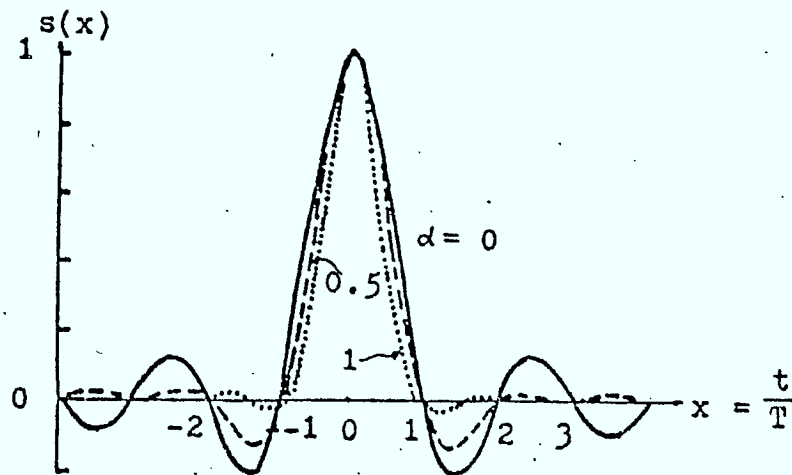


Figure 2.0.6 - Impulse response for Various Roll-offs

and Transmit filter = $T_x(f) = \frac{H(f)N^{\frac{1}{4}}(f)}{|H(f)|^{\frac{1}{2}}}$ (2.0.6)

If the noise spectral density $N(w)$ is flat and $H(w)$ is real, the above expression is reduced to $R_x(f) = T_x(f) = |H(f)|^{\frac{1}{2}}$. This result is not surprising because the receive filter is "matched" to the transmit filter for maximum SNR at the output. This is true for an impulse input to the transmit filter. In our case the input is a train of rectangular pulses (Fig. 2.0.1b) which has a $\frac{\sin x}{x}$ spectrum with first zero crossing at a frequency equal to the reciprocal of the pulse width (Fig. 2.0.7). Thus, a $\frac{x}{\sin x}$ equalization should be used to create an impulse input to the transmit filter.

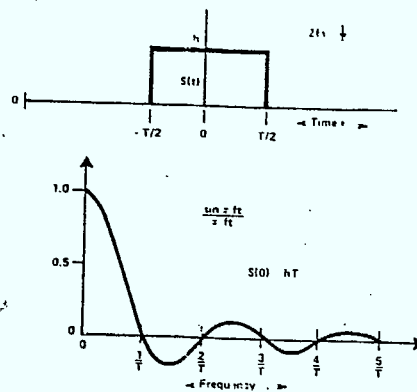


Figure 2.0.7 - Spectral Amplitude of Rectangular Pulse

2.1.0 Simulation Model

The model used for computer simulation is shown in Fig. 2.1.0 where $\sqrt{\alpha}$ represents the square root of the raised cosine filter. The composite filter, $T_x(f)$, is

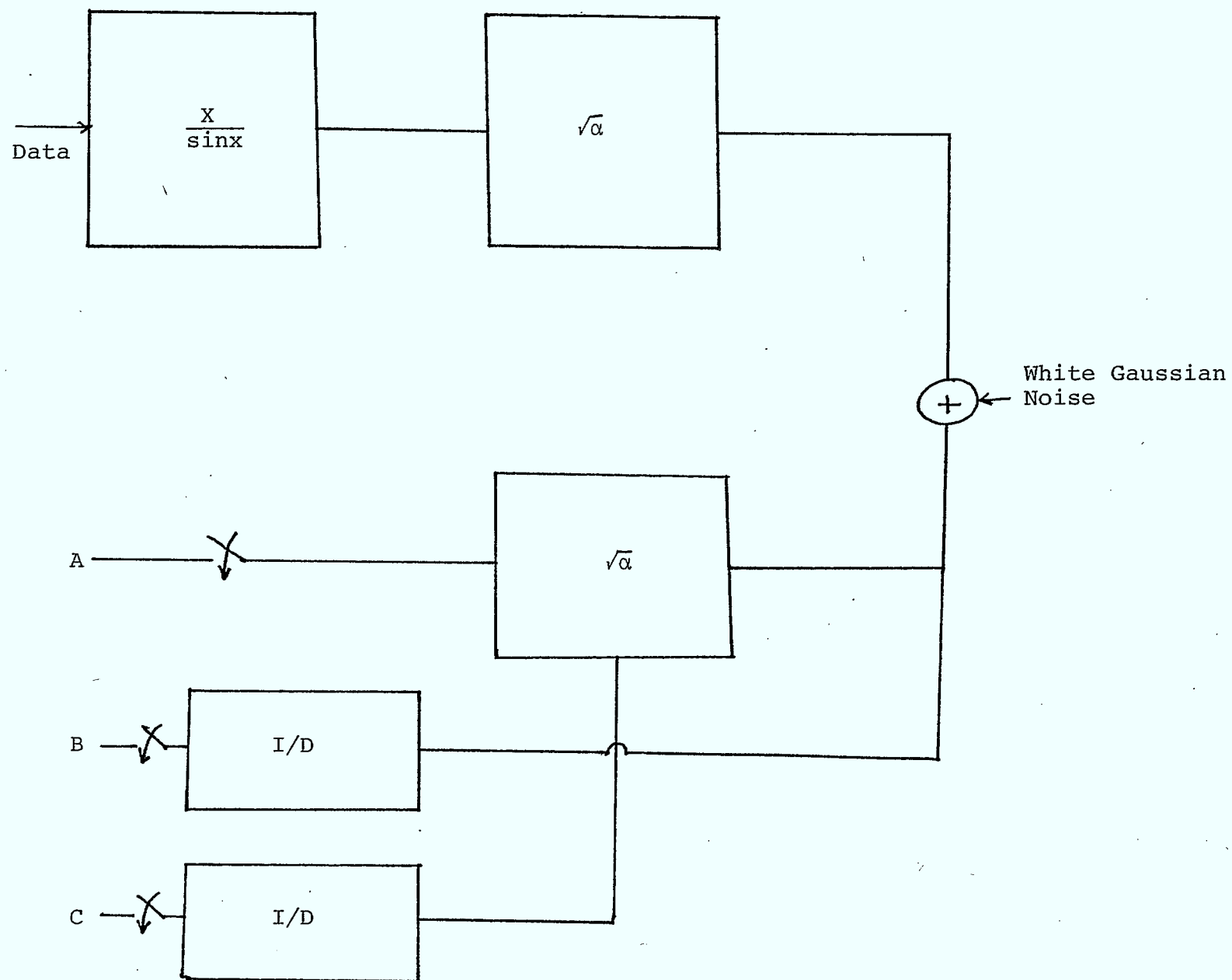


Figure 2.1.0 - Simulation Model

mathematically represented as

$$T_x(f) = \begin{cases} \frac{\pi f/2f_1}{\sin(\pi f/2f_1)} & 0 < f < f_1 - f_x \\ \frac{1}{2} [1 - \sin \frac{\pi}{2\alpha} (f/f_1 - 1)] \cdot \frac{\pi f/2f_1}{\sin(\pi f/2f_1)} & f_1 - f_x < f < f_1 + f_x \\ 0 & f > f_1 + f_x \end{cases} \quad (2.1.0)$$

while

$$R_x(f) = \begin{cases} 1 & 0 < f < f_1 - f_x \\ \frac{1}{2} [1 - \sin \frac{\pi}{2\alpha} (f/f_1 - 1)] & f_1 - f_x < f < f_1 + f_x \\ 0 & f > f_1 + f_x \end{cases} \quad (2.1.1)$$

Three detection schemes are used for the study and are shown in Fig. 2.1.0.

The input time signal is assumed to be made up of two streams, 127 symbols PRBS sequence in length with 16 samples per symbol so that the total number of samples = 2032.

Since the number of samples should be an integer power of two for the Fast Fourier Transform (FFT), the first symbol is loaded into the last 16 sample space so that the total number of samples = 2048. The symbols are loaded in the form of complex data with real part corresponding to I channel and the imaginary part corresponding to Q channel.

Whenever the filtering operation is performed, the time signal is transformed to the frequency domain by FFT

and multiplied with the filter frequency transfer function and transformed back into the time domain. The noise at the input of receive filter is assumed to be Gaussian and the noise power at the output of the filter is computed according to theory. Thus, the signal is simulated in the absence of noise. The system performance is evaluated by simulation in terms of E_b/N_o (energy per bit to noise power density ratio) where,

E_b = energy per bit measured at receiver filter input,
and N_o = noise power in unit bandwidth, measured at
the same point.

The P_e in a bit is calculated by assuming symbols in I and Q channels to be independent. Thus,

$$P_e = \frac{1}{2}[P_{e_I} + P_{e_Q}] = \frac{1}{2} \operatorname{erfc}\left(\frac{A}{\sqrt{2}\sigma}\right)$$

where P_{e_I} is the probability of error in I channel, P_{e_Q} is the probability of error in Q channel and A is the signal amplitude (at the sampling instant in scheme A, and the averaged signal amplitude over one symbol period, T_s , in schemes B and C (Fig. 2.1.0)) and noise variance at the output of receive filter, is given by

$$\sigma^2 = \frac{N_o}{2} \int_{-\infty}^{\infty} |W(f)|^2 df \quad (2.1.3)$$

where $W(f) = R_x(f)$ in scheme A
 $= G(f)$ in scheme B
 $= R_x(f)G(f)$ in scheme C

with $R_x(f) = \sqrt{\alpha}$ and $G(f) = \frac{\sin \pi f T_s}{\pi f T_s} =$ transfer function of a integrator (Fig. 2.1.0).

For computer simulation, the P_{e_i} for the amplitude A_i $i = 1, 2, \dots, 128$ symbols is calculated by,

$$P_{e_i} = \frac{1}{2} \operatorname{erfc} \left(\frac{A_i}{\sqrt{2}\sigma} \right) \quad (2.1.4)$$

for either channel I or Q, and the total

$$P_e = \frac{1}{2} \left[\frac{1}{128} \sum_{i=1}^{128} P_{e_i} \right] \quad (2.1.5)$$

with the assumption of independent equiprobable data.
 Also, the transfer function, $G(f)$, for discrete case, $G(k)$, is

$$G(k) = \frac{\sin \frac{\pi k N_1}{N}}{\sin \frac{\pi k}{N}} \quad (2.1.6)$$

where N_1 = number of samples per symbol

N = total number of samples used for data and

$$f = k \Delta f \quad (2.1.7)$$

where $\Delta f = \frac{N_1}{N} f_s$

2.2.0 Numerical Results and Conclusions

The total number of samples used in the simulation is 2048 with 16 samples per symbol. The symbol rate assumed for simulation is 64 Megabauds (corresponding to 128 Mb/s) with Nyquist frequency $f_1 = 32$ MHz. The results are given for three kinds of filters, namely, $\alpha = 0, 0.5$ and 1.0. The eye diagrams to be discussed below corresponds to I channel of QPSK modulation for all schemes shown for two symbol periods.

Scheme A: Figures 2.2.0-2.2.2 show the eye diagram after the receive filter, $R_x(f)$, for different ' α ' roll-offs. The eyes are completely open (100%) at the sampling instant (middle of the eye) and have an amplitude (A) ≈ 1 for all three cases of α . Hence, the E_b/N_0 performance with this scheme of detection coincides with the theoretical (infinite bandwidth case) curve as can be seen from Figs. 2.2.3-2.2.5. The feature to be noted is that the eye diagram for $\alpha = 0$ case should be completely closed except at the sampling instant and this is not the case due to the limited length of data (128 symbols) used in the simulation.

Scheme B: Figures 2.2.6-2.2.8 show the eye diagrams for different roll-offs after the integrate and dump in absence of receive filter. The intersymbol interference present at the sampling instant increases as α decreases. The eye opening for $\alpha=1$ is 90%, $\alpha=0.5$ is 87% and $\alpha=0.0$ is

QPSK EYE DIAGRAM

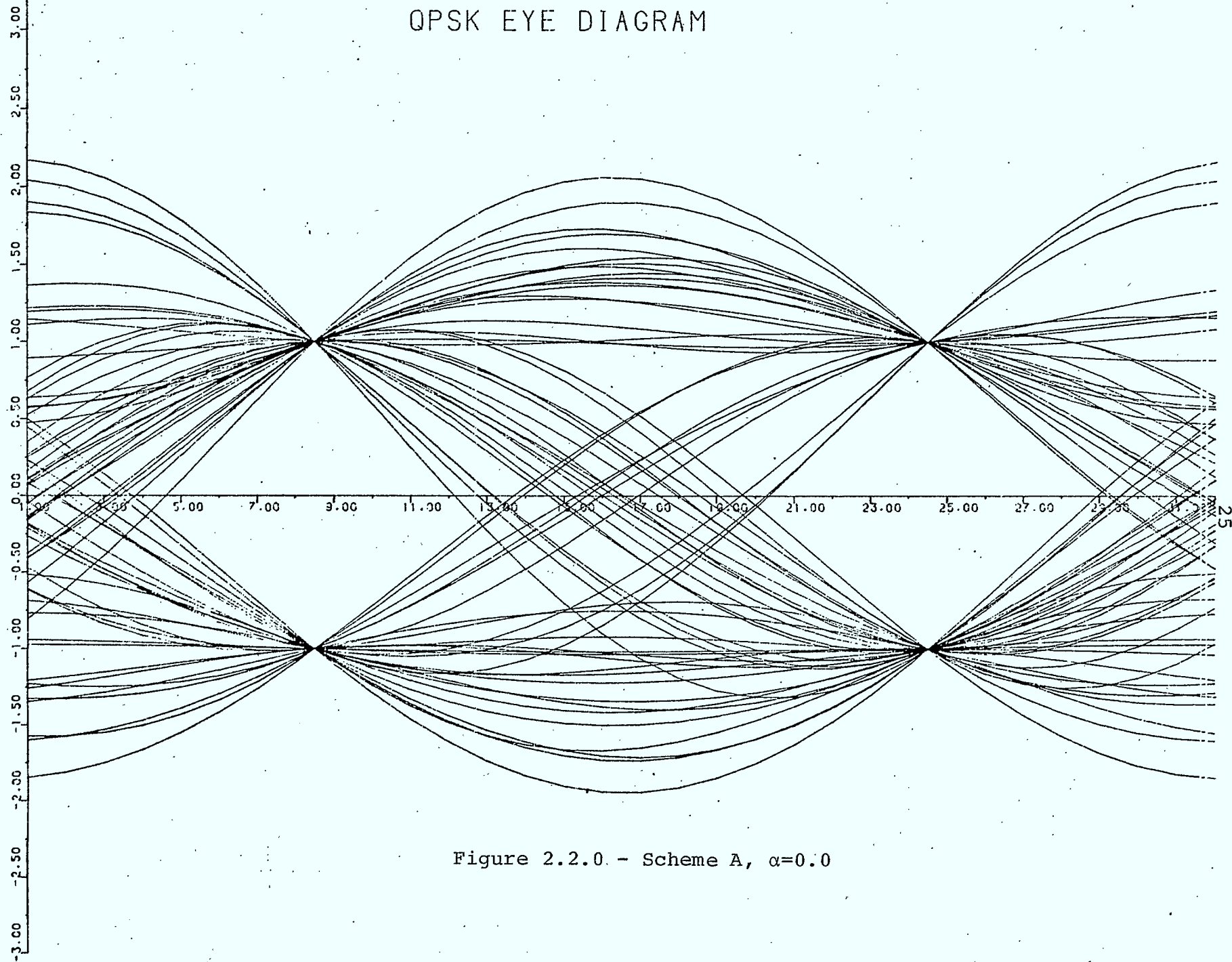


Figure 2.2.0 - Scheme A, $\alpha=0.0$

QPSK EYE DIAGRAM

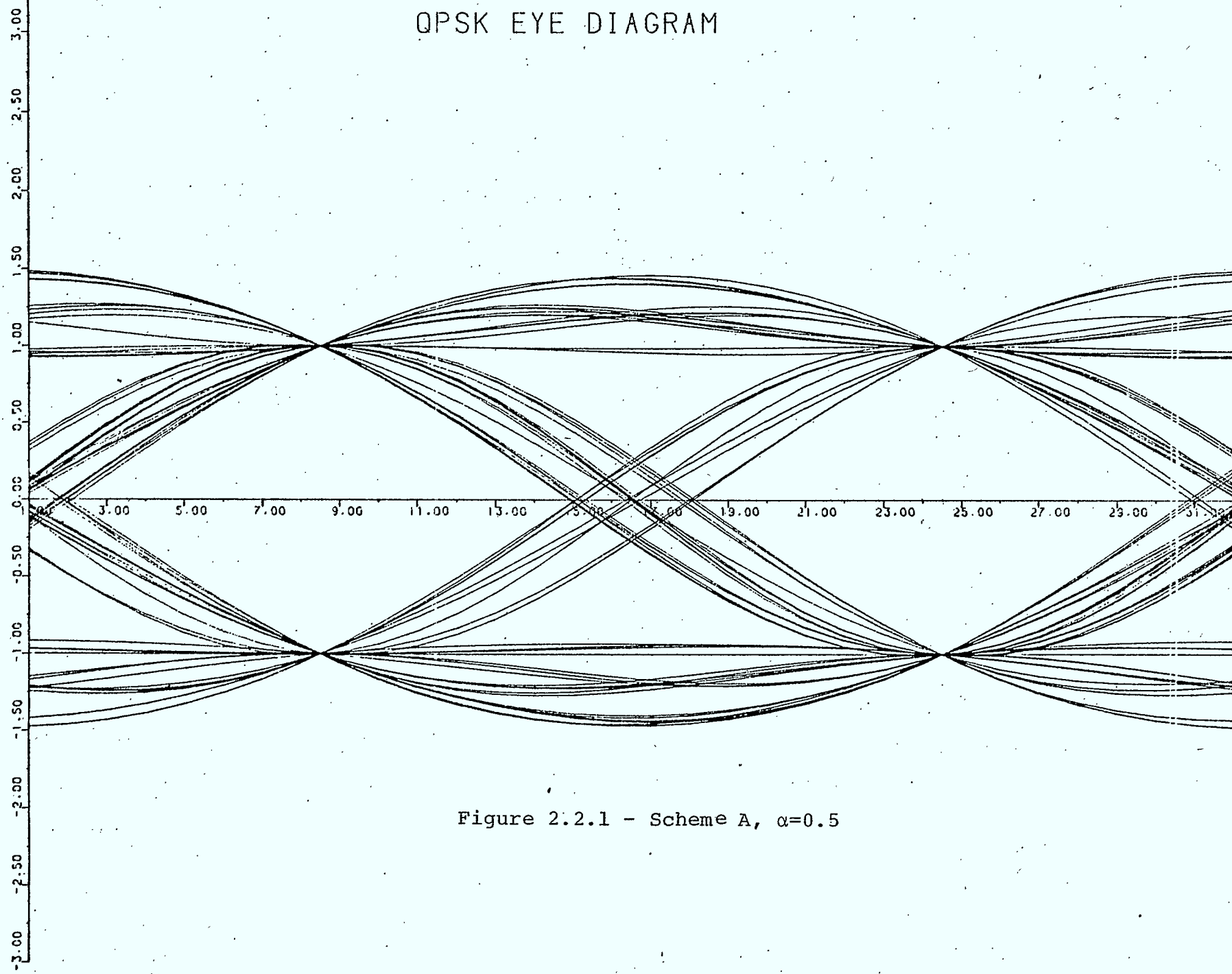


Figure 2.2.1 - Scheme A, $\alpha=0.5$

QPSK EYE DIAGRAM

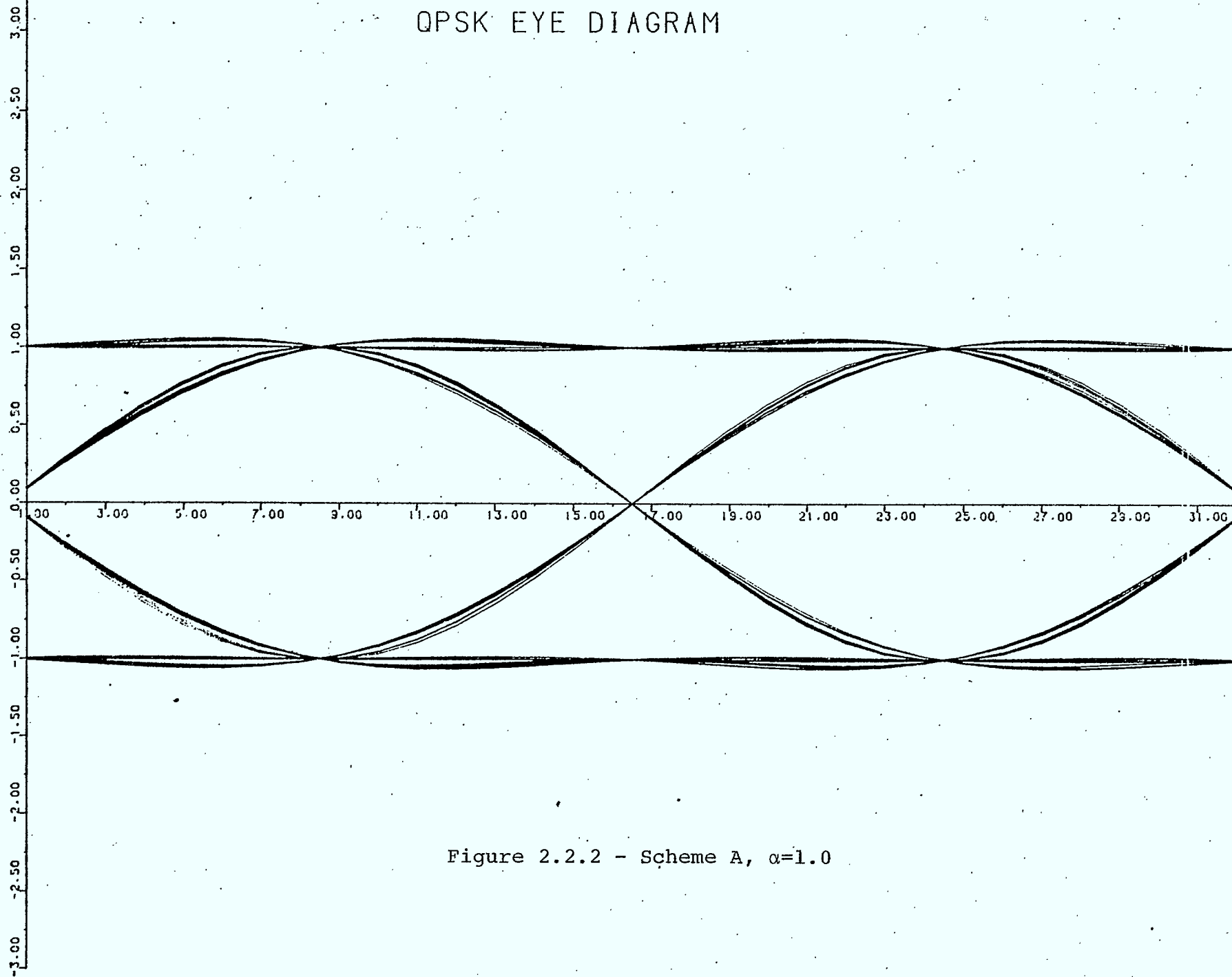


Figure 2.2.2 - Scheme A, $\alpha=1.0$

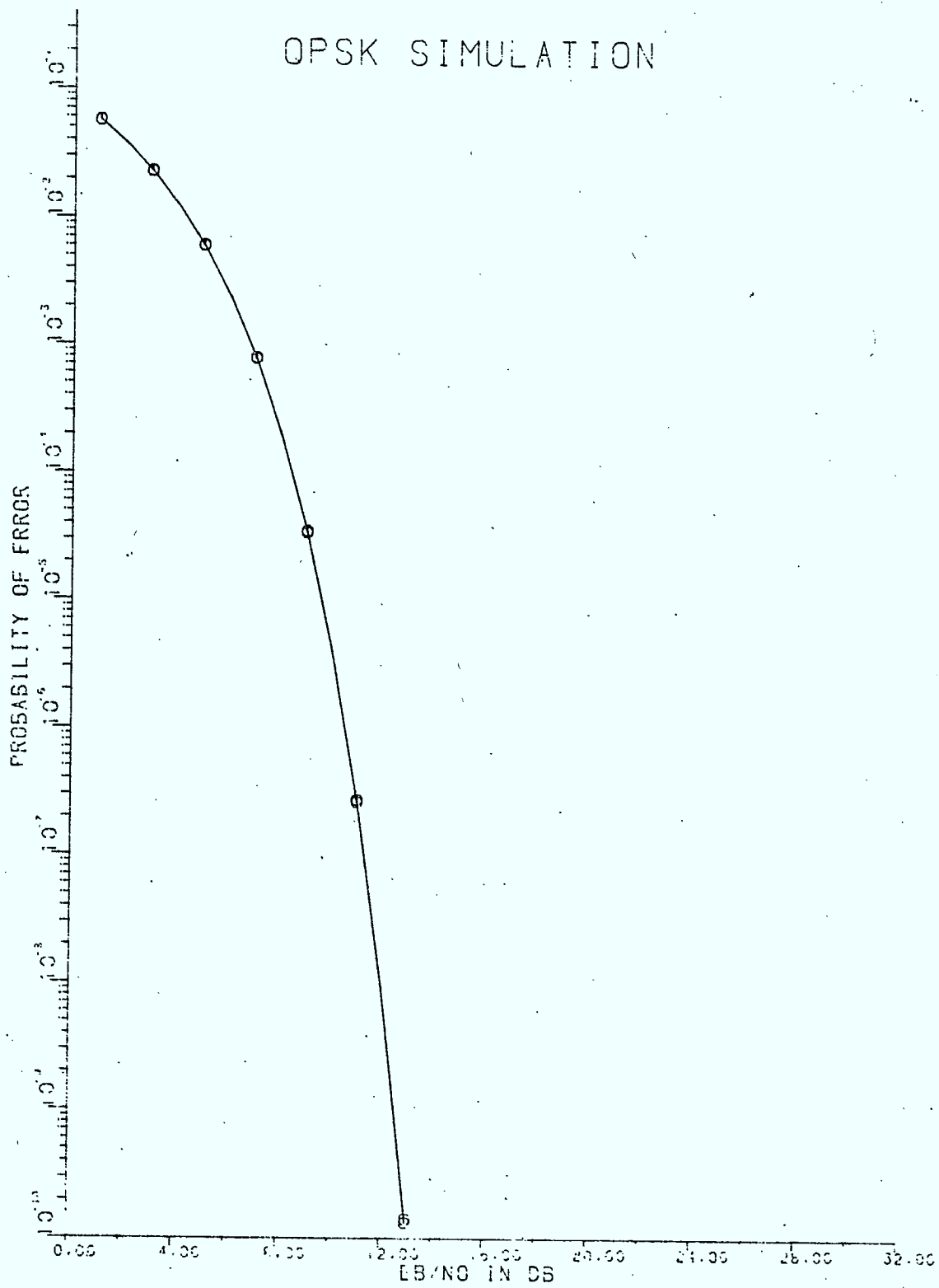


Figure-2.2.3 - E_b/N_0 vs P_e , Scheme A, $\alpha=0.0$

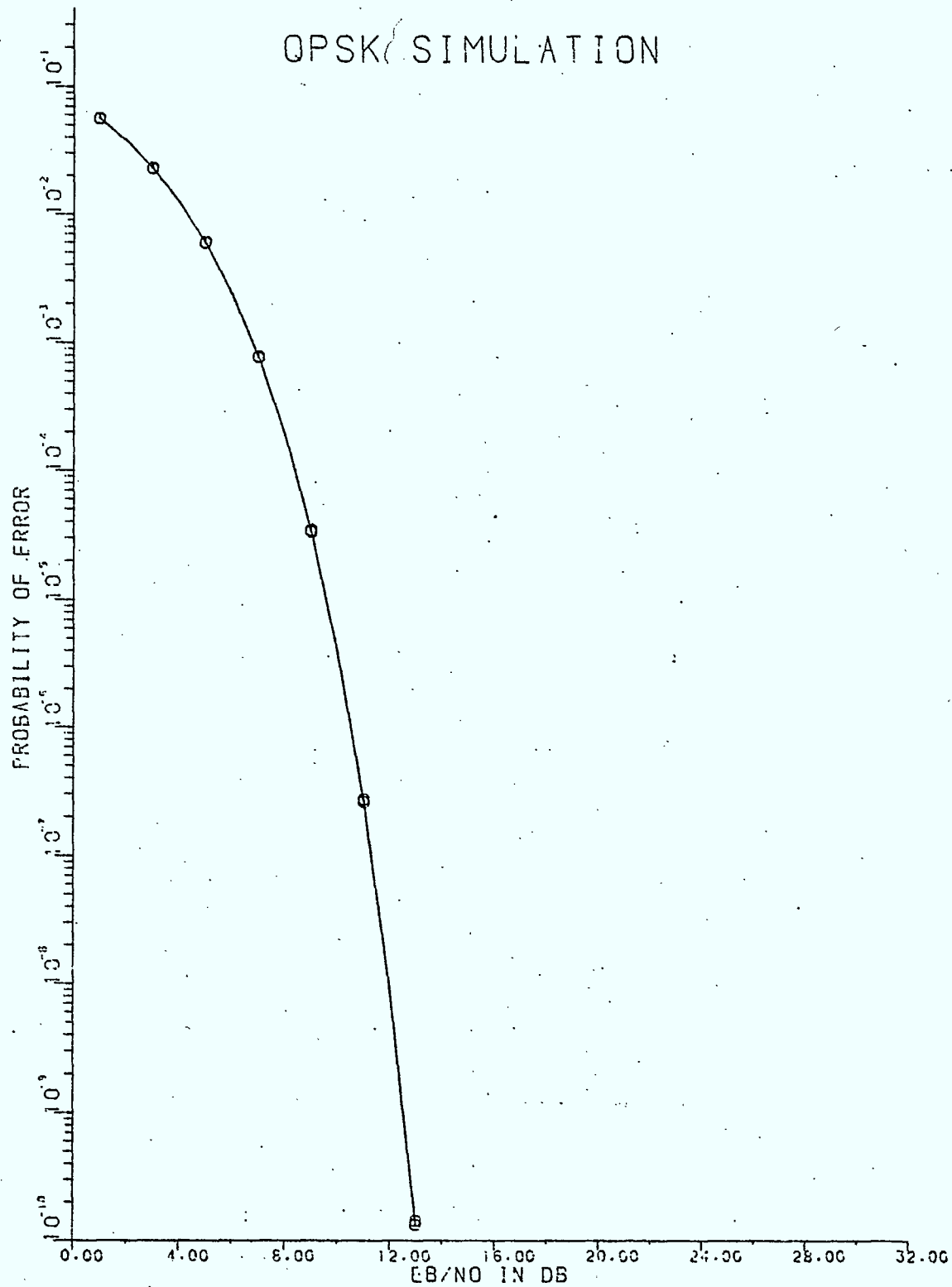


Figure 2.2.4 - E_b/N_o vs P_e , Scheme A, $\alpha=0.5$

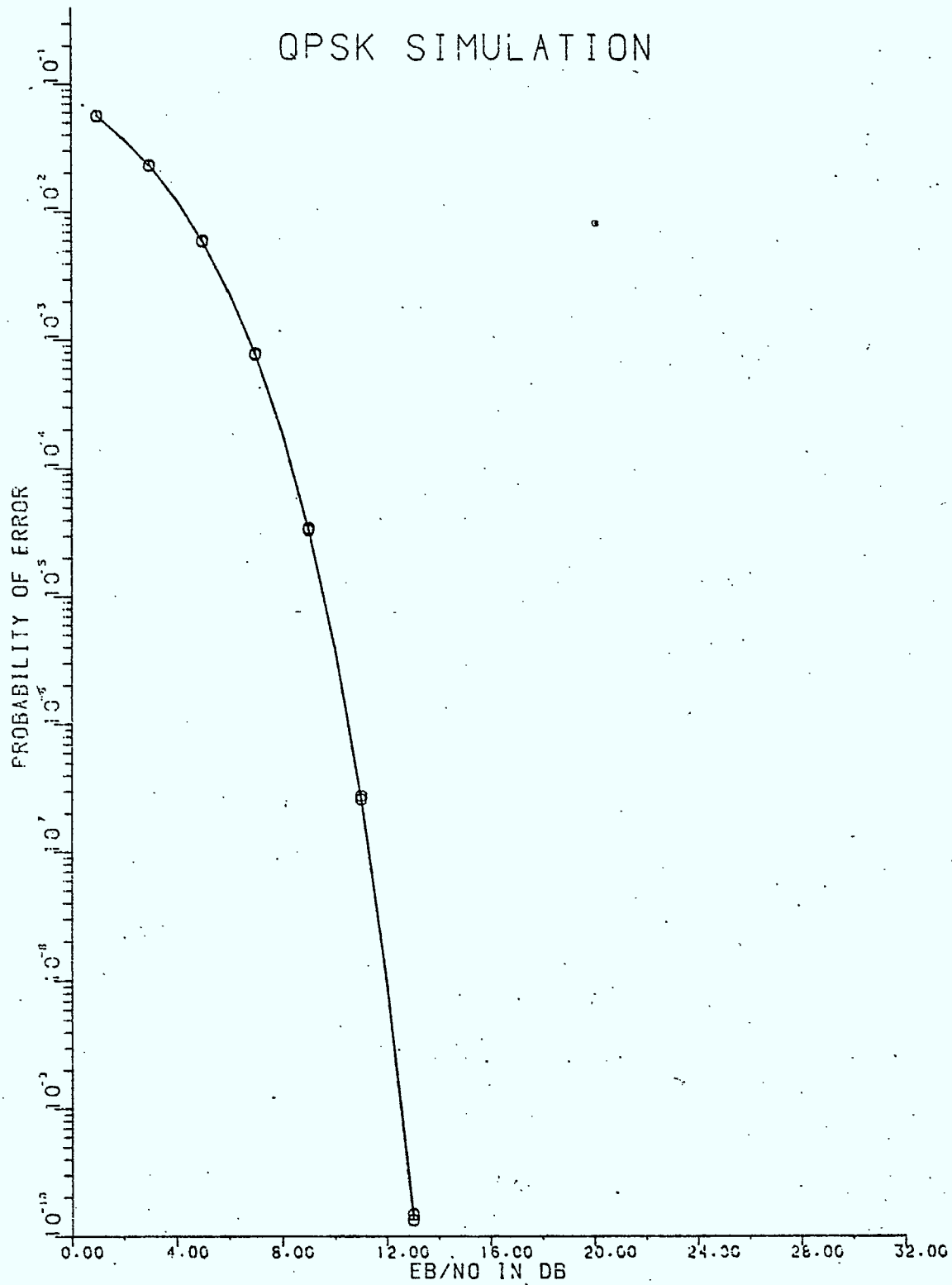


Figure 2.2.5 - E_b/N_0 vs P_e , Scheme A, $\alpha=1.0$

OPSK EYE DIAGRAM

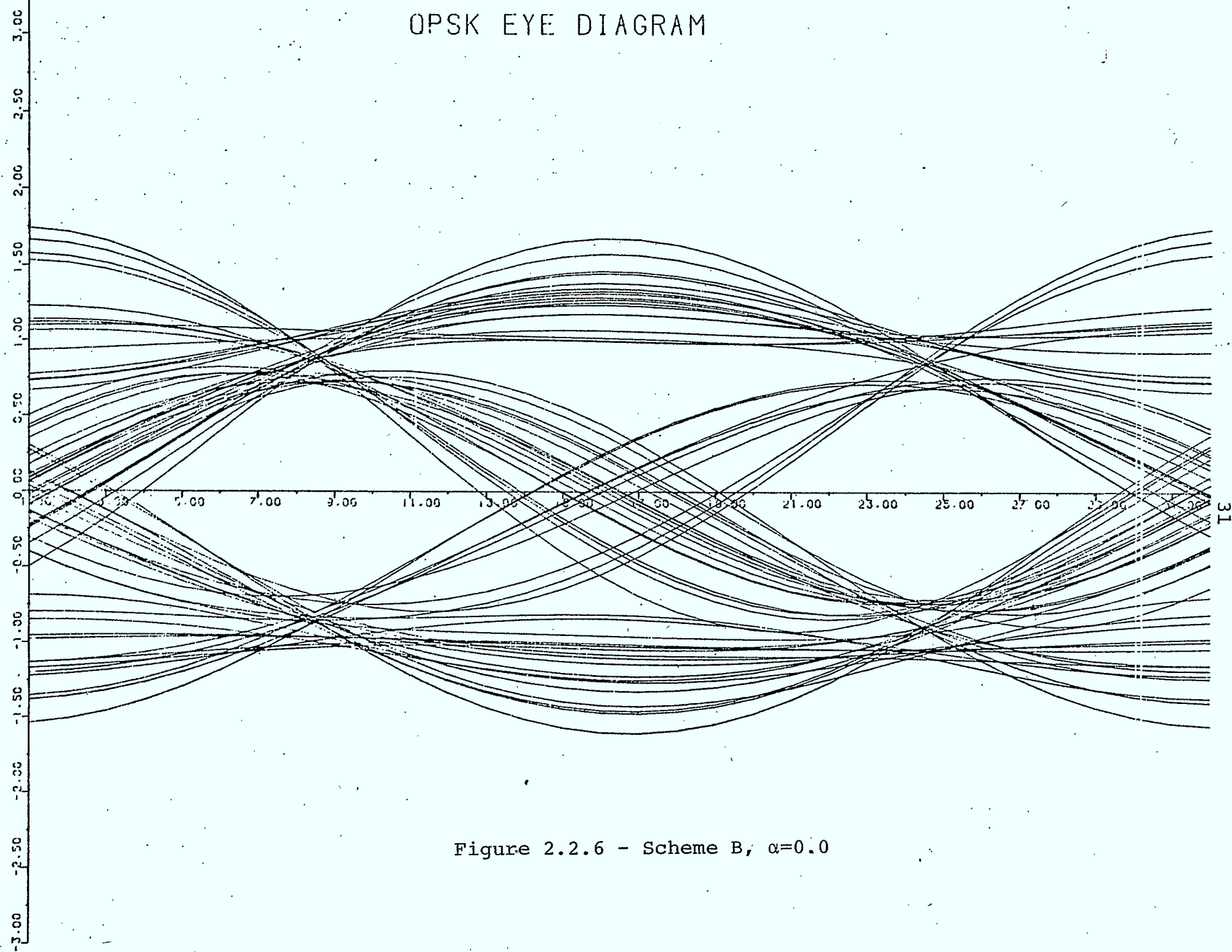


Figure 2.2.6 - Scheme B, $\alpha=0.0$

QPSK EYE DIAGRAM

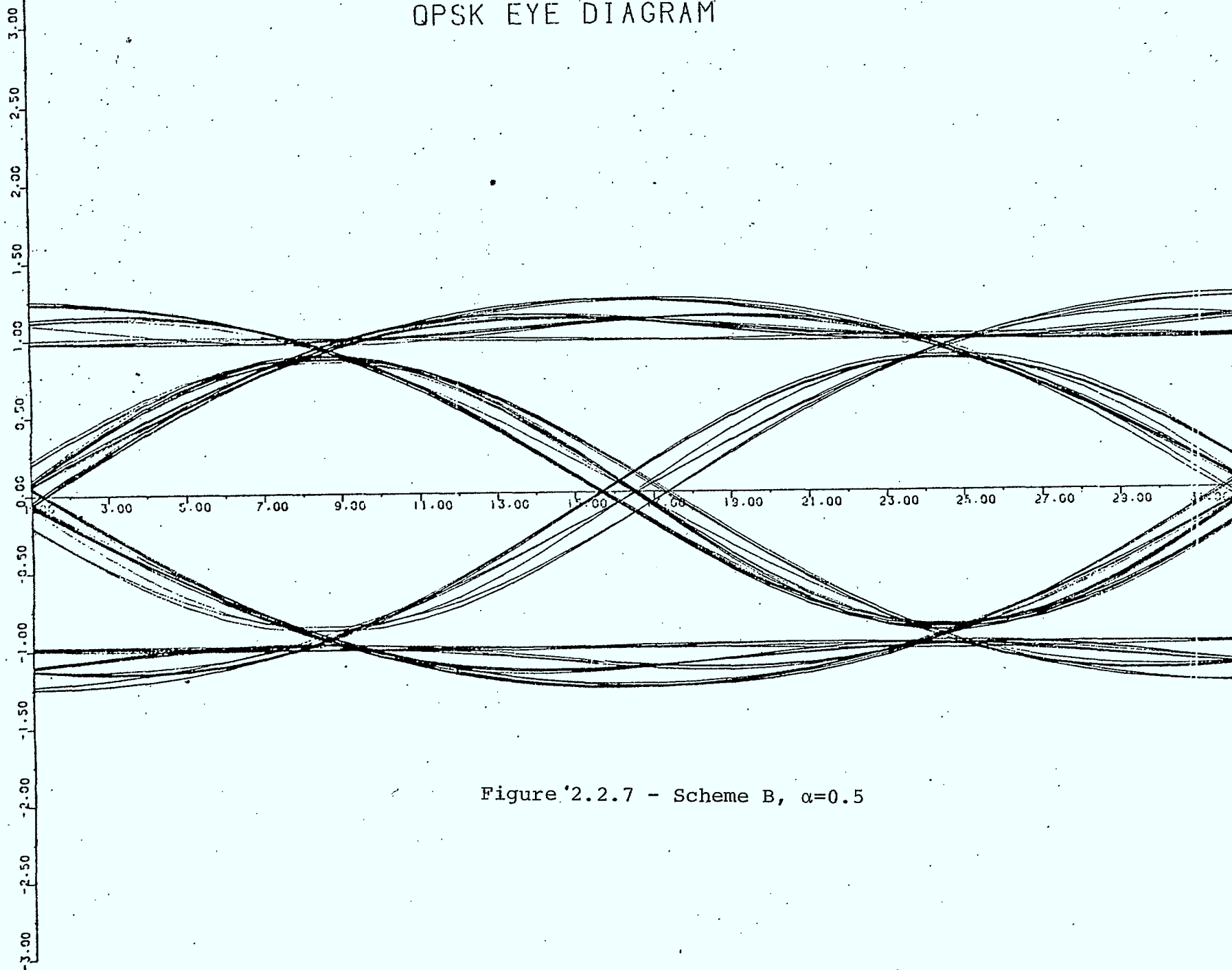


Figure 2.2.7 - Scheme B, $\alpha=0.5$

QPSK EYE DIAGRAM

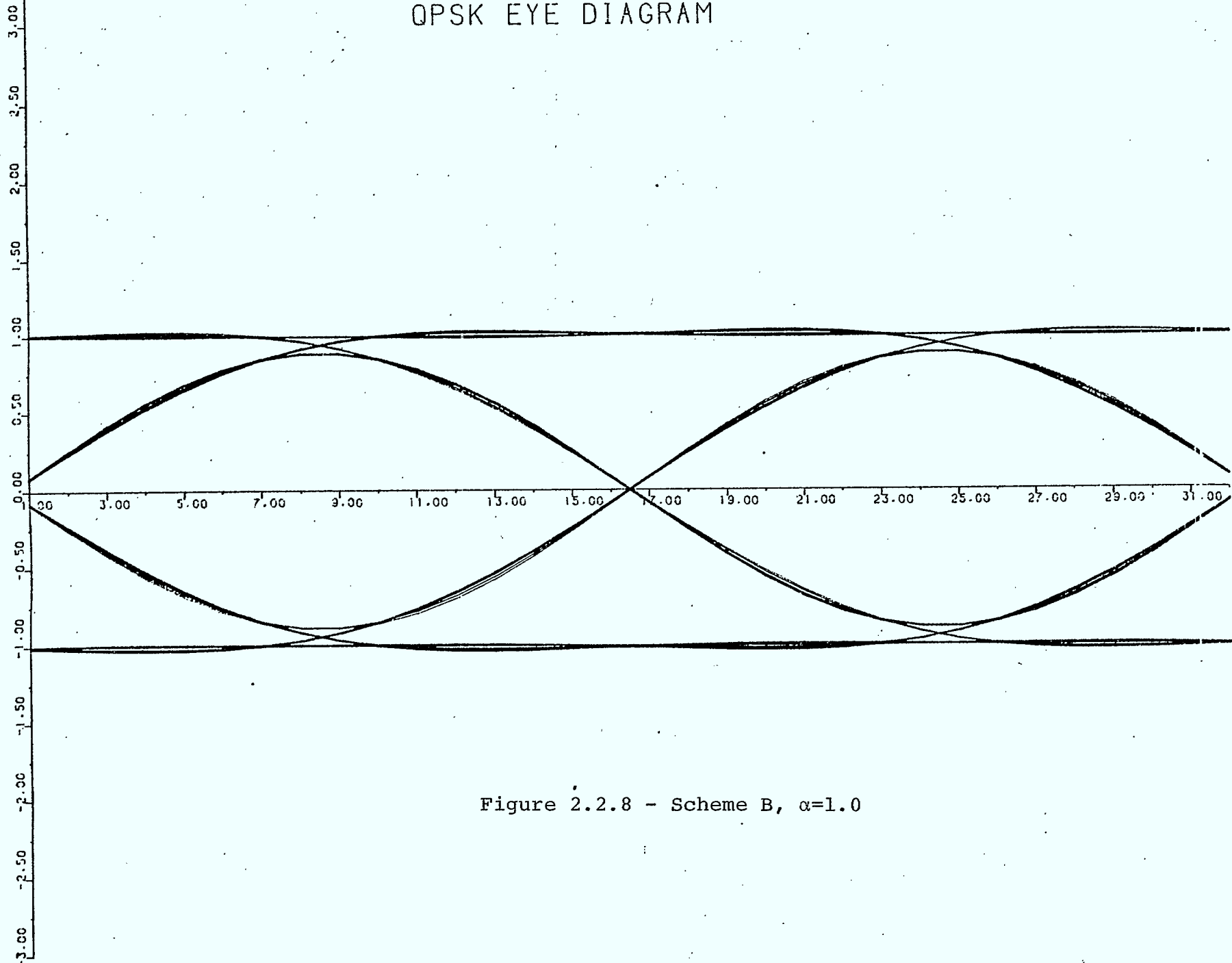


Figure 2.2.8 - Scheme B, $\alpha=1.0$

63%. Since the noise power remains constant at the output in three cases of α (Table 2.2.1) the net effect is a higher E_b/N_o requirement for decreasing α as shown in Fig.

2.2.9-2.2.11. This phenomenon clearly shows that the degradation in P_e is proportional to the eye opening.

Scheme C: Figures 2.2.12-2.2.14 show the eye diagrams for different roll-offs after the receive filter and integrate and dump detection. The ISI present at the sampling instant is more than in scheme B due to more bandlimiting. The noise power decreases with increasing α but so does the eye opening. For $\alpha=0$ the eye opening is 73%, for $\alpha=0.5$ the eye opening is 66% and for $\alpha=1$ the eye opening is 63%. The net effect is higher E_b/N_o requirement for increasing α , as shown in Figs. 2.2.15-2.2.17. This trend is the reverse of that in scheme B and it shows that there is a definite relation between eye opening and P_e degradation.

Table 2.2.1 clearly shows that the best detection scheme is the sampler in a linear channel. This is the scheme that is used for obtaining simulation results for the remainder of this report.

2.3.0 Amplitude and Slope Distortion Effects on QPSK

2.3.1 Introduction

Distortion due to amplitude and group delay slope usually occurs in a satellite channel due to imperfections in the band-pass filter design. In this section,

Table 2.2.1

Degradation for $P_e = 10^{-4}$ and Noise Power for Schemes A, B, C

| | Degradation in dB for $P_e = 10^{-4}$ | | | Noise Power with $N_0 = 1$ | | |
|--------------|--|-----|-----|----------------------------|--------|--------|
| | A | B | C | A | B | C |
| $\alpha=0.0$ | 0.0 | 2.0 | 1.0 | 32.0 | 31.984 | 24.771 |
| $\alpha=0.5$ | 0.0 | 0.8 | 1.4 | 32.0 | 31.984 | 24.172 |
| $\alpha=1.0$ | 0.0 | 0.6 | 1.6 | 32.0 | 31.984 | 22.537 |

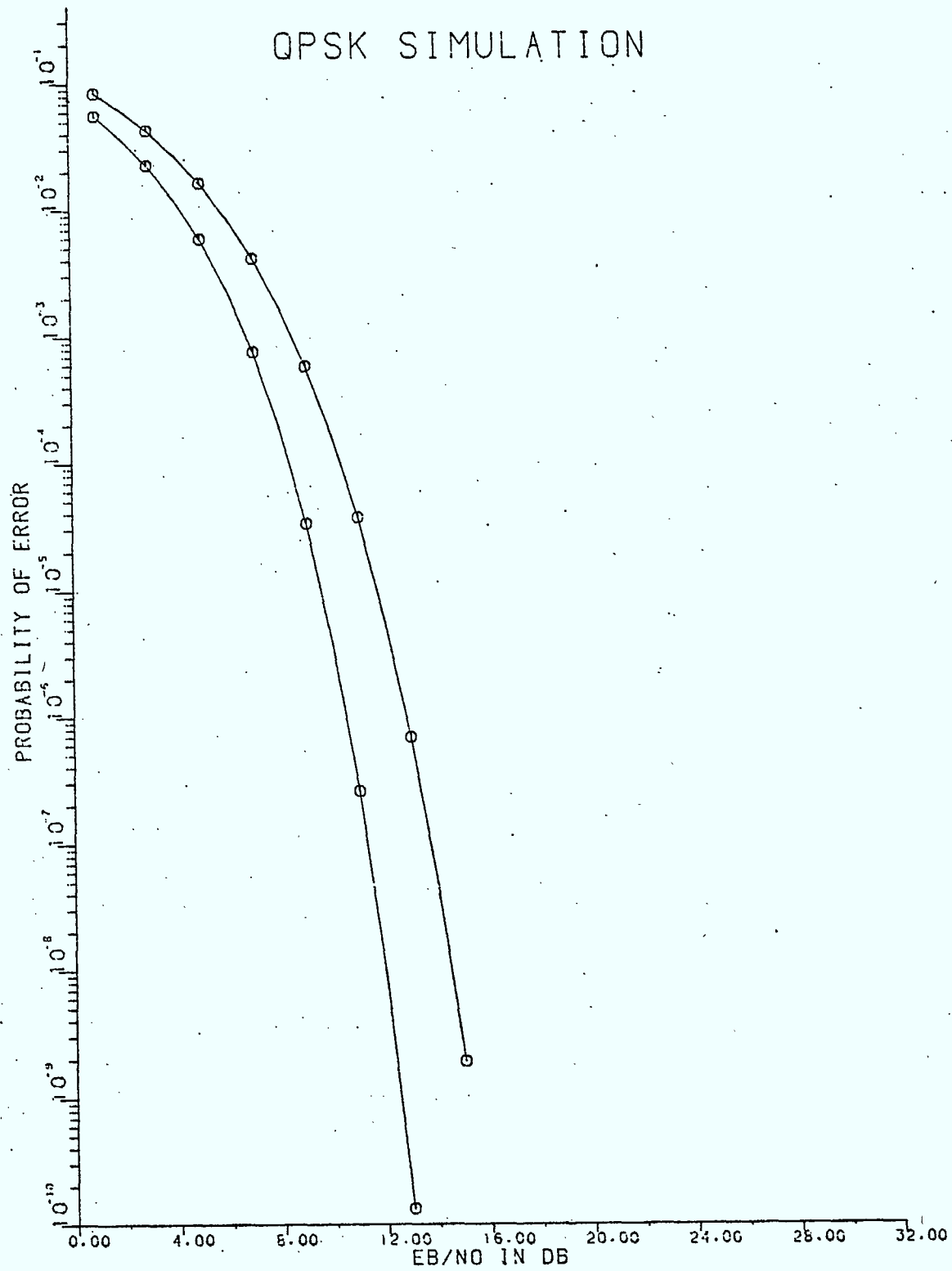


Figure 2.2.9 - E_b/N_o vs P_e , Scheme B, $\alpha=0.0$

QPSK SIMULATION

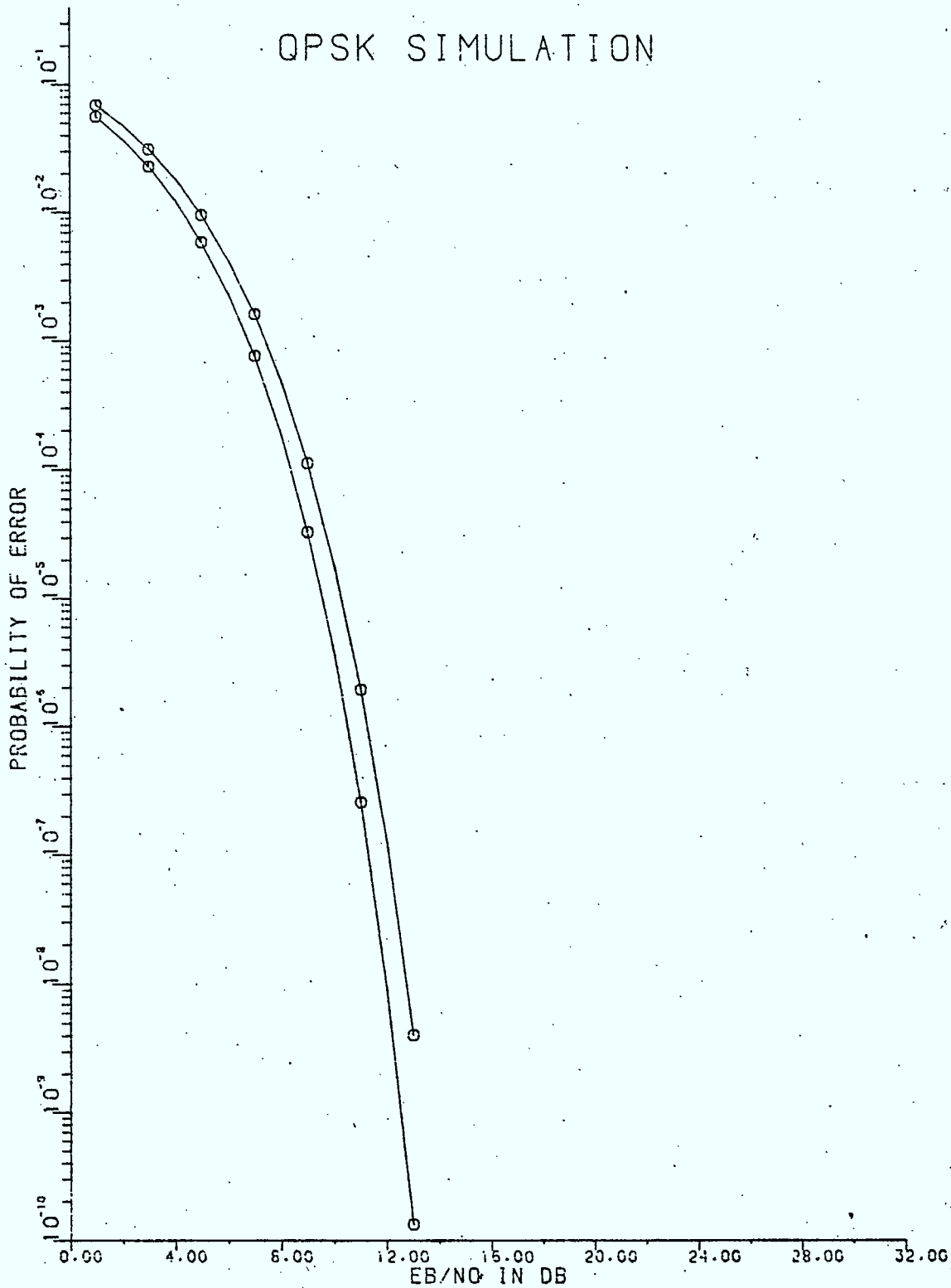


Figure 2.2.10 - E_b/N_0 vs P_e , Scheme B, $\alpha=0.5$

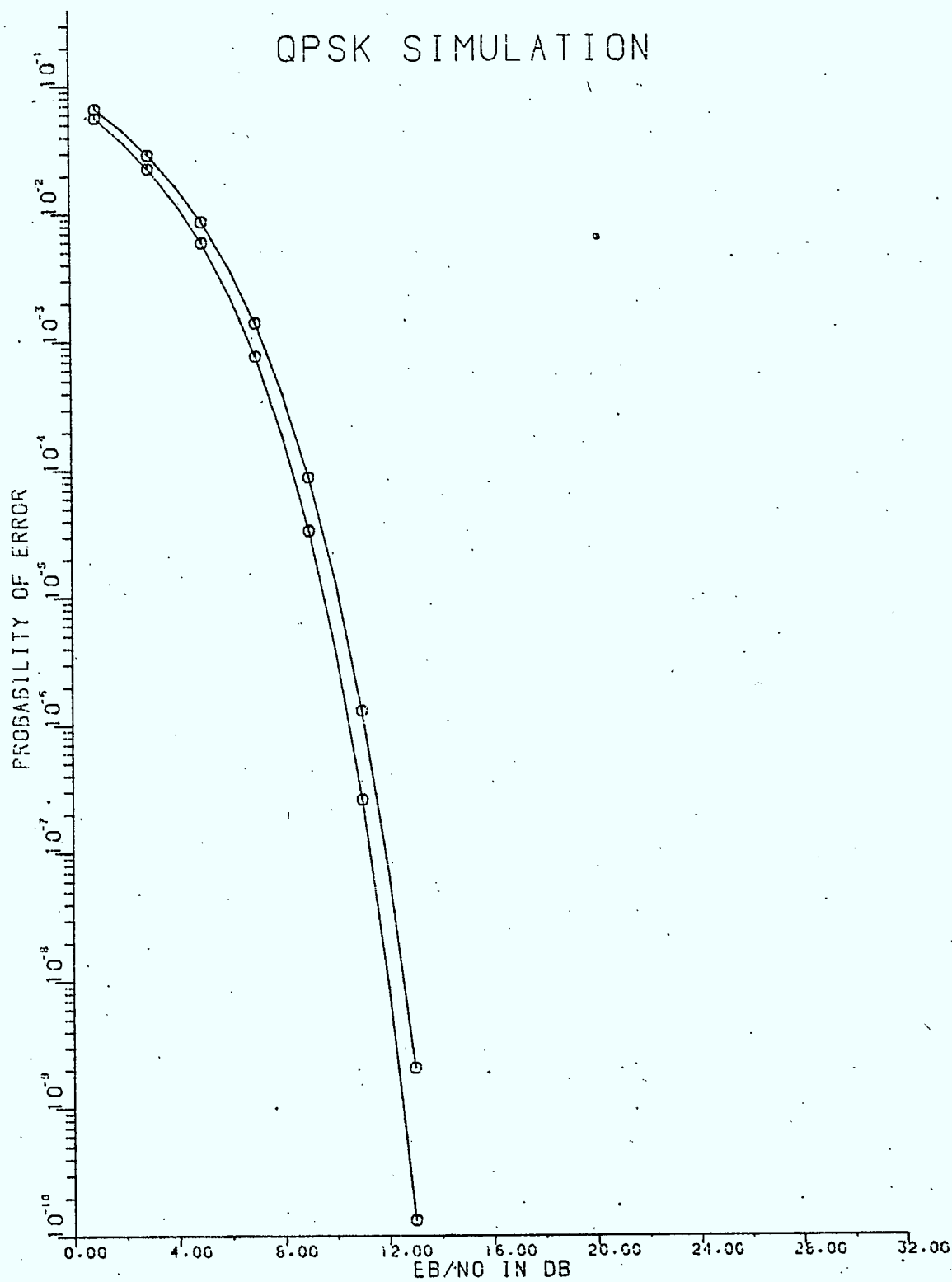


Figure 2.2.11 - E_b/N_0 vs P_e , Scheme B, $\alpha=1.0$

OPSK EYE DIAGRAM

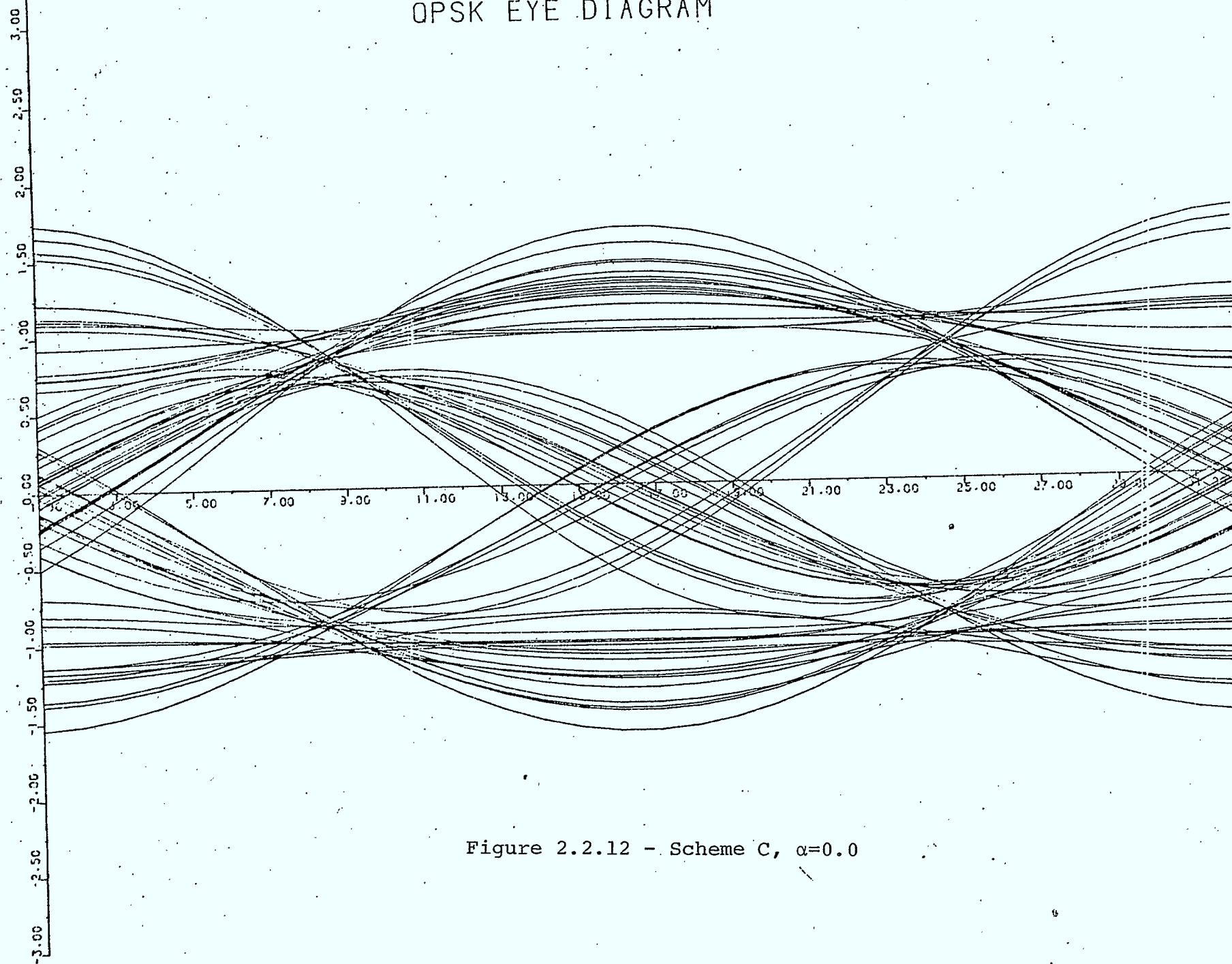


Figure 2.2.12 - Scheme C, $\alpha=0.0$

GPSK EYE DIAGRAM

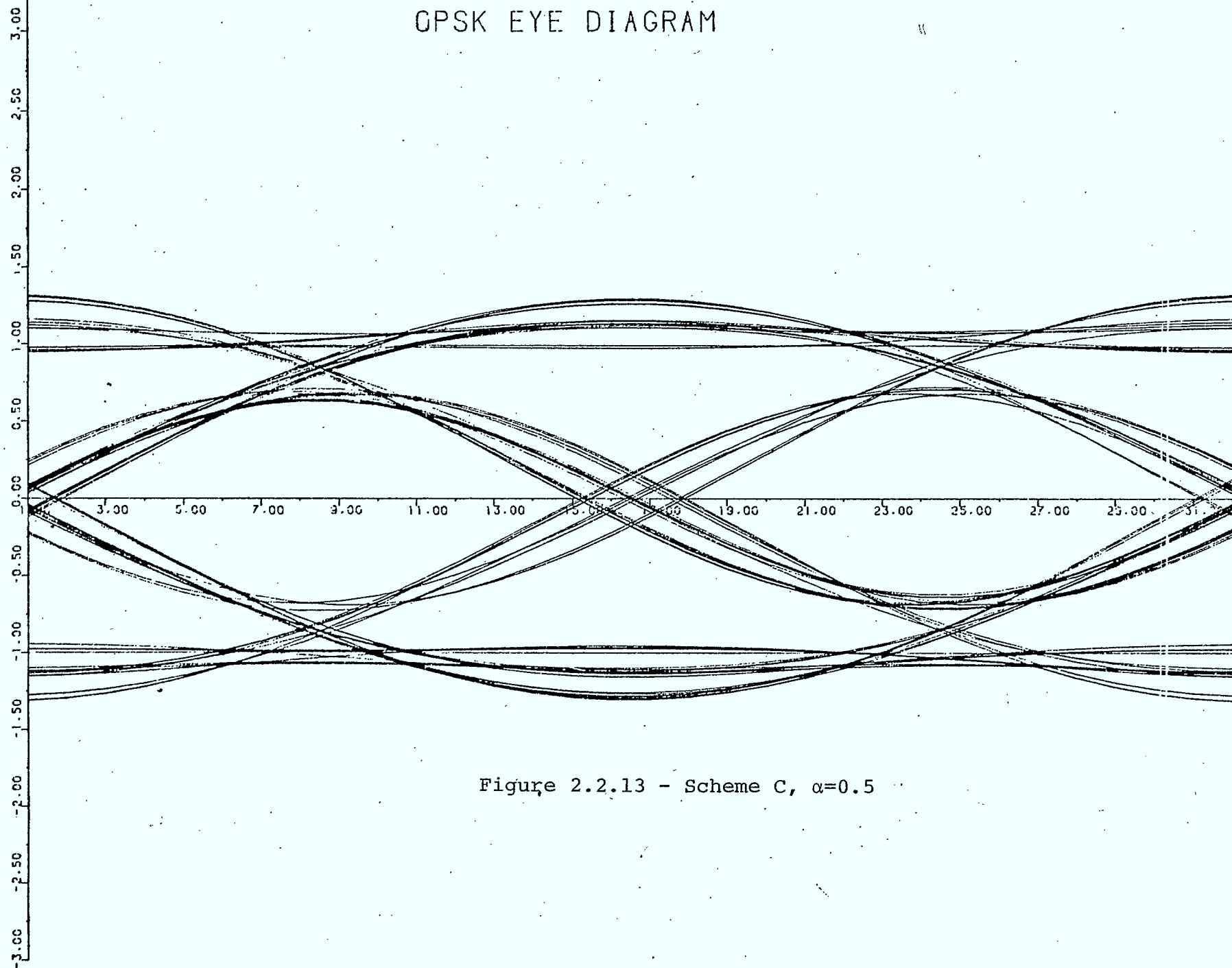


Figure 2.2.13 - Scheme C, $\alpha=0.5$

QPSK EYE DIAGRAM

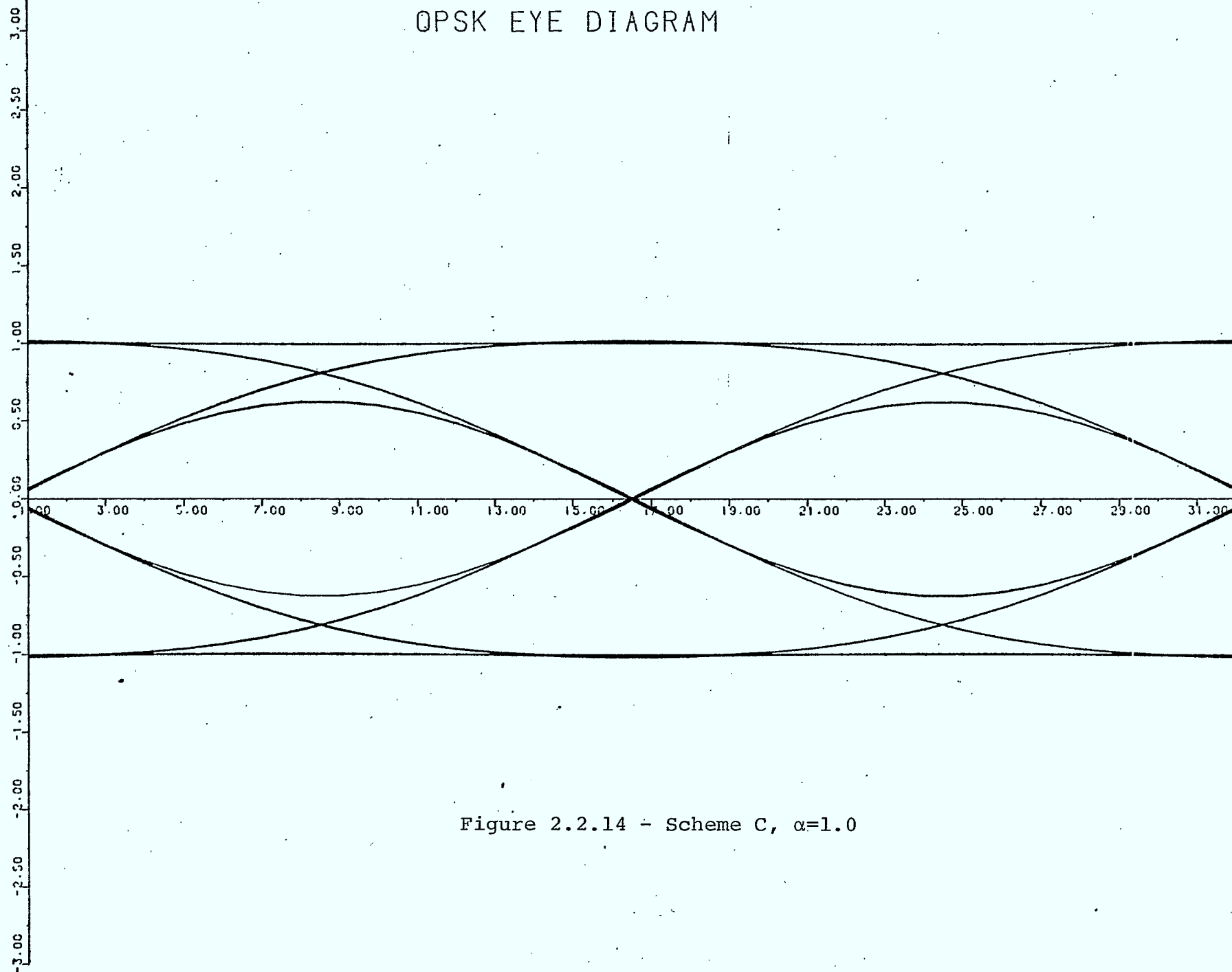
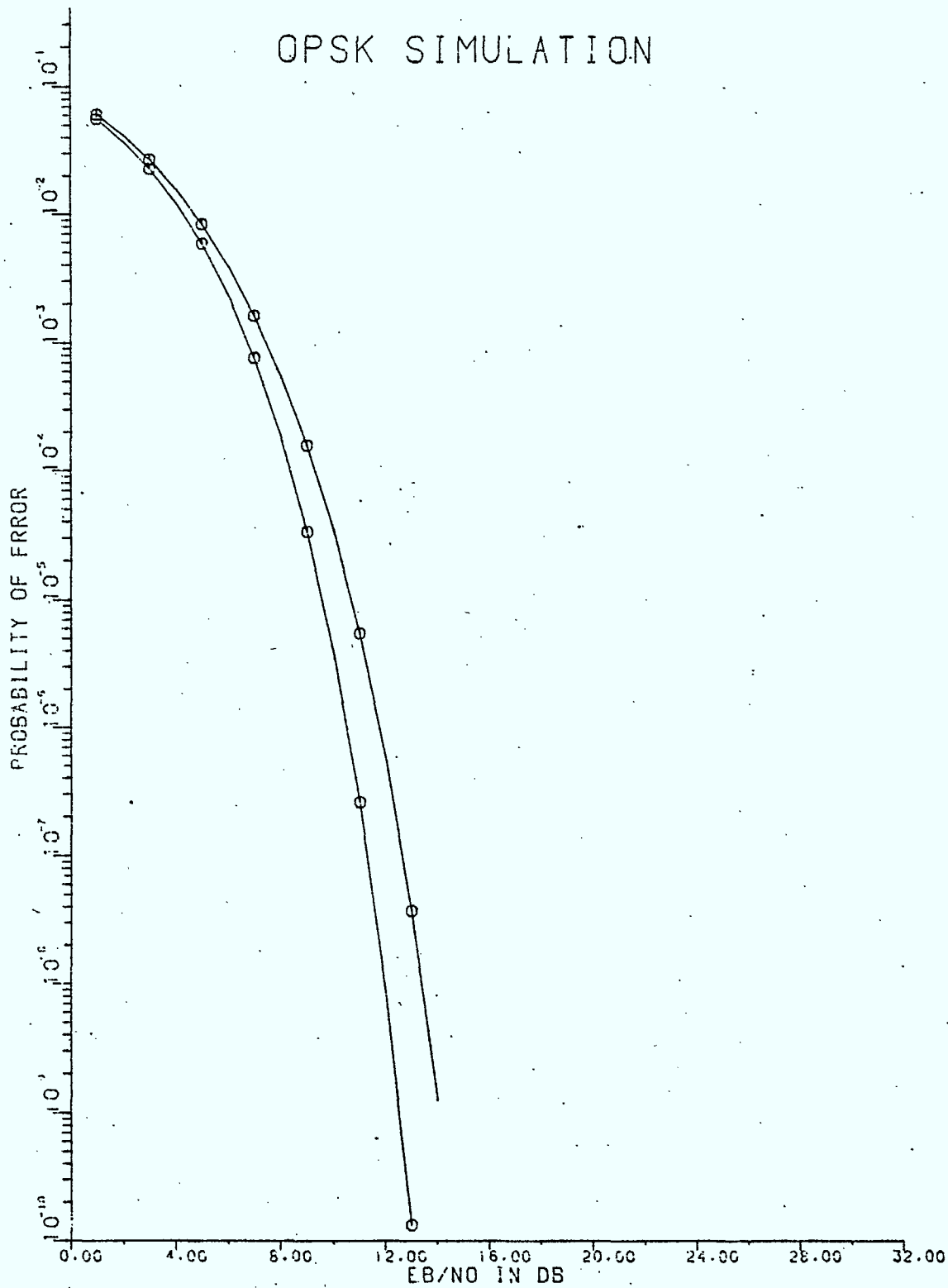


Figure 2.2.14 - Scheme C, $\alpha=1.0$

OPSK SIMULATION

Figure 2.2.15 - E_b/N_o vs P_e , Scheme C, $\alpha=0.0$

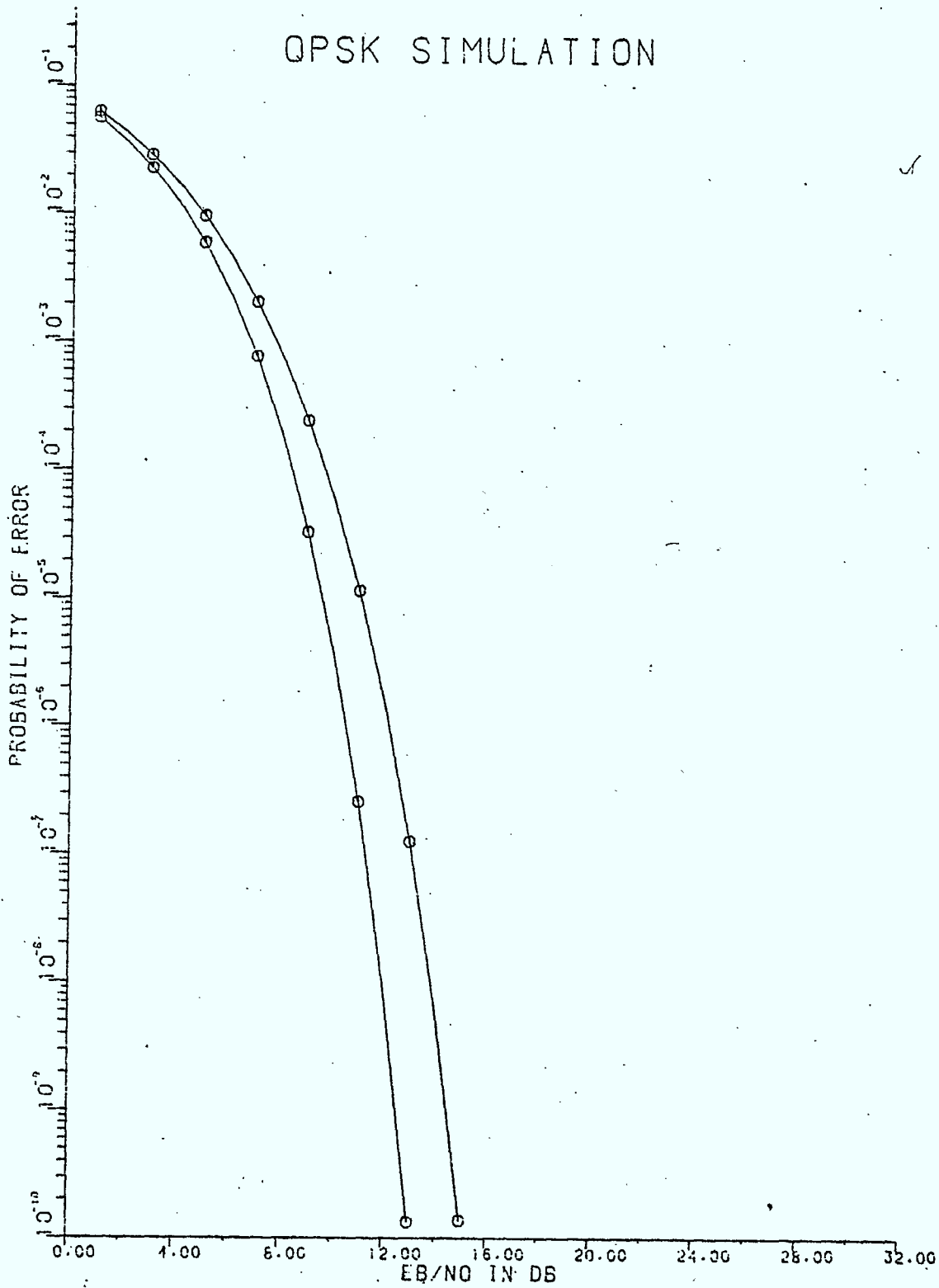


Figure 2.2.16 - E_b/N_o vs P_e , Scheme C, $\alpha=0.5$

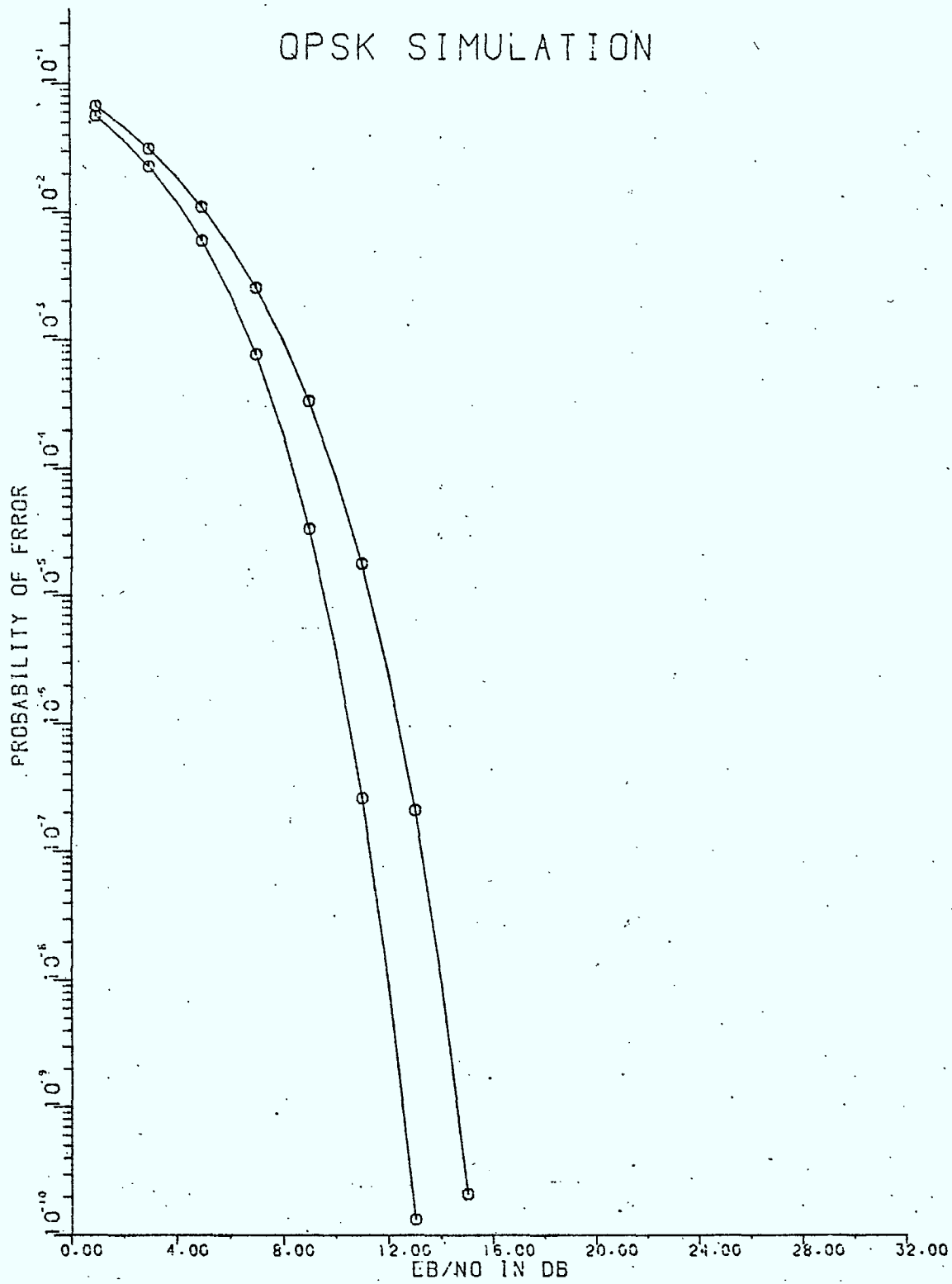


Figure 2.2.17. - E_b/N_0 vs P_e , Scheme C, $\alpha=1.0$

we present the simulation results for QPSK modulation. These results show E_b/N_0 degradation for a probability of error, $P_e = 10^{-4}$ for various amplitude and delay slopes. The model chosen for the study uses transmit and receive filters so as to create a raised cosine spectrum at the output free of intersymbol interference (ISI) as discussed in the previous section. With amplitude or delay slope in the channel ISI occurs. ISI increases as the magnitude of impairments increases, which in turn results in P_e degradation.

2.3.2 Crosstalk

The main source of degradation in P_e is "crosstalk" between I and Q channels. This phenomenon occurs due to either unsymmetry in amplitude or phase characteristic of the composite filter, $T_x(f)s(f)$ (Fig. 2.3.0), where $T_x(f)$ is the root of raised cosine filter and $s(f)$ is the frequency transfer function of the impairment. This unsymmetry results in a complex impulse response of the equivalent baseband filter. The impulse response can be represented by $h_I(t) + jh_Q(t)$ which when convolved by the input signal,

$$x(t) = \sum a_n p(t - nT_s) + j \sum b_n p(t - nT_s) \quad (2.3.1)$$

gives rise to the output signal,

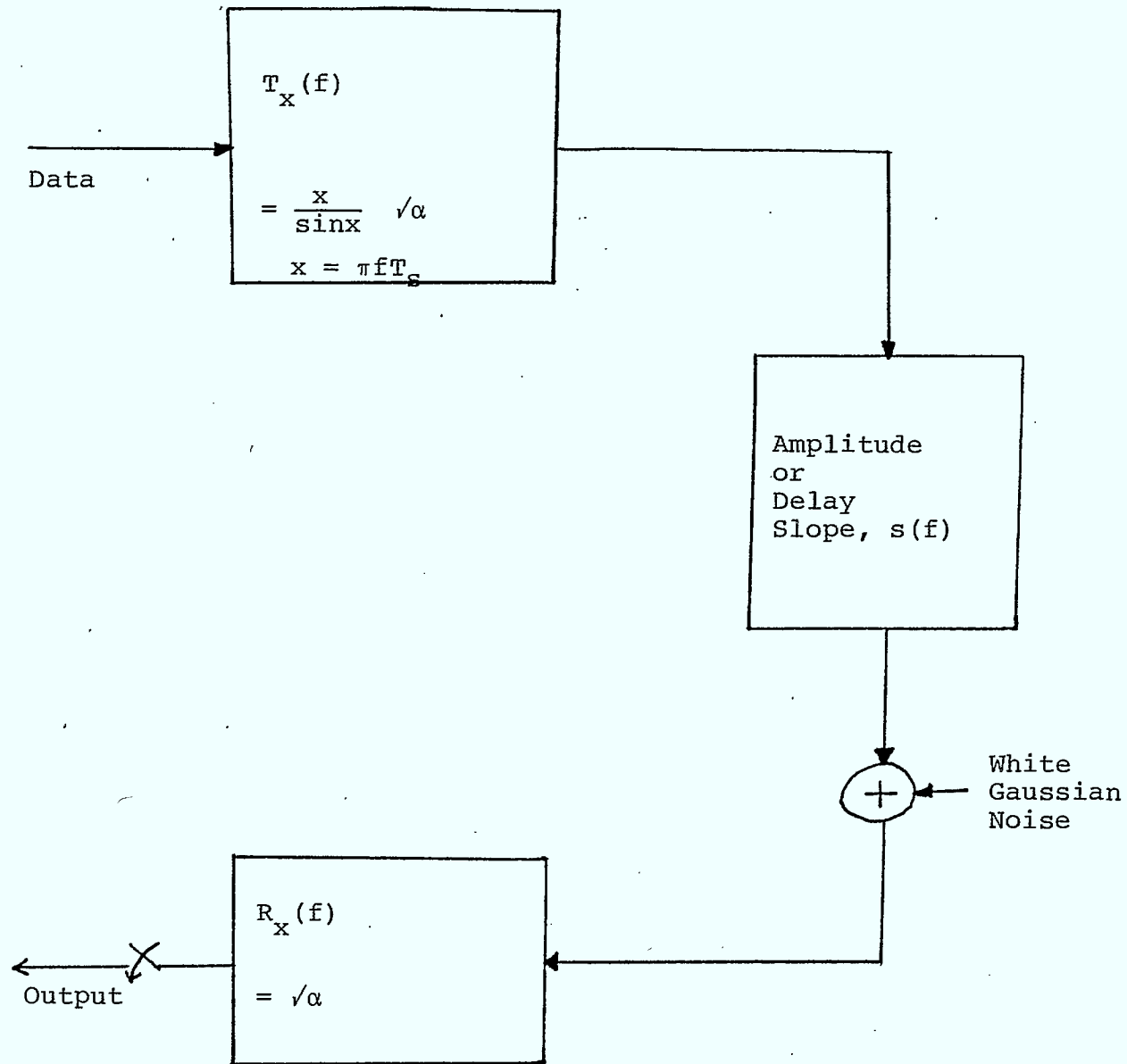


Figure 2.3.0 - Simulation Model

$$\begin{aligned}
y(t) &= [\Sigma a_n p(t-nT_s) + j \Sigma b_n p(t-nT_s)] * [h_I(t) + j h_Q(t)] \\
&= [\Sigma a_n p(t-nT_s) * h_I(t) - \Sigma b_n p(t-nT_s) * h_Q(t)] \\
&\quad \text{crosstalk term in I channel} \\
&\quad + j [\Sigma b_n p(t-nT_s) * h_I(t) + \Sigma a_n p(t-nT_s) * h_Q(t)] \quad (2.3.2) \\
&\quad \text{crosstalk term in Q channel}
\end{aligned}$$

Thus, from Equ.2.3.2 it is seen that crosstalk occurs due to the complex impulse response of the filter.

2.3.3 Modelling Impairments for Computer Simulation

i) Amplitude Slope

Amplitude slope is defined in terms of dB per MHz.

If it is 'a' dB/MHz, then

$$20 \log \frac{A_{f_1}}{A_{f_2}} = a$$

$$\text{or } A_{f_1} = A_{f_2} 10^{a/20} \quad (2.3.3)$$

where A_{f_1} and A_{f_2} are the amplitudes at frequencies f_1 and f_2 respectively. This illustrates that to simulate this type of slope the amplitude at each frequency is weighted by $10^{a/20}$.

ii) Group Delay Slope

Group delay slope is defined in terms of ns per MHz. If it is 'b' ns/MHz, then

$$\frac{d\tau}{df} = b \times 10^{-15} \text{ sec /MHz} \quad (2.3.4)$$

where τ is the group delay. The phase ' ϕ ' is derived by using the relationship

$$\tau = \frac{-d\phi}{d\omega} = -\frac{1}{2\pi} \frac{d\phi}{df} \quad (2.3.5)$$

Substituting Equ. (2.3.5) into Equ. (2.3.4) for τ ,

$$\frac{d^2\phi}{df^2} = -2\pi \times b \times 10^{-15}$$

$$\text{or } \phi = -\pi \times b \times 10^{-3} \times f^2 \quad (2.3.6)$$

where f is in MHz. To simulate this kind of slope the phase given in Eq. (2.3.6) is added to the phase of the transmit filter, $T_x(f)$.

2.3.4 Numerical Results

The bit rate used in the simulation is 128 Mb/s (64 Megabauds) with different roll-offs for the raised cosine filter (Fig. 2.3.0), namely, 0.0, 0.5 and 1.0. The eye diagrams to be discussed below correspond to the I channel of QPSK modulation for two symbol periods.

Figure 2.3.1 shows the degradation in E_b/N_0 from theory (8.4 dB) for a $P_e = 10^{-4}$ for various amplitude slopes. The curves are simulated for different roll-off ' α ' of square root of raised cosine filters ($T_x(f)$ and $R_x(f)$). Figures 2.3.2 to 2.3.6 show the eye diagrams for

$\alpha = 0.5$ with various amplitude slopes. As can be seen from Fig. 2.3.1. the degradation is greater as the amplitude slope increases. The eye opening decreases due to ISI as impairment increases. The interesting feature to be noted is that for a constant amplitude slope the degradation in P_e is more for $\alpha=0$ than for $\alpha=1$. This means that ISI increases as α decreases. For example, Figures 2.3.7-2.3.8 show the eye diagrams for $\alpha=0$ and $\alpha=1$ for our amplitude slope of .175 dB/MHZ. The eye opening for $\alpha=0$ (Fig. 2.3.7) is 33%, for $\alpha=0.5$ (Fig. 2.3.6) is 66% while for $\alpha=1$ (Fig. 2.3.8) is 90%. Thus the ISI increases as ' α ' decreases for a given amplitude slope as shown in Fig. 2.3.1.

Fig. 2.3.9 shows the curves for various delay slopes with different roll-offs ' α '. Figures 2.3.10-2.3.14 show the eye diagrams for $\alpha=0.5$ with various delay slopes. The eye opening decreases as impairment increases for a given α . Here, the feature to be noted is that degradation in E_b/N_0 is more for $\alpha=1$ than for $\alpha=0$. This means that ISI is higher as α increases. Figures 2.3.15-2.3.16 show the eye diagrams for $\alpha=0$ and $\alpha=1$ for a delay slope of .175 ns/MHz. The eye opening for $\alpha=0$ (Fig. 2.3.15) is 75%, for $\alpha=0.5$ is 54% and for $\alpha=1$ is 36%. Thus, the ISI increases as ' α ' increases for a given delay slope as shown in Fig.(2.3.9).

For ease of comparison, the impairments chosen were such that the slope in the Nyquist bandwidth was the same as that of Reference [3]. For example, D. Morais et al [3] used 44.7 Mb/s and .1 dB/MHz corresponds to approximately 2.25 dB in Nyquist bandwidth. In our case, it corresponds to .035 dB/MHz for a bit rate of 128 Mb/s. The roll-off, $\alpha=0.5$, approximates their case and degradation in P_e for amplitude slope in our case is of the same order as in Reference [3]. The delay slope degradation given in this Reference [3] defines group delay as $\tau = -\frac{d\phi}{df}$ instead of the classical definition of $\tau = -\frac{d\phi}{d\omega}$ and hence their results show delay slope has very little impact on degradation in P_e which is not true as shown in this section with conventional formula.

This section studied the effects of amplitude and group delay slopes in a satellite channel with various roll-offs for filters.

Conclusion

Three detection schemes were considered in this chapter and showed that a receive filter followed by a sampler is optimum for a Nyquist channel compared to other sub-optimum schemes. The amplitude and group delay distortion effects in this channel which are of interest to a filter designer were also presented.

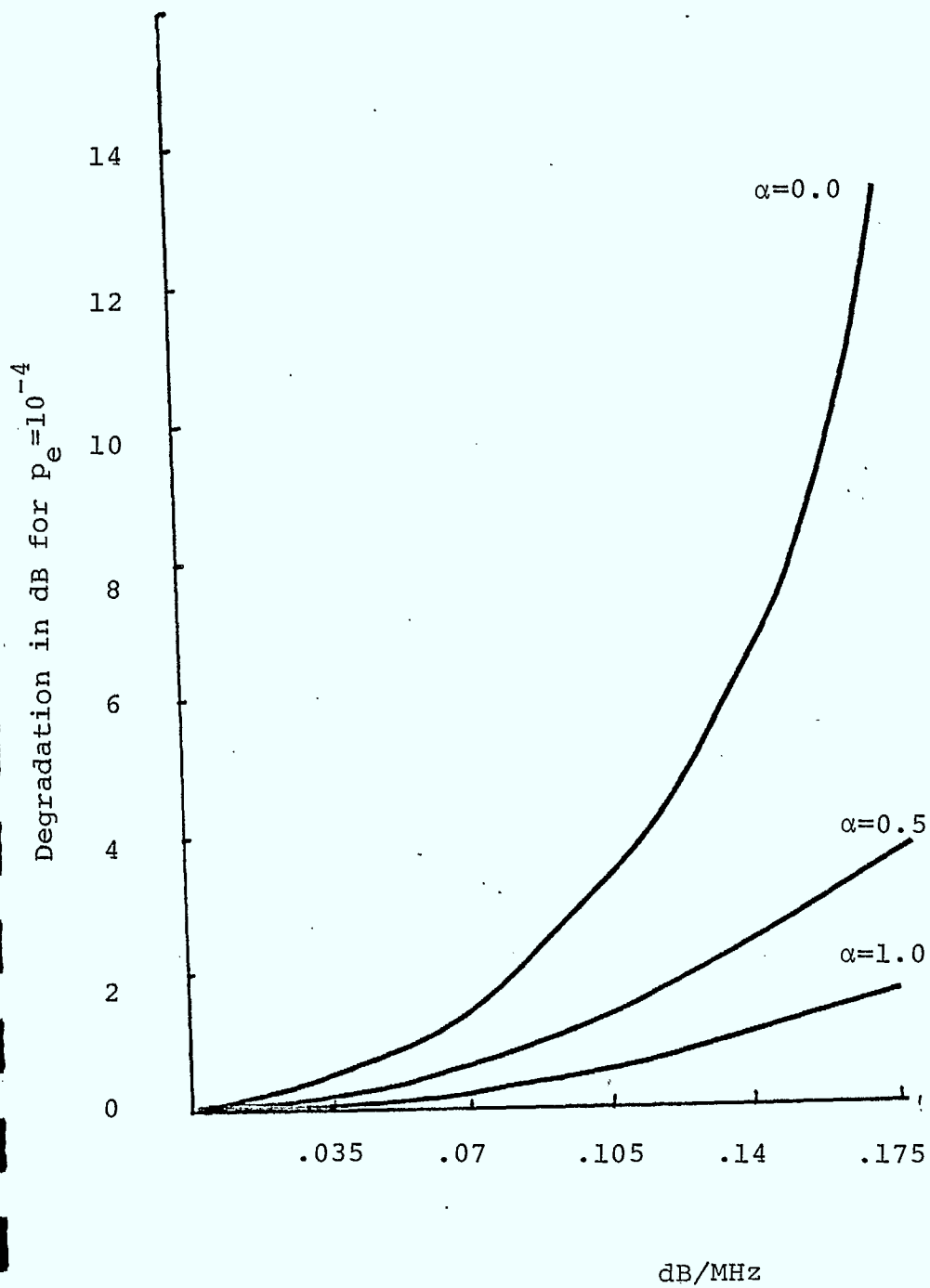


Figure 2.3.1 - Simulated Degradation in E_b/N_0 due to Amplitude Slope for Various Roll-offs

QPSK EYE DIAGRAM

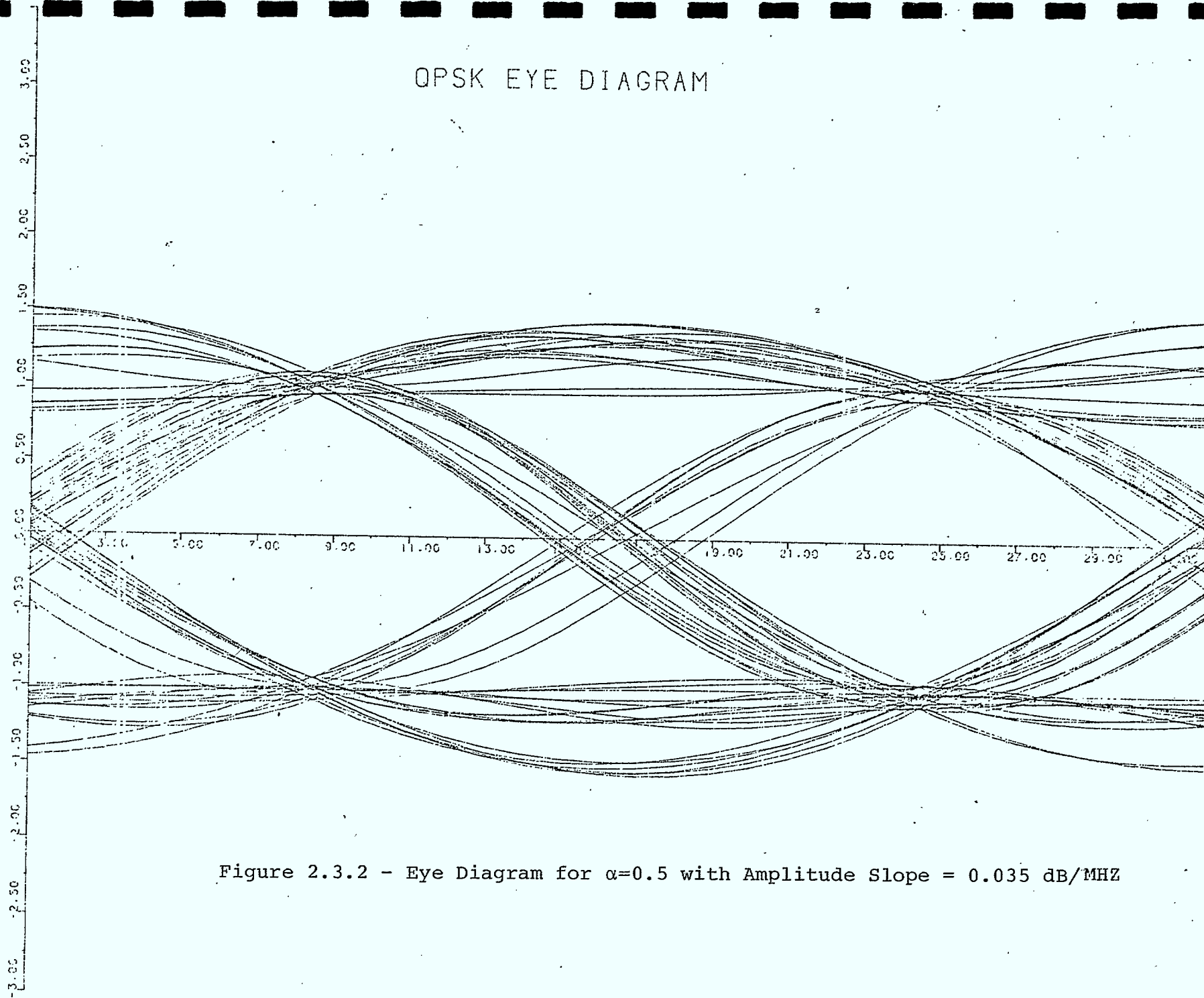


Figure 2.3.2 - Eye Diagram for $\alpha=0.5$ with Amplitude Slope = 0.035 dB/MHZ

OPSK EYE DIAGRAM

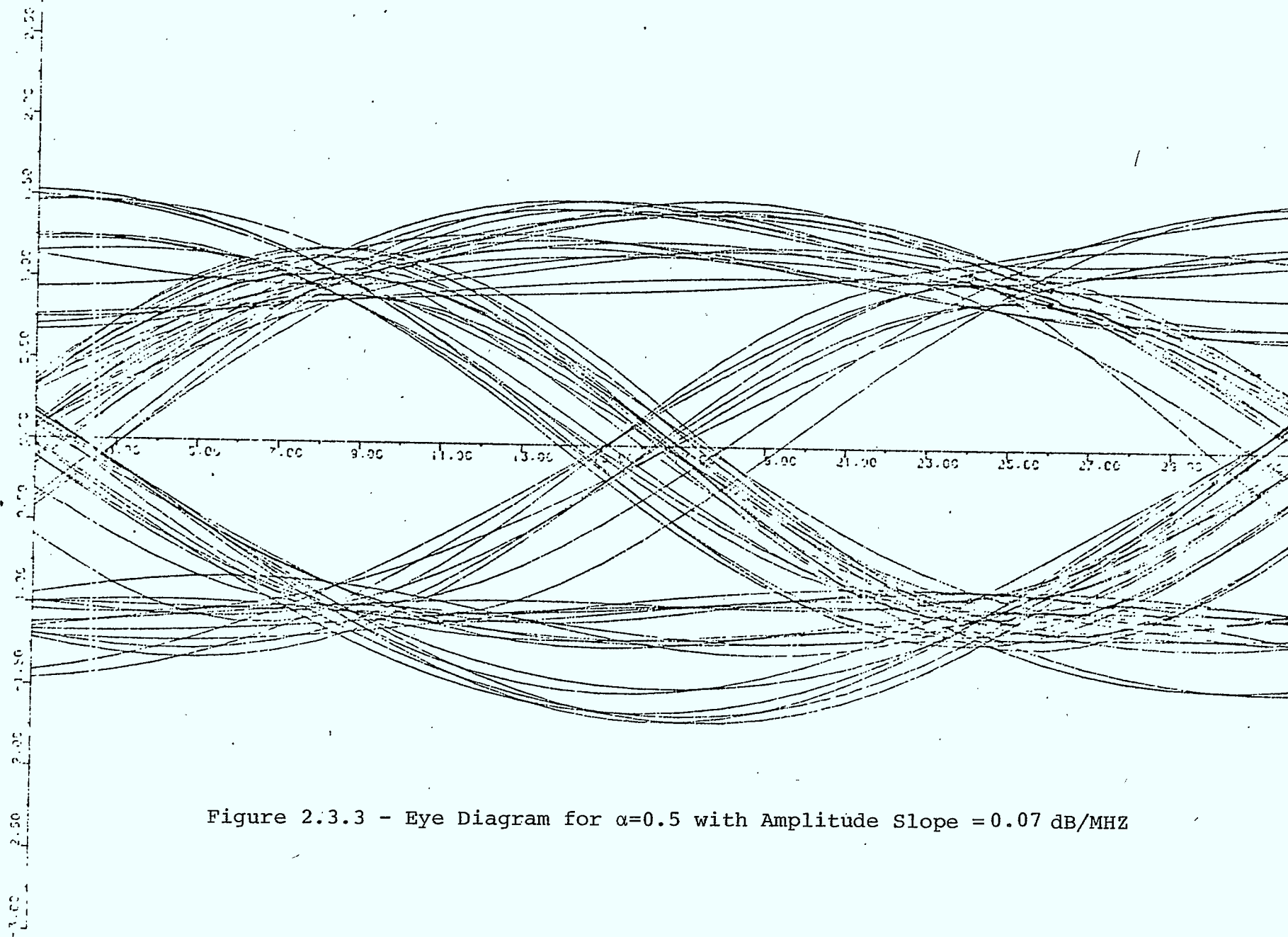


Figure 2.3.3 - Eye Diagram for $\alpha=0.5$ with Amplitude Slope = 0.07 dB/MHz

OPSK EYE DIAGRAM

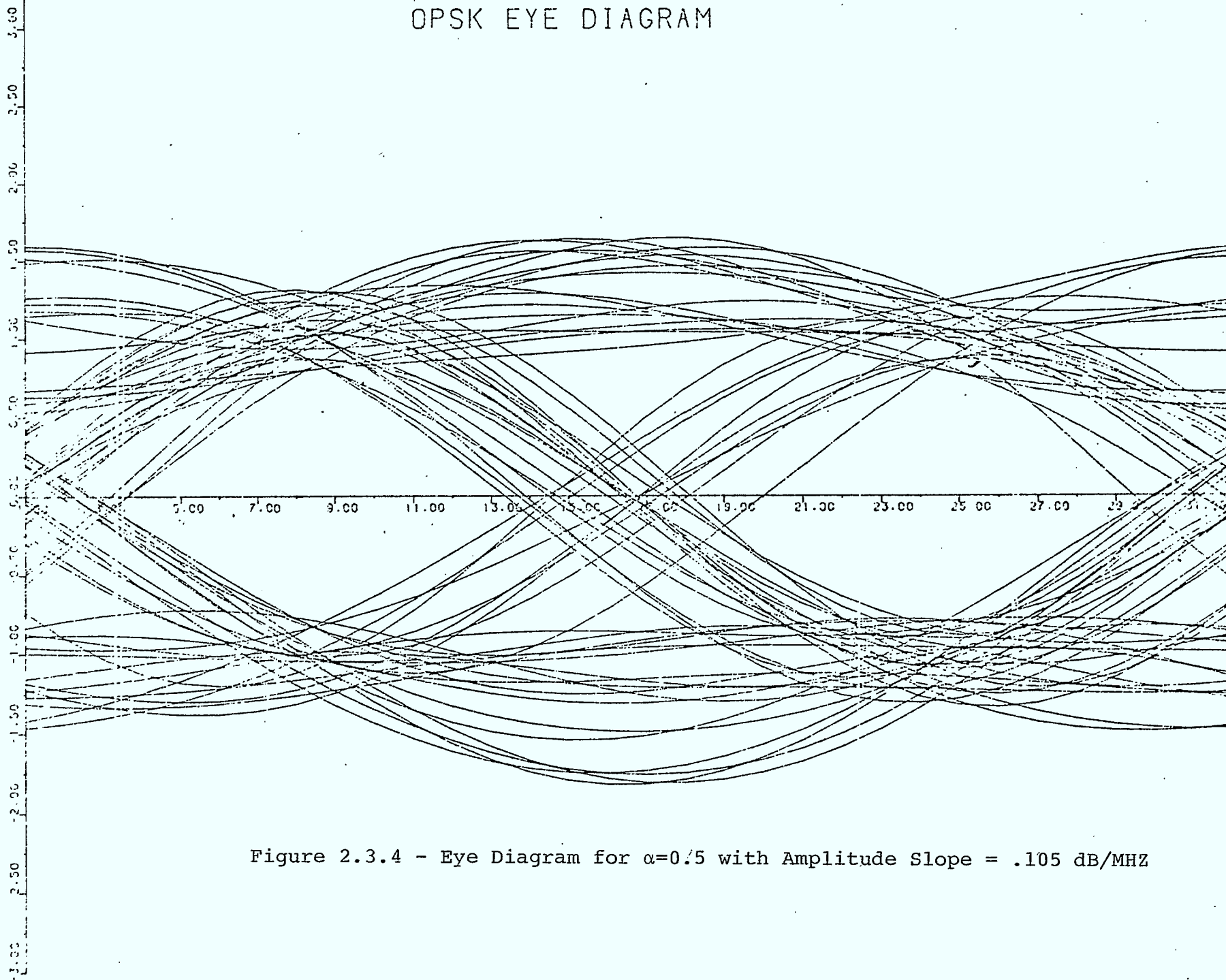


Figure 2.3.4 - Eye Diagram for $\alpha=0.5$ with Amplitude Slope = .105 dB/MHZ

OPSK EYE DIAGRAM

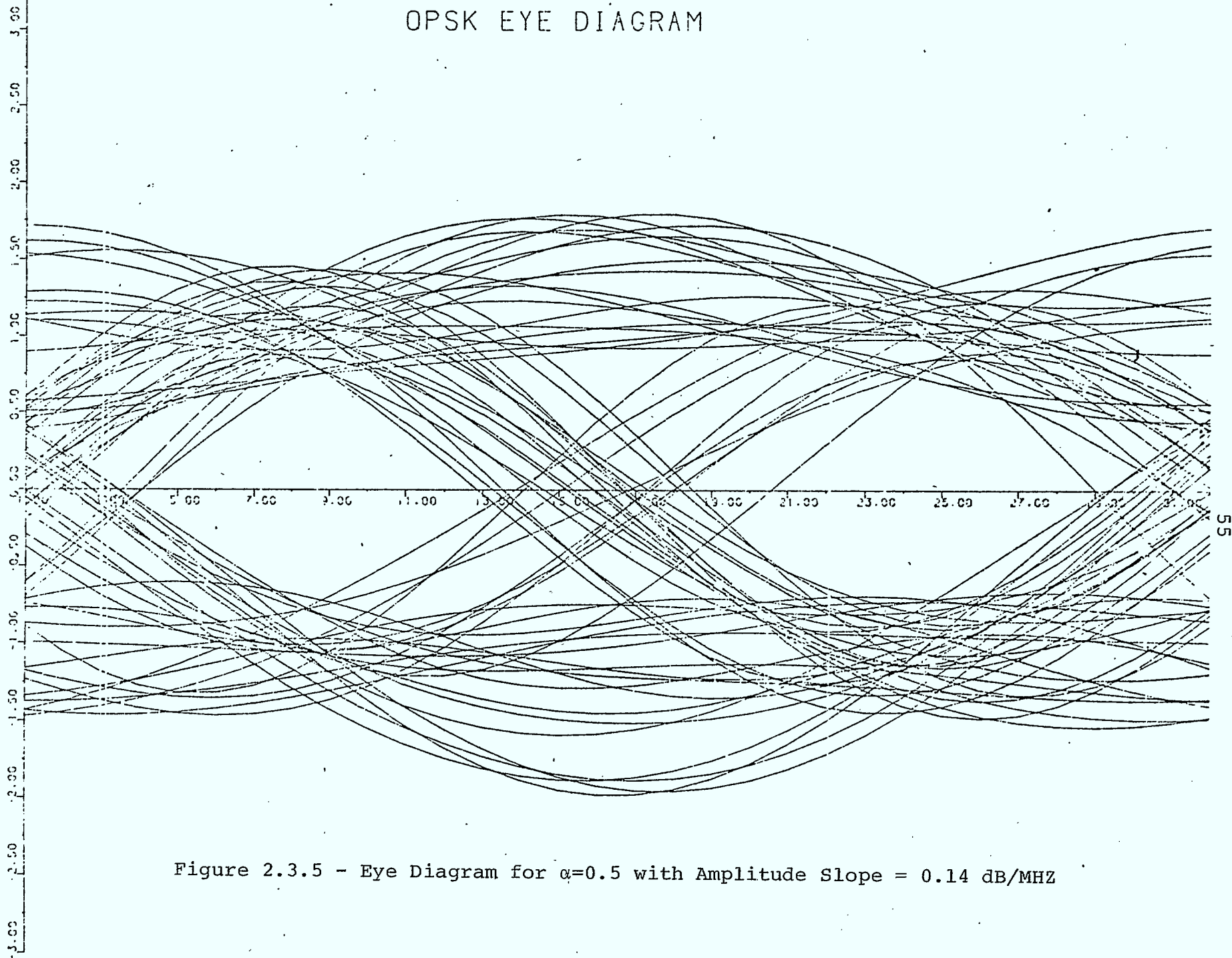


Figure 2.3.5 - Eye Diagram for $\alpha=0.5$ with Amplitude Slope = 0.14 dB/MHZ

OPSK EYE DIAGRAM

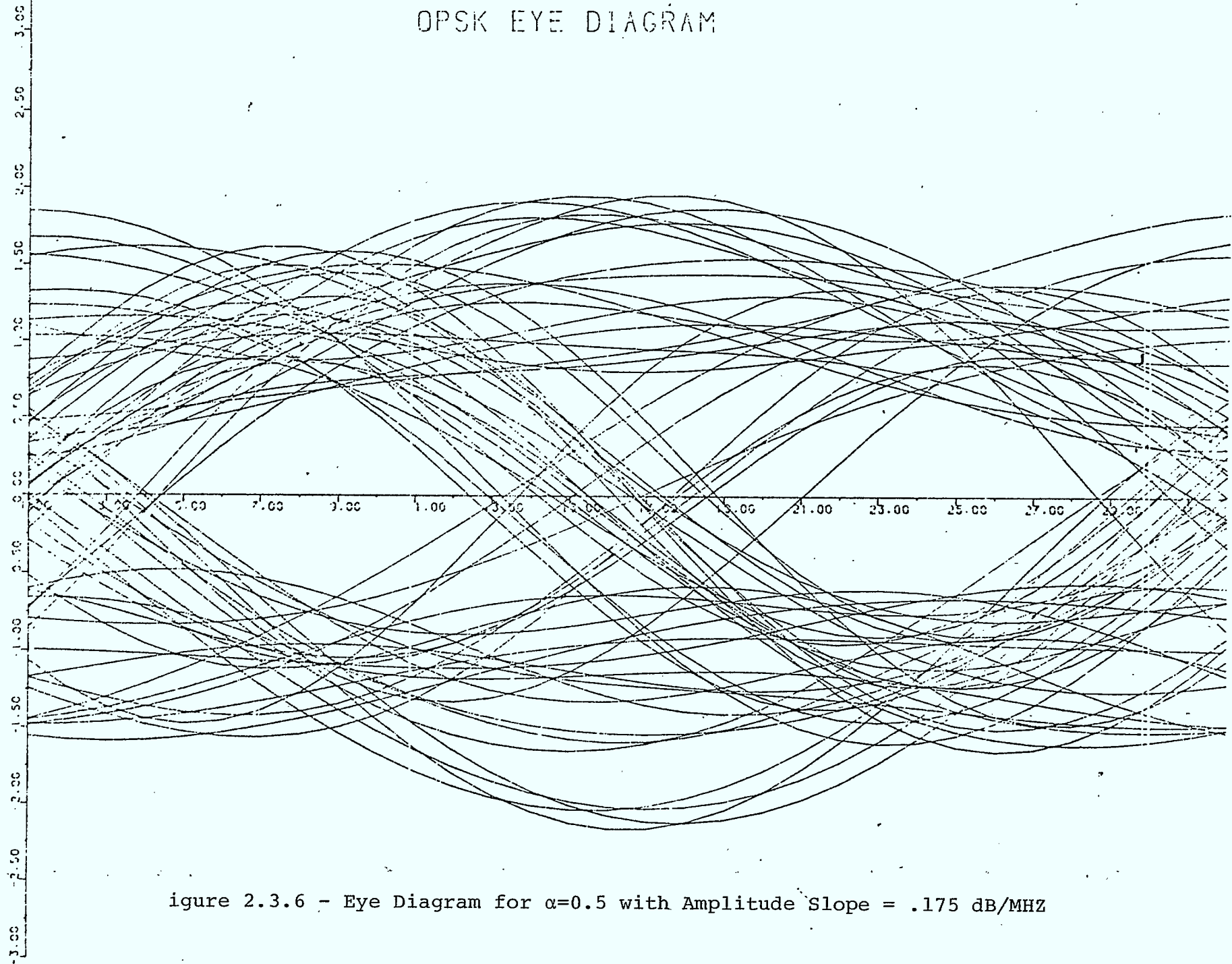


figure 2.3.6 - Eye Diagram for $\alpha=0.5$ with Amplitude Slope = $.175 \text{ dB/MHz}$

OPSK EYE DIAGRAM

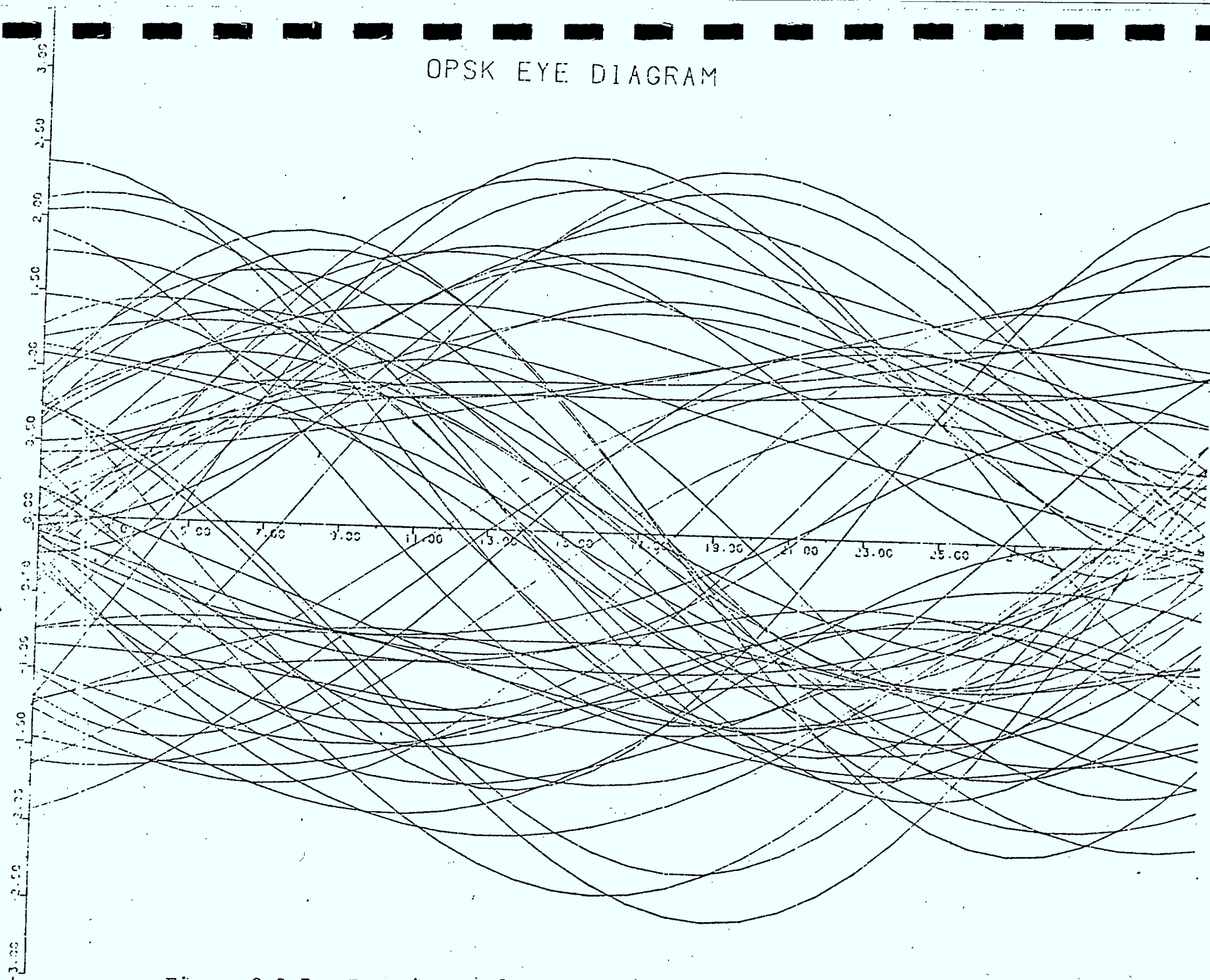


Figure 2.3.7 - Eye Diagram for $\alpha=0.0$ with Amplitude Slope = $.175 \text{ dB/MHZ}$

OPSK EYE DIAGRAM

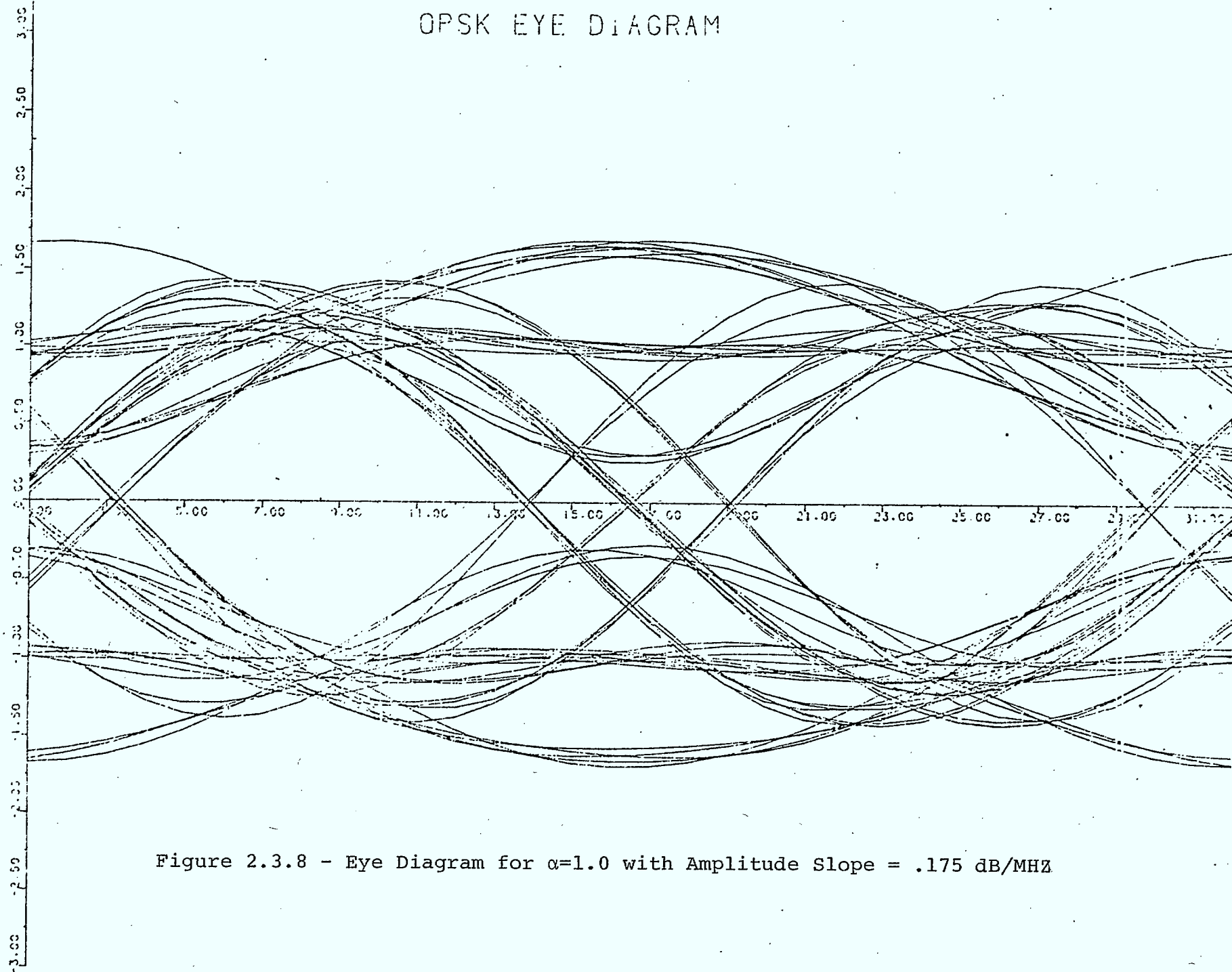


Figure 2.3.8 - Eye Diagram for $\alpha=1.0$ with Amplitude Slope = .175 dB/MHZ

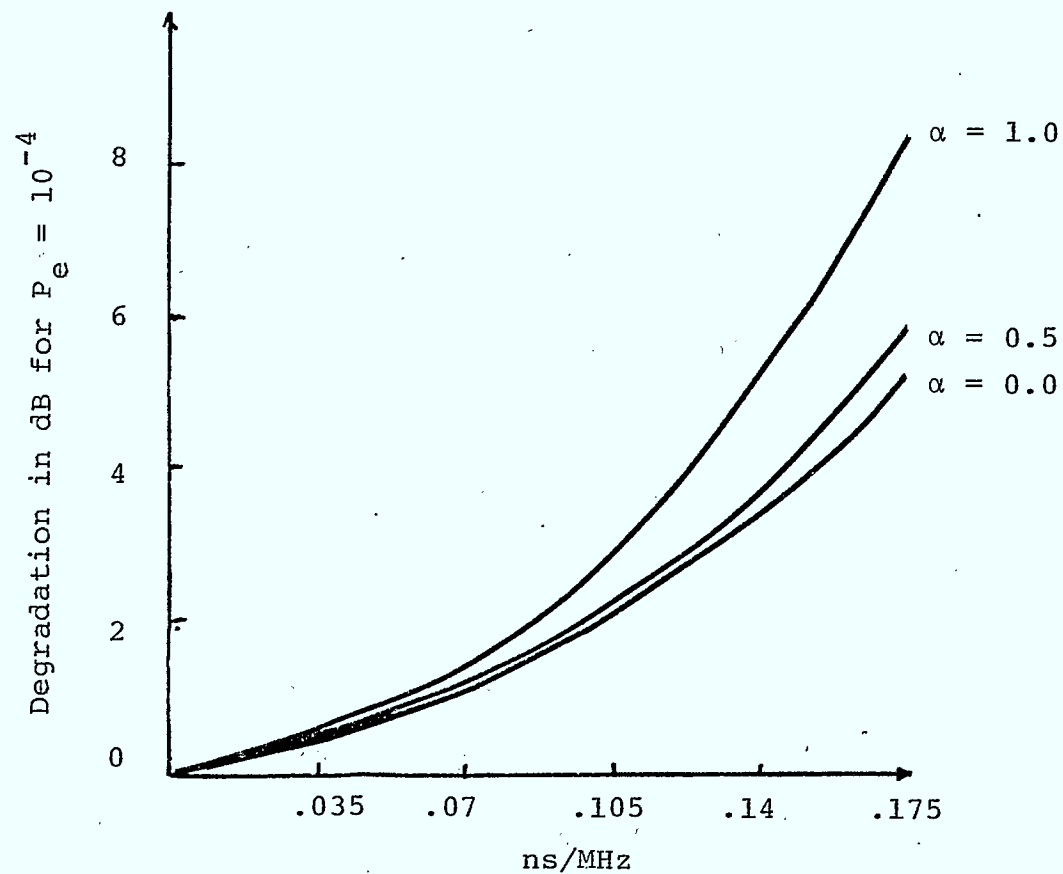


Figure 2.3.9 - Simulated Degradation in E_b/N_o due to Delay Slope for Various Roll-offs

QPSK EYE DIAGRAM

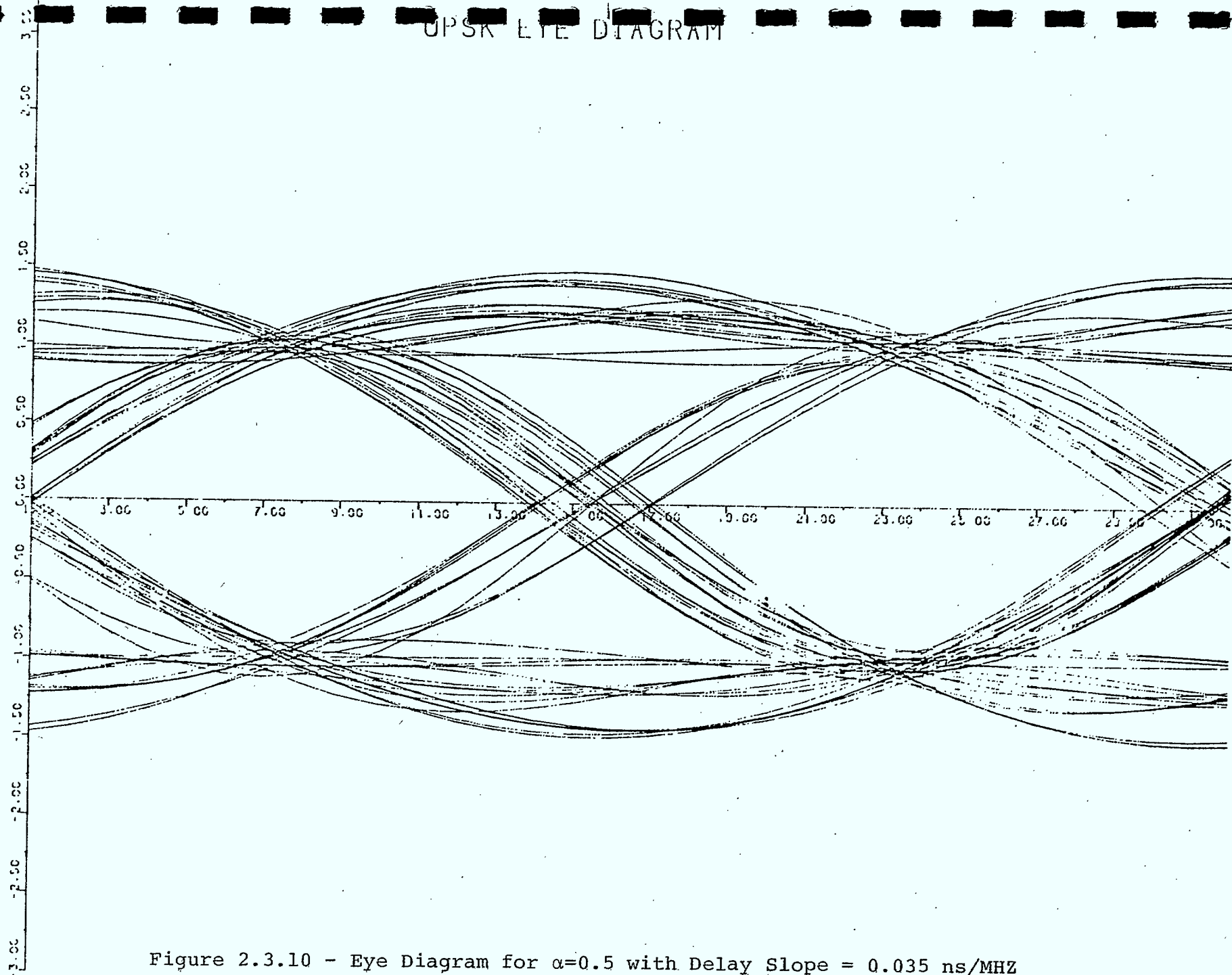


Figure 2.3.10 - Eye Diagram for $\alpha=0.5$ with Delay Slope = 0.035 ns/MHZ

QPSK EYE DIAGRAM

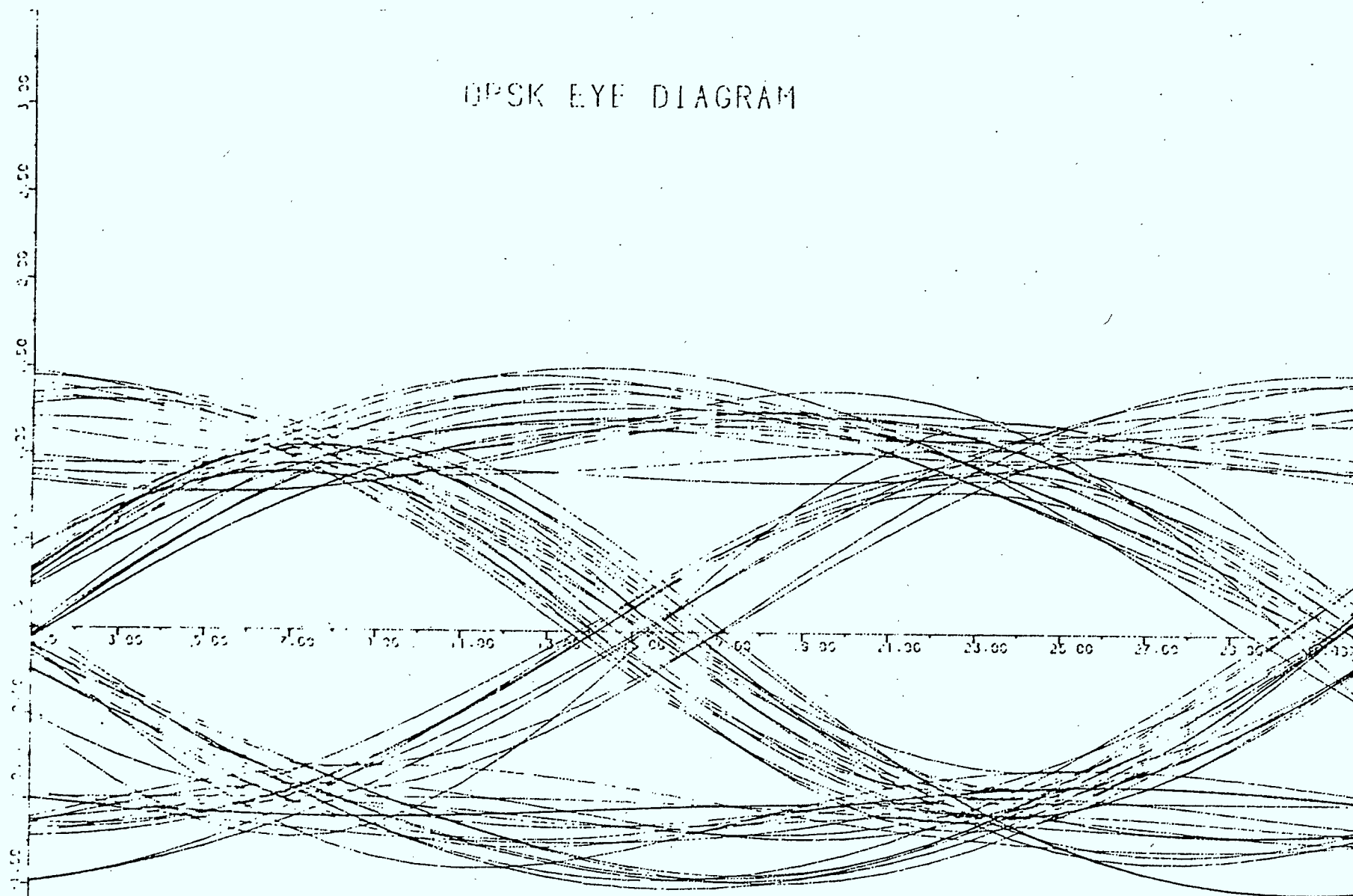


Figure 2.3.11 - Eye Diagram for $\alpha=0.5$ with Delay Slope = 0.07 ns/MHZ

OPSK EYE DIAGRAM

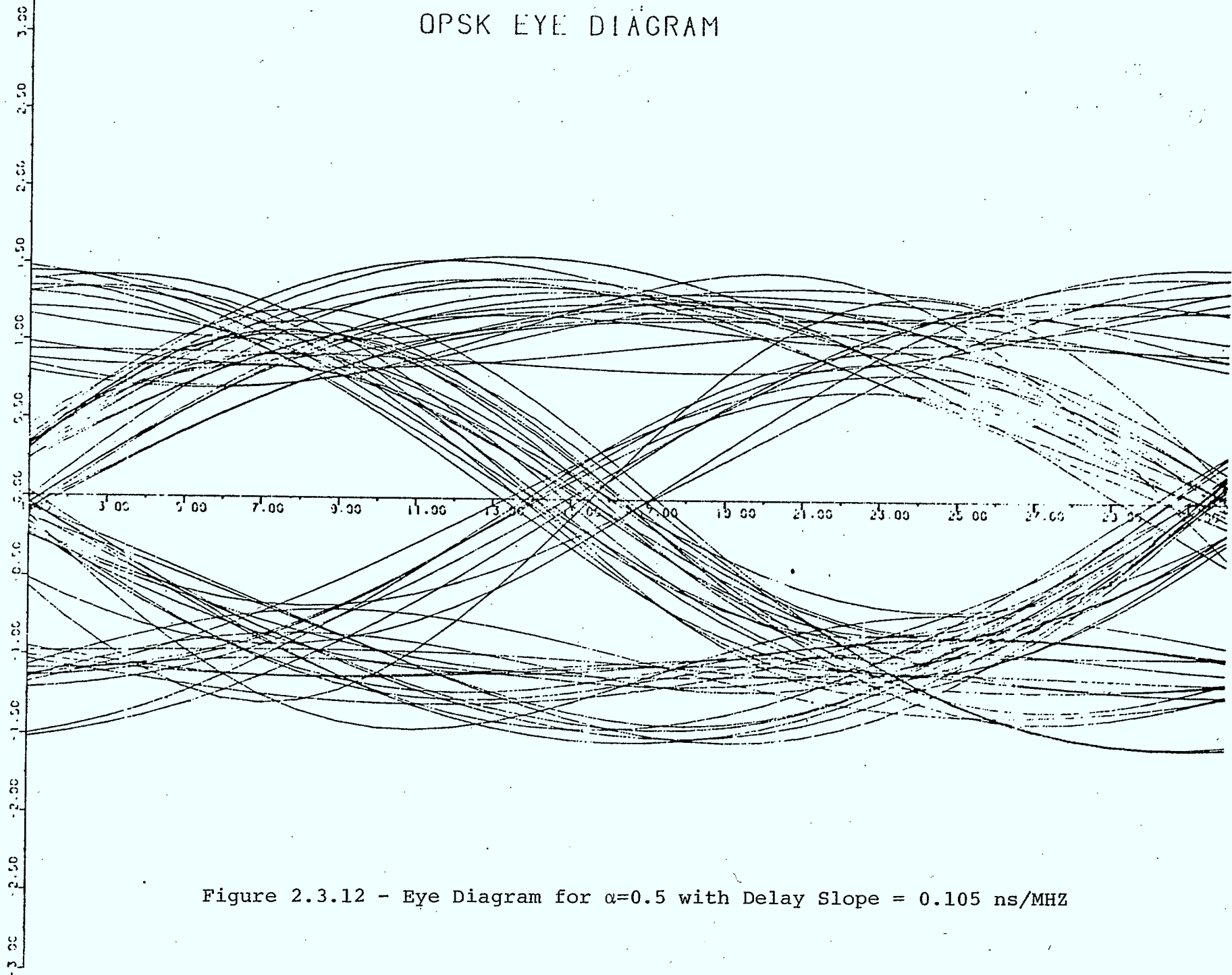


Figure 2.3.12 - Eye Diagram for $\alpha=0.5$ with Delay Slope = 0.105 ns/MHZ

OPSK EYE DIAGRAM

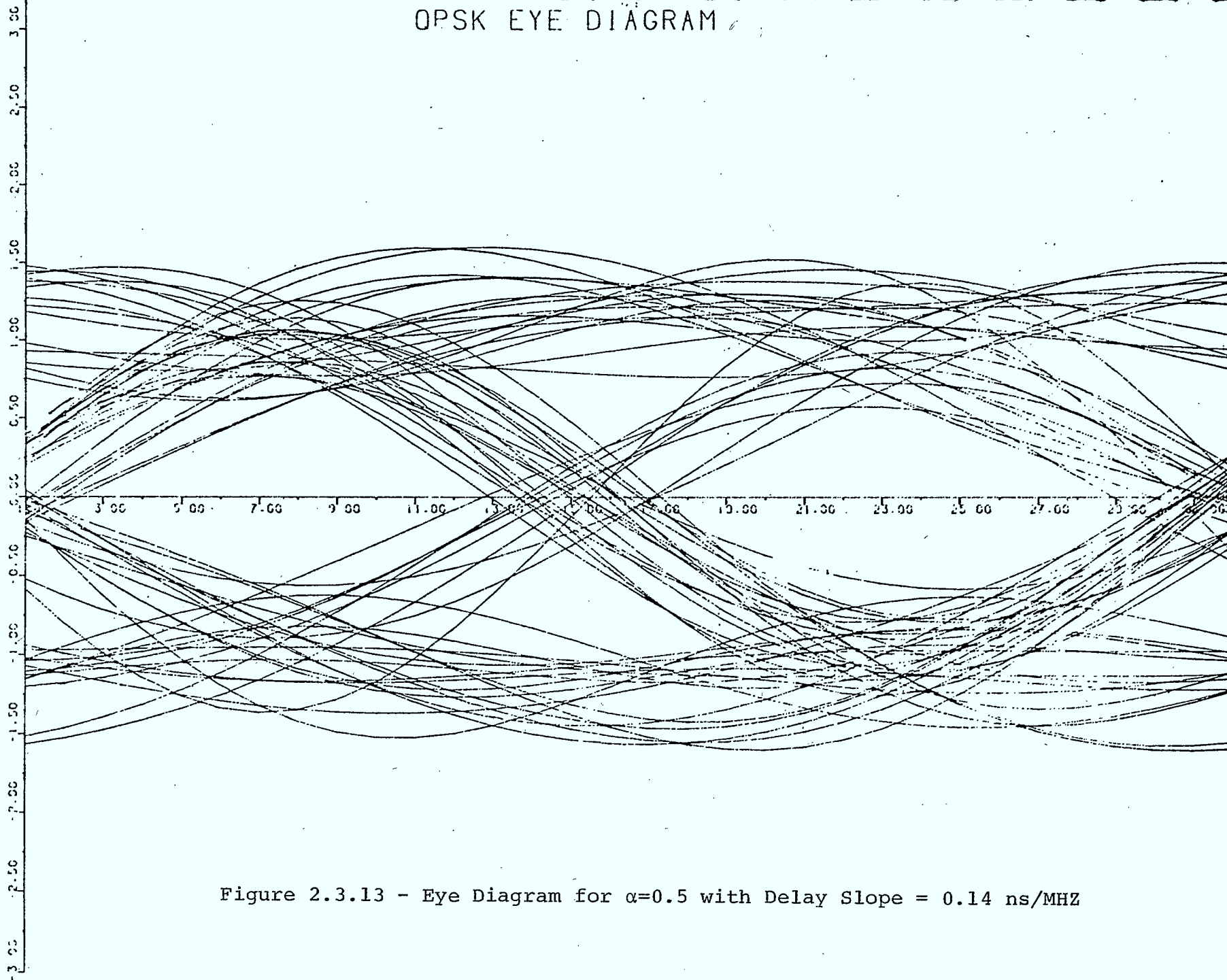


Figure 2.3.13 - Eye Diagram for $\alpha=0.5$ with Delay Slope = 0.14 ns/MHZ

OPSK EYE DIAGRAM

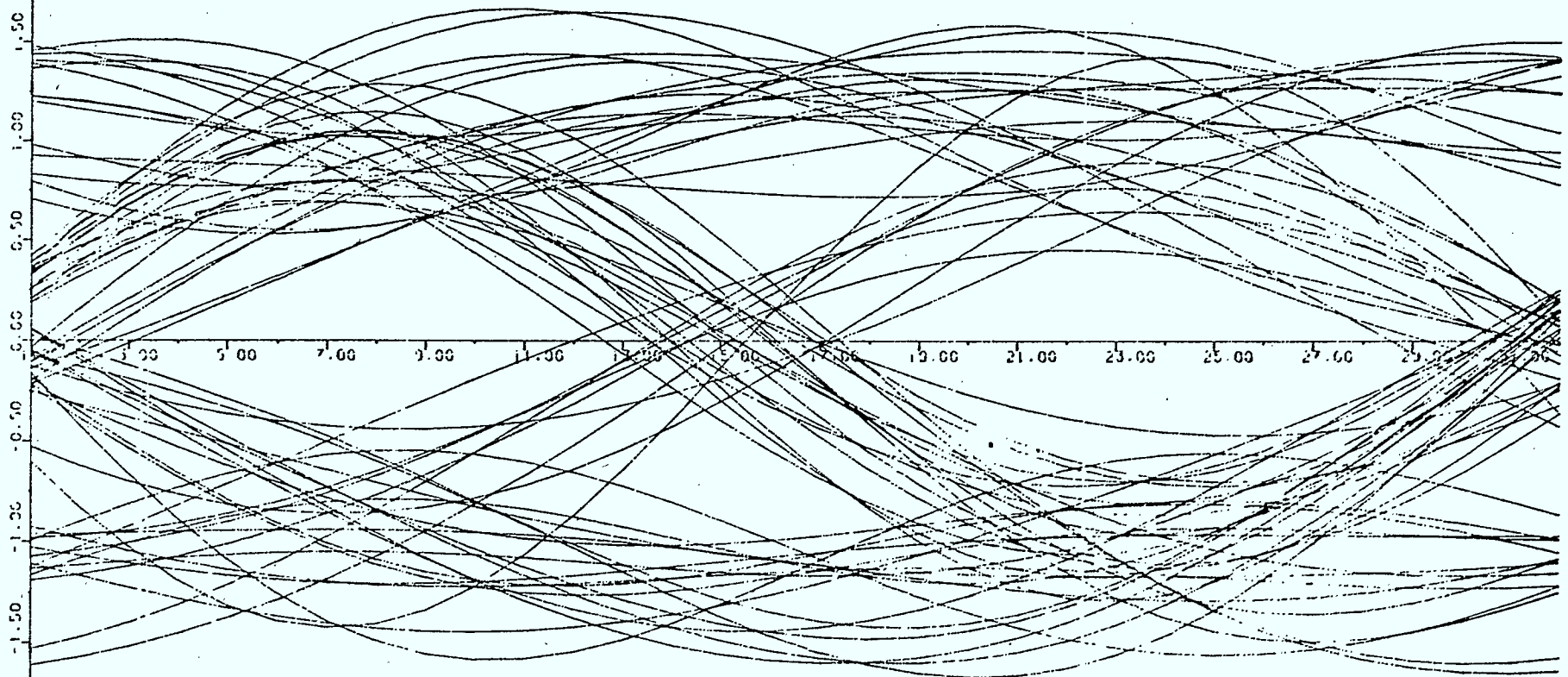


Figure 2.3.14 - Eye Diagram for $\alpha=0.5$ with Delay Slope = 0.175 ns/MHZ

DPSK EYE DIAGRAM

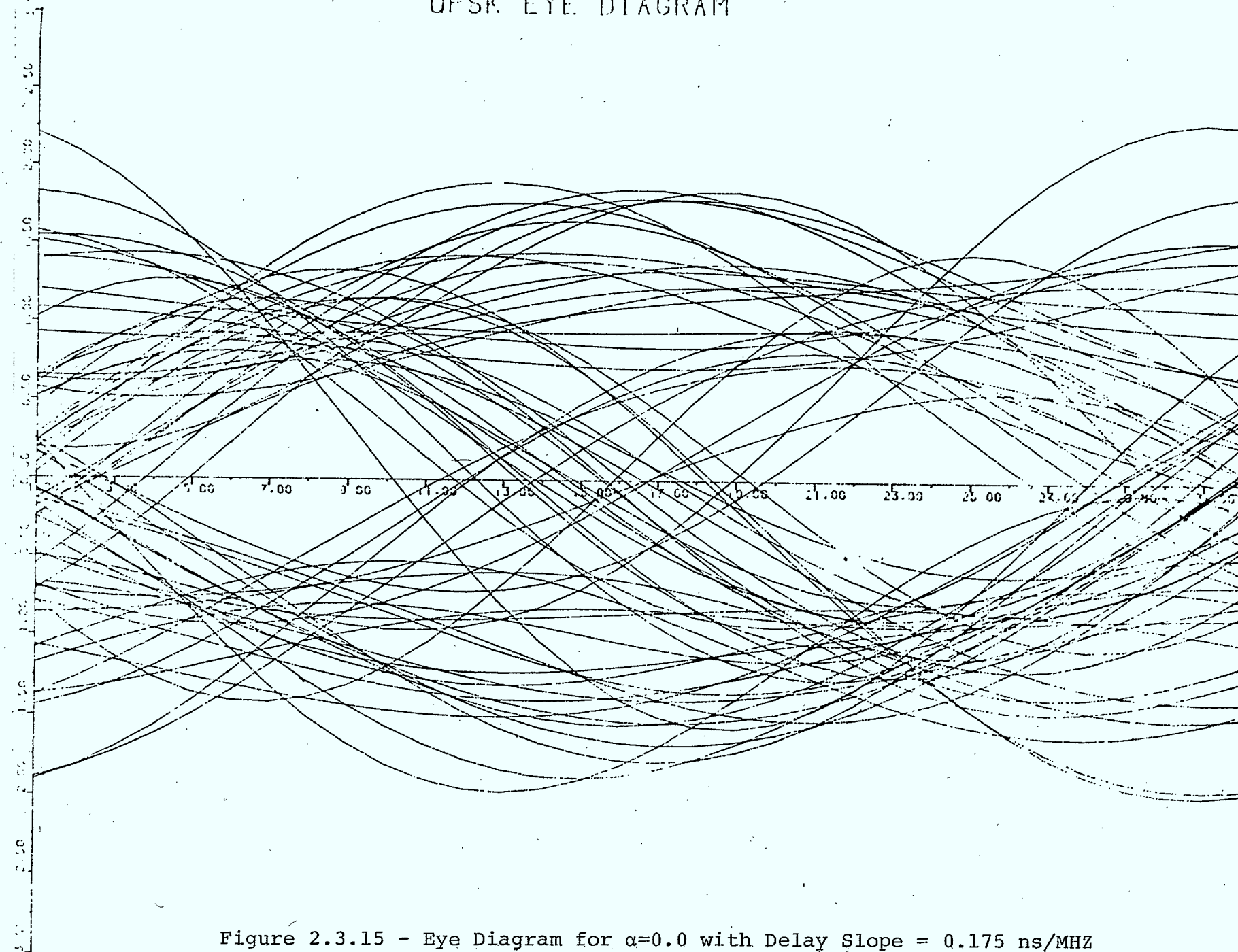


Figure 2.3.15 - Eye Diagram for $\alpha=0.0$ with Delay Slope = 0.175 ns/MHZ

QPSK EYE DIAGRAM

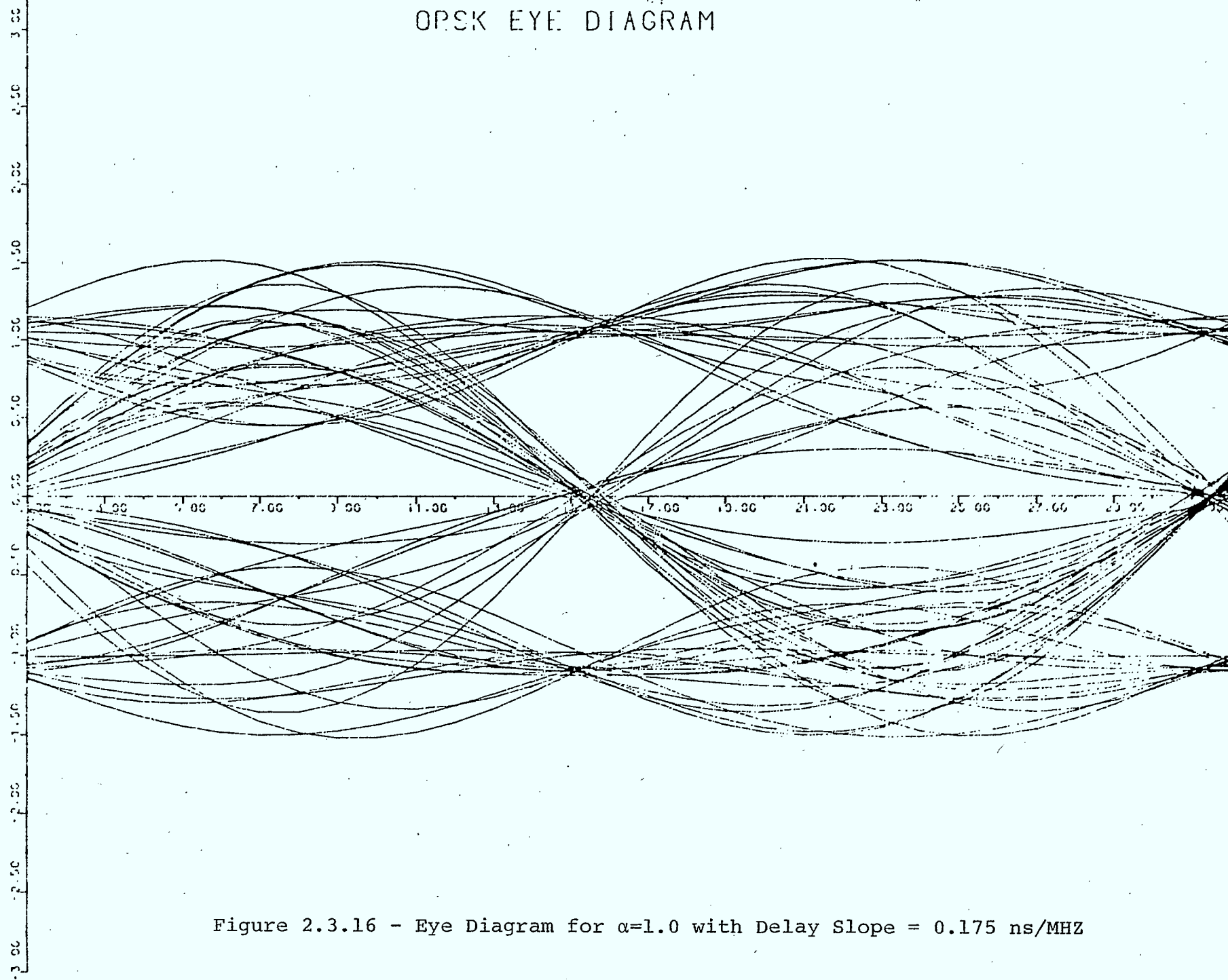


Figure 2.3.16 - Eye Diagram for $\alpha=1.0$ with Delay Slope = 0.175 ns/MHZ

REFERENCES

- [1] W. Bennett and J. Davey, "Data Transmission", McGraw Hill Book Company, 1965.
- [2] R.W. Lucky, J. Salz and E. Weldon, "Principles of Data Communication", McGraw Hill Book Company, 1968.
- [3] D. Morais, A. Sewerinson and K. Feher, "The Effects of Amplitude and Delay Slope Components of Frequency Selective Fading on QPSK, Offset QPSK and 8 PSK Systems", IEEE Trans. on Communications, vol. COM-27, No. 12, December 1979, pp. 1849-1853.

CHAPTER 3

PERFORMANCE COMPARISON OF REGENERATIVE AND CONVENTIONAL SATELLITE CHANNELS FOR QPSK

3.1.1 Introduction

In the first phase of this study, regenerative satellite were seen to offer some advantages over conventional satellite systems. Using the refinements in the computer simulation programme that are described in Chapter 2, a comparison of regenerative and non regenerative systems is made using the QPSK modulation technique. Although several other good simulation techniques are available, QPSK is considered first as it is the most widely used in existing and planned systems. A review of current systems will reveal that over 80% of all communication satellite systems having digital modulation use QPSK [1]. A study of offset-keyed QPSK and MSK is delayed until Chapter 6. In that chapter, these two modulation methods will be compared to QPSK. More advanced modulation techniques such as IJF-OKQPSK and 16-QAM are analyzed in Chapter 7.

To illustrate the advantages in the $P(e)$ performance of regenerative satellites, for QPSK, over the conventional ones, an example of a 120 Mb/s system having cascaded nonlinearities, which include AM/AM and AM/PM is used. The parameters used in this system study are those suggested in the INTELSAT V specifications [2]. Although these specifications are for a conventional translating system, it is expected that future-generation regenerative satellites will have similar specifications.

The effect of group delay variation on the advantages of regeneration is explored. It is shown that the improvement is greatest for the case when the group delay is worst. Further, it is seen that varying the amplitude characteristics of transponder filters does not have significant effects on the performance of the system. Placing the modulator filter after the TWTA in the satellite improves the regenerative system by a further 0.7 dB.

3.1.2 System Models and Simulation

The overall system models for the conventional and regenerative satellite systems are given in Figs. 3.1.1 and 3.1.2 respectively. In Fig. 3.1.1, the satellite link considered consists of the transmitting earth station, the satellite transponder and the receiving earth station. At the transmitting earth station, the transmit band-pass filter (F_1) is used to bandlimit the spectrum. The high-power amplifier (HPA), operated near saturation, causes both AM/AM and AM/PM conversion of the signal and degrades the system performance. The satellite input and output multiplex filters (F_2 and F_3), which are used to bandlimit the signal and reduce the spectral spreading caused by the TWT, may induce ISI. At the receiving earth station, the receive filter (F_4), used to bandlimit the thermal noise and reduce the adjacent channel interference, may also degrade the system performance. For computer simulation purposes, the filter F_2' is usually lumped with the on-board filter F_2 . For the regenerative system simulation reported in this chapter, we restrict our attention to a class of systems where the uplink E_b/N_o is much higher than the downlink E_b/N_o . This is true in several systems [2]. We can hence assume, as a first approximation, that the uplink $E_b/N_o \approx \infty$. In Fig. 3.1.2, this is equivalent to bypassing the HPA and the filters F_1 , F_2 and F_4 , i.e. the blocks in the shaded area are omitted.

The nonlinear satellite channel specified for the INTELSAT V system is simulated to evaluate the system perfor-

mance. The systems in Figs. 3.1.1 and 3.1.2 are simulated using the complex baseband equivalent models [3].

In Fig. 3.1.1, the data source is an equiprobable pseudo-random binary NRZ sequence, at a rate of 60 Megabaud corresponding to 120 Mb/s. The data loading is as described in Chapter 2. The modulator transmit filter, F_1 , is simulated as a filter whose transfer function has a square root of raised-cosine ($\sqrt{\alpha=0.4}$) shape with $\frac{x}{\sin x}$ amplitude equalization, while the receive filter, F_4 , has a transfer function whose shape is the square root of raised-cosine ($\sqrt{\alpha=0.4}$). The transponder filters, F_2 and F_3 , termed input MUX and output MUX filters, are simulated as a filter with a raised-cosine shape ($\alpha=0.1$ and $\alpha=0.2$) with a 3 dB cut-off frequency = 40MHz. The group delays of all the filters are assumed to be parabolic, $\tau = af^2$, where 'a' is in ns/MHz² and f is in MHz. The coefficient 'a' for transmit (F_1) and receive filter (F_4) is equal to 0.002 ns/MHz². The amplitude and group delay characteristics are chosen to fit the INTELSAT V masks as shown in Figs. 3.1.3 and 3.1.4 for F_1 and F_4 respectively. Two cases are considered for the MUX filters:

Case 1) 'a' = 0.011ns/MHz² for F_2 and 0.0075ns/MHz² for F_3

Case 2) 'a' = 0.015ns/MHz² for F_2 and 0.01ns/MHz² for F_3 .

Case 2 is the worst-case group delay and the chosen characteristics just fits the specified mask (Figs 3.1.5b and 3.1.6b). For Case 1, as seen on figures, the group-delay curve passes through the middle of the specified mask.

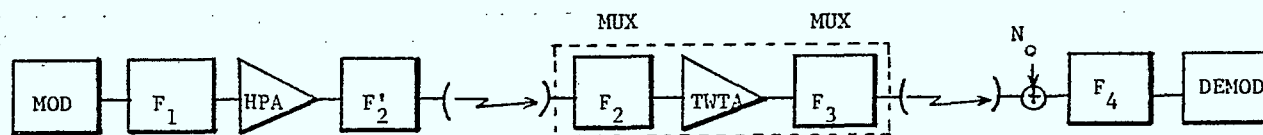


Fig. 3.1.1 Conventional Communication Satellite System Model

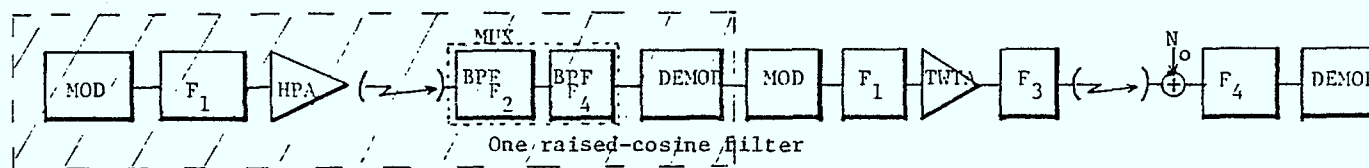
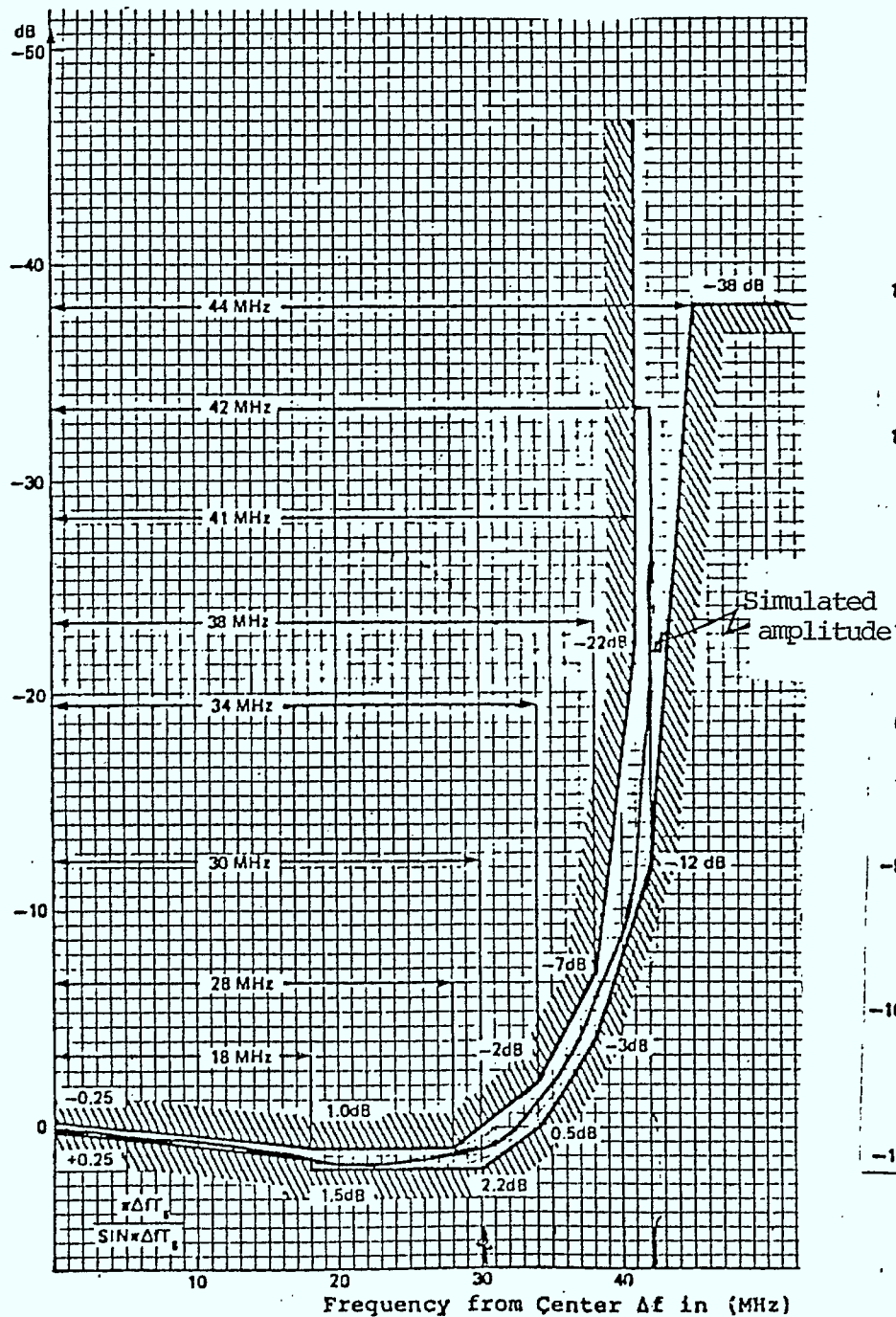
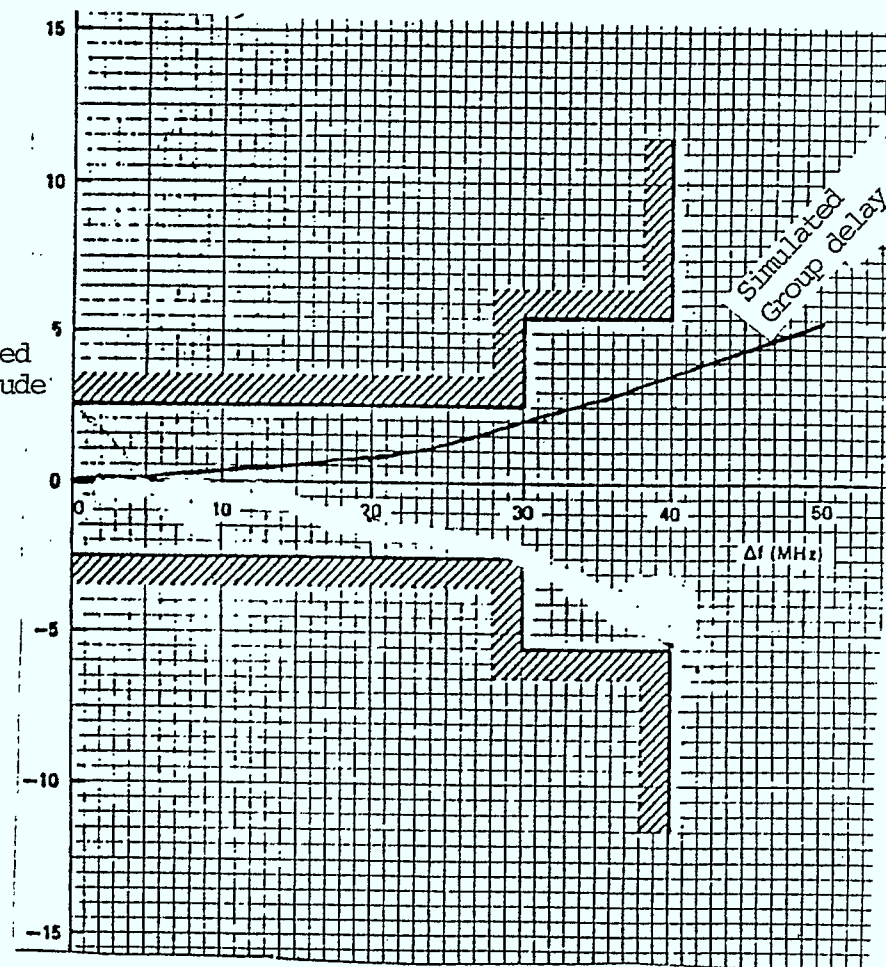


Fig. 3.1.2 Regenerative Satellite System Model

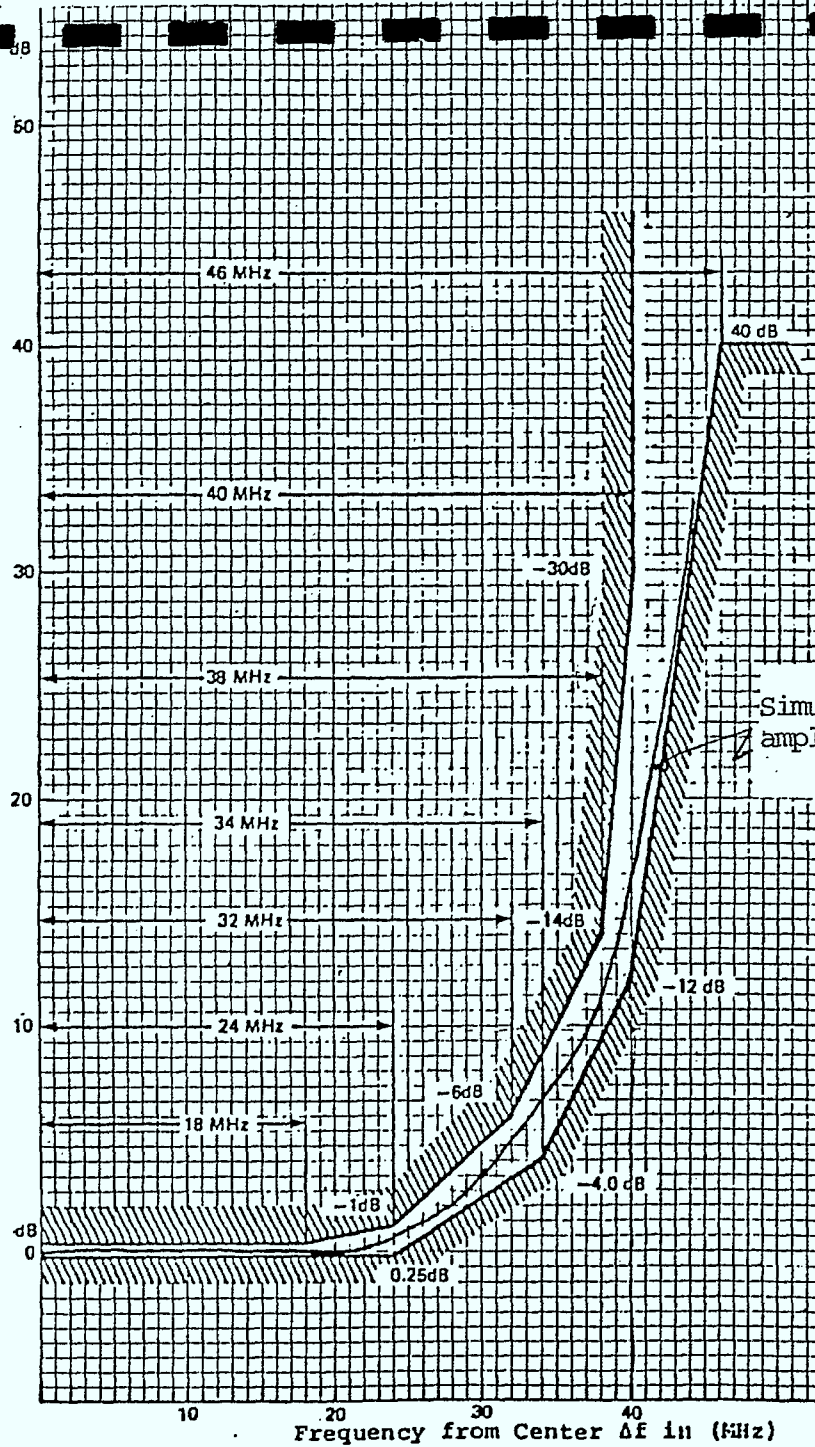


(a) Amplitude characteristic

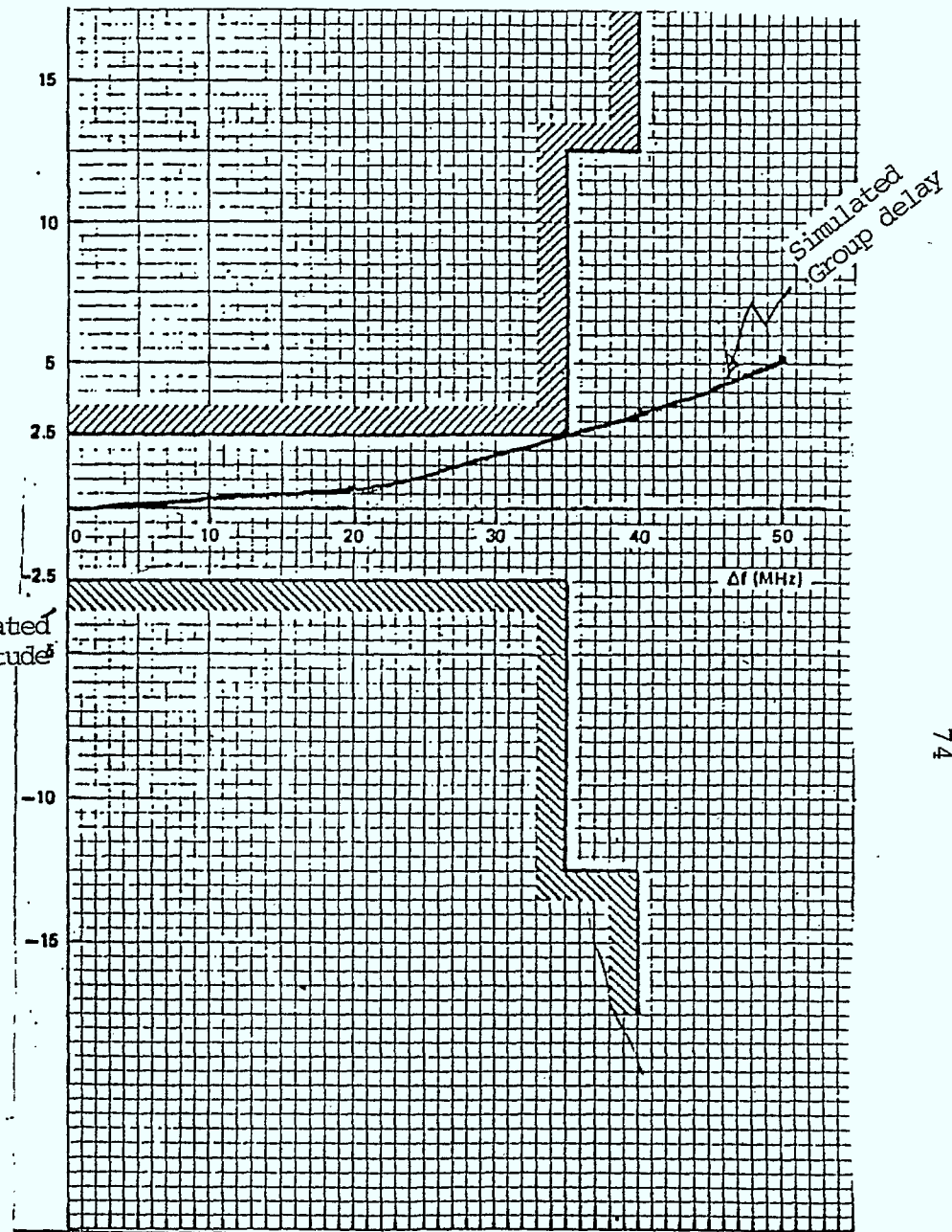


(b) Group delay characteristic

Fig. 3.1.3 Modulator filter (F_1)

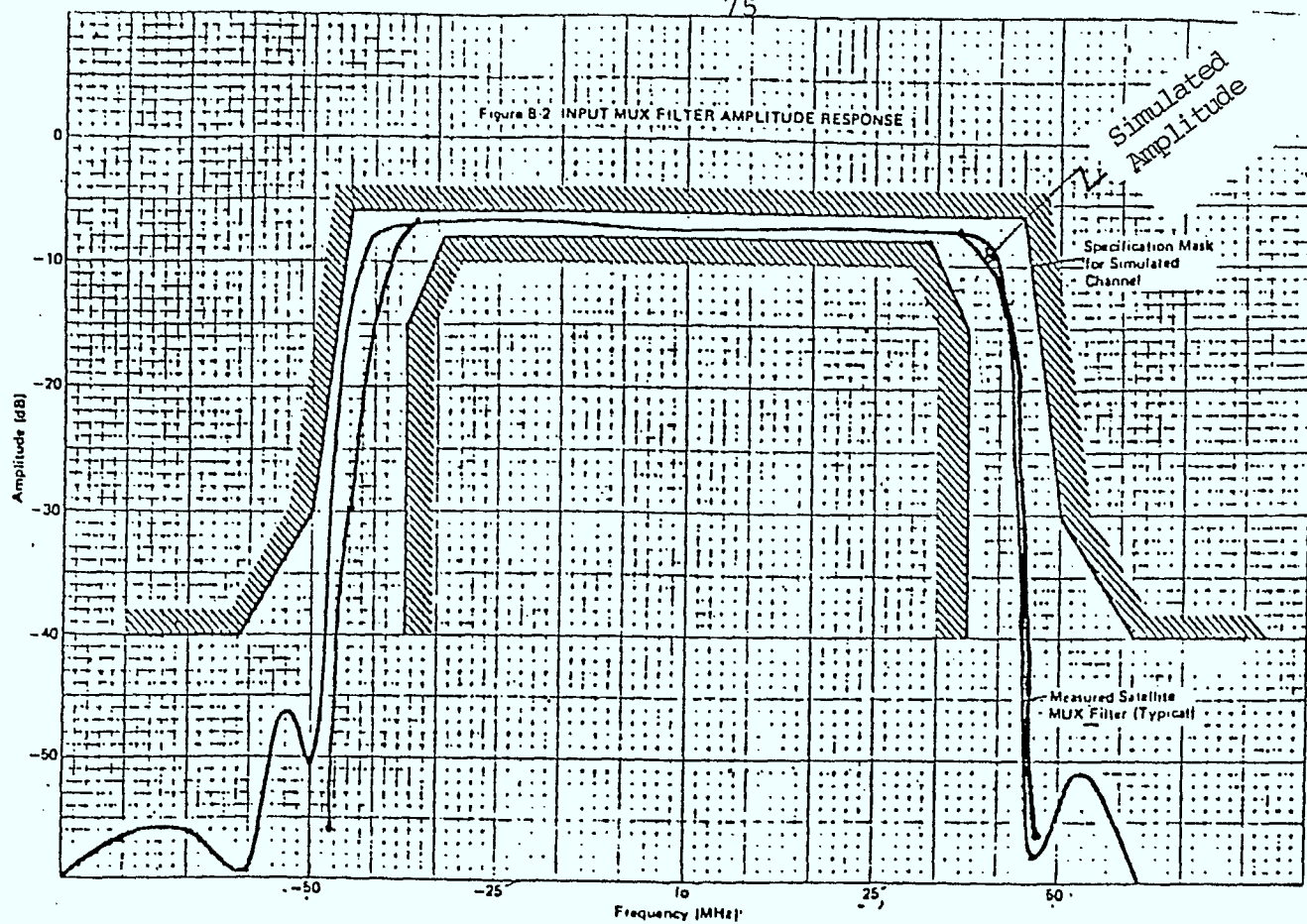


(a) Amplitude characteristic

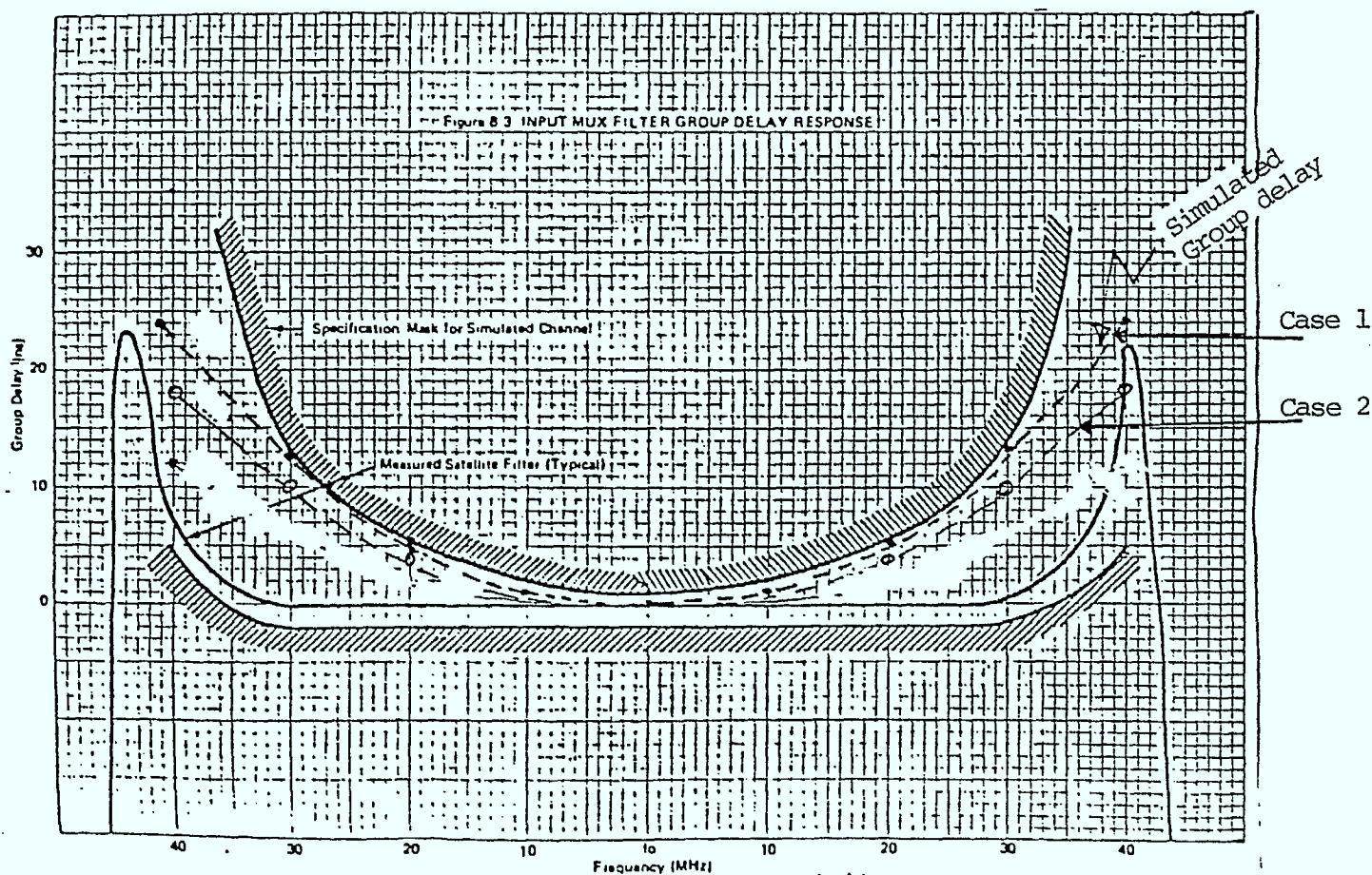


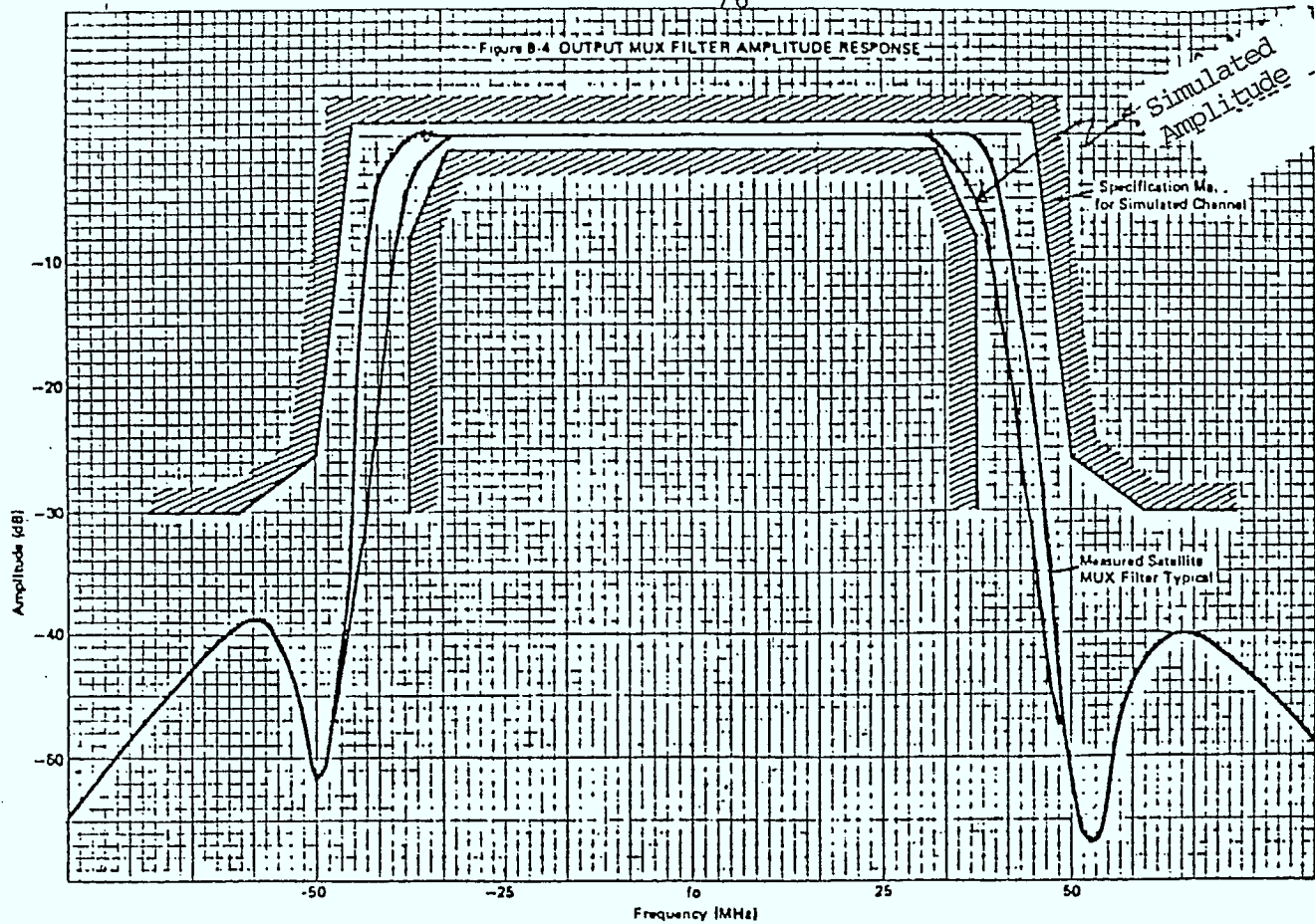
(b) Group delay characteristic

Fig. 3.1.4 De-modulator filter (F_4)

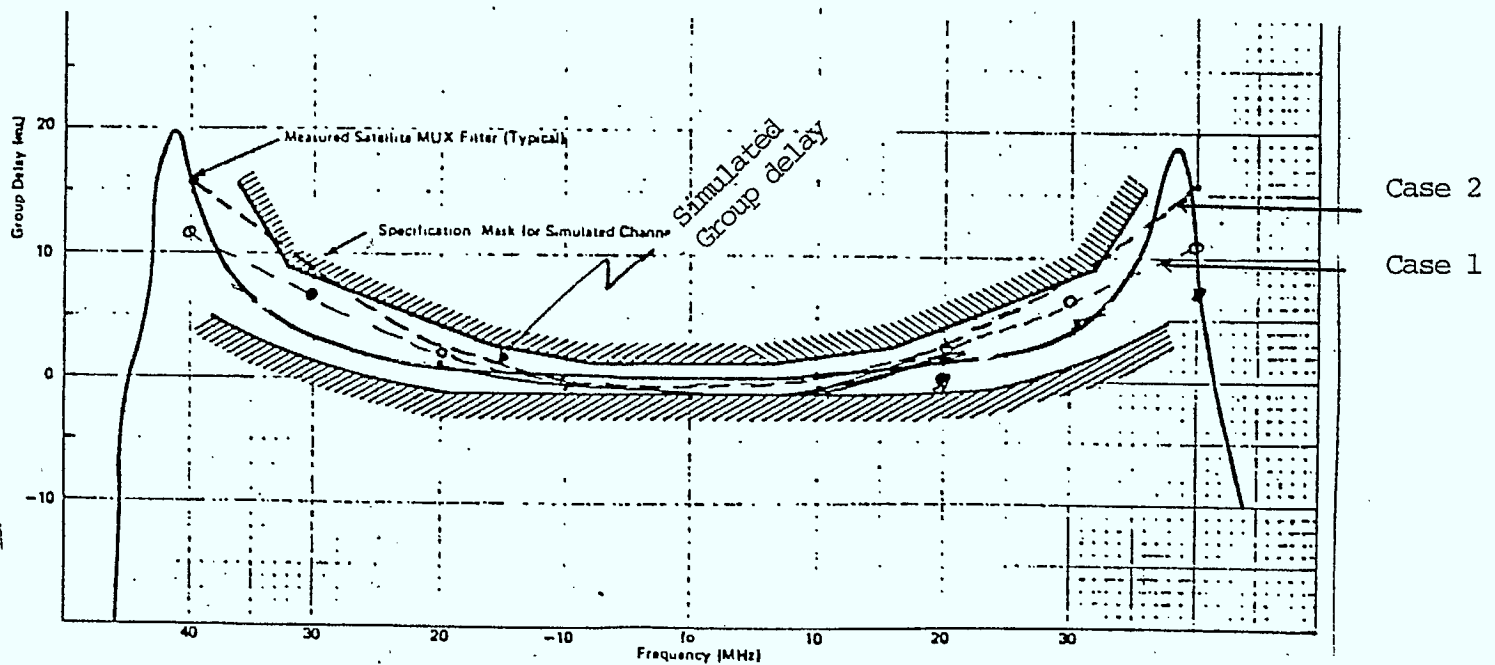


(a) Amplitude characteristic

(b) Group delay characteristic
Fig. 3.1.5 INPUT MUX FILTER (F_2)



(a) Amplitude characteristic



(b) Group delay characteristic

Fig. 3.1.6 OUTPUT MUX FILTER (F_3)

The characteristics for the HPA and TWTA obtained from the data in Table 2 of attachment [2] are used to model the nonlinear devices. The nonlinearities can be described by two polynomials $p(r)$ and $q(r)$ [4] so that if the input modulated signal is written as

$$z_i(t) = [x(t) + jy(t)] e^{j\omega_c t}, \quad \omega_c = \text{carrier frequency}$$

then the output signal of nonlinear device is

$$z_o(t) = [x'(t) + jy'(t)] e^{j\omega_c t}$$

where $x'(t) = x(t)p(r(t)) - y(t)q(r(t))$

$$y'(t) = x(t)q(r(t)) + y(t)p(r(t))$$

and $r(t) = \sqrt{x^2(t) + y^2(t)}$ = envelope of incoming signal.

The AM/AM characteristic curve is represented by

$$\text{AM/AM} = \sqrt{(rp(r))^2 + (rq(r))^2}$$

and the AM/PM characteristic curve is given by

$$\text{AM/PM} = \tan^{-1} \frac{q(r)}{p(r)}$$

The polynomials $rp(r)$ and $rq(r)$ may be expressed as

$$rp(r) = \sum_{i=1}^M a_{2i-1} r^{2i-1}$$

$$\text{and } rq(r) = \sum_{i=1}^M b_{2i-1} r^{2i-1}$$

where M is the order of the polynomial, and all even coefficients are zero. For the given HPA and TWTA characteristics, the coefficients determined using the polynomial fitting routine are:

i) TWTA

$$\begin{aligned} a_1 &= 2.185509, a_3 = -1.934083, a_5 = 0.9807836, \\ a_7 &= -0.23133886, a_9 = 0.01963255 \\ b_1 &= 0.2641891, b_3 = 1.338875, b_5 = -0.9973087, \\ b_7 &= 0.2675812, b_9 = -0.02400961 \end{aligned}$$

ii) HPA

$$\begin{aligned} a_1 &= 1.916288, a_3 = -0.9358132, a_5 = 0.1942392, \\ a_7 &= -0.02832262, a_9 = 0.01840305, a_{11} = -0.004282407 \\ b_1 &= -0.059659, b_3 = 1.907669, b_5 = -1.846724, \\ b_7 &= 0.8615552, b_9 = -0.1990954, b_{11} = 0.01815157. \end{aligned}$$

Figure 3.1.7 shows the curves obtained using the polynomial fitting routine. These are shown as the continuous lines, and are in close agreement with the given points indicated by dots in the graph.

The AM/AM and AM/PM curves are specified in terms of backoffs in dB. The normalization used here corresponds to mean power, that is, the power is assumed to be unity at the 0 dB input/output backoff point. This normalization makes the scheme independent of the absolute saturated power of the devices. Therefore, if a modulated signal, $z_i(t)$, having an average power 'p' is the input to a nonlinear device operated at 'q' dB backoff, the normalized input signal, $z_i^n(t)$, becomes

$$z_i^n(t) = \frac{z_i(t)}{\sqrt{p}} \cdot 10^{-q/10}$$

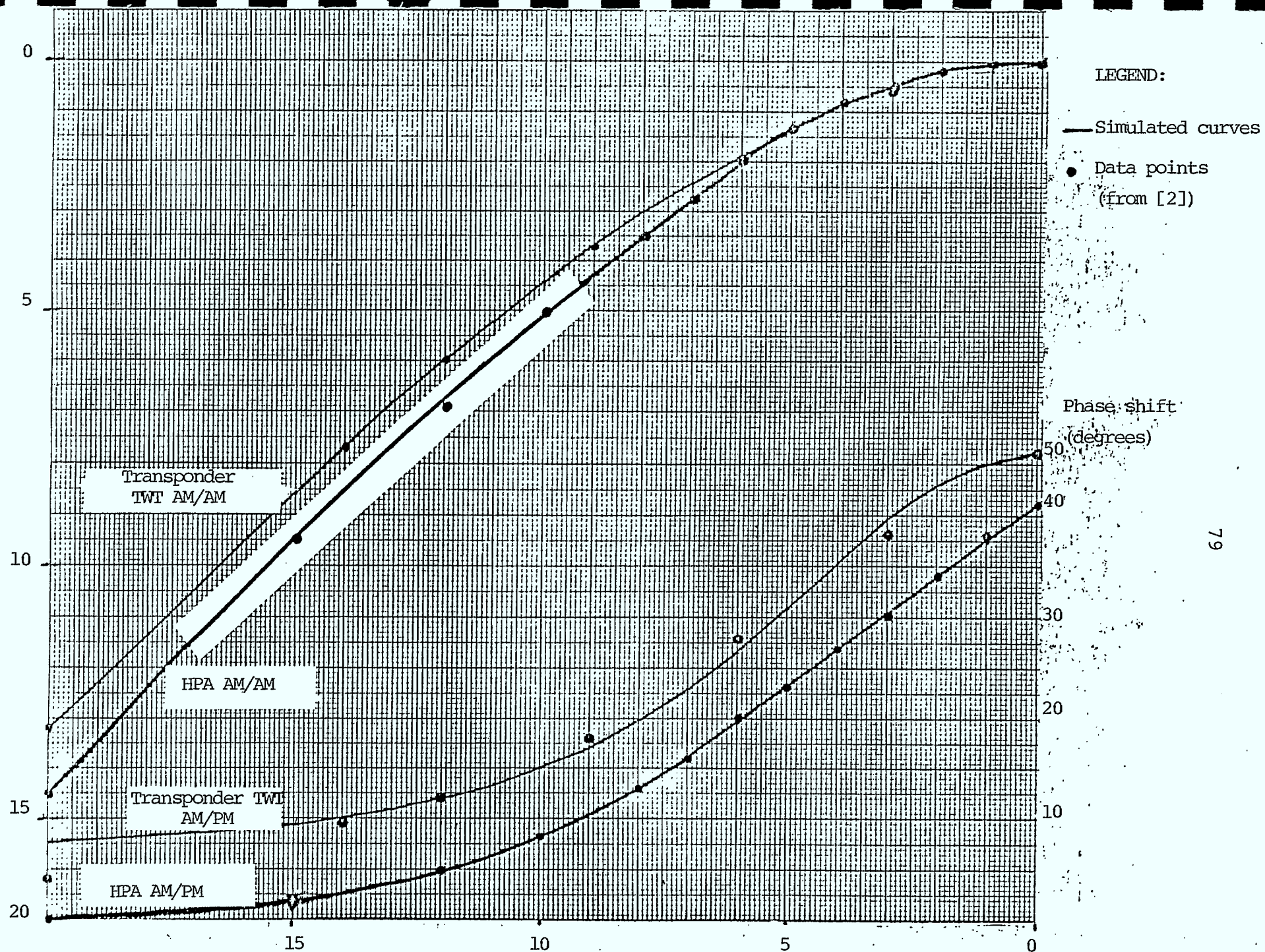


Fig. 3.1.7 AM/AM and AM/PM characteristics of HPA and TWT input backoff (dB)

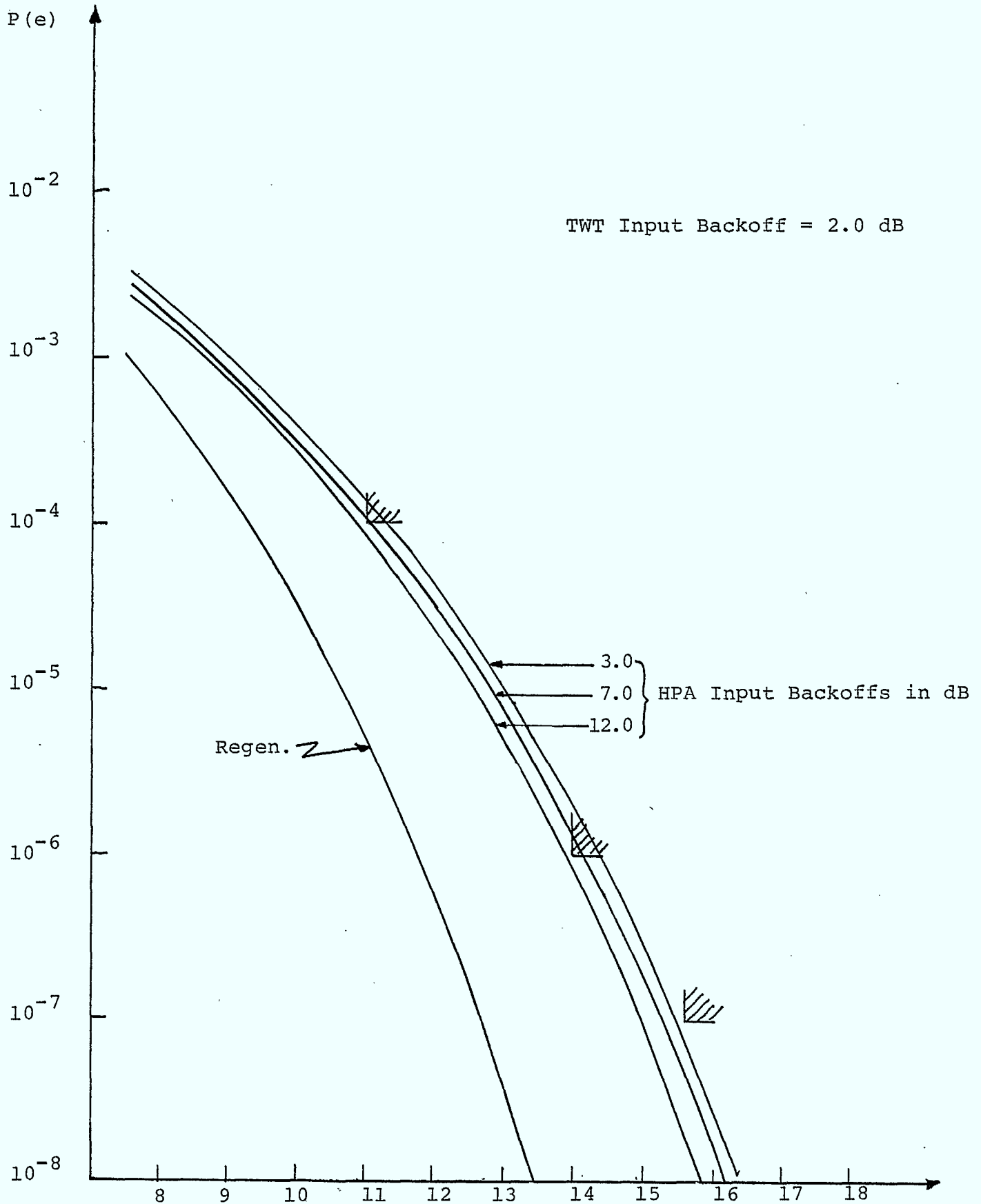
At the demodulator, the detection process comprises of a threshold comparator and a sampling device where the sampling is adjusted so as to be at the maximum eye opening as described in Chapter 2.

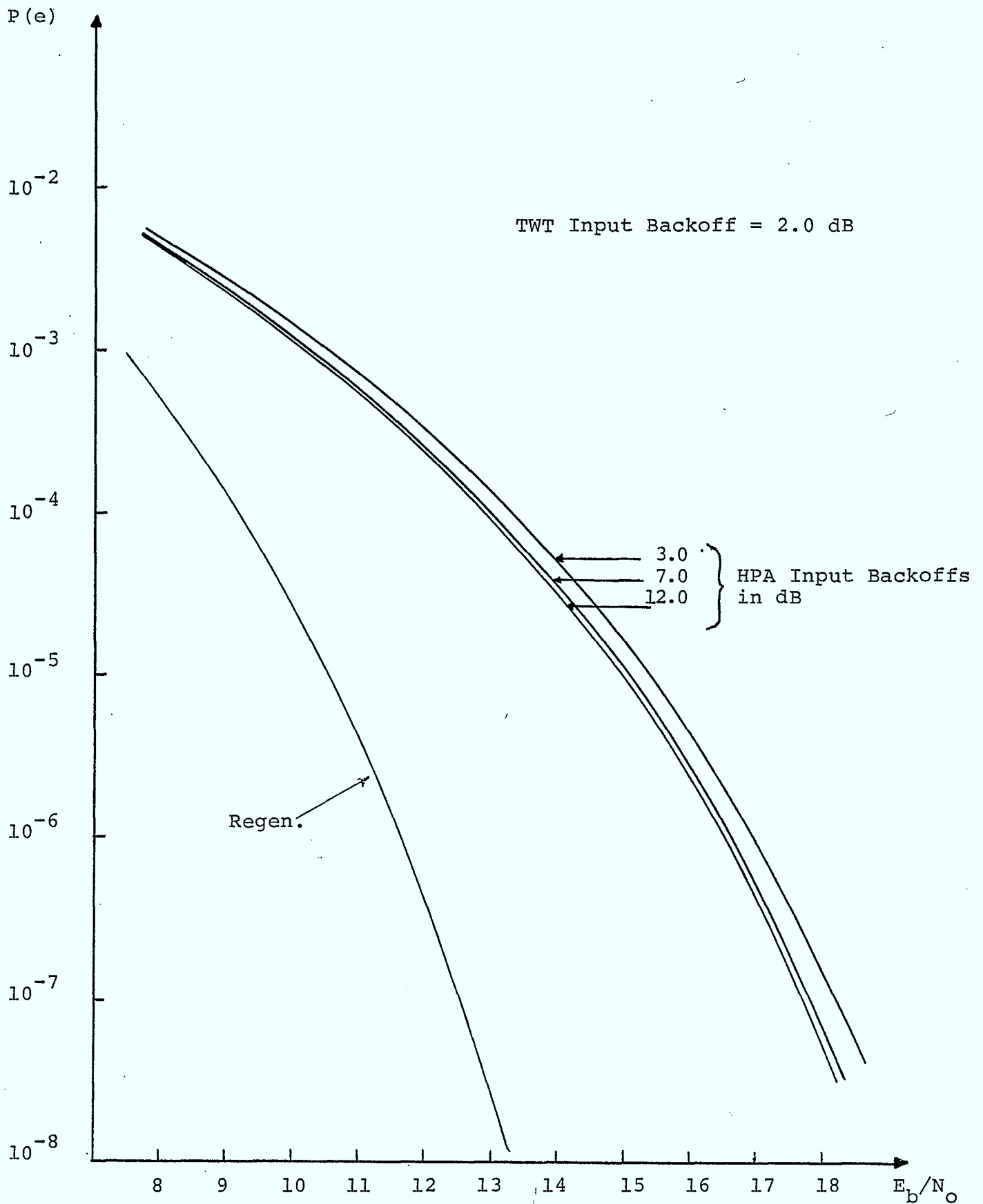
3.1.3 Results

The simulation results for the 120 Mb/s system for QPSK are shown in Figs. 3.1.8 and 3.1.9. In all cases, the the satellite TWTA is assumed to operate at 2.0 dB input backoff (corresponding to an output backoff of about 0.2 dB, i.e. the TWTA is run at saturation). In the conventional mode, results are shown for the earth-station HPA operating at different input backoffs from 0 dB to 12 dB.

In Fig. 3.1.8, the results for the group delay of Case 1 are shown. For a probability of error of 10^{-4} , conventional-mode systems do not meet the Intelsat $\frac{E_b}{N_o}$ requirement of less than 11.0 dB, unless the HPA input backoff is greater than 7.0 dB. Only at a probability of error of 10^{-7} do all HPA backoffs meet the specifications. Comparing conventional and regenerative systems, the latter offers a 2.0 dB gain in E_b/N_o for a P_e of 10^{-4} . At a probability of error of 10^{-6} the corresponding gain in E_b/N_o is 2.6 dB. It is clearly seen that by using regeneration, the E_b/N_o requirements of 11.0 dB at 10^{-4} and 14.0 dB at 10^{-6} are exceeded.

Figure 3.1.9 shows the results for the worst-case group delay of the MUX filters. In this case, the group delay is seen to have a considerable effect on the performance of the conventional system; the performance falls far short

Fig. 3.1.8 - $P(e)$ Performance of QPSK, Case 1

Fig. 3.1.9 - $P(e)$ Performance of QPSK - Worst Case Group Delay

of the E_b/N_0 requirements. At a probability of error of 10^{-4} , the performance is 2 dB away from the requirement and at a P_e of 10^{-6} this margin is 2.6 dB. In this case, a 4 dB gain results (for $P_e=10^{-4}$) from the use of a regenerative system compared to a translating system. At a probability of error of 10^{-6} , the gain in E_b/N_0 from regeneration is about 5 dB. Regeneration thus enables the satellite system to meet the E_b/N_0 requirements that were otherwise impossible. It appears that more gain is obtained by using a regenerative system when the group delay of the filters is higher.

The effect of amplitude variation of the MUX filter characteristic is considered next. Different filter shapes which fit the specified amplitude mask are simulated. This is achieved by varying the 3 dB frequency cutoff of the filters and the roll-off factor α . The performance for a conventional channel with HPA and TWTA input backoffs of 7.0 dB and 2.0 dB respectively is shown in Fig. 3.1.10. The maximum variation in performance is only 0.2 dB at a probability of error of 10^{-4} and about 0.3 dB at 10^{-6} . It thus seems that, unlike group delay, amplitude variations (within the mask) do not cause appreciable difference in the system performance.

Simulation were also done to evaluate the effect of filter positioning in the regenerative system. In Fig. 3.1.11, the equivalent regenerative satellite system is shown. In Fig. 3.1.11(a) the shaping filter precedes the

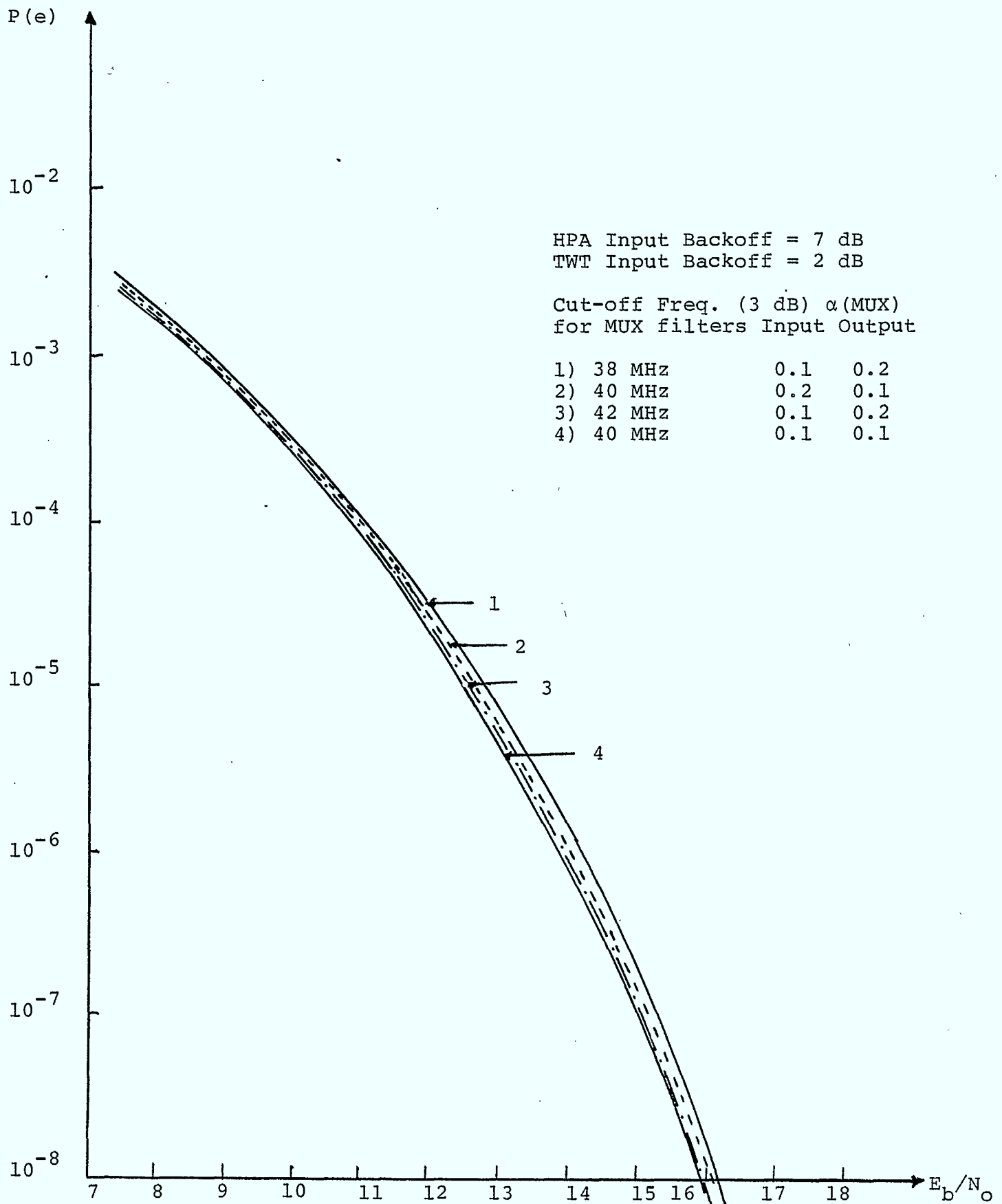


Fig. 3.1.10 - Effect of Amplitude Variation in MUX Filters for QPSK

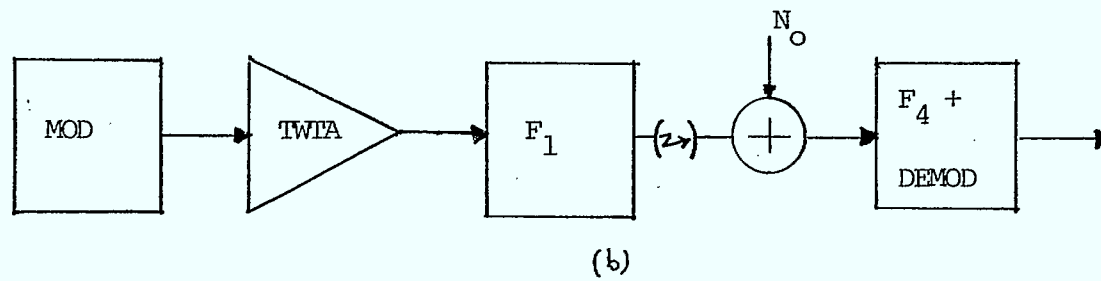
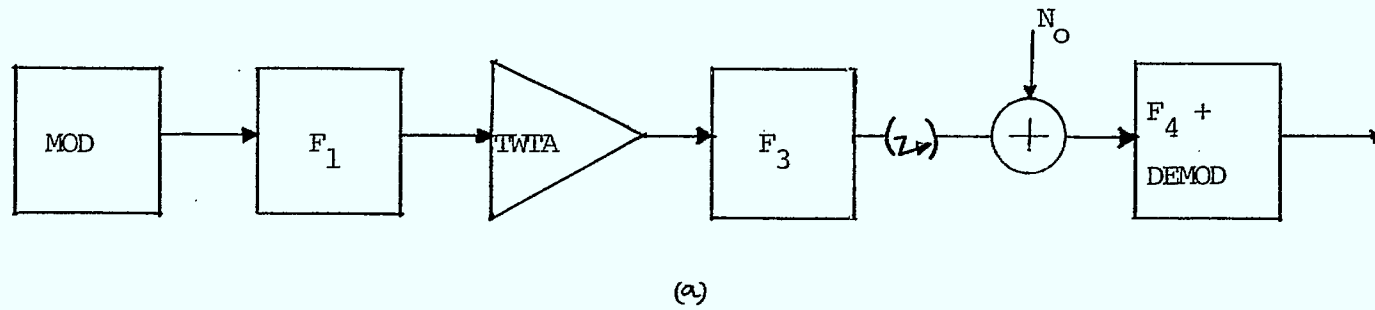


Fig. 3.1.11 - Effect of Different Filter Positioning on QPSK

TWTA at the satellite repeater, while in Fig. 3.1.11(b) the shaping filter is placed after the TWTA. In the latter case, the output MUX filter is replaced by filter F_1 , since the bandwidth of the shaping filter is narrower than that of the MUX filter. Figure 3.1.12 shows the probability of error performance for the two cases considered for QPSK. It is seen that if the filter is placed after the TWTA, a 0.7 dB gain in E_b/N_0 results at a probability of error of 10^{-4} and 1.0 dB at a $P_e=10^{-6}$. An improvement in the performance of the system is expected for the system model of Fig. 3.1.11(b) since the input signal to the TWTA is constant-envelope and hence AM/AM and AM/PM degradations will be greatly reduced.

3.1.4 Conclusion

Regeneration in the satellite can offer an improvement of a communication satellite system. For QPSK, the gain resulting is between 2 dB and 4 dB at a probability of error of 10^{-4} depending on the filter characteristics. Variations in the amplitude characteristics do not cause appreciable differences in performance as long as the variations are within the specified mask. However, group delay variations cause considerable difference, being as much as 2.4 dB in the conventional case. The gain to be realised by regeneration is highest when the channel characteristics are worst. By placing the shaping filter after the TWTA a further 0.7 dB advantage in E_b/N_0 results for $P_e=10^{-4}$.

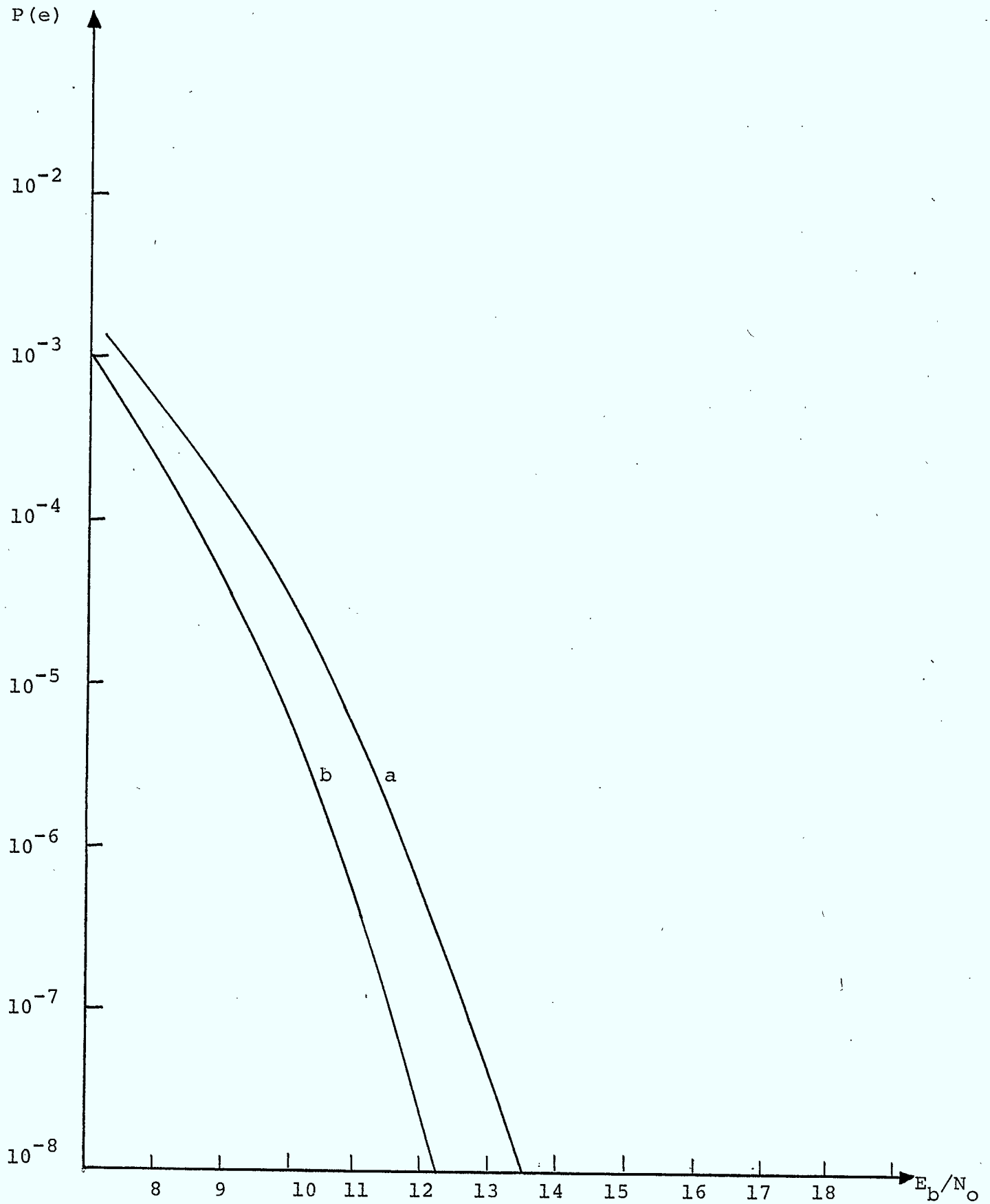


Fig. 3.1.12 - Effect of Different Filter Positioning For QPSK

REFERENCES

- [1] Electronics-Staff of Satellite Systems Engineering, Inc.:
»More Communications in Orbit«, Electronics, Sept. 11,
1980. p. 148-151, N.Y. 1980.
- [2] Intelsat TDMA/DSI System Specifications, BG-42-6SE,
June 1980.
- [3] K. Feher, A Guibord, M. Wachira and J. Huang, »Regenera-
tive Transponder for More Efficient Satellite Systems«,
Report to Communications Research Centre, DOC, Ottawa,
Feb. 1980.
- [4] M.J. Eric, »Intermodulation Analysis of Nonlinear Devices
for Multiple Carrier Inputs«, CRC Report No. 1234,
Ottawa, Nov. 1972.

CHAPTER 4

SPECTRAL SPREADING IN REGENERATIVE SATELLITE SYSTEMS

4.1.1 Introduction

Why Evaluate the Spectrum?

The spectrum is an unrenewable resource, i.e. there is a limit to the number of users that can share a frequency band. Once this limit is passed, adjacent interchannel-interference occurs. Maximum efficiency is the use of the spectrum will therefore give a larger number of services access to a communal frequency band. Once the limit has been reached any new users have to switch to higher frequency bands. This entails considerable expense due to the new technologies that have to be developed.

The choice of the modulation is of paramount importance since it determines the spectrum and the number of users for one of the satellite communication frequency bands. The QPSK modulation has been employed in this report because of the seemingly wide popularity it enjoys at present [1].

A factor which limits the spectral efficiency of all digital modulations is the spectrum spreading due to nonlinearities. The intensity of this partial regeneration of the spectrum to a $(\sin x)/x$ spectrum depends on the type of digital modulation used and the nature of the nonlinearity. An analytical model for predicting the spectrum of the QPSK when there is a single nonlinearity does already exist [2] but for multiple nonlinearities no analytical model which takes into account both the amplitude and the

phase transformations has yet been developed. In this report we perform only digital simulations of QPSK signal, passing through one nonlinearity that models an Intelsat V ground station HPA.

Several applications exist for the method examined in the following pages. They are of two main types:

1. For manufacturers of equipment to predict, before the construction of prototypes, whether the equipment will be of satisfactory performance and will meet the required specifications.
2. For system planification studies where spectral spreading and probability of error of several modulations are compared.

A more precise case for the first application would be when the spectral spreading overlaps a considered spectrum on a desired channel. This channel could be situated on the same transponder, as for example with the SCPC PSK system, or of course, on a separate transponder (the Intelsat TDMA system). The necessity to predict experimental results with precision is due to the fact that these experiments require a lot of very expensive microwave equipment: HPA, transponders etc. Furthermore, discovery that a piece of equipment does not meet requirements after it has been assembled, entails expensive modifications and possible late delivery penalties in addition to loss of revenue that the exploiting company may suffer.

The International standards organizations such as Intelsat impose limits on spectrum spreading at the output of the HPA for TDMA equipment [3]. Norms also exist for intermodulation standards between several services when these use the same HPA.

This alone is sufficient justification for the development of a practical and inexpensive method for estimating the spectrum.

It should be mentioned that these considerations apply whether the satellite is regenerative or not.

4.1.2 Computation of Power Spectrum

A flow chart of the program used to compute the power spectrum after a nonlinearity is illustrated in Fig. 4.1.1 along with the model used. In this simulation the signal is composed of 1024 QPSK symbols. Each symbol is composed of 16 identical complex numbers, i.e. 16 times one of the following: (1, -1), (-1, -1), (-1, 1), (1, 1). The fortran array representing the signal has therefore 16384 elements in it. The filtering used in this simulation is of the same model as that used in the Intelsat V system, that is, an $x/\sin x$ amplitude equalizer followed by a root raised cosine filter with a roll-off of 0.4.

The HPA characteristic is that of a typical ground station TWT also used in the Intelsat V system. It is shown in Fig. 4.1.2.

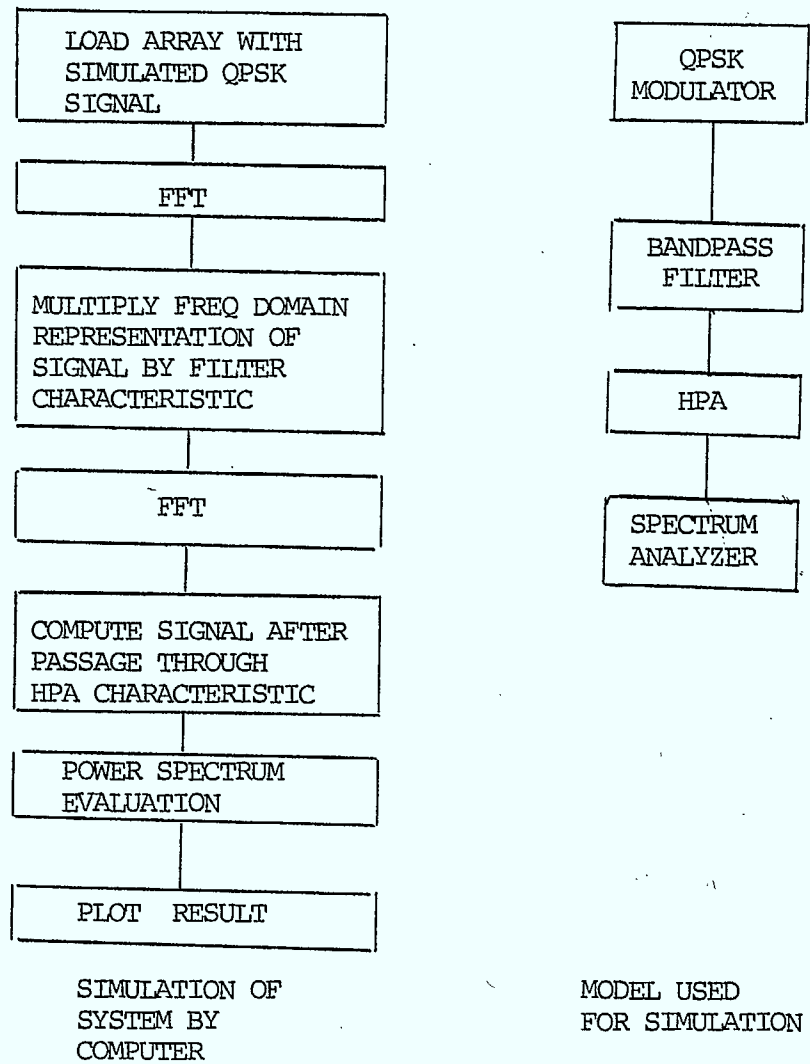


Fig. 4.1.1 Flow chart of program to compute the power spectra after a nonlinearity and system model used.

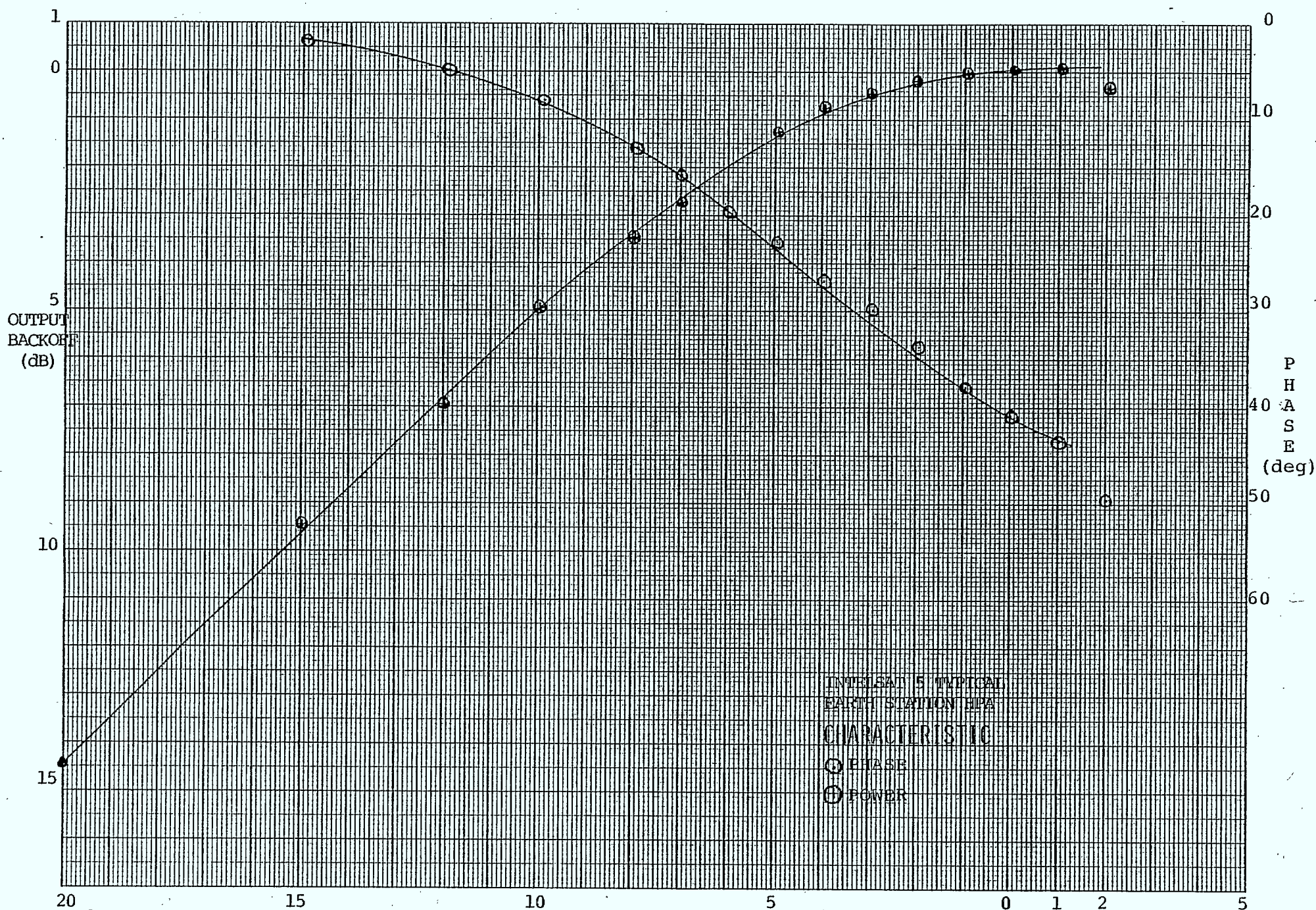


Figure 4.1.2 - INPUT BACKOFF (dB)

The algorithm used was first described by Welch [4]. The principle employed is simple (see Fig. 4.1.3). The time sequence is partitioned into L segments, each of which are windowed to limit the effect of the finite length record. The power spectrum estimate is obtained by taking the square of the norm of the amplitude spectrum which is obtained by taking the FFT of the sequence. This estimate of the power spectrum is called the periodogram. Each periodogram has L estimates of the power spectrum corresponding to L frequencies.

The window can be compared with the IF filter of a spectrum analyser. Since the window is a weighting function that multiplies the data in the time domain, it is equivalent to the convolution of the "true spectrum" with the transform of the time domain window. The sidelobes of this window impose a restriction on the accuracy of the power spectrum estimate. If the sidelobe was not much smaller than the spectra to be estimated, the estimate at one frequency would be a superposition of the spectra at that frequency and the contribution from the side lobes of the window. This leakage effect is one source of error in power spectrum estimation. A desirable characteristic for the window is that it has a rapid transition from the mainlobe to the sidelobe. Two windows were used for this simulation: the Parzen and the Kayser with a parameter of 1.5. Figures 4.1.4 and 4.1.5 illustrate the result of these calculations. In this simulation the length of a segment was chosen to be 256. It can be proved mathematically that dividing the data into

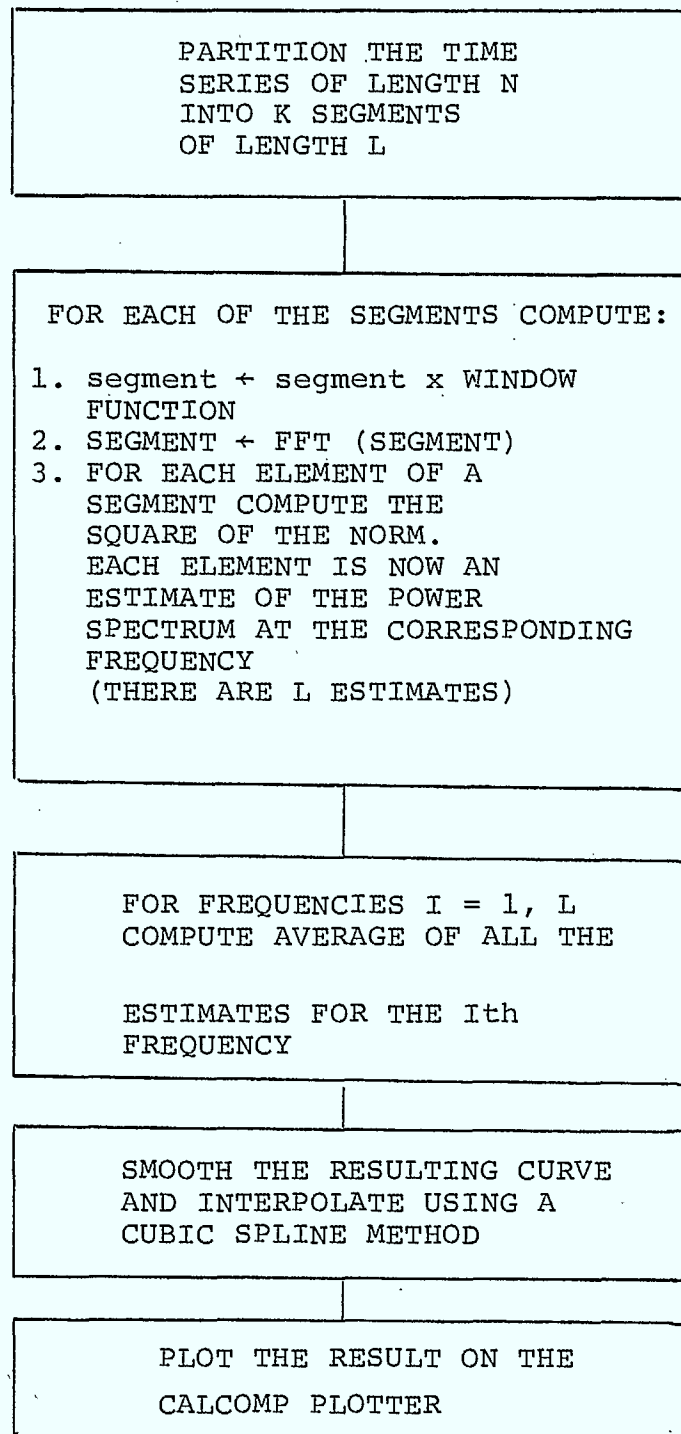


Figure 4.1.3 Flow chart of power spectrum evaluation algorithm.

many segments reduces the variance of the estimate. The resulting curve also looks smoother. The limitation on this is that if segments became too small the spectrum estimate of the NRZ would not be of good quality. The end result would be of reduced accuracy. Furthermore reducing the number of points per segment decreases the resolution. The window affects the resolution in the following way: The lobe width is of the order of 1 to 2 times the resolution of the FFT obtained by taking the inverse of the record length.

On the other hand an increase in resolution can be obtained by increasing the number of points in each segment. The number of segments will be reduced and the limited number of estimates to be averaged will cause considerable ripple in the graph. From another point of view the variance on the estimates will have increased. To reduce the variance and still retain the resolution a larger number of symbols must be taken.

The effect of limited resolution does not have much impact on regions of the spectra where there is a slow variation. However in rapidly varying regions, such as around the Nyquist frequency in a bandlimited system, resolution must be great so as to see rapidly varying power spectra. The effect of limited resolution on rapidly varying transitions in the spectrum will be to convolve the true rapidly varying spectra with a wide window. The result will be to change the rapidly varying transition to a slower one. For spectrum spreading this type of computation will yield a pessimistic result. In other words, it will calculate the spectrum higher than reality.

INTELSAT V HPA
FOR 0 - 14 dB INPUT BACKOFF
LINEAR CHANNEL SPECTRUM
IS GIVEN.
PARZEN WINDOW IS USED.

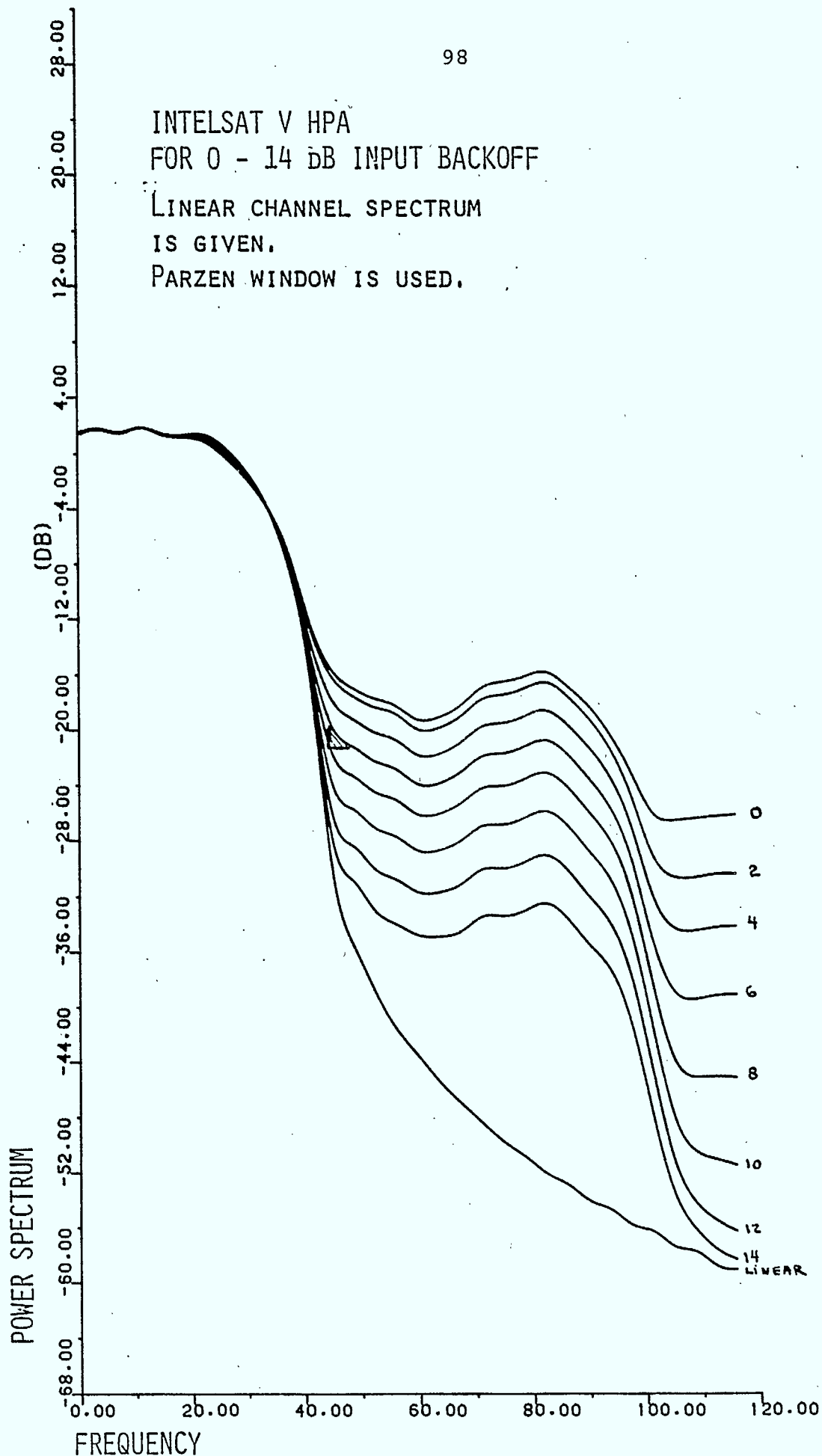


Fig. 4.1.4 Method of modified periodogramme (Parzen window)

INTELSAT V HPA

FOR 0 - 14 dB INPUT BACKOFF

LINEAR CHANNEL SPECTRUM

IS GIVEN.

KAYSER WINDOW IS USED.

PARAMETER = 1.5

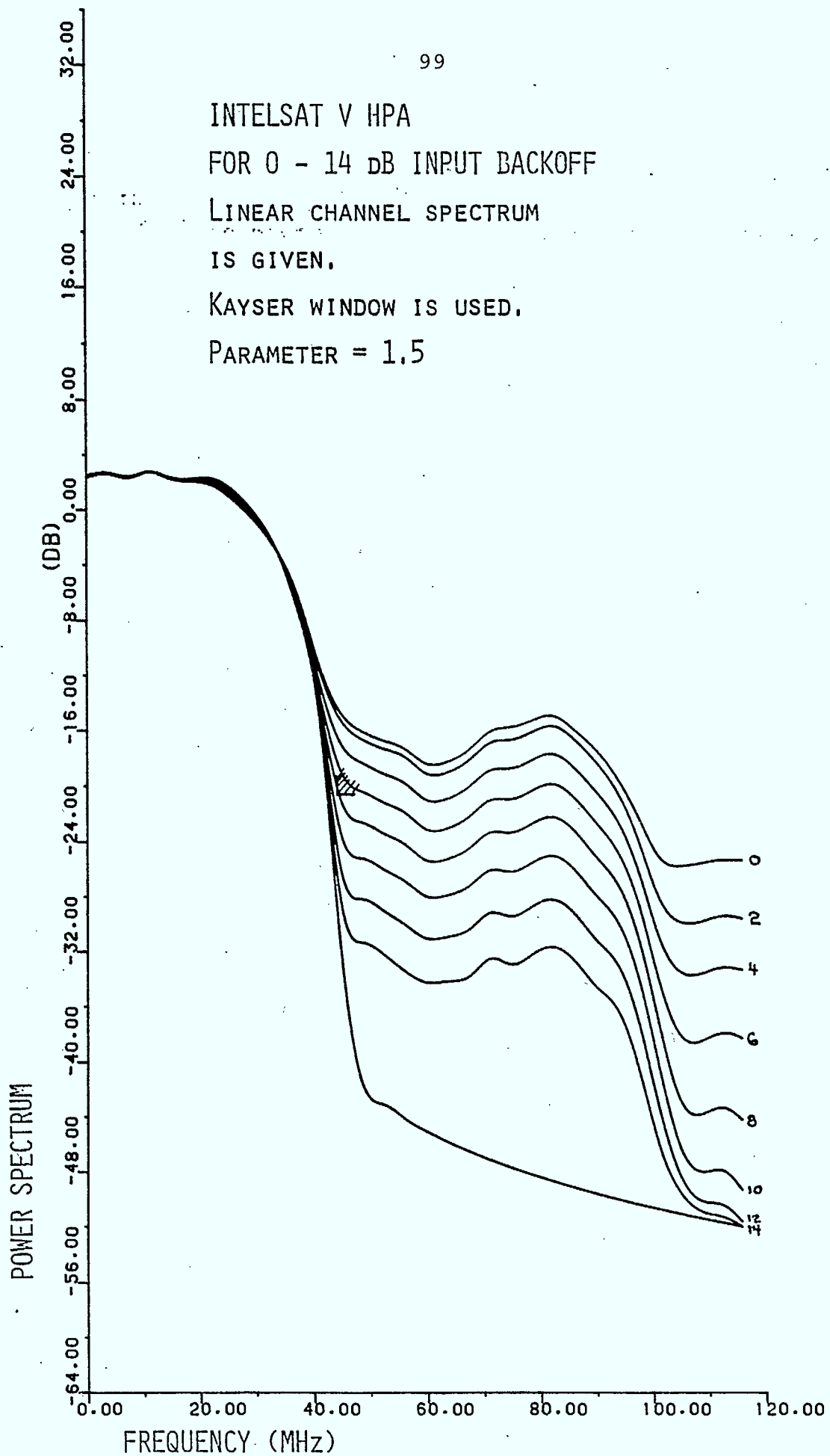


Fig. 4.1.5 Method of modified Periodogramme (Kayser window)

4.1.3 Application to INTELSAT V Case

The considerations given in the previous section have been applied to the Intelsat V case. A problem of importance is to answer the following question: what is the input backoff required to have an out-of-band emission resulting from spectrum spreading of 23 dBW/4 KHZ, at 44 MHZ away from the center frequency.

A computationally efficient solution is to scale the signal power after passage in the HPA to the same value for different input backoffs and then to plot the result. The 0 dB of the spectrum scale is set at the density at frequency 0. It can be seen that in all cases the mainlobes for all the backoffs are at the same power level. The results of the calculation are shown in Fig. 4.1.4 and 4.1.5. The curves were generated for 0, 2, 4, 6, 10, 12, 14 dB input backoff and a curve generated indicating the linear case. The tapering off of the linear case past the nyquist frequency is due to the extremely small power past $1.4 \times \text{Nyquist frequency}$. This very small quantity is being convolved with the sidelobes of the window.

The graph indicates that the Intelsat V spec would be met by using an input backoff of 10 dB. It was pointed out earlier that this result tends to be pessimistic. Some preliminary results using 16 times more resolution indicate that an input backoff of 8 dB can meet the specification.

Due to lack of time the effect of bursting the data on the power spectrum was not investigated.

REFERENCES

- [1] Electronics, McGraw Hill Publishing, Sept. 1980.
- [2] Shimbo, Robinson, Fang, "Comsat Technical Review, Vol. 3, No. 2, August 1973, p. 227.
- [3] Intelsat TDMA/DSI system specification document no. BG/T - temp 32-107 (rev 1) 1980.
- [4] Welch, P.D., The use of Fast Fourier transform for the estimation of power spectra: A method based on time averaging over short, modified periodograms, IEEE trans on audio & Electroacoustics, Vol. AV-15, No. 2, June 1967.

CHAPTER 5

EVALUATION OF DPSK AND DQPSK SYSTEMS

5.1.1 Introduction

Differential phase-shift keying (DPSK) is a modified form of phase-shift keying. In DPSK, the digital information is encoded in the relative phase changes between two symbols rather than in the absolute phases. As such, there is no need to acquire the synchronous carrier at the receiver [1]. This has several impounding effects when DPSK is used in the regenerative satellite. The omission of the carrier recovery circuitry on board the satellite not only means a great saving in weight, but also, with less hardware, there is less risk of failure. As the realization of a carrier recovery circuitry with sufficient stability may be the most difficult task, with DPSK, the regenerative satellite becomes more easily achievable.

However, lack of a coherent carrier for demodulation implies that DPSK may require higher carrier-to-noise ratio (C/N) for the same bit error rate in comparison to the coherent PSK [2]. This is because a bit determination in DPSK is made on the basis of the signal in two successive bit intervals. Noise in one bit interval may consequentially cause errors in two successive bits, i.e., there is a tendency for bit errors to occur in pairs. Nevertheless, this higher C/N requirement may be easily compensated for by increasing the earth-station transmission power.

One other inherent benefit of DPSK is that it has already the built-in function of differential encoding/decoding. If the signal is doubly differentially encoded at the earth transmit station,

the differential encoding at the satellite can then be omitted. In this case, however, whenever errors occur, both the up-link and down-link errors are doubled.

The most important problem in implementing the DPSK demodulation on board the satellite is the stability of the one-symbol delay element. This delay-time variation results in the phase-error of the reference signal and deteriorates the bit error rate. Although this delay-element stability problem can be minimized by implementing it at IF, this approach somewhat reduces the weight-saving advantage of DPSK that arises owing to the omission of the carrier recovery circuitry. Recent development of MIC technology, however, has resulted in a delay filter that can be used as a 1-symbol delay unit in a DQPSK (differential quaternary PSK) demodulator with a C/N degradation less than 0.2 dB at $\text{BER}=10^{-4}$ in comparison with that using an ideal delay line [3].

The purpose of this chapter is to evaluate the performance of a DQPSK satellite system using computer simulation. Only the DQPSK is considered as the 4-phase system. QPSK has been, over the years, the most utilized modulation scheme for satellite applications. The satellite system under consideration is that of the INTELSAT V specifications, which are evaluated using QPSK in Chapter 3.

Although it has been proposed that DQPSK be used for the up-link and QPSK for the down-link in the regenerative satellite [4] [5], only the DQPSK for both the up- and down-links will be considered in this chapter. Our concentration will be on establishing the performance degradations caused by the group delays of the filters, the nonlinear effects of the high power amplifier (HPA) and the travelling wave tube amplifier (TWTA), and the combined effects of imperfect filtering and cascaded nonlinearities.

5.2.0. Computer Simulation Technique

The computer simulation technique for DQPSK is basically similar to that of QPSK described in Chapter III. The only difference lies in the DQPSK signal generation and decoding, descriptions of which are given in Sections 5.2.1 and 5.2.2. The simulation program was modelled according to the block diagram shown in Fig. 5.1.1.

At the earth transmit station, a DQPSK modulator generates an equivalent complex baseband DQPSK signal as described in Section 5.2.1. This complex baseband DQPSK signal is then bandlimited by a low-pass complex equivalent $(\frac{x}{\sin x} + \sqrt{\alpha=0.4})$ transmit filter. The filtered signal is then passed through a high power amplifier, (HPA), characteristics of which are as specified for INTELSAT V. The HPA is assumed to operate at 10 dB input backoff.

At the satellite input MUX filter, the desired signal is corrupted by thermal noise. For this project, the adjacent and co-channel interference effects were not considered.

The corrupted signal then passes through the on-board DQPSK demodulator/regenerator. The regenerated signal is then either DQPSK or QPSK remodulated, bandpass filtered and then power amplified by the transponders travelling wave tube amplifier (TWTA) for down-link transmission.

The input and output MUX filters are both at 30% excess Nyquist frequency, which is identical to the baudrate of the input data stream. The input MUX filter has an $\alpha = 0.1$ roll-off factor

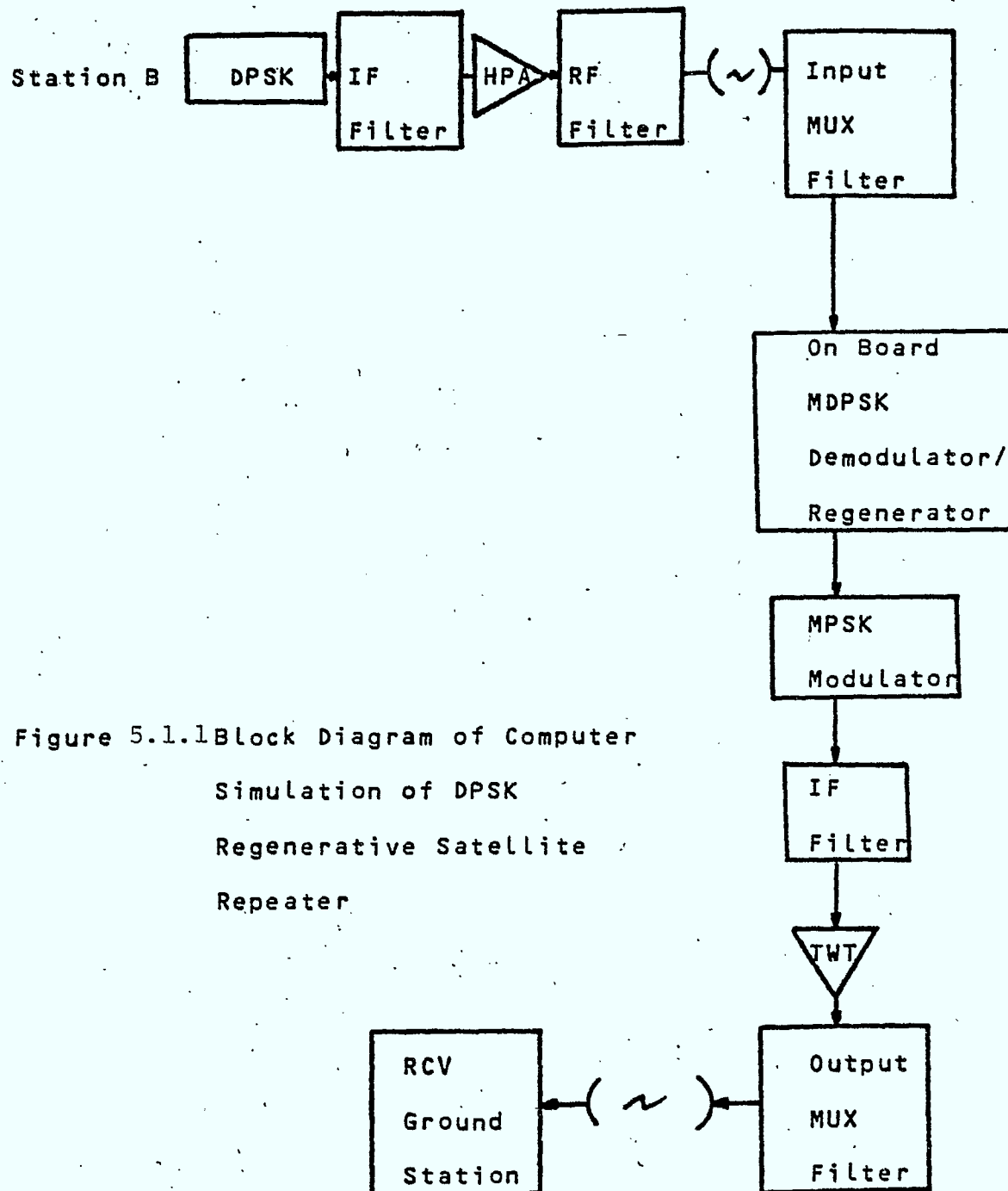


Figure 5.1.1 Block Diagram of Computer Simulation of DPSK Regenerative Satellite Repeater

and output MUX filter $\alpha = 0.2$.

At the receive earth station, the receive signal passes through an $\sqrt{\alpha=0.4}$ receive filter to bandlimit the front-end thermal noise and adjacent channel interference (not considered). It is then either coherently or differentially detected for the probability of error evaluation.

In this chapter, our main interest is in DQPSK. We will therefore consider DQPSK as being employed in both the up-link and down-link transmission. The simulation will be on DQPSK signal in a cascaded-nonlinearity channel (HPA + TWT) as specified in INTELSAT V. These results will be compared with those of a DQPSK demodulator/remodulator on-board the satellite.

In the actual simulation, as in the QPSK case studied in Chapter III, a complex baseband signal representing DQPSK is first generated. It is then attenuated and transformed, by means of a Fast Fourier Transform (FFT) algorithm, between its time-domain and frequency-domain representations as shown in Fig. 5.4.2. In the frequency-domain, it is modified by the complex transfer function of the bandlimiting filters. In the time-domain, it is modified by the nonlinearities of the power amplifiers employed in the system.

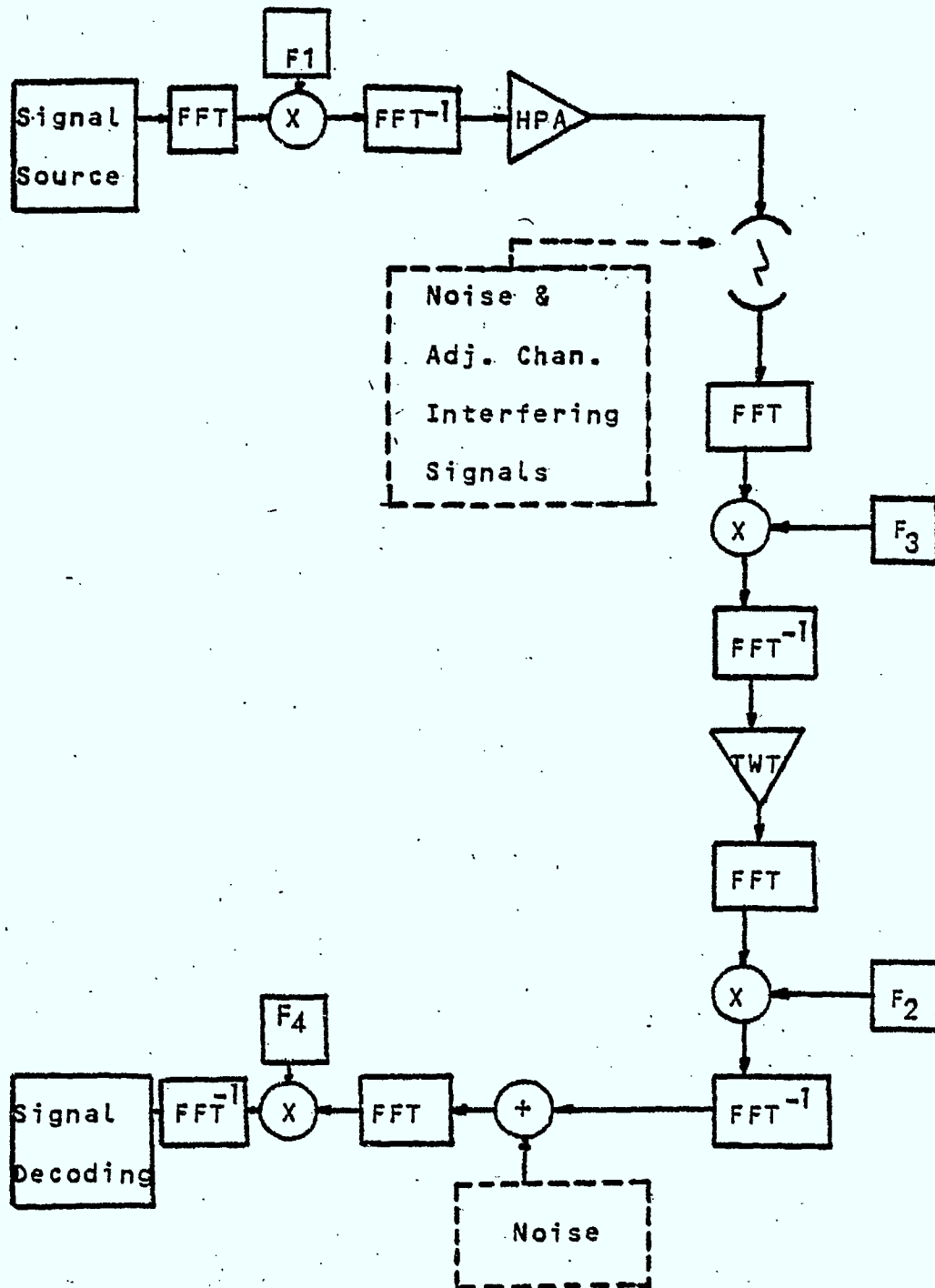


Figure 5.1.2 Signal Processing By Computer Simulation

5.2.1. Generation of a DQPSK Signal

Two random sequences are used to generate the phase differential,

$$\Delta\theta = \theta_m - \theta_{m-1} \quad (5.1)$$

where m represents the bit under consideration and $m-1$ represents its previous bit.

As in QPSK, the value of the phase differential $\Delta\theta$ may be one of the following four values:

$$0^\circ, 90^\circ, 180^\circ, \text{ or } 270^\circ$$

From Eq. (5.1), we have

$$\theta_m = \theta_{m-1} + \Delta\theta \quad (5.2)$$

And the complex envelope of a DQPSK signal becomes

$$S(t) = A(t) \cos \theta_m + A(t) \sin \theta_m \quad (5.3)$$

$$\text{where } A(t) = \pm 1 \quad \text{for } -\frac{T}{2} \leq t \leq \frac{T}{2}$$

$$= 0 \quad \text{elsewhere}$$

with T being a baud interval

The value of the in-phase and quadrature channel baseband signal over any baud interval is then proportional to:

$$\cos \theta_m = \cos \theta_{m-1} \cos \Delta\theta - \sin \theta_{m-1} \sin \Delta\theta \quad (5.4)$$

$$\sin \theta_m = \sin \theta_{m-1} \cos \Delta\theta + \cos \theta_{m-1} \sin \Delta\theta$$

The assignment of values for the in-phase and quadrature baseband channels of a DQPSK signal can thus be summarized as in Table 5.1.

Table 5.1.1 Generation of a DQPSK Signal

| PN_1 | PN_2 | $\Delta\theta$ | $\cos \phi_{m-1}$ | $\sin \phi_{m-1}$ | $I(t)$ (in-phase channel) | $y(t)$ (quadrature channel) |
|--------|--------|----------------|-------------------|-------------------|---------------------------------|-----------------------------------|
| 1 | 1 | 0° | 1 | 0 | 1 | 1 |
| 1 | -1 | 270° | 0 | -1 | 1 | -1 |
| -1 | 1 | 90° | 0 | 1 | -1 | 1 |
| -1 | -1 | 180° | -1 | 0 | -1 | -1 |

5.2.2 Decoding of the DQPSK Signal

As described in [6], the decoding of a DQPSK signal requires the multiplication of the incoming signal by its delayed replica. The delay element required is one unit baud. Hence when considering the probability of error, as mentioned in Section 5.1.0, noise at two time instants is involved. The retrieval of information of the DQPSK signal may thus be obtained by evaluating the difference of the phase angles represented by two successive symbols.

In phase vector diagram as shown in Fig. 5.1.3, the difference between these two phase vectors has a definite probability of lying anywhere on the phase plane, depending on the channel distortion and the thermal noise. This probability can be described by a density function obtained by the convolution of the two phase density functions representing the two symbols.

Now consider two successive signal symbols received at the receiver and designate them as S_{m-1} and S_m . Let the sampled amplitudes for symbols S_{m-1} and S_m be A_{m-1} and A_m , respectively.

The phase density functions representing S_m and S_{m-1} are given by:

$$P_{m-1}(\theta_{m-1}) = \frac{e^{-P_{m-1}}}{2\pi} + \frac{P_{m-1}}{\pi} \cos \theta_{m-1} e^{-P_{m-1} \sin^2 \theta_{m-1}} \operatorname{erfc}(-\sqrt{P_{m-1}} \cos \theta_{m-1}) \quad (5.5)$$

$$P_m(\theta_m) = \frac{e^{-P_m}}{2\pi} + \frac{P_m}{\pi} \cos \theta_m e^{-P_m \sin^2 \theta_m} \operatorname{erfc}(-\sqrt{P_m} \cos \theta_m)$$

$$\text{where } P_{m-1} = \frac{A_{m-1}^2}{2\alpha^2} \quad \text{and} \quad P_m = \frac{A_m^2}{2\alpha^2}$$

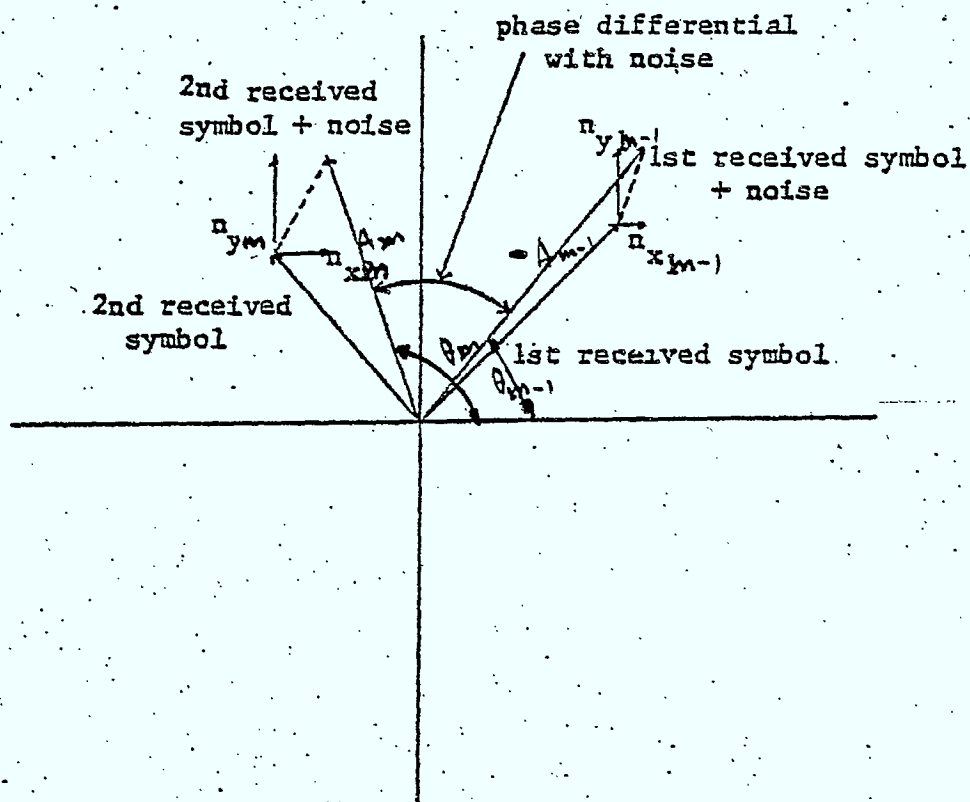


Figure 5.1.3: DPSK signal space or phasor representation showing the effect of additive noise.

α^2 is the RMS noise power and

$$\text{erfc}(x) = \frac{2}{\sqrt{\pi}} \int_0^x e^{-u^2} du$$

The probability density function of the phase differential

$$\Delta\theta = \theta_m - \theta_{m-1} \quad (5.6)$$

is then given by the convolution integral

$$P(\Delta\theta) = \int_{-\pi}^{\pi} P_m(\theta) P_m(\theta + \Delta\theta) d\theta \quad (5.7)$$

If there is no intersymbol interference (ISI) at the sampling instants, the phase differential between the two successive symbols will be midway between the boundaries for correct decisions. In the presence of ISI, the resulting phase differential is displaced from the center, thus increasing the probability of error when there is high noise power at the sampling instants.

Figure 5.1.4 shows the relative position of the phase differential with respect to the decision boundaries in the presence of ISI. The probability of error for the phase differential is obtained by integrating over the regions for incorrect decisions, i.e., by using the integration given in Eq. (5.7). In the case of severe ISI, when the receive phase differential is in error even in the absence of noise, the probability of error for a given phase differential is obtained by 1- Integral of Eq. (5.7) over the correct decision region.

5.2.3 DQPSK Simulation Results

For reference, the performance of DQPSK in an infinite bandwidth channel was first calculated using Eq. (5.7). The calculated result is plotted as curve A in Fig. 5.1.5.

Next, the performance of DQPSK in a linear channel, with the transmit filter having a $(\frac{x}{\sin x} + \sqrt{\alpha})$ response and receive filter a $(\sqrt{\alpha})$ response, was evaluated through the simulation program. The results for various α 's from 0. to 1. are almost identical, and as shown in curve B for $\alpha=0.4$ Fig. 5.1.5, are very close to curve A. This is expected as according to the Nyquist theorem there is no ISI at the sampling instants. The close agreement shows that the simulation program is correct and quite accurate.

In order to evaluate the effect of imperfect filtering on the performance of DQPSK, the parabolic delays as specified in INTELSAT were incorporated into the raised-cosine response. The result for a linear channel with such group delays is plotted as curve C in Fig. 5.1.4. At the BER of 10^{-4} , the group delays of the TX and RX filters incur less than half a dB degradation from the ideal case.

The effect of the INTELSAT V TWT nonlinearity on the performance of DQPSK was next evaluated. The roll-off factor, α , of both filters was assumed to be 0.4 as specified in INTELSAT V. The parabolic delays specified in the INTELSAT filters were again incorporated. The result is given in curve D of Fig. 5.1.4. This curve is nearly identical

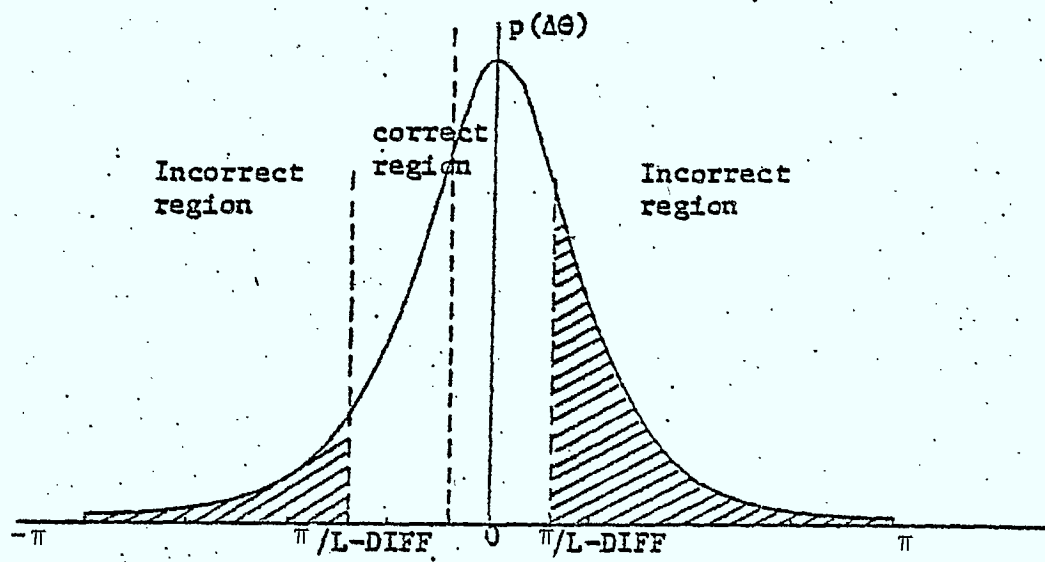


Figure 5.1.4: Effect of ISI on DPSK decision regions

Fig.5.1.5 DQPSK BER Performance
Through an INTELSAT V System

to that of a regenerative DQPSK satellite system when the uplink signal to noise is assumed to be infinity while the downlink noise is controlling.

Finally, the performance of DQPSK in cascaded nonlinearities with HPA at 10 dB input backoff and with TWT at 2 dB input backoff was evaluated. The TX filter was again $(\frac{x}{\sin x} + \sqrt{\alpha=0.4})$ and the RX filter $\sqrt{\alpha=0.4}$. The satellite input MUX filter with $\alpha=0.1$ and output MUX filter with $\alpha=0.2$ were both at 30% excess Nyquist frequency. These four filters were also assumed to have the parabolic delay characteristics such as specified in INTELSAT V. The simulation result is plotted in curve E of Fig. 5.1.4. It shows a degradation of about 3.5 dB at $\text{BER} = 10^{-4}$ and 4.5 dB at $\text{BER} = 10^{-6}$ from the ideal case.

REFERENCES

- [1] R.W. Luchy, J. Salz and E.J. Weldon, Jr., "Principles of Data Transmission", McGraw-Hill, New York, 1970.
- [2] M. Kato and H. Inose, "DDM differentially coherent detection scheme of DPSK signals", Trans. IEEE (Japan), vol. J59-A, No. 2, pp. 133-140, Feb. 1976.
- [3] Y.S. Lee, "14-GHz MIC 16-ns delay filter for differentially coherent QPSK regenerative repeater", IEEE MTT-S International Microwave Symposium, Ottawa, Canada, pp. 37-40, June, 1978.
- [4] K. Koga, T. Muratani and A. Ogawa, "On-board Regenerative Repeaters Applied to Digital Satellite Communications", Proc. of the IEEE, vol. 65, No. 3, pp. 401-410, March 1977.
- [5] Y.S. Lee, "Simulation Analysis for differentially coherent quaternary PSK regenerative repeater", COMSAT Tech. Review, Vol. 7, No. 2, pp. 447-474, Fall, 1977.
- [6] H.C. Chan, D.P. Taylor, S.S. Haykin, "Comparative Evaluation of Digital Modulation Techniques", Communication Research Laboratory, McMaster University, Hamilton, Ontario, Canada, Internal Report CRL-18.

CHAPTER 6

A STUDY OF OKQPSK AND MSK MODULATION METHODS

6.1.1 Introduction

To make a communication satellite system power efficient, the earth station HPA and the satellite TWTA are operated near saturation. This causes degradations in the performance of the system when QPSK is used. The degradations are usually explained to be caused by the envelope fluctuations of the filtered signal; in QPSK, the envelope fluctuation can be very high. When the envelope-fluctuating (AM) signal passes through a non-linear device, AM/AM and AM/PM conversions cause signal distortion and result in spectral spreading which results in interchannel interference (ICI). Hence, if the input to the HPA or TWTA has constant envelope or minimum envelope fluctuation, ICI will be reduced accordingly, improving the system performance. The envelope fluctuation of OK QPSK is at most 3 dB whereas the MSK signal envelope is constant. Thus, MSK and OKQPSK appear attractive for use on satellite systems. Although the main lobe of the MSK spectrum is 1.5 times wider than that of OKQPSK, by using proper pulse shaping, the spectral efficiency of MSK and OKQPSK are identical to that of QPSK i.e. 2 b/s/Hz [1,2].

In this chapter, the effect of filtering and hardlimiting is explored for MSK, OKQPSK and QPSK. Both the spectral density and probability of error performance are considered. Using the simulation model as that used in Chapter 3, the effect of using

regenerative satellite system is investigated for MSK and OKQPSK. The same 120 Mb/s system having a cascade of two nonlinearities is used. The results are also compared to those of QPSK.

6.1.2 Bandlimiting and Hardlimiting of QPSK, OK-QPSK and MSK

This section covers the study of the effects of filtering and limiting on the spectral densities, symbol waveshapes and probability of error (P_e) versus signal-to-noise (S/N) performances of systems employing the various modulation methods. A mathematical model and physical insight into the crosstalk phenomenon quadrature channels, created in the systems as a result of filtering followed by hardlimiting, are given. It is shown that for systems incorporating an amplitude limiting amplifier in the transmitter, the transmitter filtering necessary to limit the radiated spectrum is more easily realized with OK-QPSK than with QPSK or MSK.

Figure 6.1.1 shows the block diagram of the equivalent baseband model of digital systems studied along with the various filter characteristics necessary for the following study and discussions.

The power spectral densities of MSK and QPSK/OK-QPSK for balanced random data are given by [3].

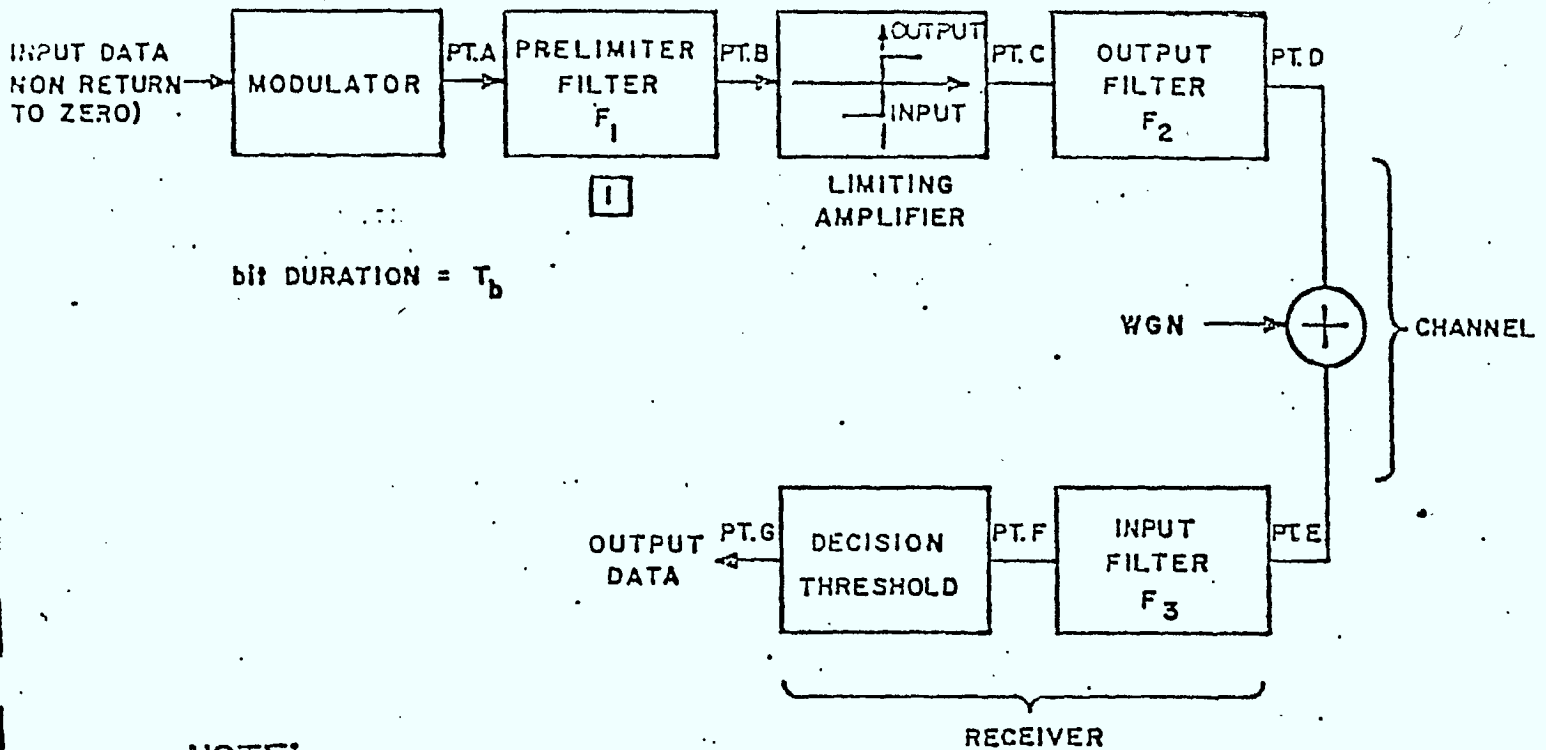
$$G_{\text{MSK}}(f) = \frac{8P_c T_b [1 + \cos 4\pi(f-f_0)T_b]}{\pi^2 [1 - 16T_b^2(f-f_0)^2]^2} \quad (6.1.1)$$

$$G_{\text{QPSK/OK-QPSK}}(f) = 2P_c T_b \left[\frac{\sin 2\pi(f-f_0)T_b}{2\pi(f-f_0)T_b} \right]^2 \quad (6.1.2)$$

where f_0 - is the carrier frequency,

P_c - is power of the modulated waveform

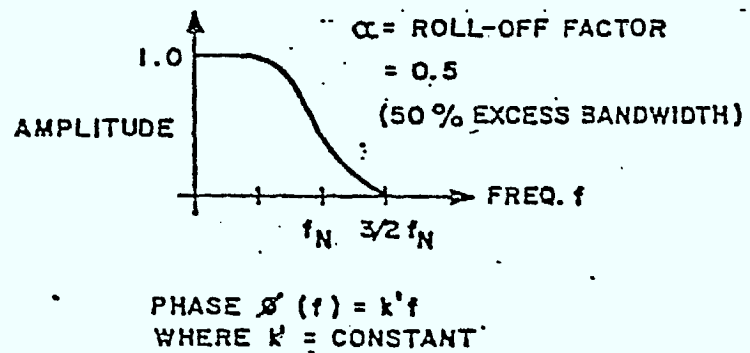
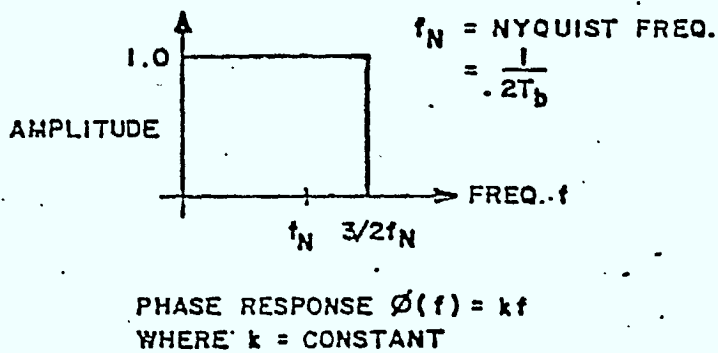
T_b - is the unit bit duration of the input data signal.



NOTE:

- [1] - PRELIMITER FILTER, F_1 , IS 4 POLE CHEBYSHEV, 0.1 dB RIPPLE, DOUBLE SIDED BANDWIDTH B.

a) BLOCK DIAGRAM



b) CHARACTERISTICS OF TRANSMITTER OUTPUT FILTER, F_2

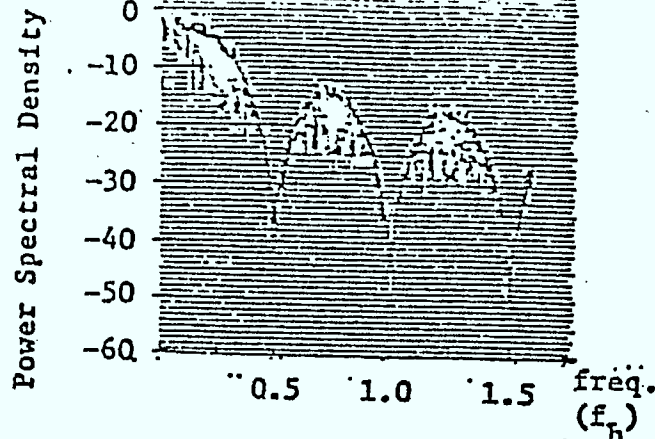
c) SPECTRUM OF SIGNAL AT OUTPUT OF RECEIVER INPUT FILTER, F_3

FIGURE 6.1.1-EQUIVALENT BASEBAND MODEL OF DIGITAL SYSTEMS STUDIED.

From these expressions we note that for large values of $(f-f_0)T_b$, the MSK spectrum fall off at a rate proportional to $[(f-f_0)T_b]^{-4}$, while for QPSK/OK-QPSK, the spectrum falls off at a rate proportional to only $[(f-f_0)T_b]^{-2}$. The main lobe of the MSK spectrum however, is wider than that of the QPSK/OK-QPSK, with the first null appearing at $(f-f_0)T_b = 0.75$, while for QPSK/OK-QPSK it appears at $(f-f_0)T_b = 0.5$.

For each of the modulation techniques under study, computer simulations of spectral densities with systems modelled as in Fig. 6.1.2 have been carried out. Figures 6.1.2, 6.1.3 and 6.1.4 are from these simulations and show, respectively, single-sided power spectral densities for QPSK, Offset QPSK and MSK. Each figure shows the unfiltered spectral density at the modulator output, as well as spectral densities at the prelimiter filter output and at the limiting amplifier output for different amounts of filtering. We note that the spectra are not smooth functions but show minor fluctuations. This is the result of the simulation data sequence being of finite length and not truly random. The spectral densities shown are relative to the density at carrier frequency. The product BT_b associated with the figures refers to the prelimiter filter 3 dB double-sided bandwidth B , and the unit bit duration T_b . The following should be noted from the figures.

- 1) The unfiltered main lobe single-sided bandwidth of QPSK and Offset QPSK is equal to $0.5 f_b$, where f_b is the transmission bit rate. However, the unfiltered main lobe single-sided bandwidth of MSK is equal to $0.75 f_b$.

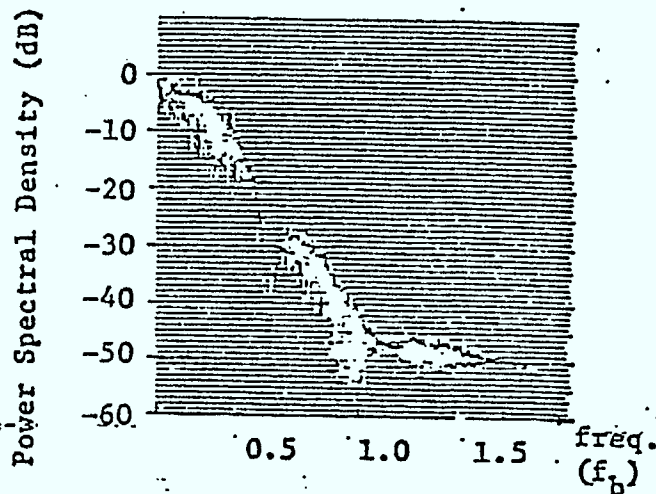


(a) Spectral Density at pt. A, Fig. 6.1.1
Unfiltered, $BT_b = \infty$.

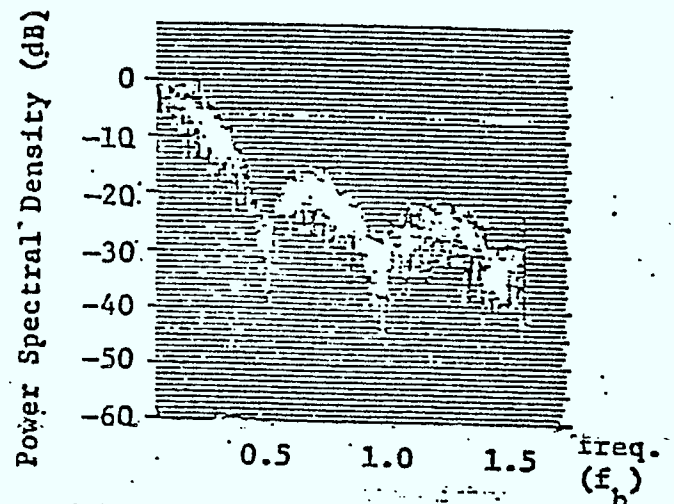
B = Prelimiter filter double-sided
3 dB Bandwidth. - 7 -

T_b = System unit bit duration.

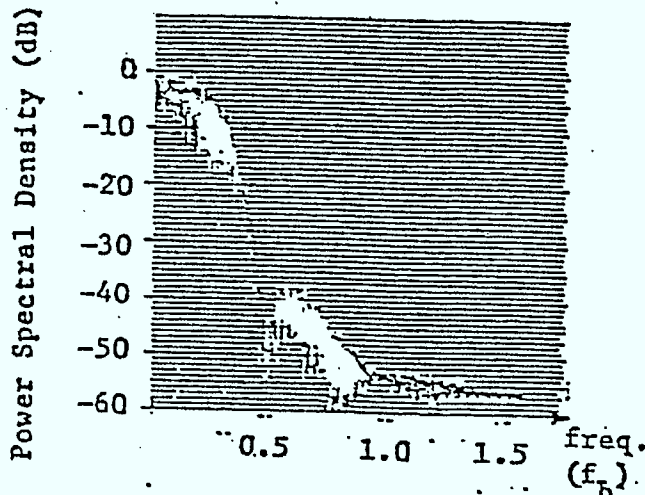
Prelimiter filter: 4-pole Chebyshev,
0.1 dB ripple.



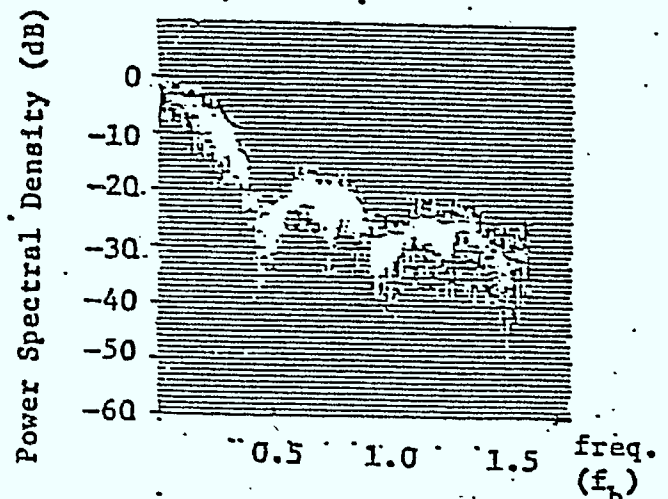
(b) Spectral Density at pt. B, Fig. 6.1.1
Filtered, $BT_b = 1$.



(c) Spectral Density at pt. C, Fig. 6.1.1
Filtered, $BT_b = 1$, then limited



(d) Spectral Density at pt. B, Fig. 6.1.1
Filtered, $BT_b = 0.75$



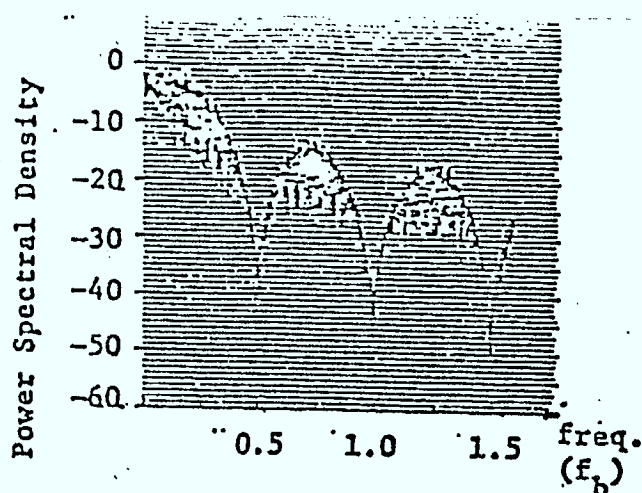
(e) Spectral Density at pt. C, Fig. 6.1.1
Filtered, $BT_b = 0.75$, then limited.

Figure 6.1.2 COMPUTED POWER SPECTRAL DENSITIES FOR QPSK

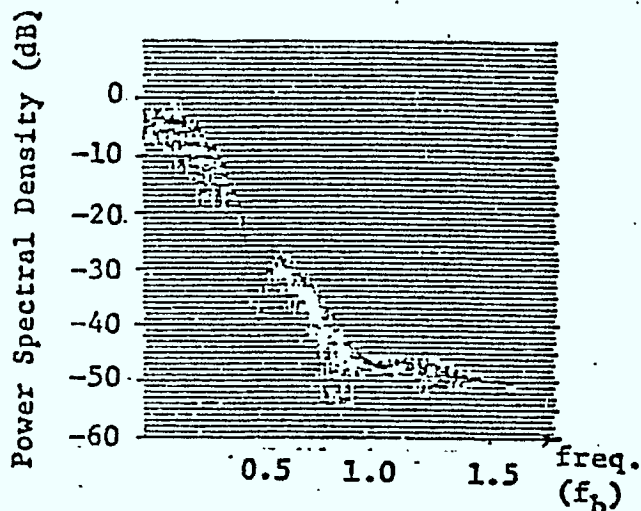
B = Prelimiter filter double-sided
3 dB Bandwidth.

T_b = System unit bit duration.

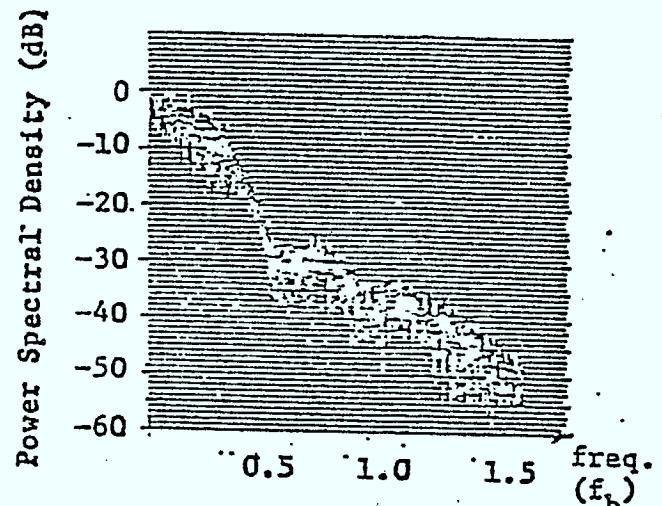
Prelimiter filter: 4-pole Chebyshev,
0.1 dB ripple.



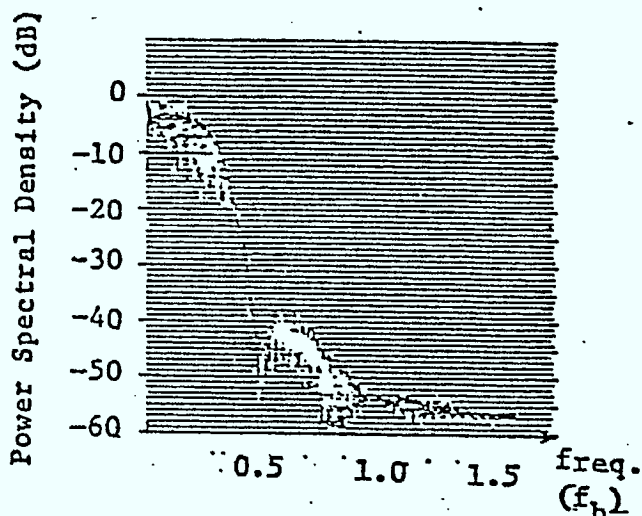
(a) Spectral Density at Pt. A. Fig. 6.1.1
Unfiltered, $BT_b = \infty$.



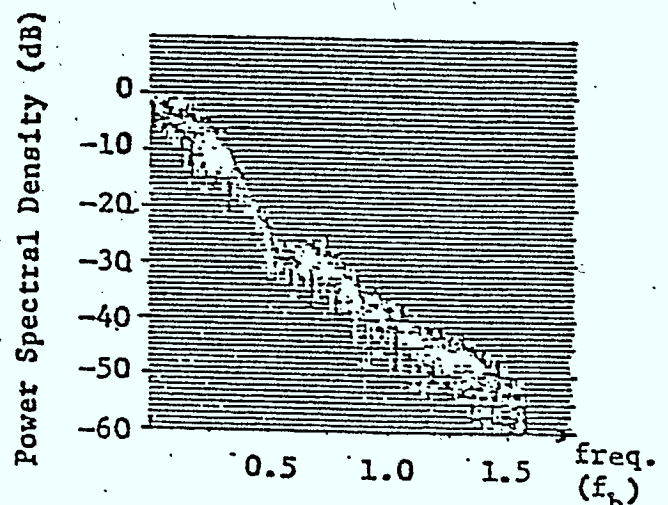
(b) Spectral Density at pt. B, Fig. 6.1.1
Filtered, $BT_b = 1$.



(c) Spectral Density at pt. C, Fig. 6.1.1
Filtered, $BT_b = 1$, then limited.



(d) Spectral Density at pt. B, Fig. 6.1.1
Filtered, $BT_b = 0.75$.



(e) Spectral Density at pt. C, Fig. 6.1.1
Filtered, $BT_b = 0.75$, then limited.

Figure 6.1.3 COMPUTED POWER SPECTRAL DENSITIES FOR OFFSET QPSK

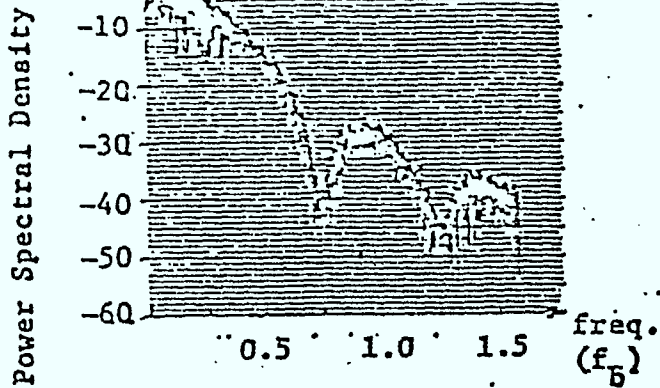
B = Prelimiter filter double-sided

3 dB bandwidth.

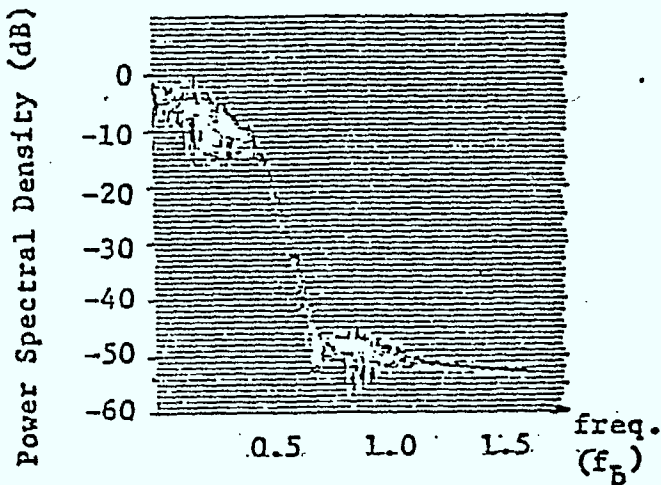
- 9 -

T_b = System unit bit duration.

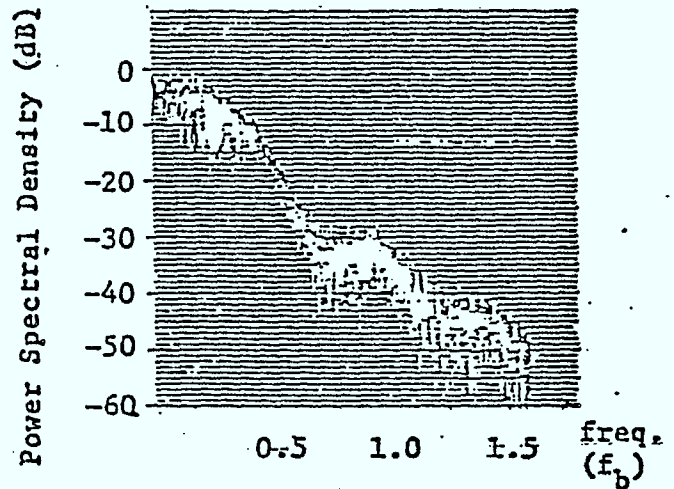
Prelimiter filter: 4-pole Chebyshev,
0.1 dB ripple.



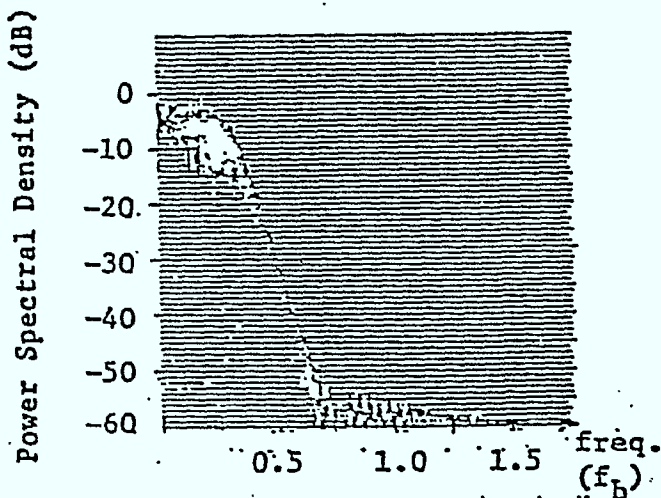
(a) Spectral Density at pt. A, Fig. 6.1.1
Unfiltered, $BT_b = \infty$.



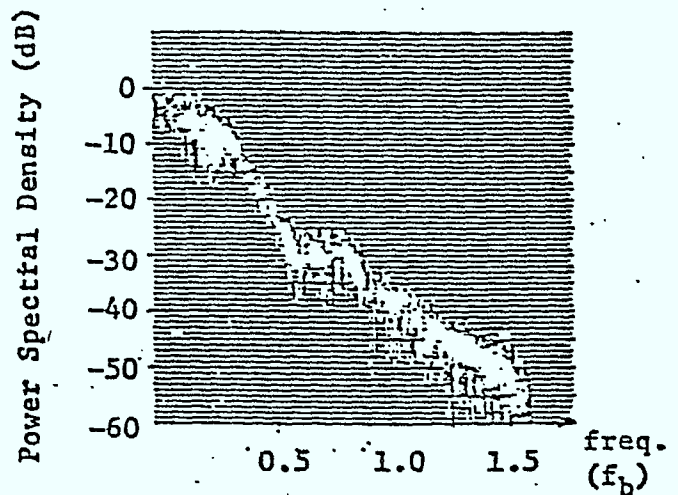
(b) Spectral Density at pt. B, Fig. 6.1.1
Filtered, $BT_b = 1$.



(c) Spectral Density at pt. C, Fig. 6.1.1
Filtered, $BT_b = 1$, then limited.



(d) Spectral Density at pt. B, Fig. 6.1.1
Filtered, $BT_b = 0.75$.



(e) Spectral Density at pt. C, Fig. 6.1.1
Filtered, $BT_b = 0.75$, then limited.

Figure 6.1.4 COMPUTED POWER SPECTRAL DENSITIES FOR MSK

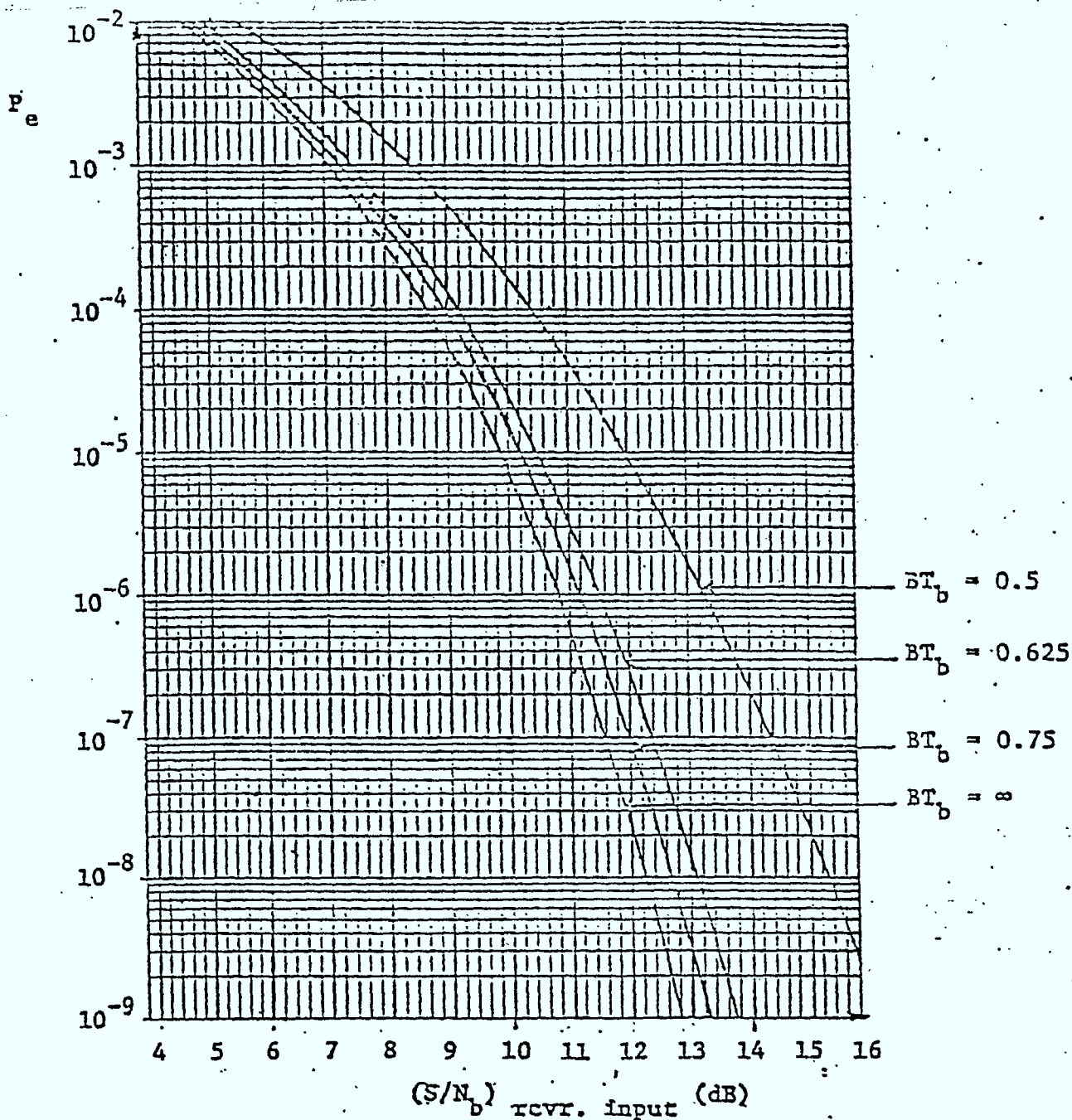
- 2) For $BT_b = 1$ and 0.75 , the main lobe for all three signal types after filtering then limiting are at about their unfiltered level.
- 3) For Offset QPSK, when $BT_b = 1$, the peak of the first sidelobe after filtering then limiting is at about its unfiltered level. When $BT_b = 0.75$, the first sidelobe after filtering and limiting is restored almost to the same level as for the case when $BT_b = 1$.
- 4) For MSK, when $BT_b = 1$ and 0.75 , the peaks of all sidelobes after filtering then limiting are partially restored to their unfiltered levels.
- 5) For QPSK, when $BT_b = 1$ and 0.75 , the peaks of all sidelobes after filtering and limiting are almost fully restored to their unfiltered levels.

6.1.3 Effects of Filtering and Limiting on P_e versus S/N Performance

For each of the modulation techniques under study, and assuming an equivalent baseband model as shown in Fig. 6.1.1, P_e versus the ratio of average received signal level to average WGN level in the bit rate bandwidth (S/N_b) rcvr. input, was computed for various values of BT_b , including BT_b equal to infinity. The results are shown in Figs 6.1.5, 6.1.6 and 6.1.7 for QPSK, Offset QPSK and MSK, respectively.

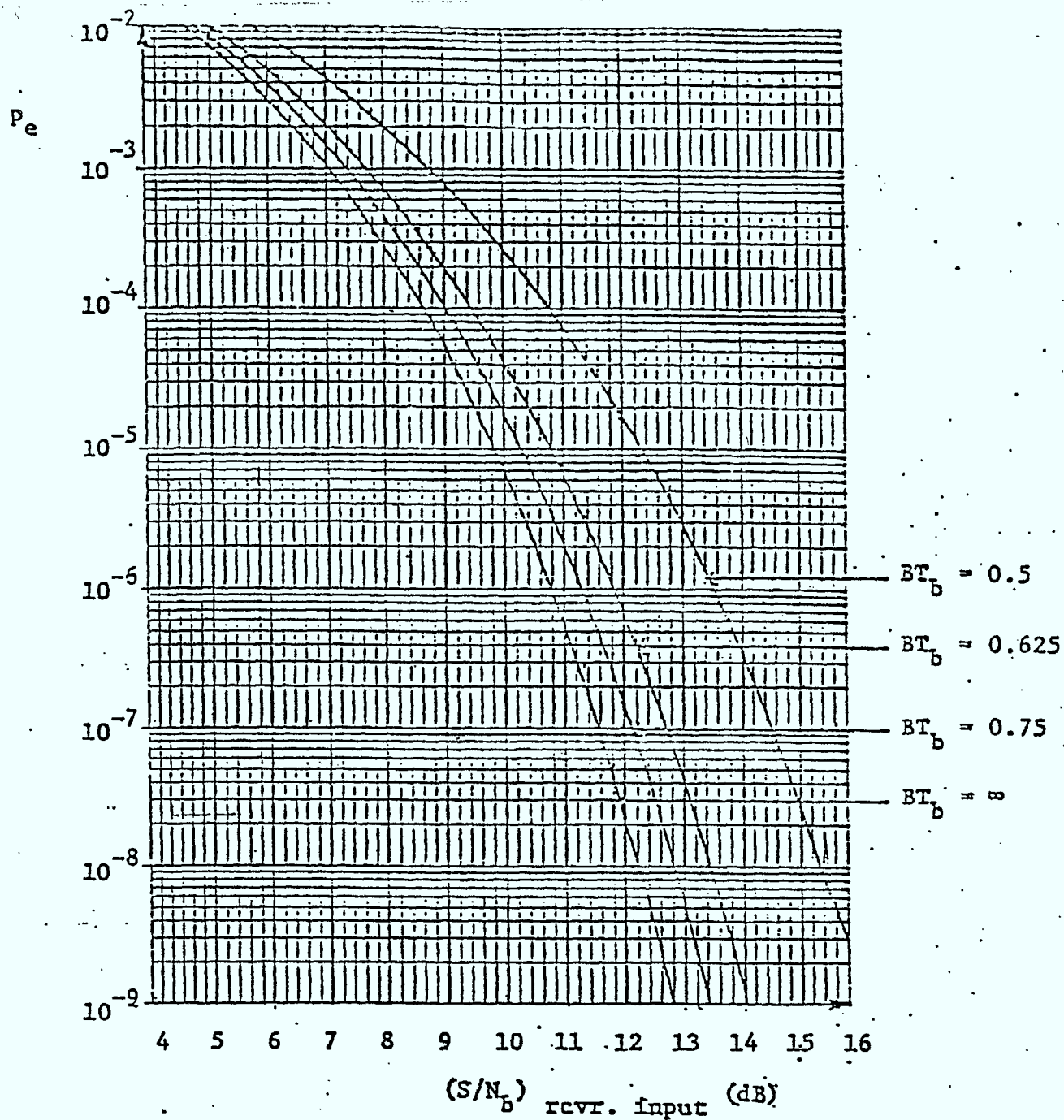
BT_b equal to infinity represents the situation where the prelimited filter is of infinite bandwidth and thus does not filter the signal. Unfiltered QPSK, Offset QPSK and MSK signals all have constant amplitude envelope versus time characteristics and therefore are not affected by the ideal limiting amplifier assumed. Thus, system performance with BT_b equal to infinity is the same as if the prelimiter filter and the limiting amplifier were absent. Under this condition there is no intersymbol interference and the S/N_b for a P_e of 10^{-4} is 8.6 dB for QPSK and 8.85 dB for MSK. For a linear system with the filtering between the transmitter and receiver partitioned for optimum P_e versus S/N_b performance, the S/N_b for a P_e of 10^{-4} is 8.4 dB [4]. Thus, we see that P_e versus S/N_b performance of our model when there is no prelimiter filtering is only slightly degraded from the theoretical optimum for linear transmission.

As the prelimiter filter bandwidth narrows to a stage where significant signal energy is filtered, the in-phase and quadrature symbol waveforms (I and Q) of the signals become distorted and the signals acquire Amplitude Modulation (AM).



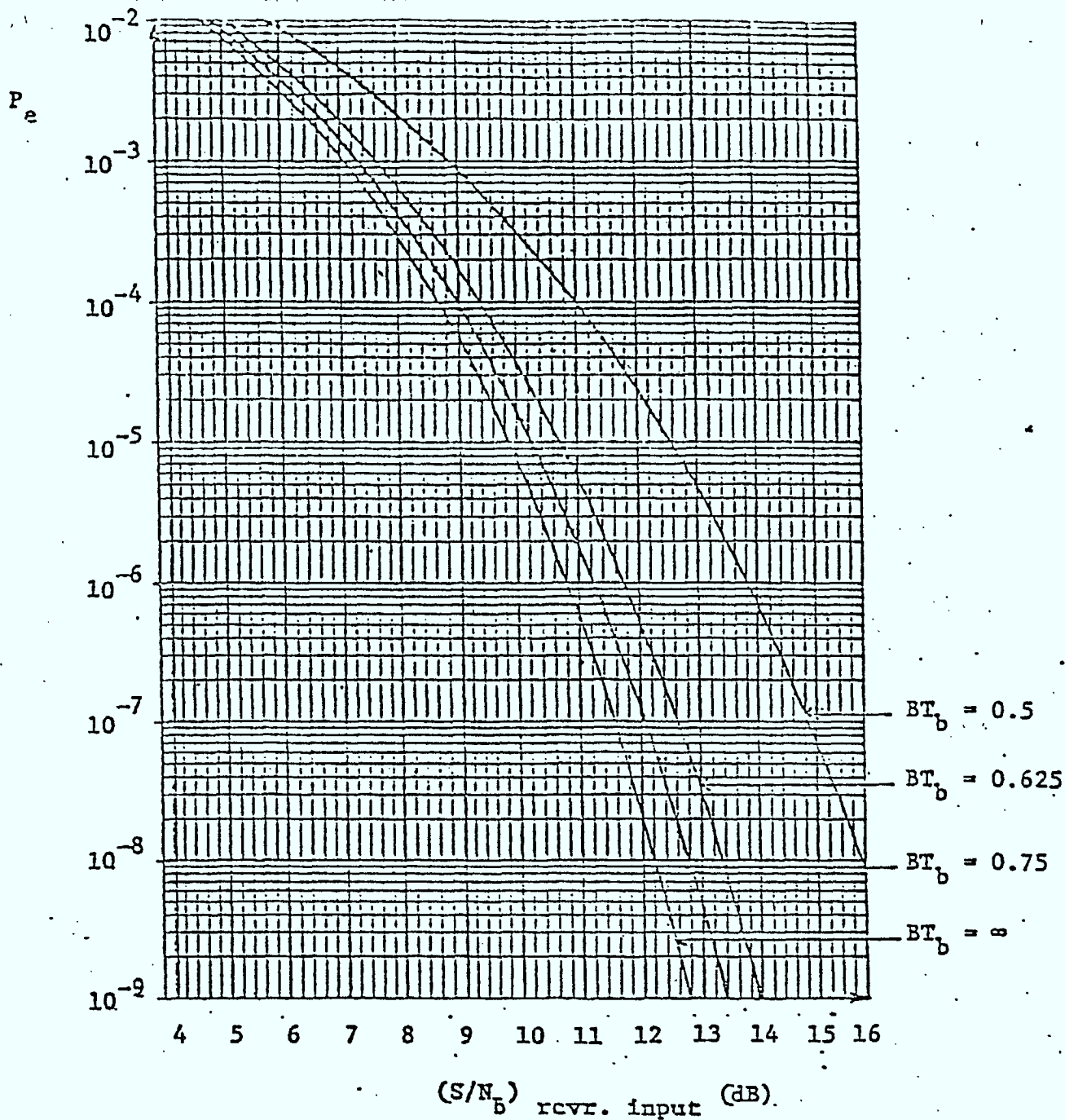
Note: B = Prelimiter Filter double-sided 3 dB bandwidth.
 T_b = System unit Bit duration.
 S = Average signal power at rcvr. input.
 N_b = Average WGN in bit rate bandwidth at rcvr. input.

Figure 6.1.5 P_e VERSUS $(S/N_b)_{rcvr. input}$ FOR QPSK SYSTEM SIMULATED



Note: B = Prelimiter Filter double-sided 3 dB bandwidth.
 T_b = System unit bit duration.
 S = Average signal power at rcvr. input.
 N_b = Average WGN in bit rate bandwidth at rcvr. input.

Figure 6.1.6 - P_e VERSUS $(S/N_b)_{rcvr. input}$ FOR OFFSET QPSK SYSTEM SIMULATED



Note: . B = Prelimiter Filter double-sided 3 dB bandwidth.
 T_b = System unit bit duration.
 S = Average signal power at rcvr. input.
 N_b = Average WGN in bit rate bandwidth at rcvr. input.

Figure 6.1.7 P_e VERSUS $(S/N_b)_{\text{rcvr. input}}$ FOR MSK SYSTEM SIMULATED

The limiting action modifies the spectral densities, removes the AM acquired during filtering, and in so doing, further distorts the I and Q symbol waveform as a result of "crosstalk" between the waveforms.

To understand how this crosstalk occurs it is necessary to study the characteristics of the ideal limiter assumed. Let $i_i(t)$ and $q_i(t)$ be the I and Q symbol waveforms into the limiting amplifier of the equivalent baseband model shown in Fig. 3.1.1 and $i_0(t)$ and $q_0(t)$ be the corresponding symbol waveforms out of the limiting amplifier. Then, since the output of the limiter has a constant amplitude envelope versus time characteristic,

$$i_0^2(t) + q_0^2(t) = C \quad (6.1.3)$$

where C is a constant dependent on the limiting amplifier output power. Also, as the memoryless infinite bandwidth limiter results in no change of signal phase,

$$\text{signal phase-out} = \text{signal phase-in},$$

that is,

$$\arctan \left(\frac{q_0(t)}{i_0(t)} \right) = \arctan \left(\frac{q_i(t)}{i_i(t)} \right);$$

thus,

$$\frac{q_0(t)}{i_0(t)} = \frac{q_i(t)}{i_i(t)}, \text{ if the principal values of } \quad (6.1.4)$$

the (arc tan) are assumed.

By replacing $q_0(t)$ in equation 6.1.4 by its equivalence as given in equation 6.1.3 we get:

$$i_0(t) = \frac{C i_i(t)}{(i_i^2(t) + q_i^2(t))^{\frac{1}{2}}} \quad (6.1.5)$$

and by replacing $i_0(t)$ in equation 6.1.4 we get:

$$q_0(t) = \frac{Cq_i(t)}{[i_i^2(t) + q_i^2(t)]^{\frac{1}{2}}} \quad (6.1.6)$$

If the unfiltered and hence non-amplitude-modulated signal from the QPSK, Offset QPSK or MSK modulator is fed into our ideal limiter, then

$$i_i^2(t) + q_i^2(t) = K^2$$

where K is a constant.

Thus, by equations 6.1.5 and 6.1.6 the output symbol waveforms are undistorted, as expected, since

$$i_0(t) = ki_i(t) \text{ and } q_0(t) = kq_i(t),$$

where $k = \frac{C}{K} = \text{constant}$.

When the modulator output signal is filtered, the signal becomes amplitude modulated and

$$i_i^2(t) + q_i^2(t) \neq K^2.$$

Thus, by equations 6.1.5 and 6.1.6, $i_0(t)$ and $q_0(t)$ become dependent on $q_i(t)$ and $i_i(t)$, respectively. This influencing of each symbol waveform by the other in quadrature is termed interphasor crosstalk.

As the transmitter output and receiver input filter combination in our model provides intersymbol interference-free transmission for unfiltered modulator output signals only, the waveform distortions created by the filtering and limiting action results in degraded P_e versus $(S/N_b)_{\text{rcvr. input}}$ performance.

Figures 6.1.5, 6.1.6 and 6.1.8 indicate the extent of the degradation.

To compare the relative performance of the three systems, the degradations as a function of BT_b and relative to the $BT_b = \infty$ case, for a P_e of 10^{-4} have been determined from Figs. 6.1.5, 6.1.6 and 6.1.7 and are shown in Fig. 6.1.8. We note that when $BT_b = 0.5$, the degradation is in the order of 2 dB for all three systems. This might seem surprisingly low, considering that the prelimiter filter is not phase-equalized and that for this value of BT_b its double-sided 3 dB bandwidth is equal to the system double-sided Nyquist bandwidth. Note, however, that this filter, being a four-pole Chebyshev type, does not have a very sharp amplitude roll-off outside the passband and exhibits relatively mild inband phase distortion. Under this condition of mild filtering, we observe that for $BT_b = 0.5$, QPSK is least degraded, followed by Offset QPSK then MSK. For $BT_b = 1$, the degradation of all three systems is less than 0.2 dB, that is, negligible.

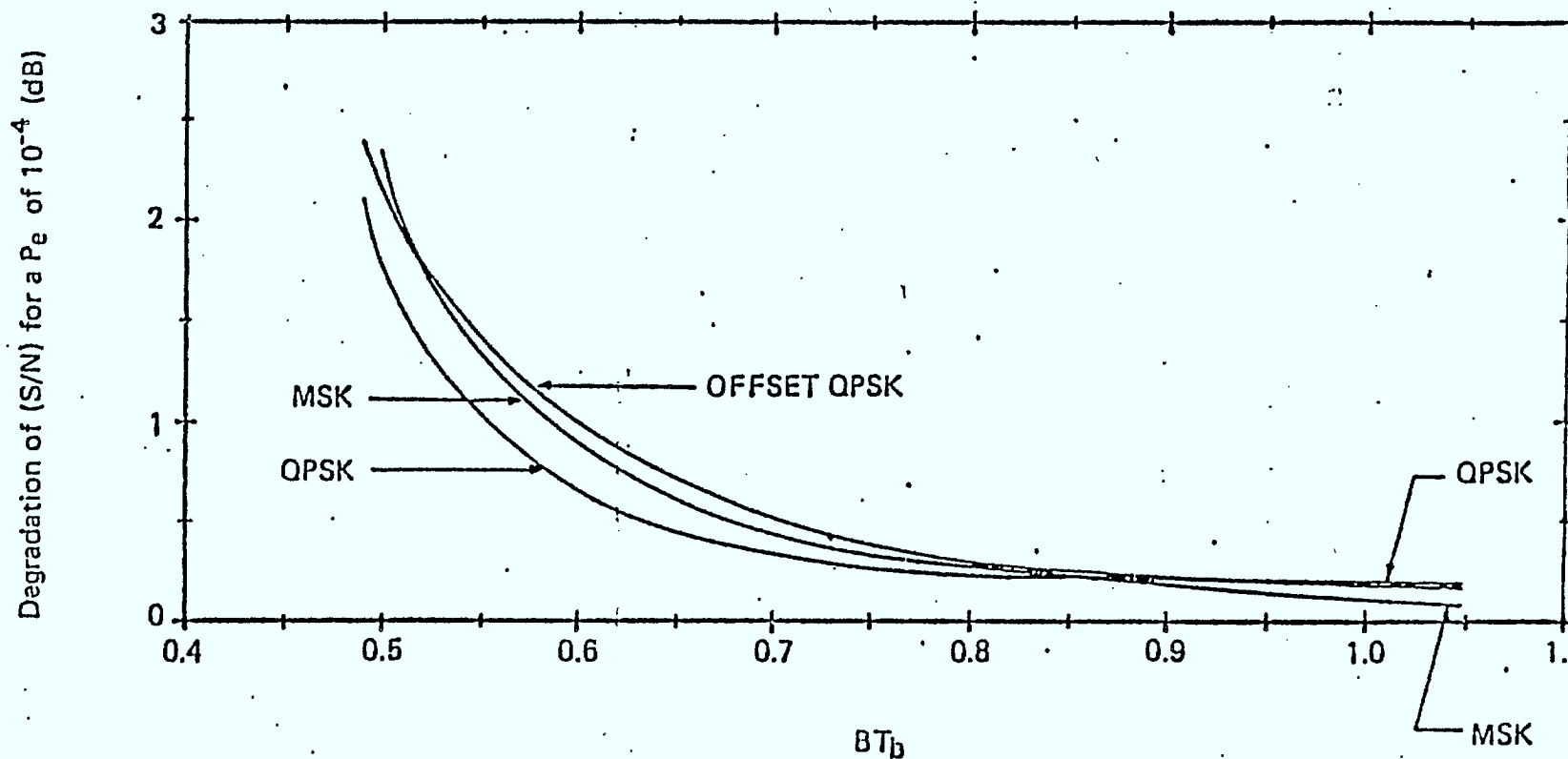


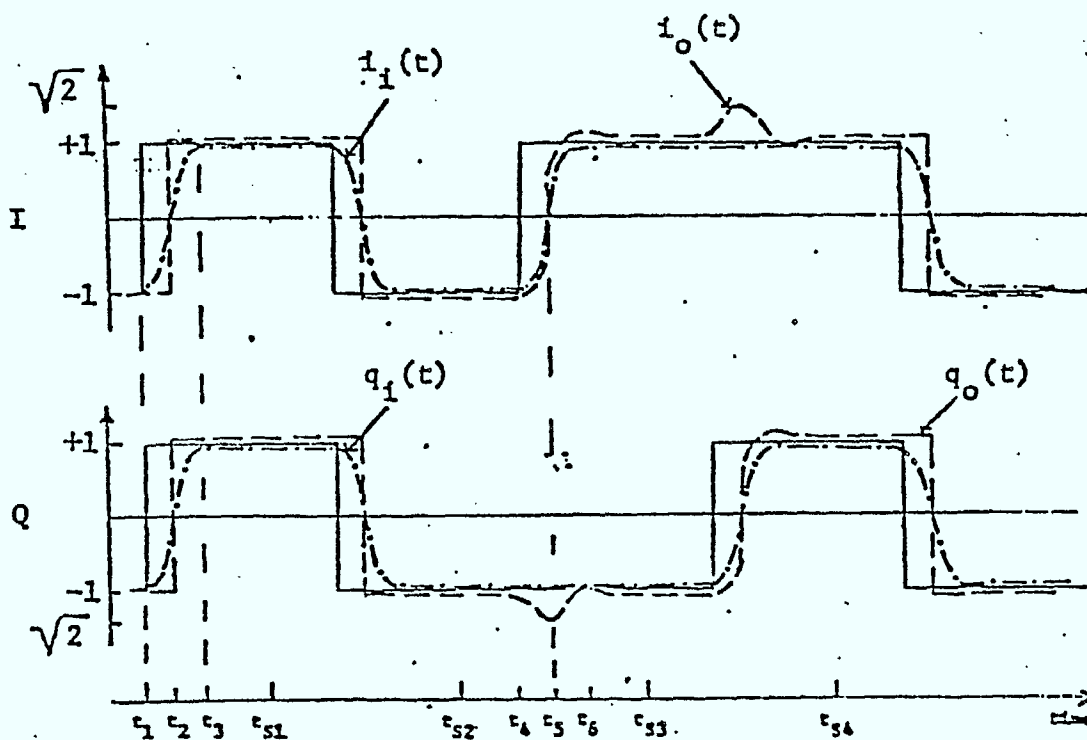
Figure 6.1.8 - DEGRADATION, DUE TO FILTERING THEN LIMITING, OF $(S/N_b)_{rcvr. input}$ VS NORMALIZED PRELIMITER FILTER BANDWIDTH.

6.1.4 Effects of Filtering and Limiting on Symbol Waveshapes

In this section we study the effects of filtering and limiting on symbol waveshapes. We consider first the case of QPSK, then Offset QPSK and finally MSK. This study of symbol waveshapes is important to the understanding of eye diagram and the effects of interphasor crosstalk on the performance of systems employing bandlimiting signals.

Typical QPSK I and Q symbol waveforms in their unfiltered, filtered, filtered then limited forms are shown in Fig. 6.1.9. Mild filtering is assumed and thus the form of the filtered waveshapes is as shown. The filtered then limited form follows from the fact that the QPSK signal at the limiter output is of a constant amplitude and of identical phase to the limiter input signal. Note that this limitation does not imply that the individual $i_0(t)$ and $q_0(t)$ signals must have constant amplitude, but only their vector sum. In the figure the amplitude of $i_0(t)$ and $q_0(t)$ are both set at value 1 during periods when no transitions are taking place. Thus, the combined limiter output signal amplitude, which is the vector sum of the amplitude of $i_0(t)$ and $q_0(t)$, is of constant value $\sqrt{2}$.

Let us consider what happens during a period such as t_1 to t_3 when both the filtered waveshapes $i_1(t)$ and $q_1(t)$ are changing polarity simultaneously. The limiter output waveshapes $i_0(t)$ and $q_0(t)$ can neither both decrease simultaneously or increase simultaneously since, were this to happen, their vector sum would not be constant at $\sqrt{2}$ but would decrease or increase, respectively. The result is therefore that both waveshapes maintain full amplitude except at the polarity



Unfiltered

Filtered

Filtered then limited

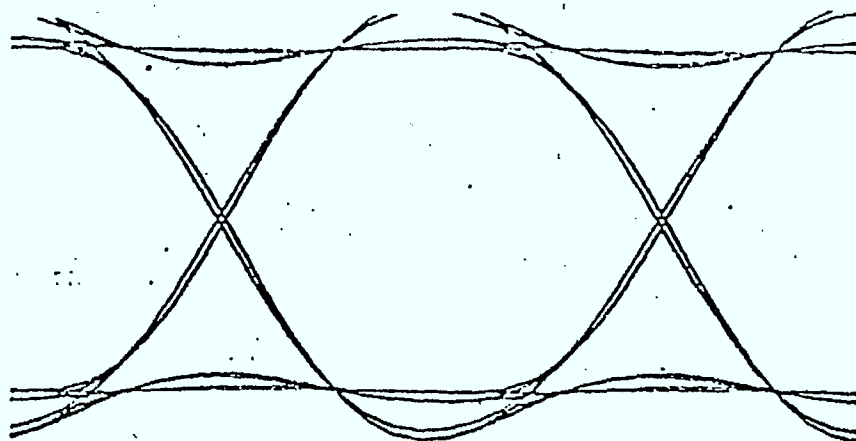
Figure 6.1.9 - EFFECTS OF FILTERING AND FILTERING THEN LIMITING ON QPSK SYMBOL WAVESHAPES.

transition instant of the input waveshapes, t_2 , where both output waveshapes experience instant polarity transition. Thus, the output waveshape $i_0(t)$ is influenced by the polarity changes taking place on the input waveshape $q_1(t)$, and similarly, $q_0(t)$ is influenced by the changes taking place on $i_1(t)$. That is, waveshape crosstalk occurs.

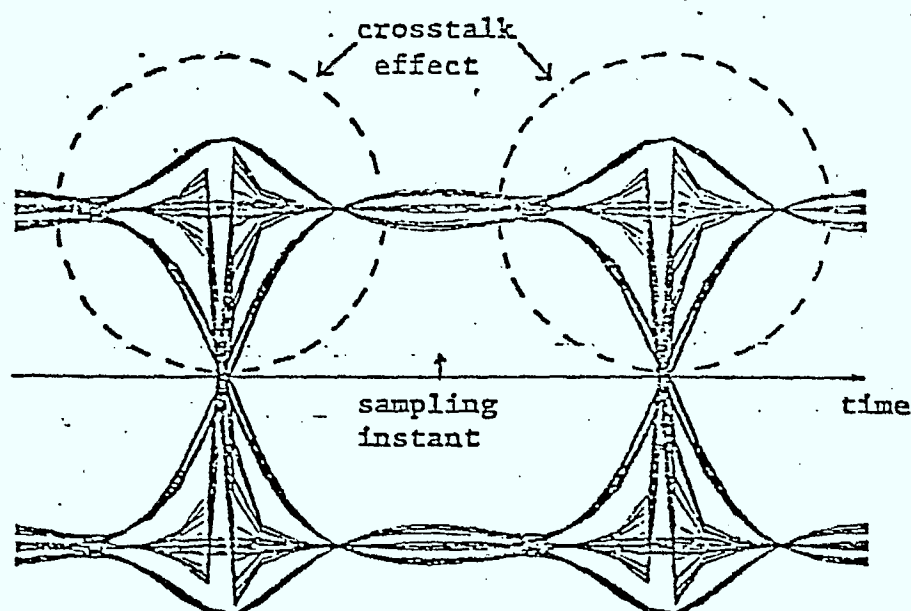
We now consider what happens during a period such as t_4 to t_6 when only one filtered waveshape changes polarity. During the particular period t_4 to t_6 , $i_1(t)$ changes polarity while $q_1(t)$ remains unchanged. As $i_1(t)$ decreases in amplitude, $i_0(t)$ decreases in amplitude and $q_0(t)$ increases in amplitude in order that the combined signal output amplitude remains constant and its phase follows that of the input signal. In particular, at time t_4 , when the amplitude of $i_0(t)$ is zero, the amplitude of $q_0(t)$ increases to $\sqrt{2}$. Thus, in periods such as this, in addition to periods such as t_1 to t_3 , waveshape crosstalk occurs.

The overall result of the fact that the limiter forces the combined signal at its output to be of constant amplitude and of phase equal to that of its input signal is the creation of filtered then limited waveforms as shown in Fig. 6.1.9. Note, however, that the effect of limiting on the filtered waveform is minimum at the all-important sampling times t_{sn} , where $n = 1, 2, \dots$

Figure 6.1.10 shows computer-generated eye diagram for QPSK. Figure 6.1.10a shows the eye diagram associated with the signal when filtered such that $BT_b = 1$. Figure 6.1.10b shows the eye diagram associated with the signal when filtered



(a) Filtered, $BT_b = 1.0$.



(b) Filtered, $BT_b = 1.0$; then limited.

Figure 6.1.10-SIMULATED EYE DIAGRAMS FOR QPSK

such that $BT_b = 1$, then limited. The strong crosstalk effects at the waveform transition points and the minimal effects at the sampling points as previously discussed are evident.

Typical Offset QPSK I and Q unfiltered, filtered and filtered then limited symbol waveforms are shown in Fig. 6.1.11. We note that the timing of the Q symbol stream is "offset" by one half of a symbol duration relative to the I stream. As was done for QPSK, we assume mild filtering, hence the filtered waveshapes shown. As a result of the symbol streams being offset with respect to each other, only one stream can change polarity over a given transition period.

Figures 6.1.12a and b show computer-generated eye diagrams for Offset QPSK. They are the equivalent diagrams to Figs 6.1.10a and b for QPSK. Waveform crosstalk in the predicted form of increased amplitude of the affected symbols at the sampling points is evident.

We now study the effect of filtering and limiting on MSK symbol waveforms. Figure 6.1.13 shows such waveforms when unfiltered, filtered and filtered then limited. Note that, as for Offset QPSK, the Q symbol stream is offset by one-half of a symbol duration relative to the I stream. If the system bit rate is f_b , then each unfiltered symbol is of the form $\cos[2\pi(-\frac{f_b}{4})t]$. We assume equivalent baseband filtering such that the passband exceeds $\frac{f_b}{4}$ but signals of frequency $\frac{f_b}{4}$ and above are attenuated. When adjacent symbols alternate in polarity, we get a full sinewave whose predominant frequency component is at $\frac{f_b}{4}$ and thus suffers limited distortion as a result of filtering. When adjacent signals have the same

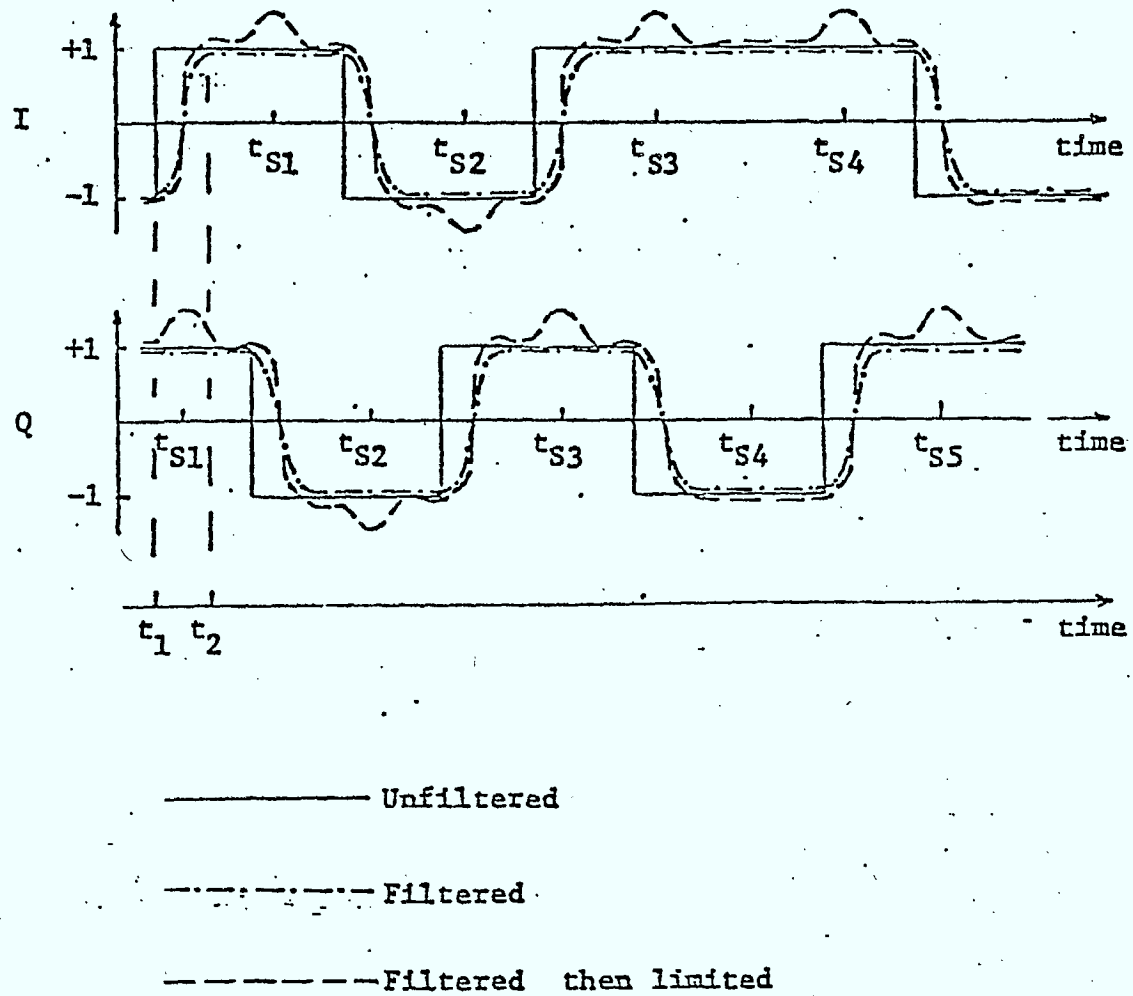
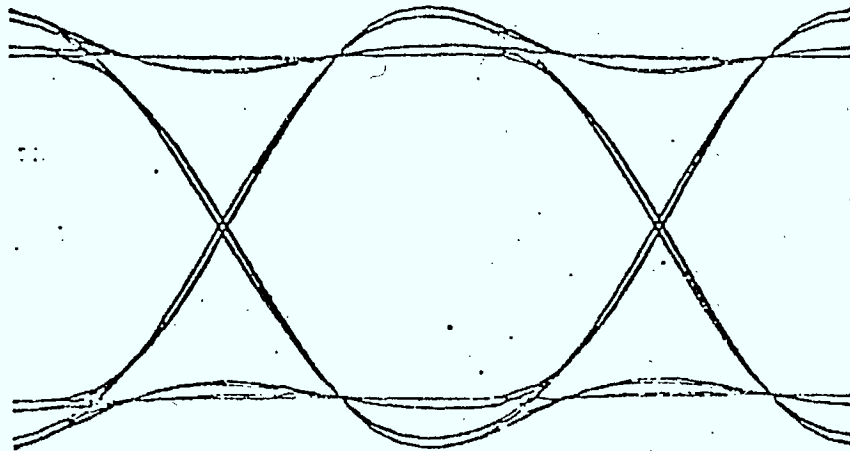
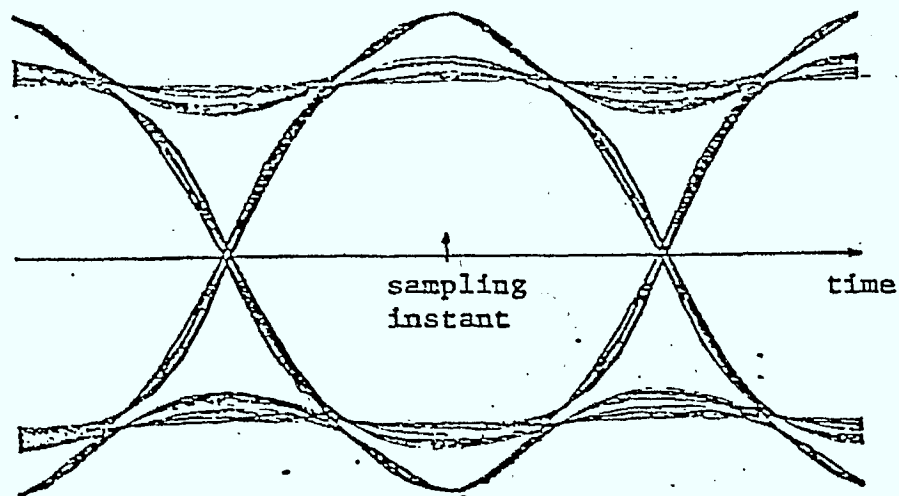


Figure 6.1.11-EFFECTS OF FILTERING AND FILTERED THEN LIMITING
ON OFFSET QPSK SYMBOL WAVESHAPES

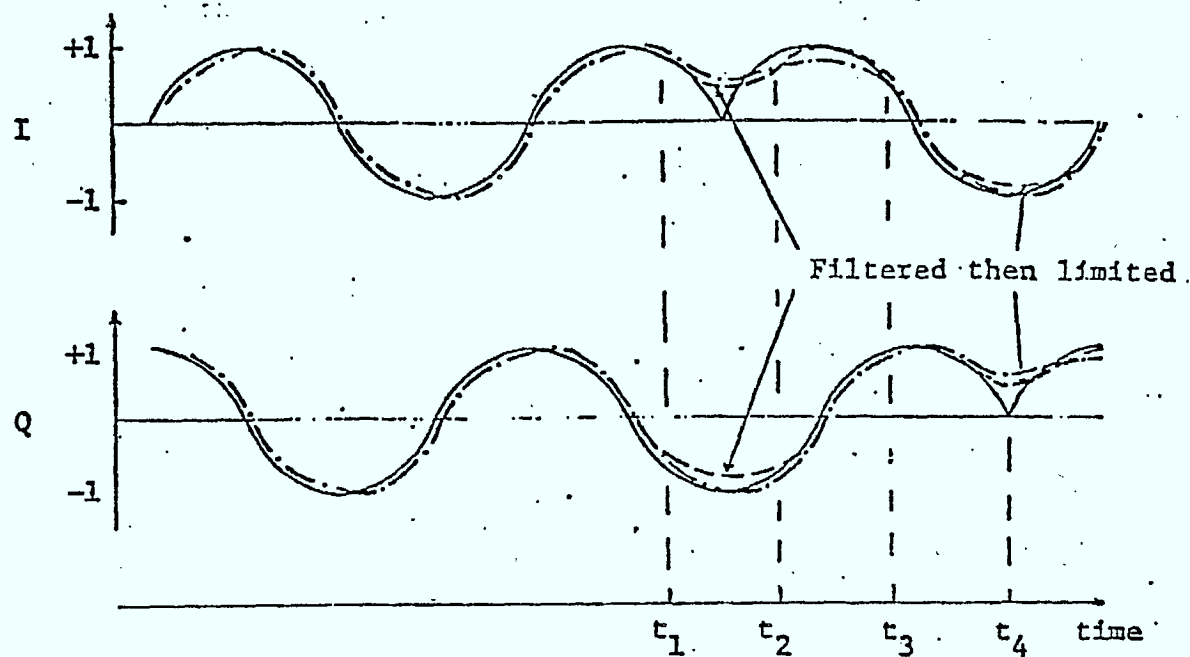


(a) Filtered, $BT_b = 1.0$.



(b) Filtered, $BT_b = 1.0$, then limited.

Figure 6.1.12-SIMULATED EYE DIAGRAMS FOR OFFSET QPSK



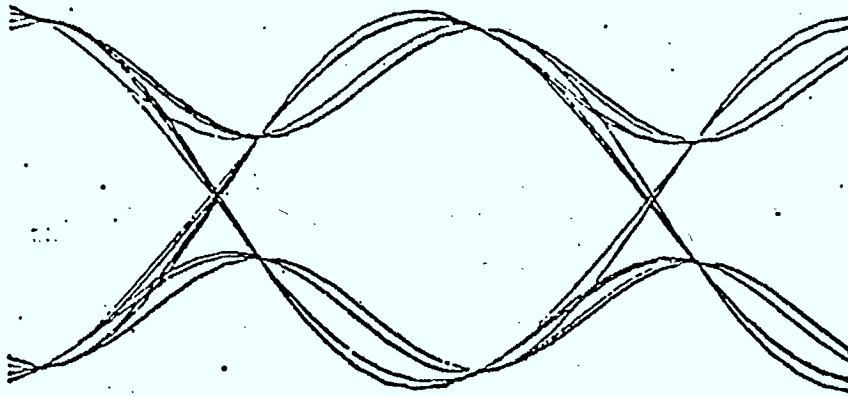
_____ Unfiltered
 - Filtered
 - - - - - Filtered then limited

Note: Filtered then limited waveshapes similar to filtered only waveshapes except where indicated otherwise.

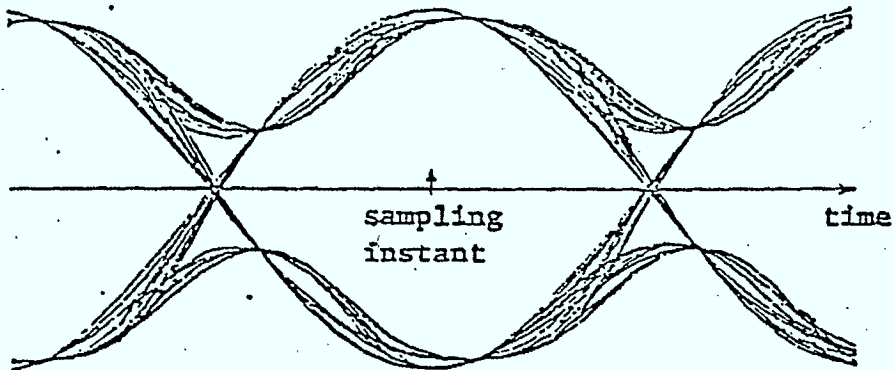
Figure 6.1.13- EFFECTS OF FILTERING AND FILTERING THEN LIMITING
ON MSK SYMBOL WAVESHAPES

polarity, they form in effect a rectified sinewave cycle consisting of a dc component and frequencies of $\frac{f_b}{2}$ and multiples thereof. Filtering this rectified sinewave cycle results in significant distortion. The overall effect of this filtering on typical waveshapes is as shown in Fig. 6.1.13. As for the cases of QPSK and Offset QPSK, limiting modifies the filtered waveforms so that the resultant output signal has a constant amplitude. In particular, during periods such as t_1 to t_2 , both waveshapes at the limiter output are reduced in amplitude relative to the amplitude at the limiter input. During periods such as t_2 to t_3 , the "rectified" waveshape, in the case I waveshape, increases in amplitude in order to compensate for the "unrectified" waveshape going through zero amplitude.

Figures 6.1.14a and b show respectively computer-generated eye diagrams associated with an MSK signal when filtered such that $BT_b = 1$, and filtered such that $BT_b = 1$, then limited. For this amount of filtering we note that the crosstalk effects due to limiting are minimal.



(a) Filtered, $BT_b = 1.0$.



(b) Filtered, $BT_b = 1.0$, then limited.

Figure 6.1.14-SIMULATED EYE DIAGRAMS FOR MSK

6.1.5 Performance of OKQPSK and MSK in conventional and Regenerative Systems

A simulation study of the performance of both regenerative and conventional satellite systems using OKQPSK and MSK modulation techniques is reported in this section. A 120 Mb/s system with cascaded nonlinearities is used. The system models shown in Figs. 3.1.1 and 3.1.2 are assumed. The filter, TWTA, and HPA characteristics are identical to those used in Chapter 3. The same two cases for the group delay characteristics are considered:

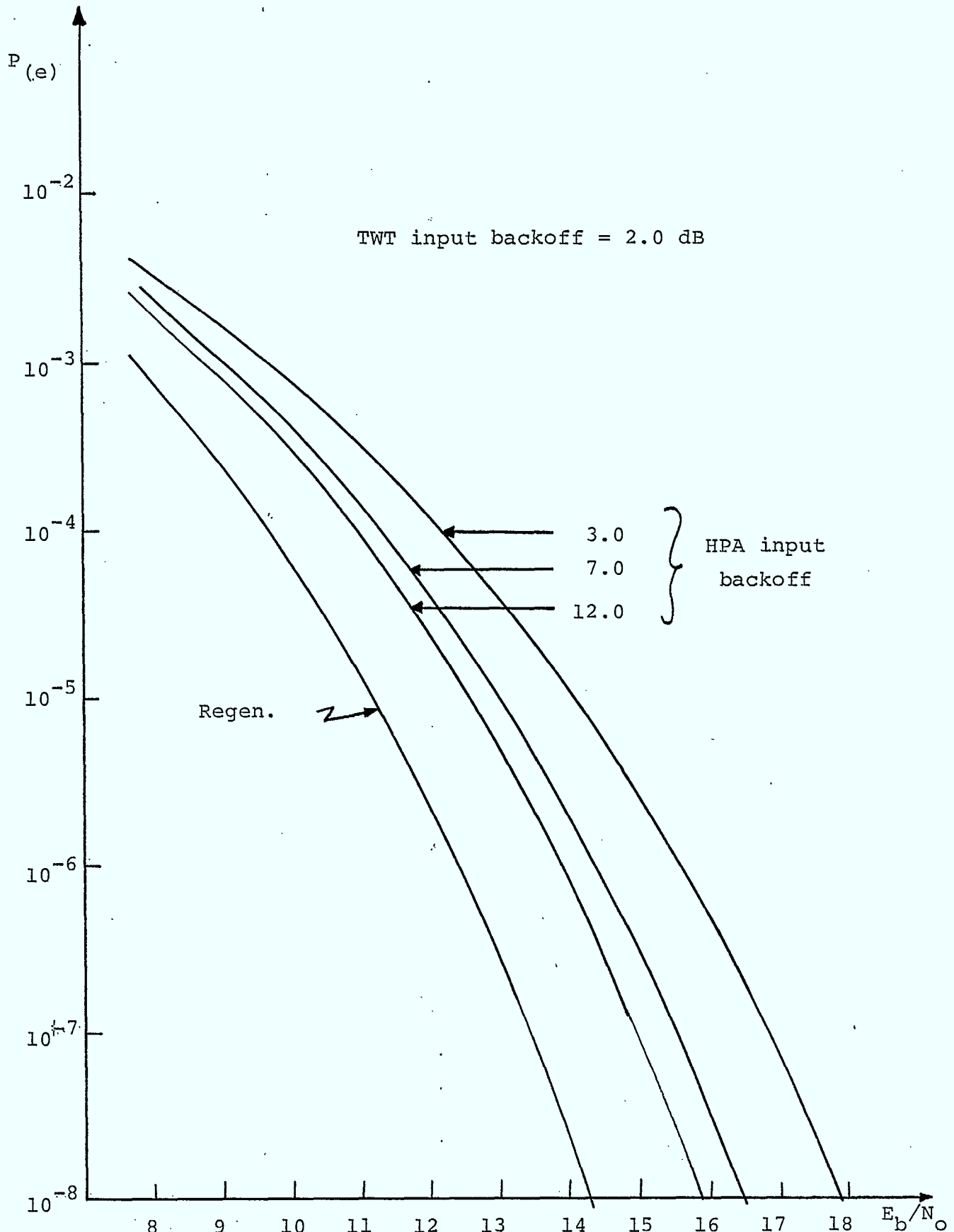
Case 1) $\tau = 0.011f^2$ for input MUX filter F_2
 and $\tau = 0.0075f^2$ for output MUX filter F_3

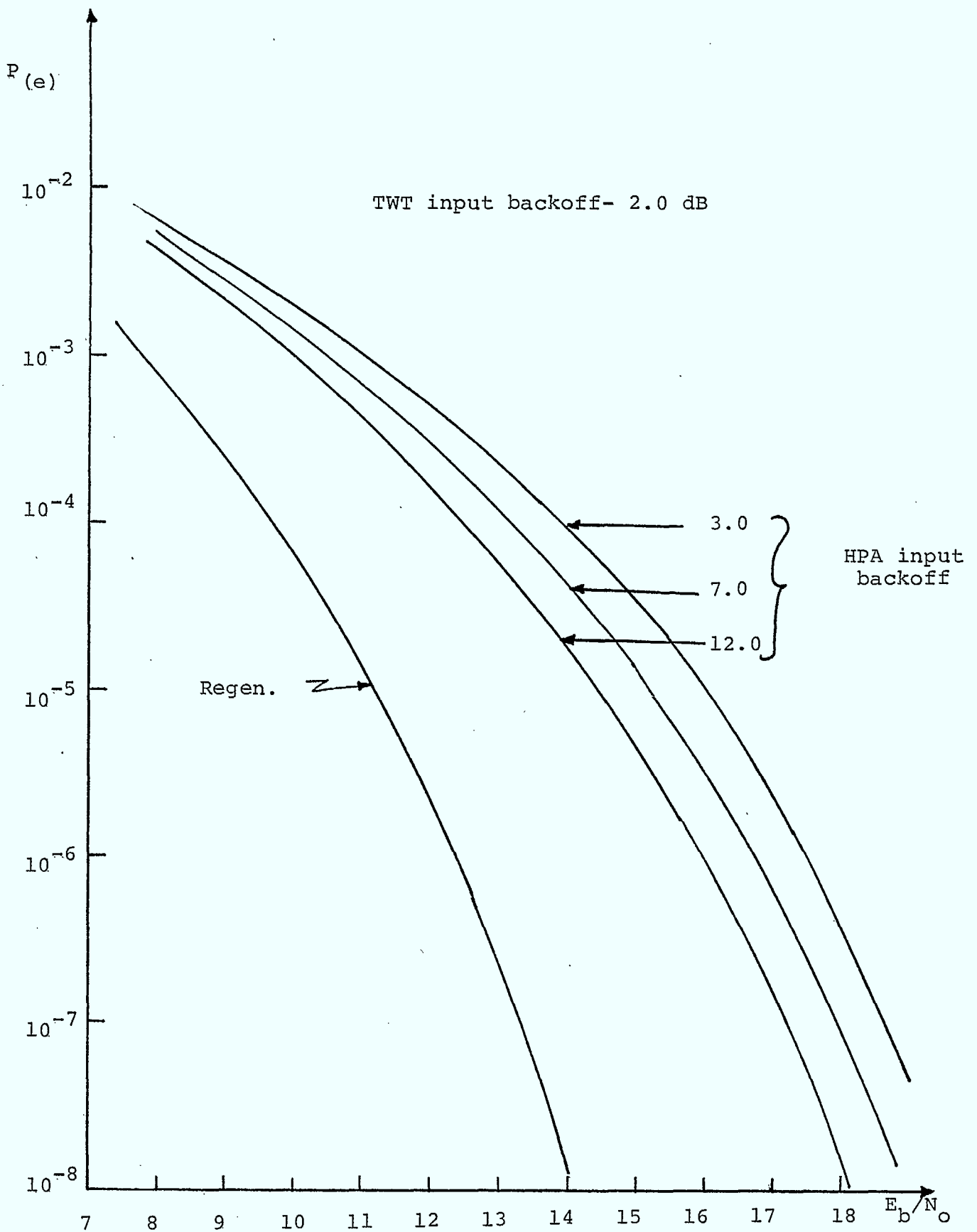
Case 2) $\tau = 0.015f^2$ for filter F_2
 and $\tau = 0.01f^2$ for filter F_3

where τ is the group delay in nanoseconds
 and f is the frequency in Megahertz.

As in the QPSK case, the TWTA is assumed to operate at 2.0 dB input backoff, and the HPA input backoff varies from 3.0 dB to 12.0 dB in the conventional mode.

In Fig. 6.1.15, the simulation results for regenerative and nonregenerative satellite systems are shown for Case 1 group delay. It is seen that for a probability of error of 10^{-4} , the non-regenerative system does not meet Intelsat E_b/N_o requirement of at most 11.0 dB unless the HPA input backoff is greater than 12 dB. The gain in E_b/N_o for regenerative systems over conventional (at 3 dB input backoff) is 2.4 dB. At a probability of error of 10^{-6} , the gain is 3.3 dB. Fig. 6.1.16 shows the same results but for the worst-case group

Fig. 6.1.15 QPSK $P(e)$ performance-case 1

Fig. 6.1.16 OQPSK $P(e)$ performance-worst case group delay

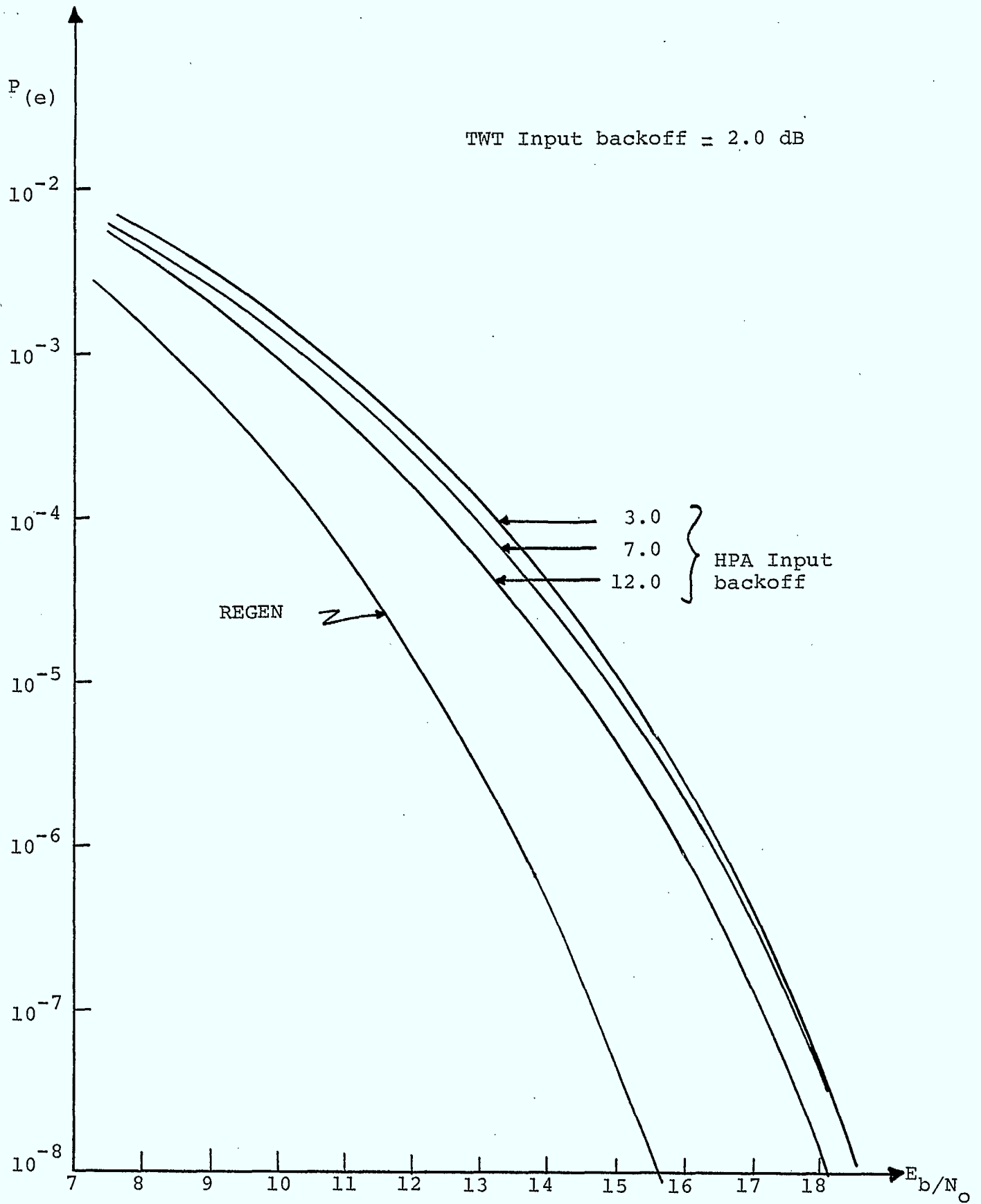
delay. In this case, the gains in E_b/N_o are 4.3 dB and 5.2 dB for probabilities of error of 10^{-4} and 10^{-6} respectively. Regeneration will thus meet the E_b/N_o requirements of 11.0 dB at $P_e = 10^{-4}$ and 14.0 dB at 10^{-6} . As in the case of QPSK, it is evident that the gain in regeneration increases as the group delay becomes worse.

Figures 6.1.17 and 6.1.18 show the results for MSK. For Case 1, the gain in E_b/N_o due to regeneration is 2.8 dB and for the worst-case group delay the gain is 5 dB at a probability of error of 10^{-4} . At a probability of error of 10^{-6} , the gains are 3.0 dB and 5.7 dB for cases 1 and 2 respectively.

In Fig. 6.1.19, the P_e vs E_b/N_o curves are shown for the regenerative systems for QPSK, OKQPSK and MSK. From this figure we conclude that QPSK outperforms OKQPSK and MSK by 0.4 dB and 1.4 dB respectively, at a probability of error of 10^{-4} .

Figure 6.1.20 depicts the results of the simulation of the uplink only for the three modulation methods under study. For this simulation, the HPA is taken to operate at an input backoff of 3.0 dB. From Figs 6.1.19 and 6.1.20 we can draw the iso-BER curves for a BER = 10^{-4} . This is shown in Fig. 6.1.21.

Using the simulation models given in Fig. 3.1.11 the effect of filter positioning in the regenerative mode is evaluated for MSK. In one case, the shaping filter precedes the TWTA at the satellite while in the other, the filter is placed after the TWTA. Figure 6.1.22 shows the results for the two cases for MSK. The results for QPSK are included for

Fig. 6.1.17 MSK $P(e)$ performance - Case 1

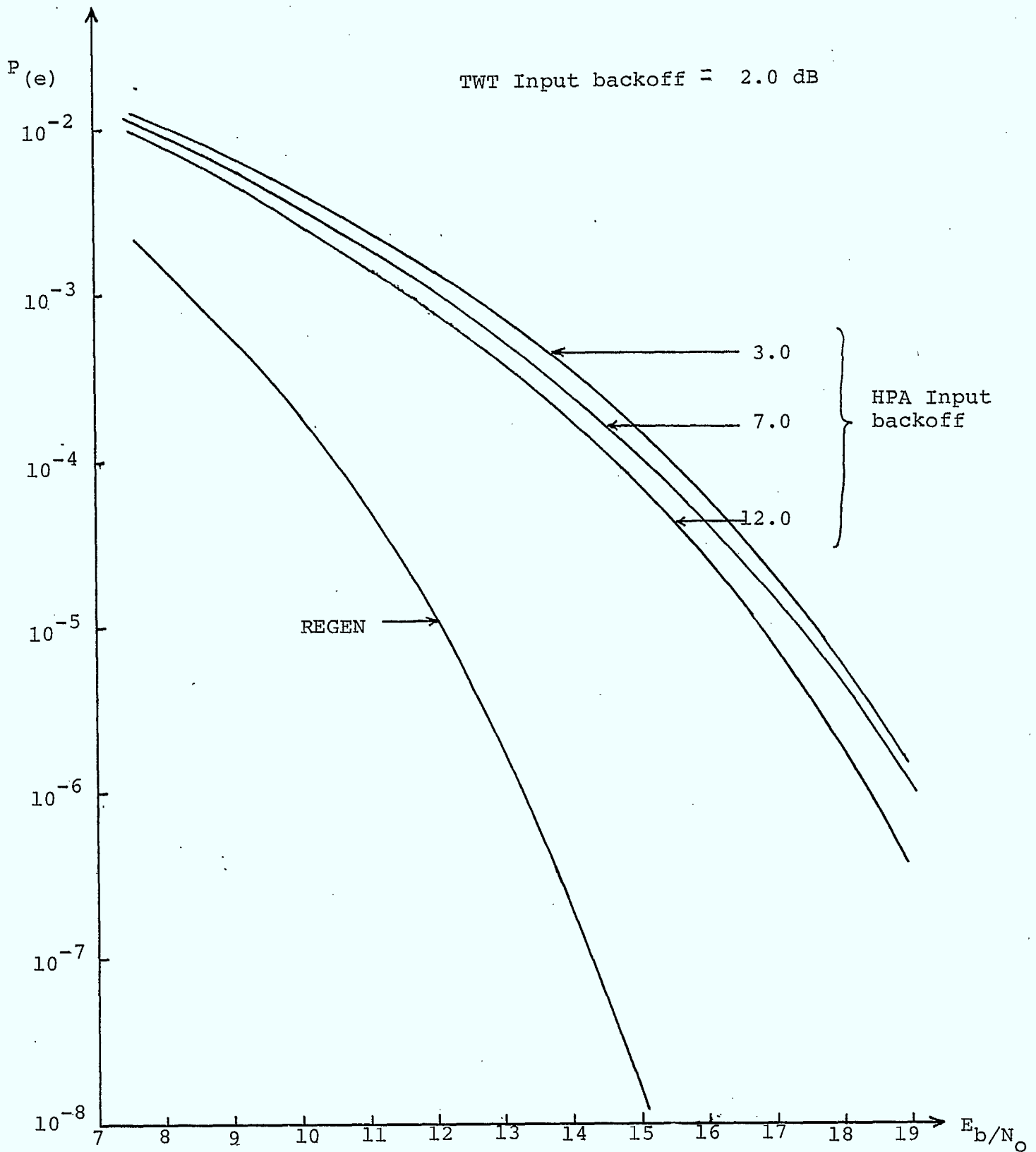


Fig. 6.1.18 MSK $P(e)$ performance - Worst case group delay

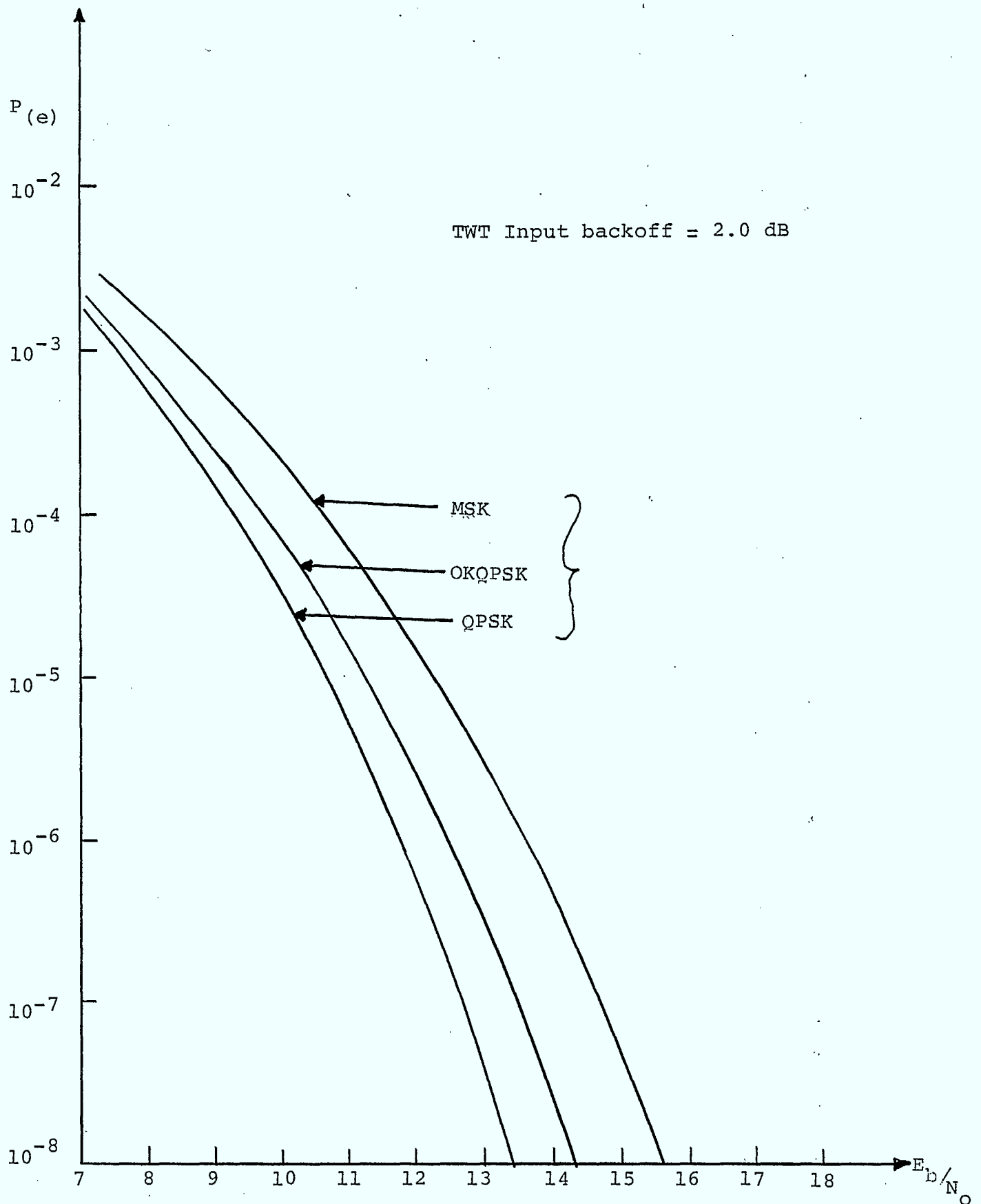


Fig. 6.1.19 Comparison of $P(e)$ performance for regenerative case

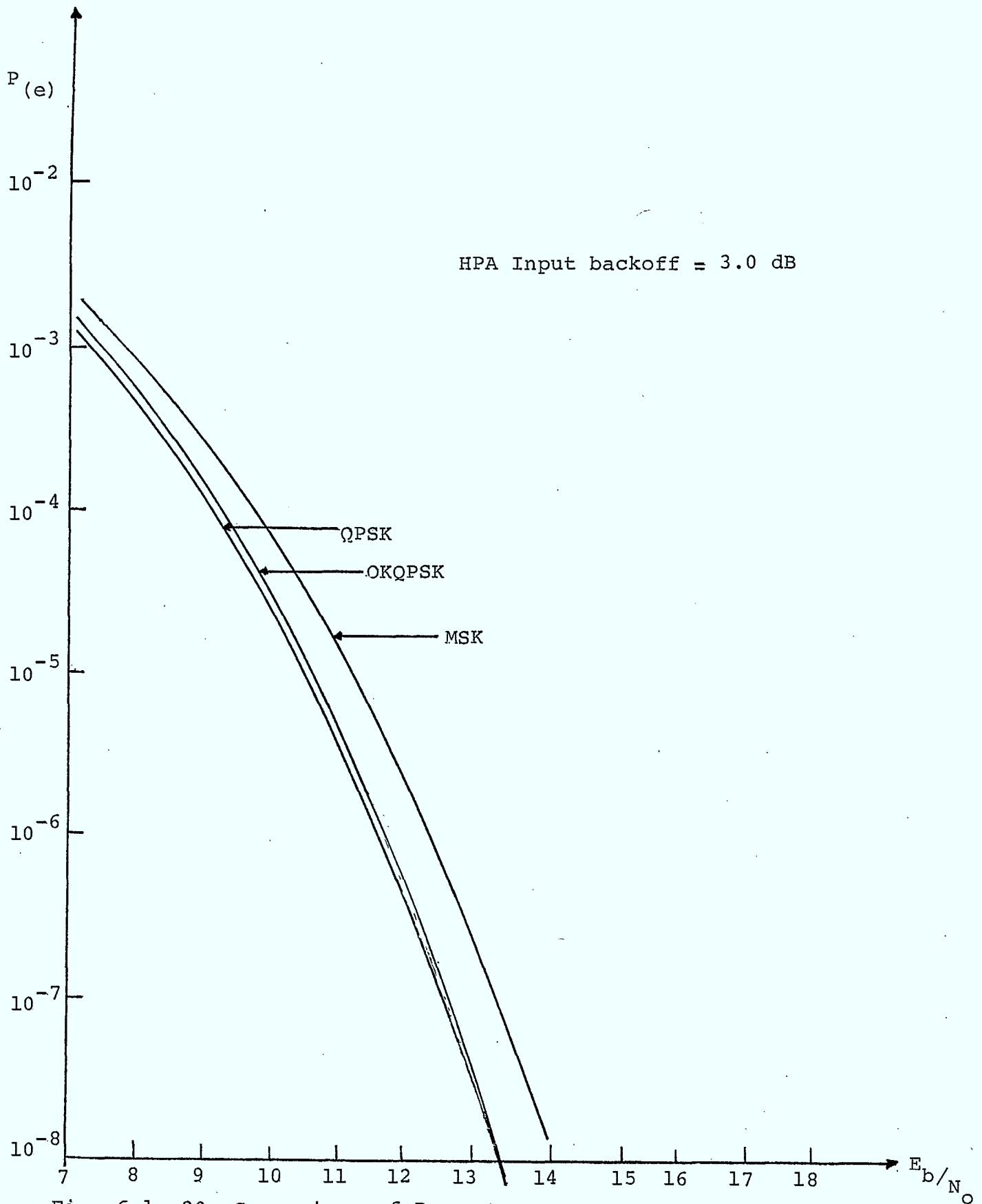


Fig. 6.1. 20 Comparison of $P(e)$ with one non-linearity (HPA)

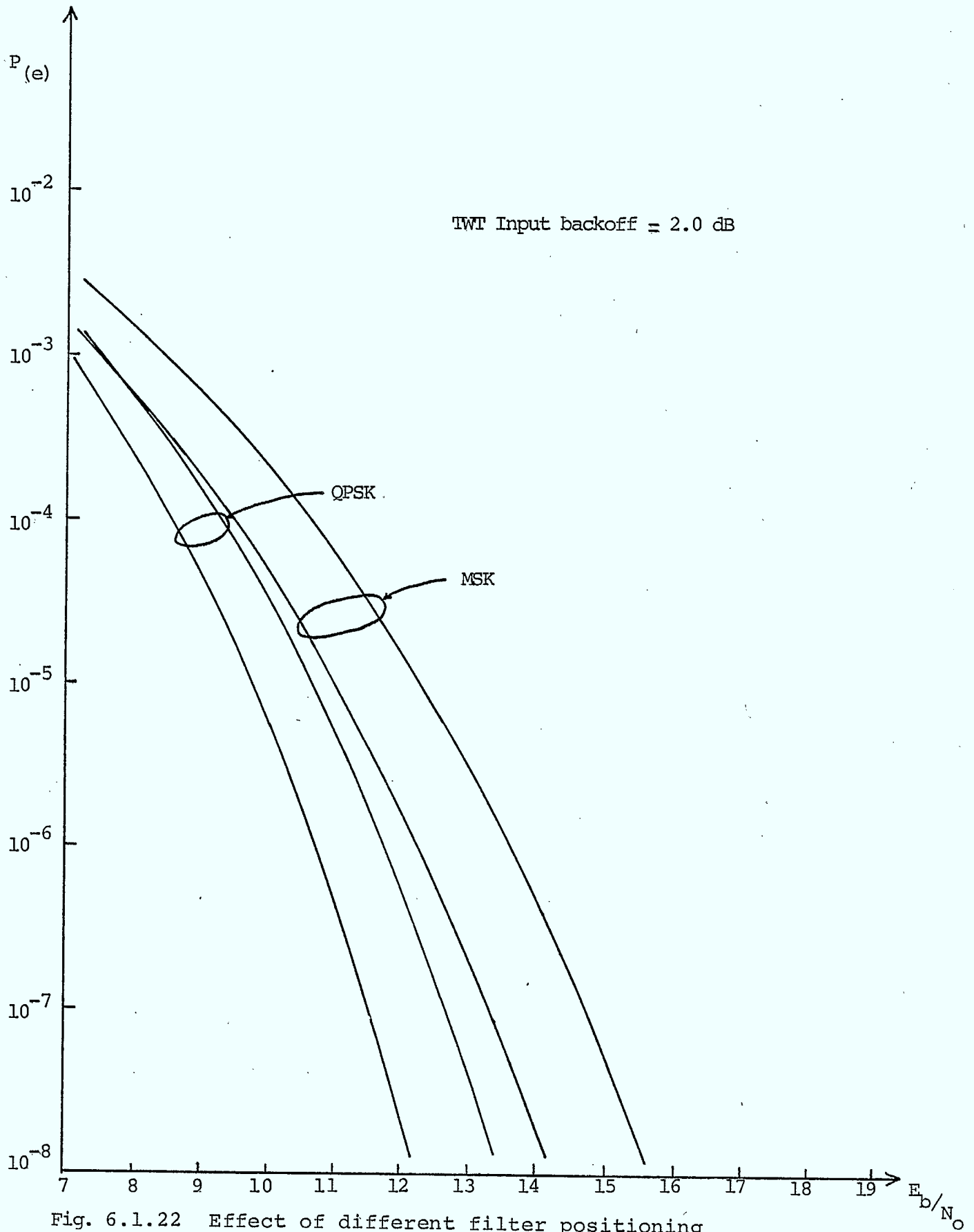


Fig. 6.1.22 Effect of different filter positioning

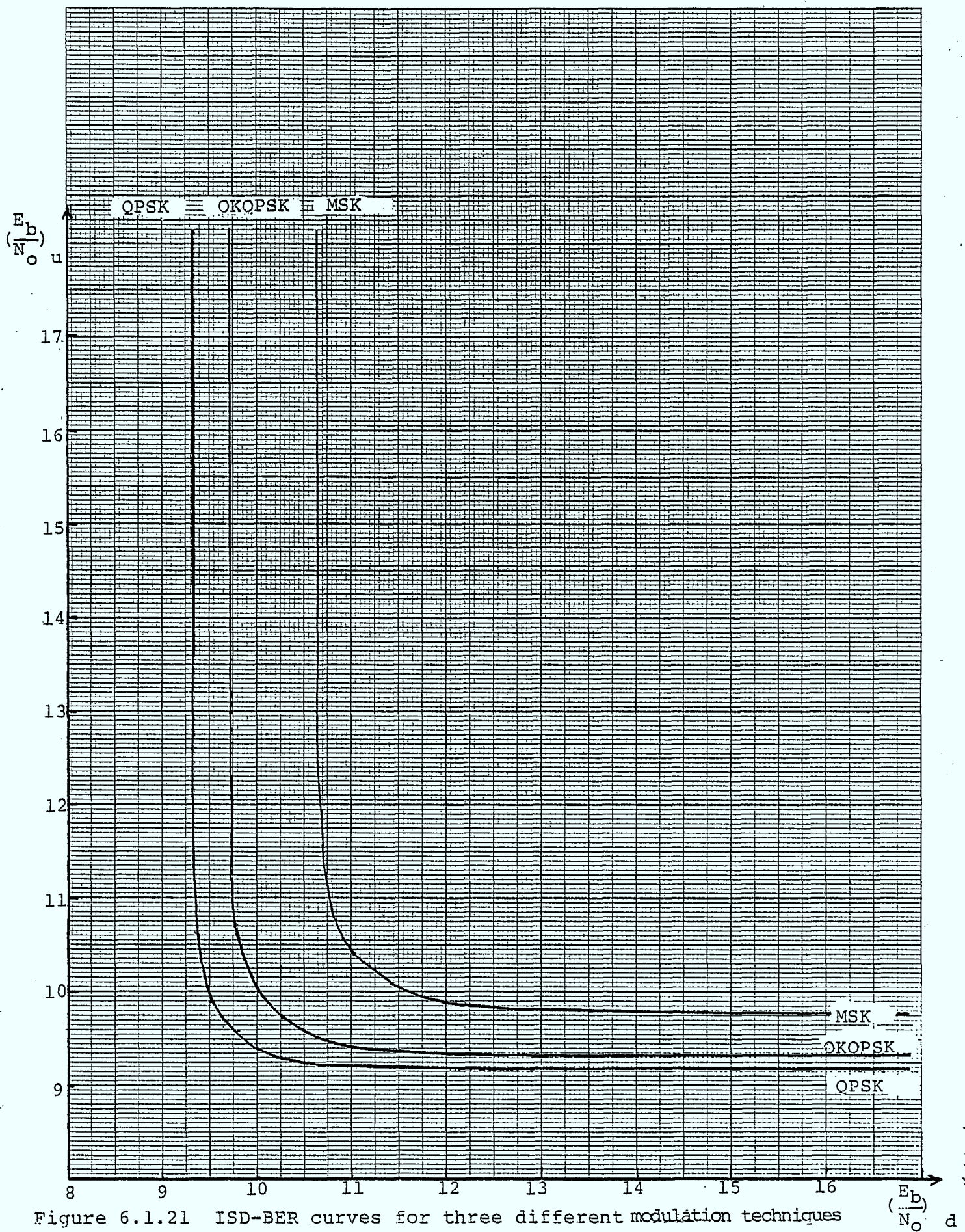


Figure 6.1.21 ISD-BER curves for three different modulation techniques

comparison. It is shown that if the filter is placed after the TWTA, the system gains about 1.2 dB in E_b/N_o at a $P_e = 10^{-4}$ and 1.4 dB at P_e at $P_e = 10^{-6}$. For OKQPSK the gains are in between those of QPSK and MSK.

6.1.6 Conclusions

Comparing QPSK, OKQPSK and MSK spectra after filtering, then hardlimiting, it was seen that QPSK suffers the greatest sidelobe generation; the first sidelobe for QPSK is about 10 dB higher than that of OKQPSK. The latter is slightly better than MSK. For the probability of error performance, the order of merit of the three systems depends on the BT_b products. For small BT_b 's (< 0.8), QPSK suffers the highest degradation relative to the $BT_b = \infty$ case, for a P_e of 10^{-4} , followed by OKQPSK and MSK. But for larger BT_b 's (≈ 1), MSK is degraded least, followed by OKQPSK and QPSK. However, for $BT_b = 1$, the degradation of all three systems is less than 0.2 dB.

Regenerative satellite systems have a better performance than conventional satellites for all three modulation techniques. The results indicate that QPSK performs better in both conventional regenerative cases than OKQPSK and MSK. In all cases, the performance of QPSK and OKQPSK are close, but that of MSK is a little worse. Further, it is shown that regeneration yields from 2 to 5.7 dB gain in E_b/N_o , depending on the modulation method. The gain is dependent upon the group delay of the filters used, being highest in the channel with the worst group delay. Placing the filter after the TWTA yields an additional advantage of 0.7 dB for QPSK and 1.2 dB for MSK.

REFERENCES

- [1] J. Bayless and R. Pedersen, "Efficient Pulse Shaping Using MSK or PSK modulation", IEEE Trans. Commun., Vol. COM-27, No. 6, June 1979, pp. 927-930.
- [2] D. MOrais and K. Feher, "Bandwidth Efficiency and Probability of Error Performance of MSK and Offset QPSK Systems", IEEE Trans. Commun., Vol. COM 27, No. 12, Dec. 1979, pp. 1794-1801.
- [3] S. Gronemeyer and A. McBride, "MSK and Offset QPSK Modulation", IEEE Trans. on Communications, Vol. COM-24, No. 8, pp. 809-820.
- [4] R. Lucky, J. Salz and E. Weldon, "Principles of Data Communication", McGraw Hill Book Company, New York, 1968.

CHAPTER 7

NEW IJF-OQPSK MODULATION TECHNIQUE AND ITS APPLICATIONS TO ON-BOARD REGENERATIVE SATELLITE SYSTEMS

7.1.1 Introduction

The TDMA transmission technique has been introduced to achieve higher efficiency and flexibility in satellite communication systems [1]. Due to the single-carrier-per-transponder mode of operation, TDMA technique reduces the nonlinear effects of the transponder TWTA by avoiding intermodulation products encountered in FDMA systems. However, it still undergoes degradation caused by the combined effects of the bandlimited environment of the transponder channel, and the cascaded nonlinearities of the earth station HPA and transponder TWTA. It is this degradation that limits an efficient use of earth station and satellite power resources.

Onboard regeneration techniques [3, 4] are called to further improve the performance of satellite links using TDMA schemes. In regenerative satellite systems, the uplink and downlink are isolated by the onboard demodulation-remodulation processing. This prevents the direct transfer of noise accumulated on the uplink to the downlink, and only bit errors made in the onboard detection processing of the uplink are passed to the downlink. The isolation of the uplink and downlink also separates the effects of cascaded nonlinearities, hence avoiding the transfer of signal distortions occurring on the uplink to the downlink. Furthermore, onboard remodulation allows

the derivation of a unique carrier for all downlink signals, hence may eliminate station-to-station variations and doppler differences encountered on the uplink, and results in burst-to-burst carrier coherence. This contributes to the improvement of the demodulator performance and to the reduction of the link degradation.

In this part (7.1.0), the potential applications of a new class of Intersymbol Interference and Jitter Free Offset Keyed Quadrature Phase Shift Keying (IJF-OQPSK) modems [5,6] to regenerative satellite systems are presented.

In Section 7.1.2, the spectral properties and probability of error, (P_e), performance of Intersymbol Interference and Jitter Free (IJF) baseband signals are summarized.

In Section 7.1.3., the properties of the IJF-QPSK and IJF-OQPSK signals in linear channels are studied in great detail. Their envelope fluctuation, phase transition and power spectra are presented. It is shown that the IJF-QPSK and IJF-OQPSK signals have significant spectral advantages over QPSK, OQPSK and MSK and a negligible P_e degradation relative to the optimum QPSK performance. Experimental results are in agreement with theoretical predictions.

In Section 7.1.4, the spectral properties of the IJF-QPSK and IJF-OQPSK signals in a hardlimited channel are presented. The inphase to quadrature crosstalk

effects due to hardlimiting are analytically and experimentally investigated. Finite-state Markov chain models are used to calculate power spectra of hardlimited IJF-QPSK and IJF-OQPSK signals. The models provide insight into the spectrum spreading action of the ideal hardlimiter on the IJF-QPSK and OQPSK signals. The comparison of analytical, simulated and experimental results shows an excellent agreement. The experimental and simulated results also indicate that the IJF-OQPSK signal exhibits much less spectrum spreading than QPSK, OQPSK and MSK in a hardlimited channel. The simulated results show that the hardlimited channel introduces a P_e performance degradation of 0.7 dB (in E_b/N_o) relative to the linear channel with IJF-OQPSK modems.

Section 7.1.5 is reserved for the study of the spectral spreading and P_e performance of the IJF-OQPSK signal in cascading nonlinear conventional and regenerative satellite links respectively, using a computer simulation. As an illustrative example, the Intelsat-TDMA nonlinear channel characteristics [8] are used in the simulation of cascaded nonlinear channels. This example highlights the advantages of post-Intelsat V regenerative satellites. Computer simulation results indicate that the IJF-OQPSK modem has better spectral

spreading and P_e performance in cascaded nonlinear channels, than the QPSK. These results stimulate the applications of the IJF-QQPSK modulation technique in regenerative satellite links. Computer simulation is used to study the P_e performance of IJF-QQPSK modems in the regenerative satellite link. The results show that a gain of at least 2 dB is obtained with the regenerative satellite link, relative to the conventional nonlinear channel. The performance of a regenerative satellite link using IJF-QQPSK modems is also compared to one using conventional QPSK modems. The simulation results indicate that a regenerative satellite link using IJF-QQPSK modems has better performance than one using QPSK modems, specially when the HPA and TWTA operate in saturation.

7.1.2 Characteristics of IJF Baseband Signals

Consider an IJF signal encoder using the non linear switching filter concept [2] shown in Fig. 7.1.1. The input of the encoder is a non-return-to-zero (NRZ) signal.

$$x(t) = \sum_{n=-\infty}^{+\infty} x_n g(t-nT_s) \quad (7.1.1)$$

where

$$g(t-nT_s) = \begin{cases} 1, & |t-nT_s| \leq T_s/2 \\ 0, & |t-nT_s| > T_s/2 \end{cases}$$

and

$$x_n = \pm 1 \quad \text{with probability } \frac{1}{2}$$

The encoded signal is represented by:

$$y(t) = \sum_{n=-\infty}^{+\infty} y_n(t) \quad (7.1.2a)$$

where

$$y_n(t) = \begin{cases} s_1(t-nT_s) = s_e(t-nT_s), & \text{if } x_n = x_{n-1} = +1 \\ s_2(t-nT_s) = -s_e(t-nT_s), & \text{if } x_n = x_{n-1} = -1 \\ s_3(t-nT_s) = s_o(t-nT_s), & \text{if } x_n = +1, x_{n-1} = -1 \\ s_4(t-nT_s) = -s_o(t-nT_s), & \text{if } x_n = -1, x_{n-1} = +1 \end{cases} \quad (7.1.2b)$$

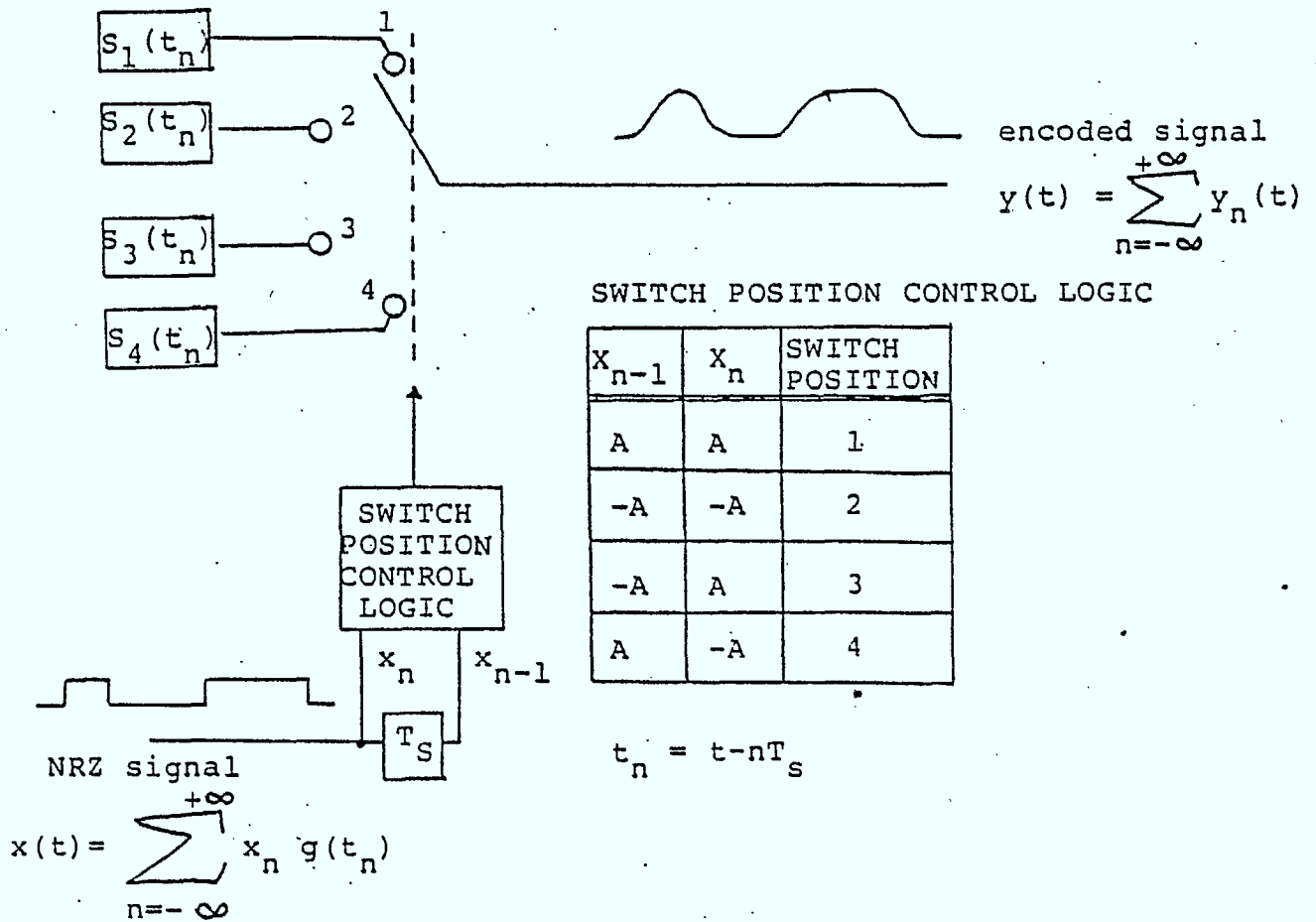


Fig. 7.1.1 Block diagram of the IJF signal encoder using the NLSF concept

The power spectral density (PSD) function of the encoded signal $y(t)$ is [5,6].

$$\begin{aligned} Y(f) &= \frac{1}{T_s} [S_e(f) \cos \pi f T_s - j S_o(f) \sin \pi f T_s]^2 \\ &= \frac{1}{T_s} |S(f)|^2 \end{aligned} \quad (7.1.3)$$

where

$s_e(t-nT_s)$ and $s_o(t-nT_s)$ are even and odd single-interval pulses defined as:

$$s_e(t-nT_s) = s_e(-t+nT_s), \text{ for } |t-nT_s| < T_s/2 \quad (7.1.4a)$$

$$s_o(t-nT_s) = -s_o(-t+nT_s), \text{ for } |t-nT_s| < T_s/2 \quad (7.1.4b)$$

$$s_e(t-nT_s) = s_o(t-nT_s) = 0, \text{ for } |t-nT_s| \geq T_s/2 \quad (7.1.4c)$$

$$s_e(T_s/2) = s_o(T_s/2) \neq 0 \quad (7.1.4d)$$

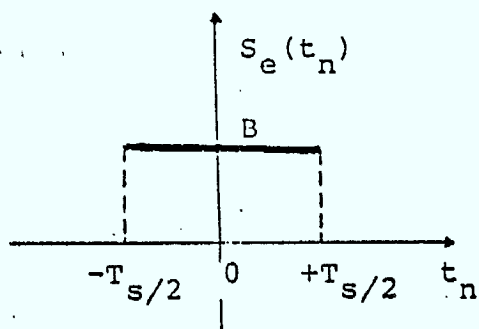
$s(t)$ is an even double-interval pulse defined as

$$s(t) = \begin{cases} \frac{1}{2} [s_e(|t| - \frac{T_s}{2}) - s_o(|t| - \frac{T_s}{2})], & 0 \leq |t| \leq T_s \\ 0, & |t| > T_s \end{cases} \quad (7.1.4e)$$

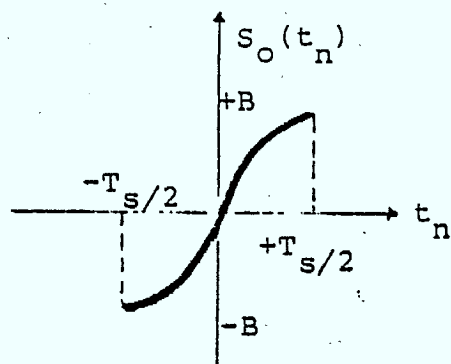
and $S_e(f)$, $S_o(f)$, $S(f)$ are Fourier transforms of $s_e(t)$, $s_o(t)$, $s(t)$ respectively.

Figure 7.1.2 illustrates an example of the IJF signal encoding with

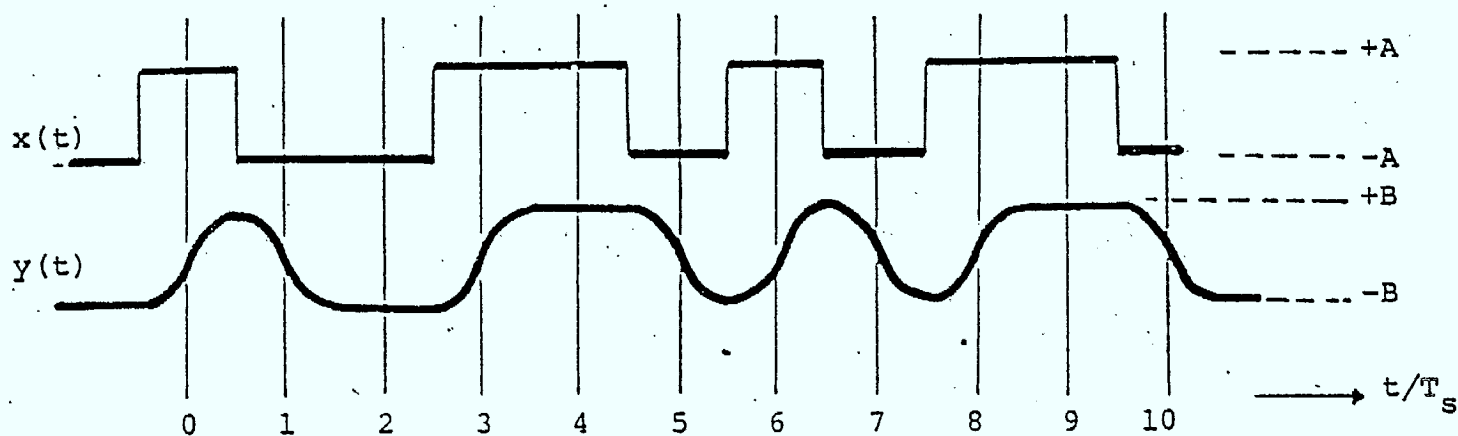
$$s(t) = \begin{cases} \frac{1}{2} (1 + \cos \frac{\pi t}{T_s}), & |t| \leq T_s \\ 0, & \text{elsewhere} \end{cases} \quad (7.1.5a)$$



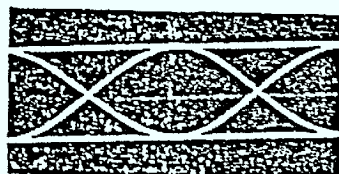
$$(a) \quad s_e(t_n) = \begin{cases} B, & |t_n| \leq \frac{T_s}{2} \\ 0, & \text{elsewhere} \end{cases}$$



$$(b) \quad s_o(t_n) = \begin{cases} B \sin \frac{\pi t_n}{T_s}, & |t_n| \leq \frac{T_s}{2} \\ 0, & \text{elsewhere} \end{cases}$$



(c) $x(t)$ and $y(t)$



(d) Measured eye diagram
of $y(t)$
bit rate: 32 kb/s

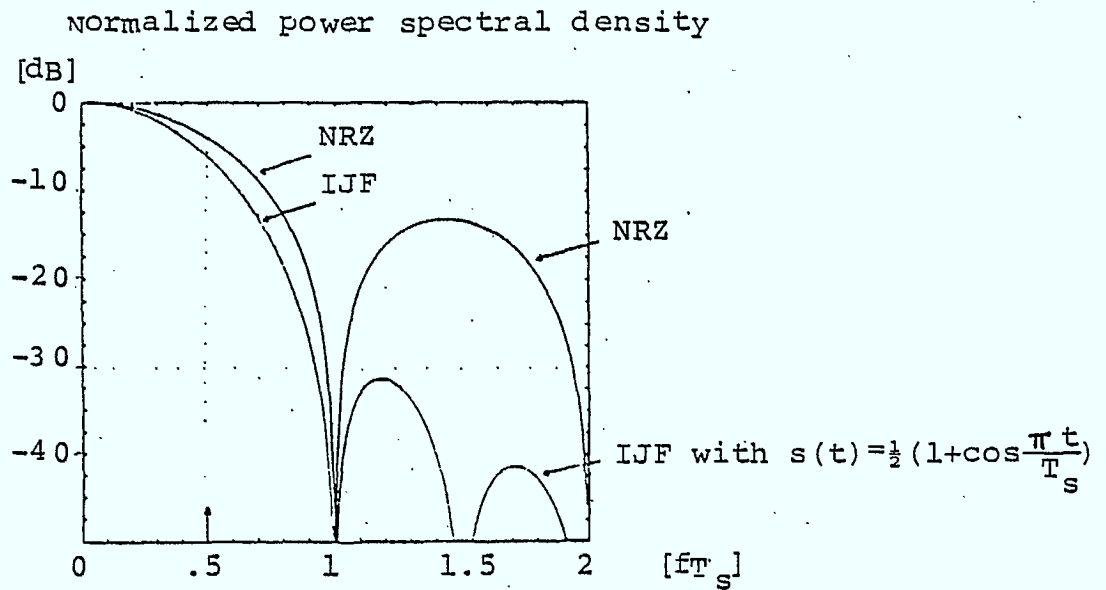
Fig. 7.1.2 An example of an IJF signal encoding
using the NLSF concept

The normalized PSD of the encoded IJF signal is represented by

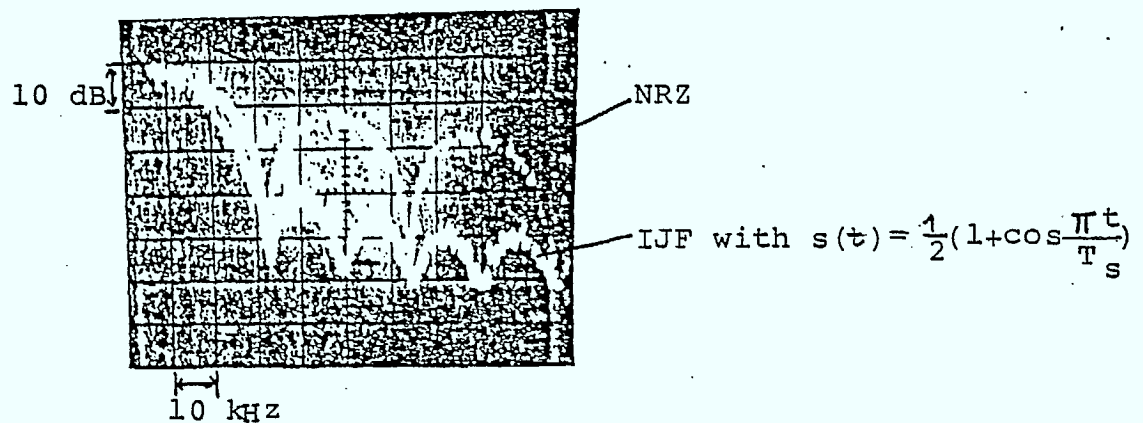
$$\frac{Y(f)}{Y(0)} = \left| \frac{\sin 2\pi x}{2\pi x} \left(\frac{1}{1-4x^2} \right) \right|^2 \quad (7.1.5b)$$

where $x = fT_s$

As shown in Fig. 7.1.3, the IJF signal has the same mainlobe occupancy as the NRZ signal, while its sidelobes are very much lower than those of the NRZ signal.



(a) Computed power spectra of NRZ and IJF signals



(b) Measured power spectra of NRZ and IJF signals
(Bit rate: 32 kb/s)

Fig. 7.1.3 Power spectra of the NRZ and IJF signals

The IJF receive filter has a linear phase response and the following amplitude characteristics:

$$F(x) = \frac{R(x, \alpha)}{S(x)} \quad (7.1.6)$$

x is the normalized frequency, $x = fT_s$,

T_s is the symbol interval,

$S(x)$ is the Fourier transform of the IJF double-interval pulse $s(t)$,

and

$R(x, \alpha)$ is the raised-cosine filter, defined as

$$R(x, \alpha) = \begin{cases} 1, & 0 \leq |x| \leq \frac{1}{2} (1-\alpha) \\ \frac{1}{2} \{1 - \sin(\frac{1}{\alpha}(x - \frac{1}{2}))\} \frac{1}{2} (1-\alpha) \leq |x| \leq \frac{1}{2} (1+\alpha) \\ 0, & |x| \geq \frac{1}{2} (1+\alpha). \end{cases}$$

It is shown that the receive signal in the linear channel has zero ISI.

For $s(t) = \frac{1}{2} (1 + \cos \frac{\pi t}{T_s})$, the performance degradation in E_b/N_0 versus the value of α of the raised cosine filter $R(x, \alpha)$ is minimum (0.276 dB) at $\alpha = 0.6$ [5,6].

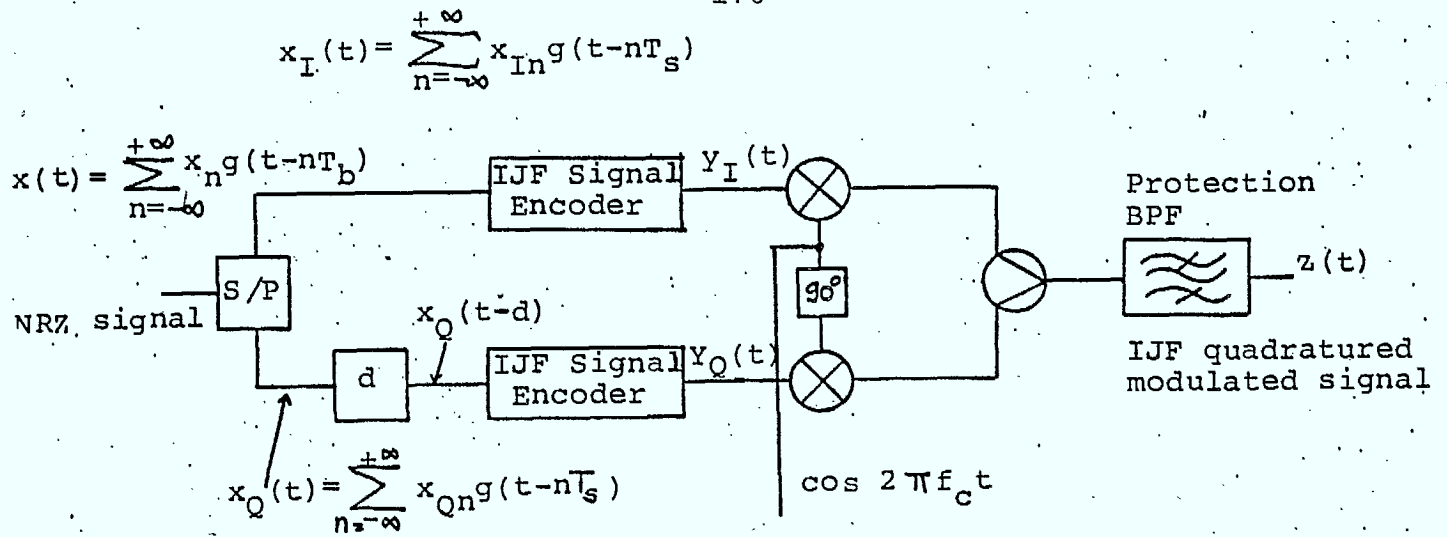
7.1.3 Characteristics of IJF Quadrature Modulated Signals in Linear Channels

Figures 7.1.5a and b show the block diagrams of the Intersymbol Interference and Jitter Free Quadrature Phase Shift Keying modulator and demodulator respectively. The IJF-OQPSK modulator differs from the conventional modulator only in the IJF signal encoders, while the IJF-OQPSK demodulator is identical to that for conventional OQPSK.

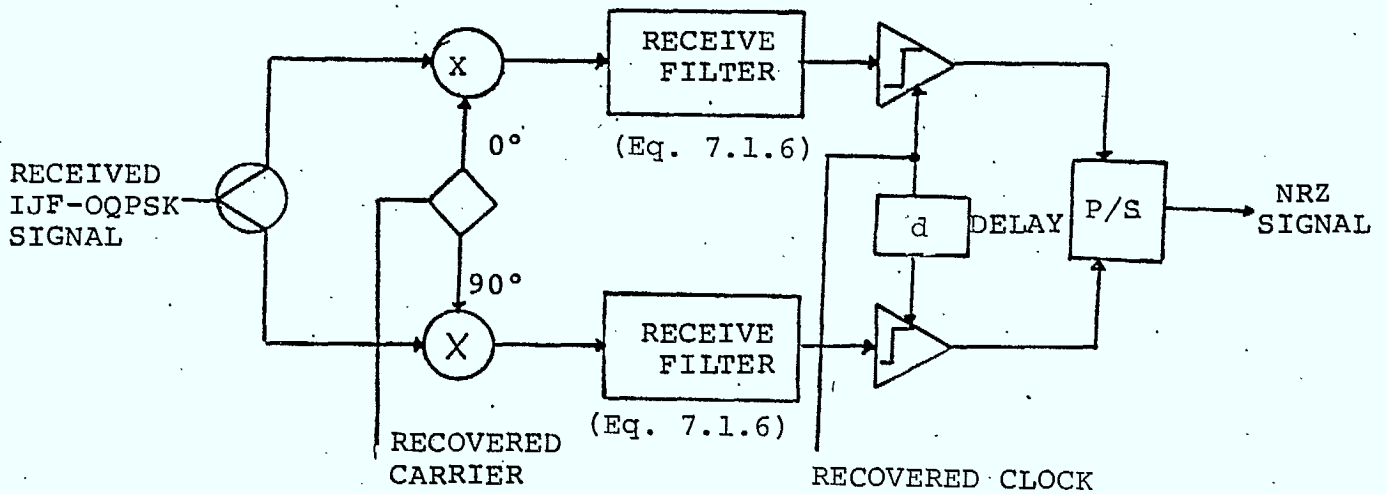
The NRZ input signal, $x(t)$, is serial-to-parallel converted into two NRZ data streams, $x_I(t)$ and $x_Q(t)$. The symbol interval T_s of $x_I(t)$ or $x_Q(t)$ is twice the bit interval T_b of $x(t)$, i.e. $T_s = 2T_b$.

The data stream $x_Q(t)$ is delayed by d where $0 \leq d < T_s$ to produce $x_Q(t-d)$. NRZ signals, $x_I(t)$ and $x_Q(t-d)$ are encoded into IJF signals $y_I(t)$ and $y_Q(t)$. These are used to modulate the quadrature carriers, $\cos w_c t$ and $\sin w_c t$, which are then summed to produce the IJF quadrature modulated signal $z(t)$.

$$\begin{aligned} z(t) &= y_I(t) \cos w_c t + y_Q(t) \sin w_c t \\ &= A(t) \cdot \cos [w_c t + \phi(t)] \end{aligned} \quad (7.1.7)$$



(a) IJF-quadrature phase-shift keying modulator



(b) IJF-quadrature phase shift keying demodulator

Fig. 7.1.4 Block diagram of an IJF quadrature phase-shift keying Modem.

where $A(t)$ and $\Phi(t)$ are the envelope and phase of the IJF quadrature modulated signal,

$$A(t) = \sqrt{y_I^2(t) + y_Q^2(t)} \quad (7.1.8a)$$

and

$$\Phi(t) = -\tan^{-1} \left(\frac{y_Q(t)}{y_I(t)} \right) \quad (7.1.9b)$$

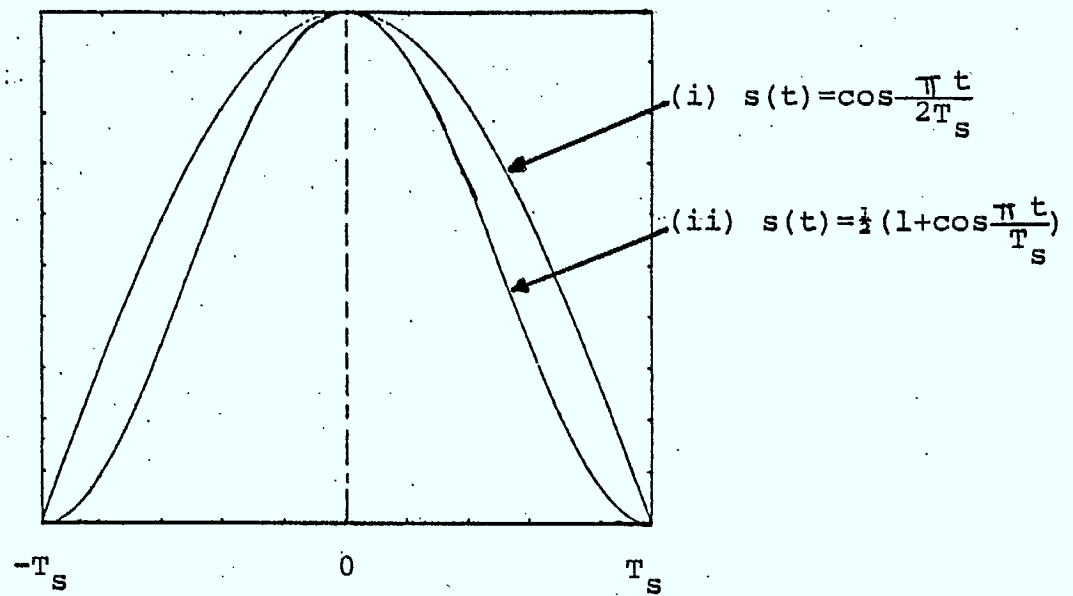
Based on Eq.(7.1.3) and the structure of a quadrature modulator, the PSD function of the IJF quadrature modulated signal, $Z(t)$, can be derived as:

$$Z(f) \approx K |S(f-f_c)|^2 \quad (7.1.10)$$

where K is a constant.

Figures 7.1.5, 7.1.6 and 7.1.7 show the eye diagrams of some IJF signals and their corresponding modulated power spectra and out-of-band-to-inband energy ratios. As indicated in Figs. 7.1.6 and 7.1.7 the IJF quadrature modulated signals have significant spectral advantages over QPSK, OQPSK, and MSK signals.

Figures 7.1.8 a, b, and c show the envelope fluctuation, phase transition and signal space diagram of the IJF-QPSK signal respectively. Since the transition times in $y_I(t)$ and $y_Q(t)$ coincide, the envelope of the IJF-QPSK signal exhibits serious fluctuations and its phase transitions are abrupt.

(a) $s(t)$

(b) Eye diagrams

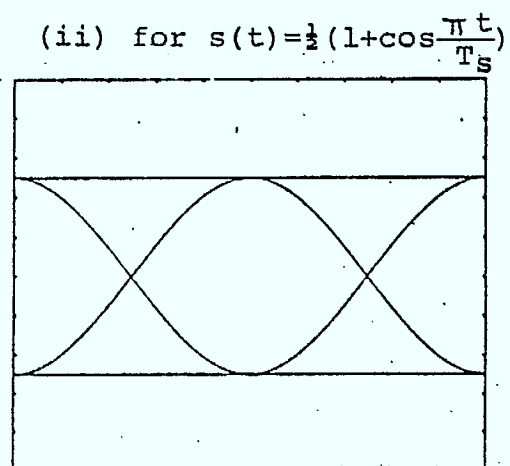
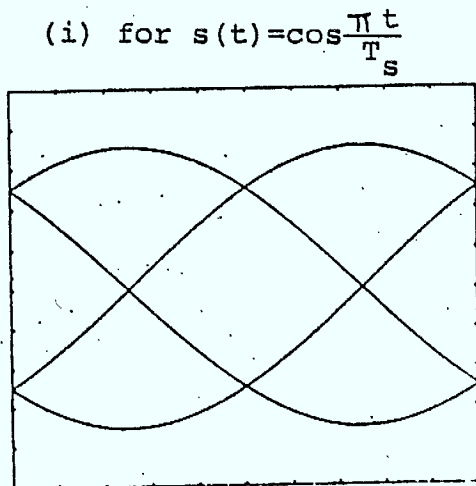


Fig. 7.1.5 Time domain representations of some IJF signals

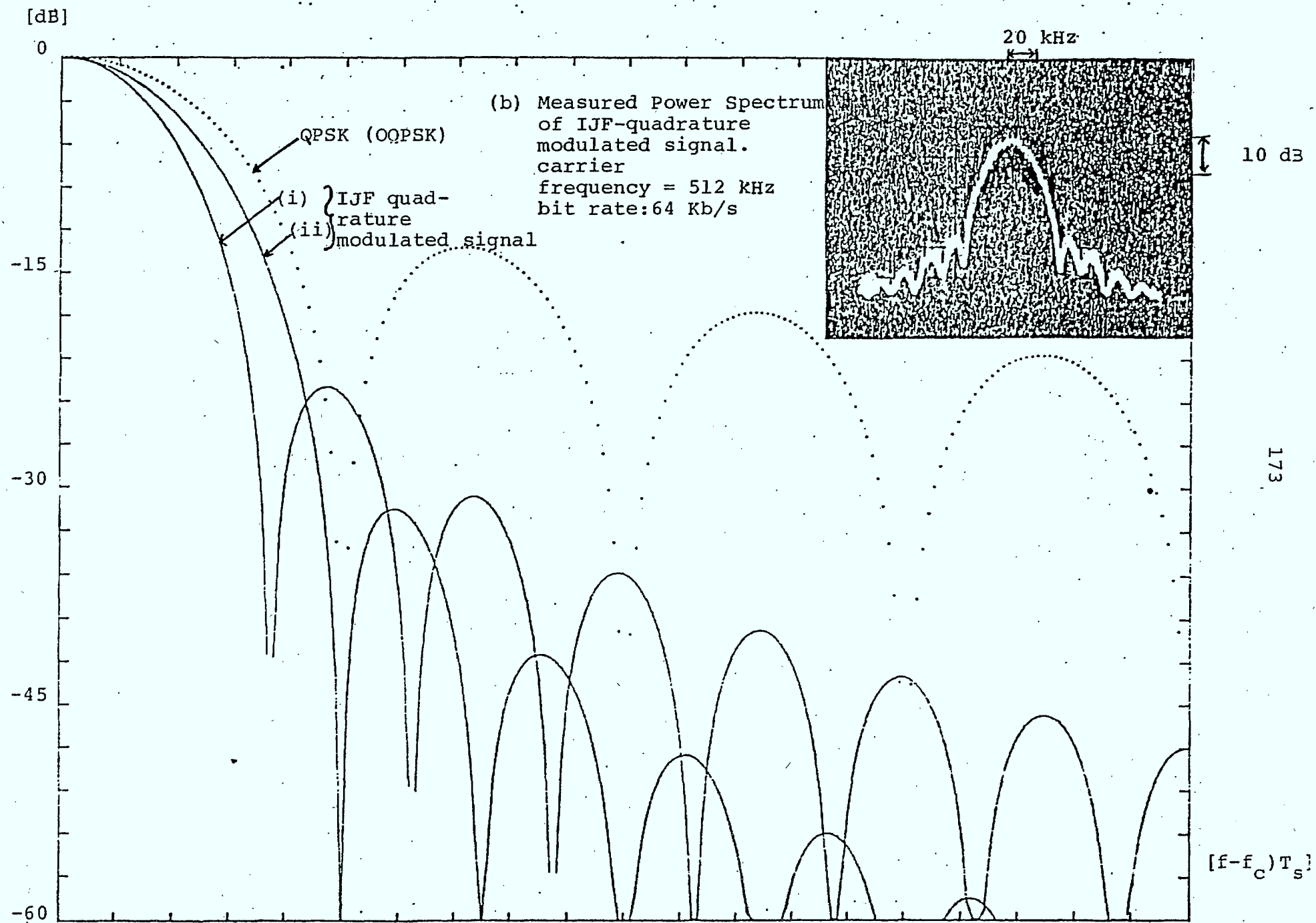


Fig. 7.1.6 Normalized power spectra of some IJF quadrature modulated signals

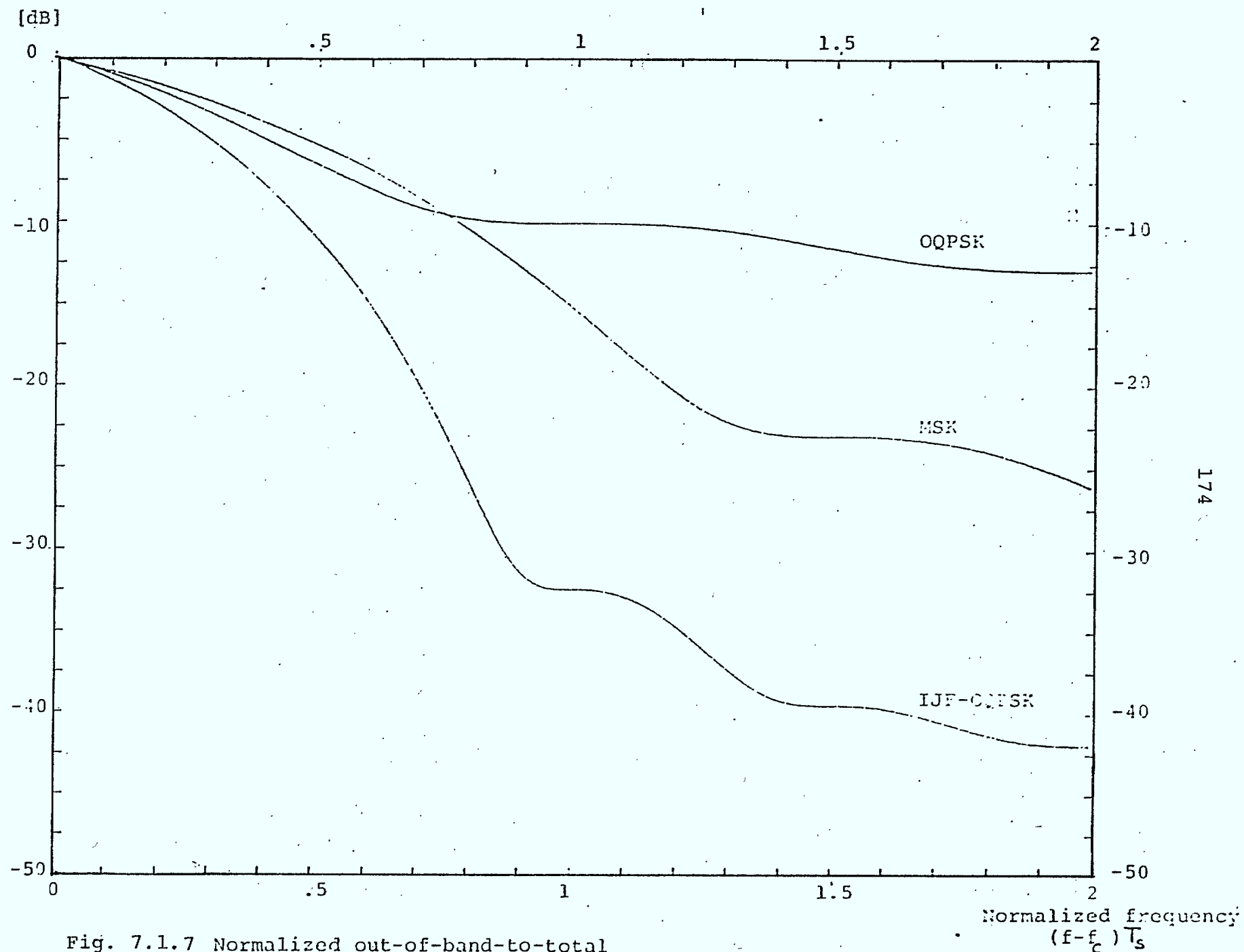
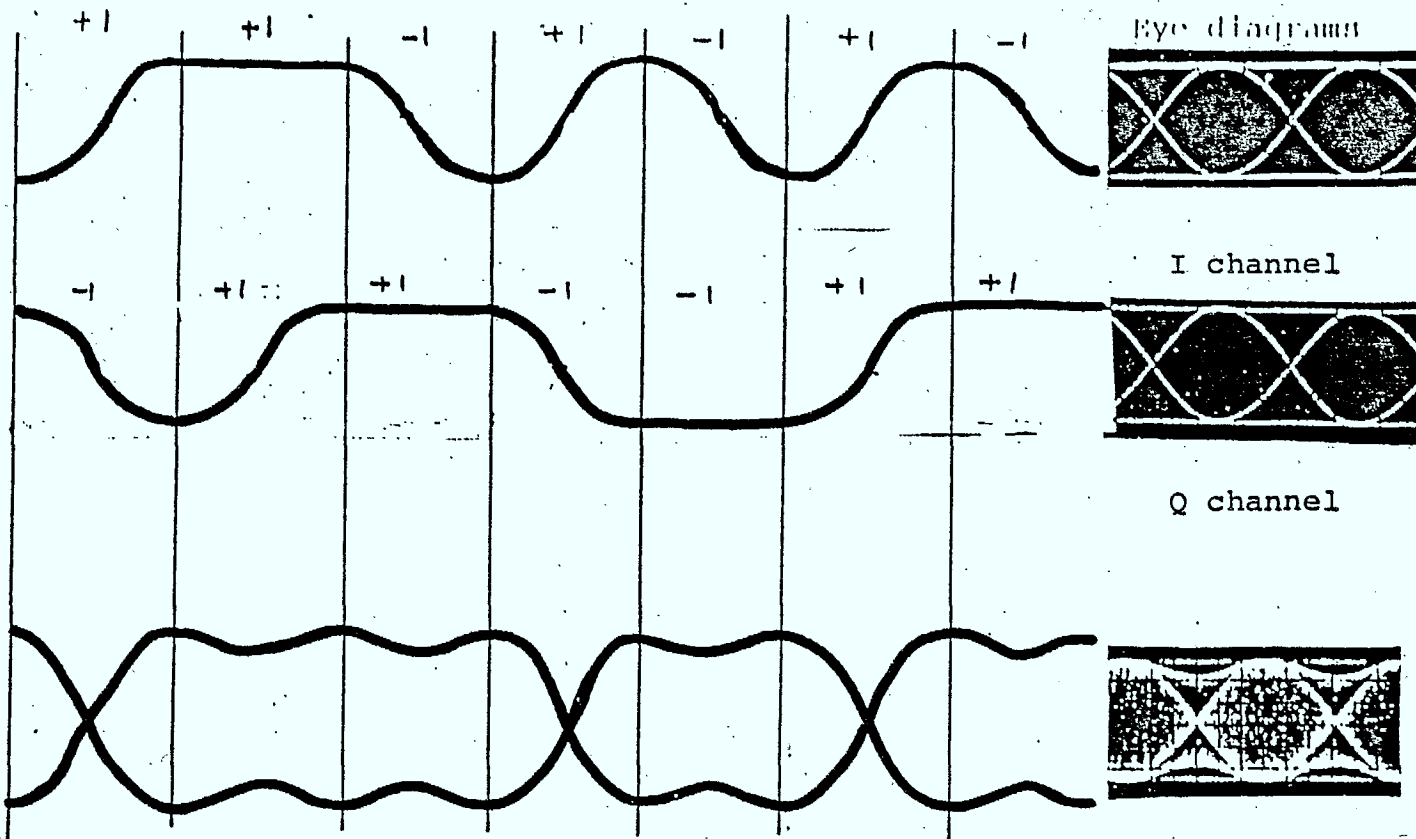
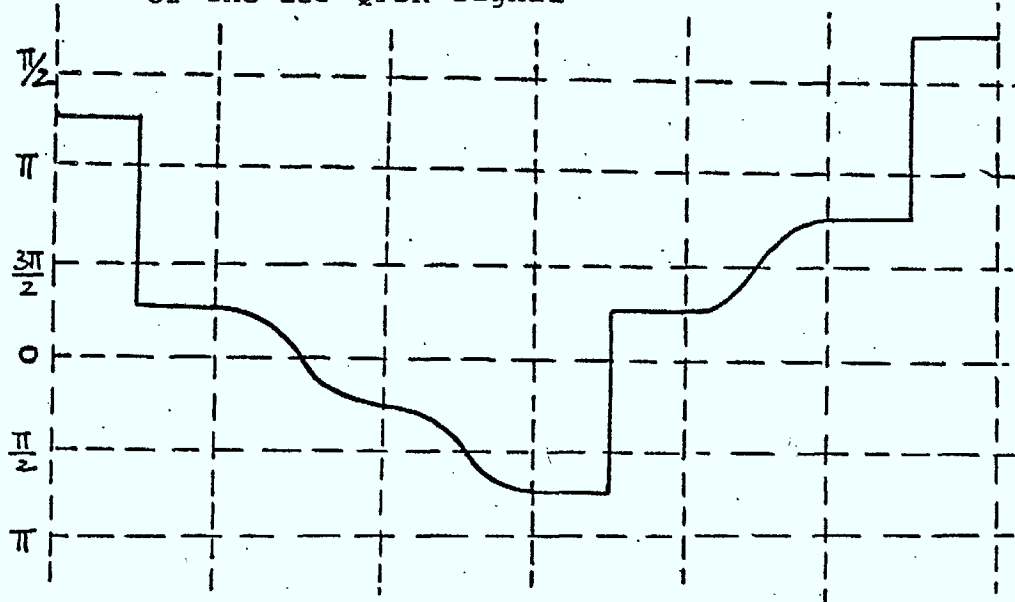


Fig. 7.1.7 Normalized out-of-band-to-total energy ratios of OQPSK (QPSK), MSK, IJF-OQPSK signals



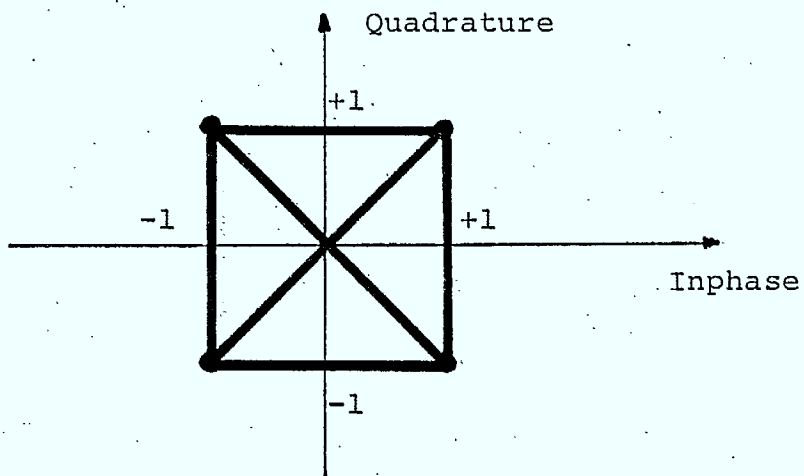
(a) An example of the envelope fluctuation of the IJF-QPSK signal

IJF-QPSK
Measured results
 bit rate: 64 Kb/s
 carrier : 512 kHz

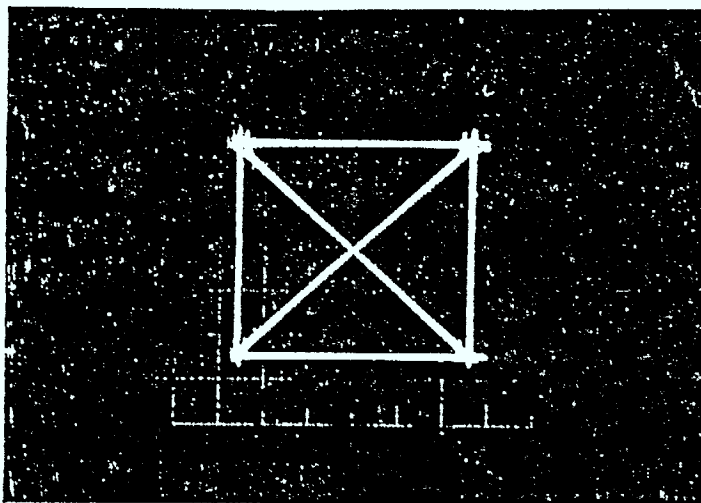


(b) An example of the phase transition of the IJF-QPSK signal

Fig. 7.1.8 Envelope fluctuation and phase transition of the IJF-QPSK signal



(i) Computed signal space diagram

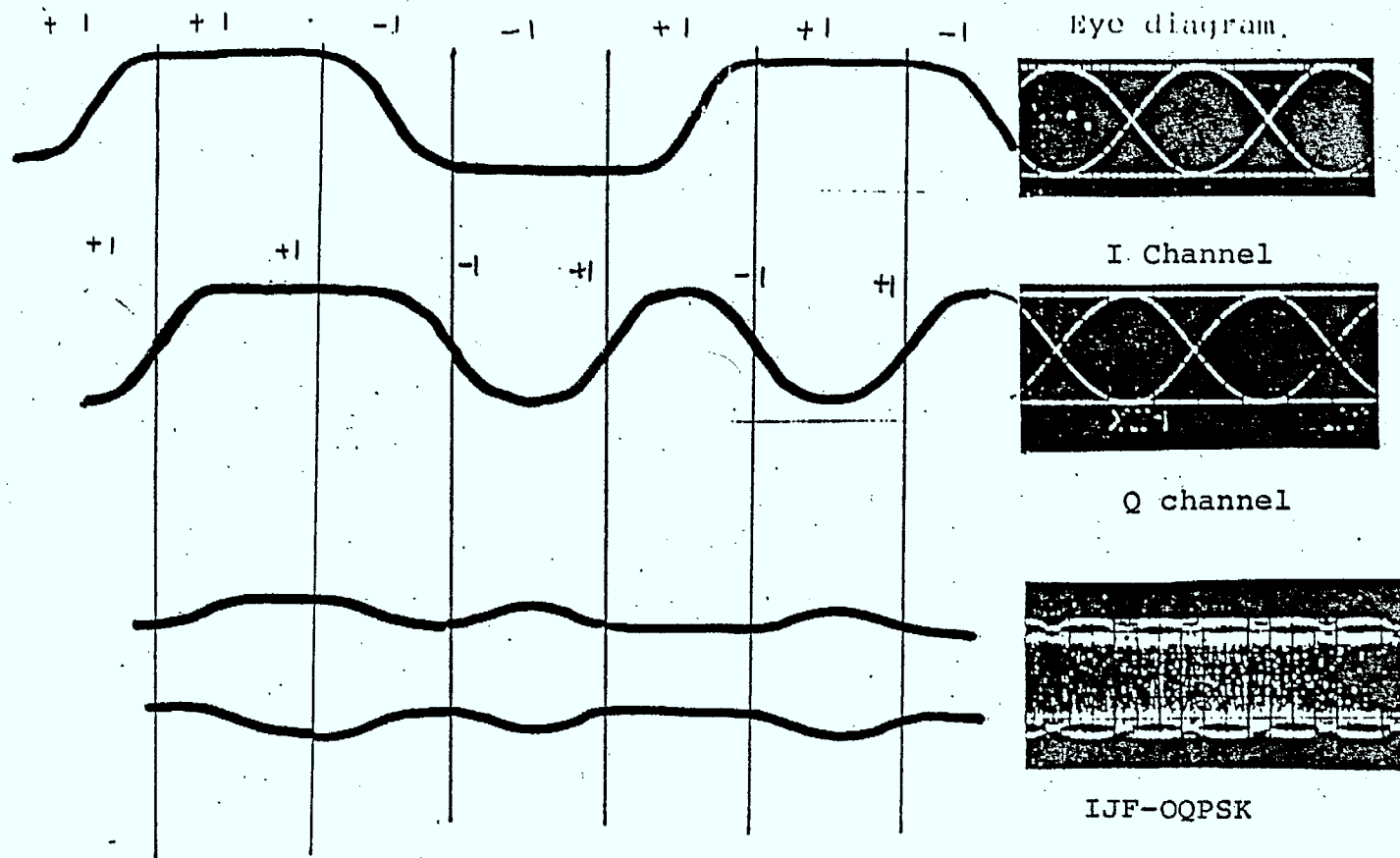


(ii) Measured signal space diagram of the IJF-QPSK signal

Bit rate: 64 Kb/s
Carrier : 512 kHz

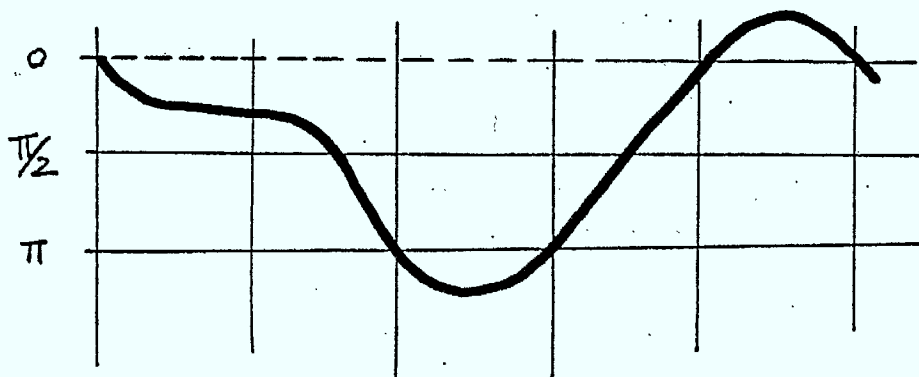
By delaying the data stream $x_Q(t)$ by T_b relative to $x_I(t)$, the resultant IJF-QQPSK signal exhibits a maximum envelope fluctuation of 3 dB and its phase transitions are continuous and smooth as shown in Figs. 7.1.9 a and b respectively.

In an AWGN linear channel, the P_e performance of IJF-QPSK and IJF-QQPSK signals is identical to that of IJF baseband signals.



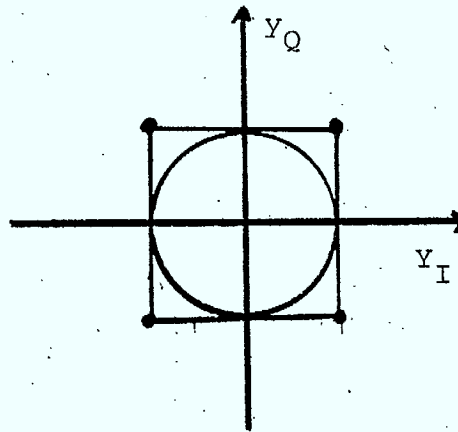
(a) Envelope Fluctuation

bit rate: 64 Kb/s
carrier: 512 kHz

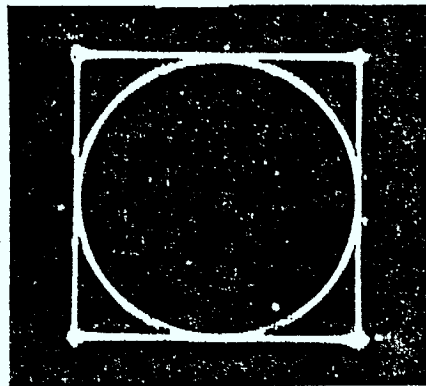


(b) Phase transition of IJF-OQPSK signal

Fig. 7.1.9 An example of the amplitude fluctuation and phase transition of the IJF-OQPSK signal



(i) computed signal space diagram



(ii) measured signal space diagram
of IJF OQPSK signal

Bit rate: 64 Kb/s
Carrier : 512 kHz

Fig. 7.1.9 c Signal space diagram of the IJF-OQPSK signal

7.1.4 Properties of IJF Quadrature Modulated Signals in a Hardlimited Channel

To maximize power efficiency, the HPA (high power amplifier) used in a transmitter typically operates in a nonlinear mode. Consider the IJF-quadrature modulator followed by a saturated HPA shown in Fig.7.1.10a. The saturated HPA is modelled as an ideal hardlimiter that produces a constant output envelope and no change to the phase of the IJF-quadrature modulated signal. The transfer characteristic of the ideal hardlimiter is shown in Fig.7.1.10b. Such a model closely approximates Gunn and Impatt diode injection locked amplifiers.

The hardlimited IJF quadrature modulated signal $z'(t)$ can be represented as:

$$\begin{aligned} z'(t) &\cong y'_I(t) \cos 2\pi f_c t + y'_Q(t) \sin 2\pi f_c t \\ &= C \cos (2\pi f_c t + \Phi'(t)) \end{aligned} \quad (7.1.11)$$

where $y'_I(t)$ and $y'_Q(t)$ are inphase and quadrature equivalent baseband components of the hardlimited IJF quadrature modulated signal and

$$y'^2_I(t) + y'^2_Q(t) = C^2 : \text{constant} \quad (7.1.12)$$

and

$$\Phi'(t) = -\tan^{-1} \left(\frac{y'_Q(t)}{y'_I(t)} \right) \quad (7.1.13a)$$

Since the ideal limiter has no memory,

$$\Phi'(t) = \Phi(t) \quad (7.1.13b)$$

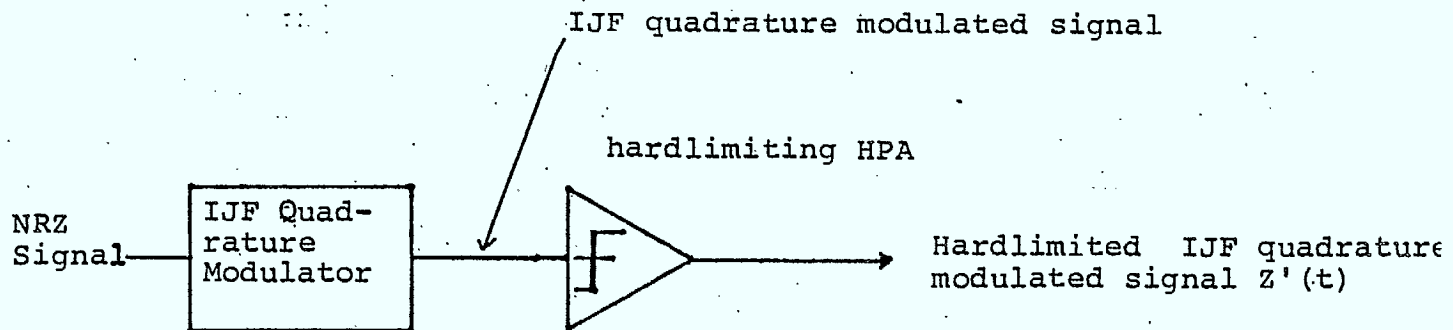


Fig.7.1.10a Block diagram of an IJF quadrature modulator followed by a hardlimiting HPA

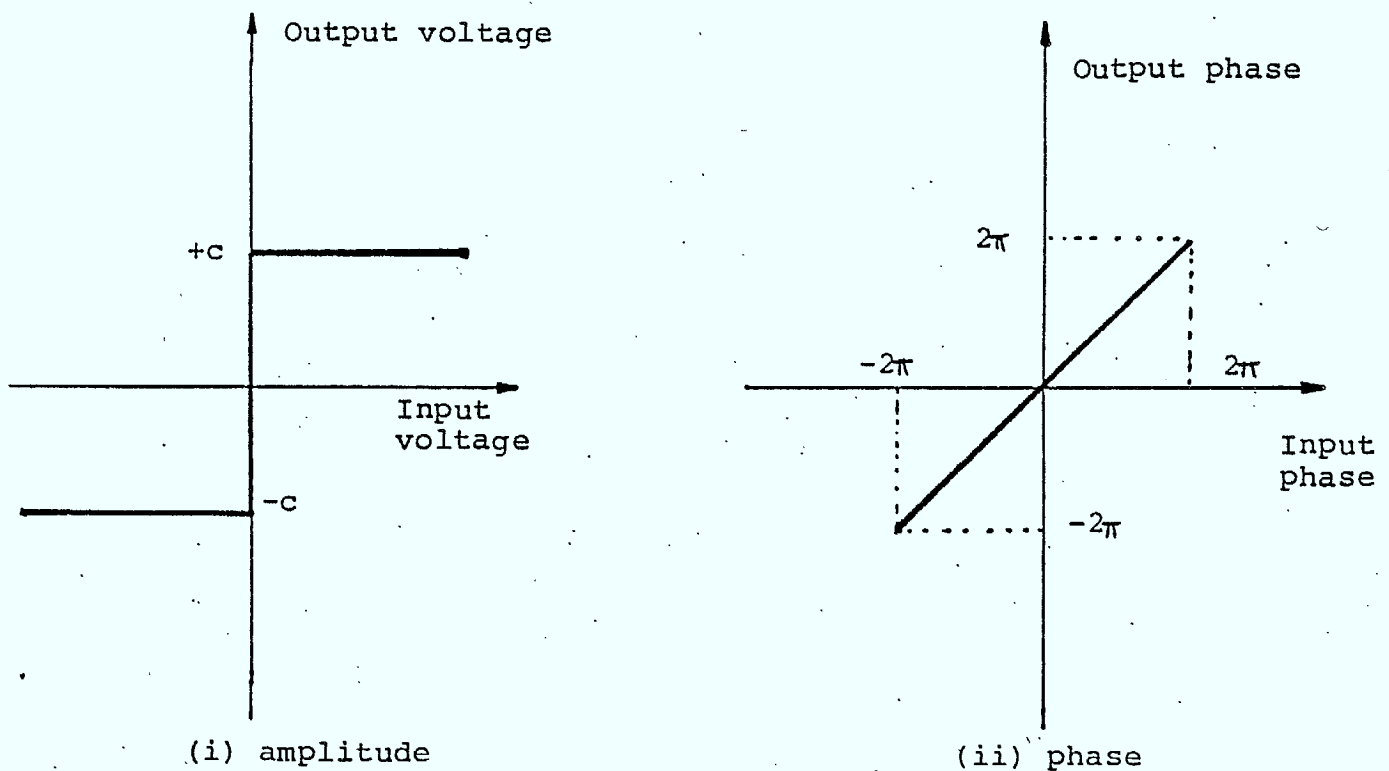


Fig.7.1.10b Transfer characteristics of the ideal hardlimiter

From Eqs. (7.1.9b, 7.1.13a and b), it can be shown that

$$\frac{y'_Q(t)}{y'_I(t)} = \frac{y_Q(t)}{y_I(t)} \quad (7.1.14)$$

By substituting Eq. (3.4) into Eq. (3.2), it follows that

$$y'_I(t) = c \frac{y_I(t)}{\sqrt{y_I^2(t) + y_Q^2(t)}} \quad (7.1.15a)$$

and

$$y'_Q(t) = c \frac{y_Q(t)}{\sqrt{y_I^2(t) + y_Q^2(t)}} \quad (7.1.15b)$$

Equations (7.1.15a,b) indicate that for any change in $y_I(t)$ (or $y_Q(t)$), $y'_Q(t)$ or ($y'_I(t)$) are affected. In other words, hardlimiting introduces crosstalk between the inphase and quadrature equivalent baseband components.

a. Properties of Hardlimited IJF-QPSK signals

Figures 7.1.11a,b illustrate the inphase and quadrature equivalent baseband components of a hardlimited IJF-QPSK signal. Since the transitions in $y_I(t)$ occur at the same time, the eye diagrams of the inphase and quadrature equivalent baseband components, $y'_I(t)$ and $y'_Q(t)$, of the hardlimited IJF-QPSK signal remain ISI and jitter free. However the hardlimiter introduced sharp transitions in $y'_I(t)$ and $y'_Q(t)$. This implies that the high frequency spectral components of the hardlimited IJF-QPSK signal are higher than those of the IJF-QPSK.

Let the equivalent baseband component $y'_I(t)$ or $(y'_Q(t))$ be represented by:

$$y'_I(t) = \sum_{n=-\infty}^{+\infty} h(t-nT_s) \quad (7.1.16)$$

where $h(t-nT_s)$ is the waveshape of $y'_I(t)$ in each symbol interval $(n-\frac{1}{2})T_s \leq t \leq (n+\frac{1}{2})T_s$. Based on Eqs. 7.1.2b and 7.1.15a the possible waveshapes of $h(t-nT_s)$ are

$$v_1(t_n) = -v_8(t_n) = C \frac{s_e(t_n)}{\sqrt{2s_e^2(t_n)}} \quad (7.1.17a)$$

$$v_2(t_n) = -v_7(t_n) = C \frac{s_e(t_n)}{\sqrt{s_e^2(t_n) + s_o^2(t_n)}} \quad (7.1.17b)$$

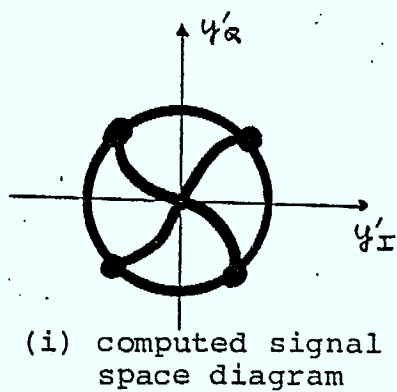
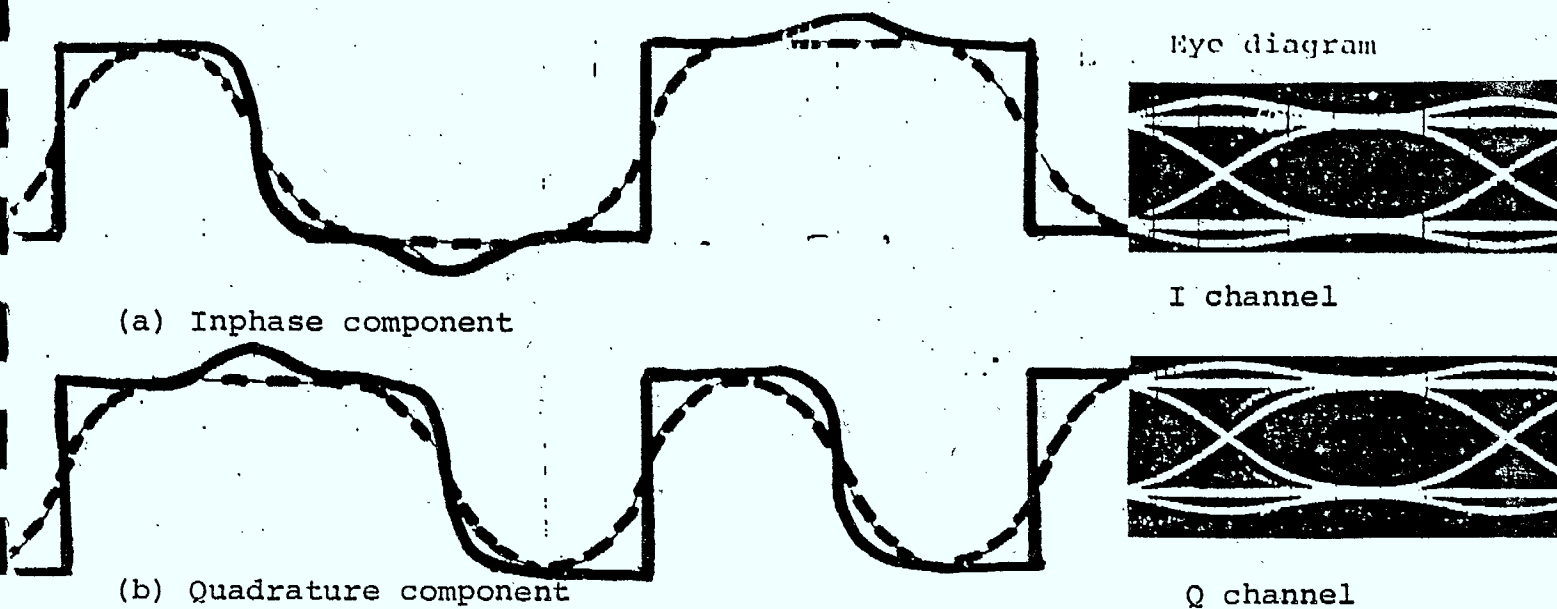
$$v_3(t_n) = -v_6(t_n) = C \frac{s_o(t_n)}{\sqrt{s_e^2(t_n) + s_o^2(t_n)}} \quad (7.1.17c)$$

$$v_4(t_n) = -v_5(t_n) = C \frac{s_o(t_n)}{\sqrt{2s_o^2(t_n)}} \quad (7.1.17d)$$

where $t_n = t - nT_s$

and $s_e(t_n), s_o(t_n)$ are defined by eqs. (7.1.4a,b,c,d)

An example of the waveshapes $v_i(t)$, $i=1, 2, \dots, 8$, is shown in Fig. 7.1.12.



(c) Hardlimited IJF-QPSK signal space diagrams

Fig. 7.1.11 Effects of hardlimiting on I and Q equivalent baseband components of the IJF-QPSK signal (dotted lines show $y_I(t)$ and $y_Q(t)$).

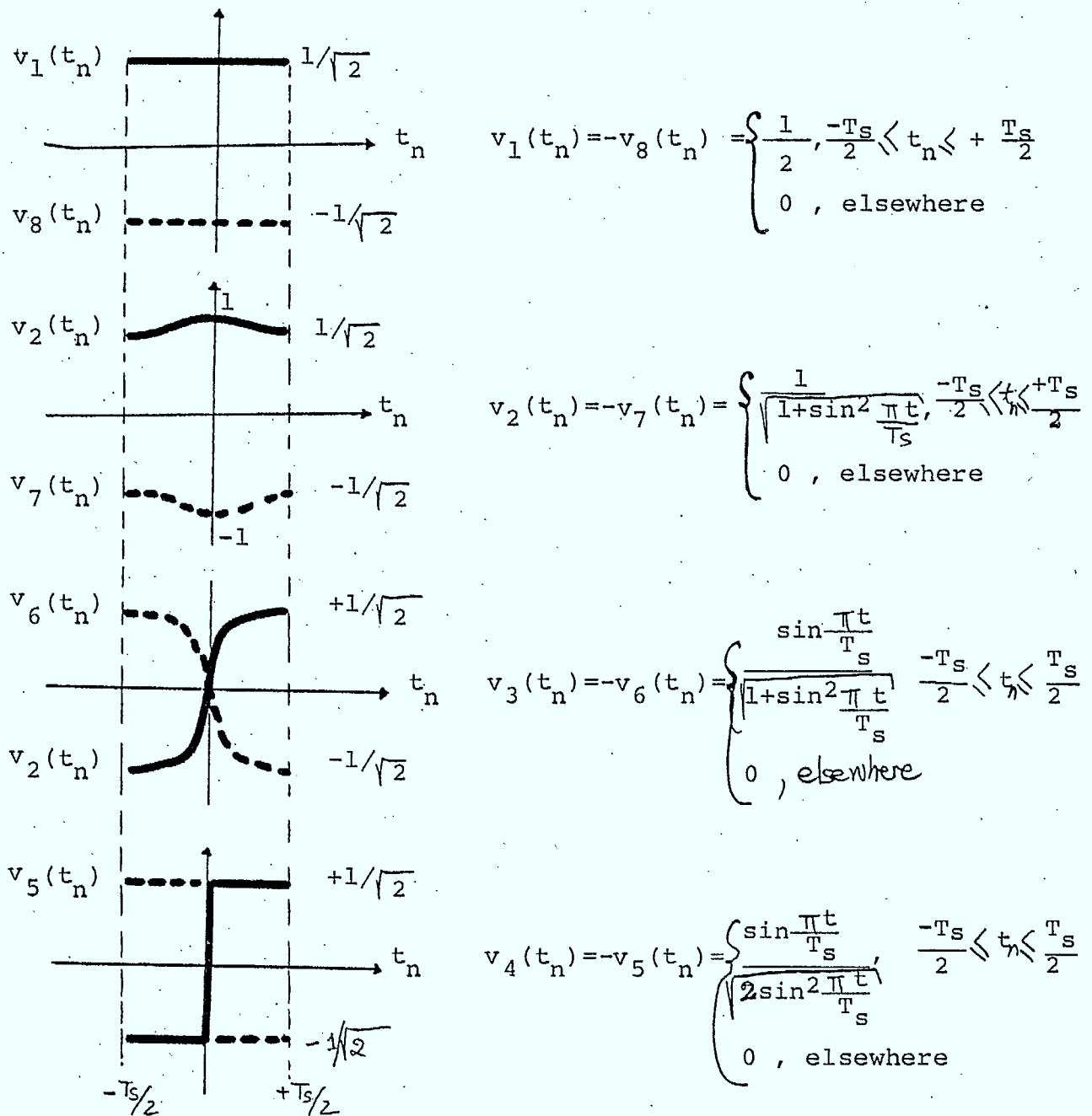


Fig. 7.1.12 An example of the waveshapes $v_i(t)$, for $i=1, 2, \dots, 8$

$$s_e(t_n) = \begin{cases} 1, & -\frac{T_s}{2} \leq t_n \leq \frac{T_s}{2} \\ 0, & \text{elsewhere} \end{cases}$$

$$s_o(t_n) = \begin{cases} \sin \frac{\pi t}{T_s}, & -\frac{T_s}{2} \leq t_n \leq +\frac{T_s}{2} \\ 0, & \text{elsewhere} \end{cases}$$

$$\begin{aligned}
P_{11} &= P \{ h(t_n) = v_1(t_n) \mid h(t_{n-1}) = v_1(t_{n-1}) \} \\
&= P \{ y_I(t_n) = s_1(t_n), y_Q(t_n) = s_1(t_n) \text{ or } s_2(t_n) \mid \\
&\quad y_I(t_{n-1}) = s_1(t_{n-1}), y_Q(t_{n-1}) = s_1(t_{n-1}) \\
&\quad \text{or } s_2(t_{n-1}) \} \\
&= P \{ y_I(t_n) = s_1(t_n) \mid y_I(t_{n-1}) = s_1(t_{n-1}) \} \cdot \\
&\quad P \{ y_Q(t_n) = s_1(t_n) \text{ or } s_2(t_n) \mid y_Q(t_{n-1}) \\
&\quad = s_1(t_{n-1}) \text{ or } s_2(t_{n-1}) \} \\
&= \frac{1}{2} \cdot \frac{1}{2} = \frac{1}{4}
\end{aligned}$$

Other p_{ik} 's, $i, k = 1, 2, \dots, 8$ can be obtained in a similar manner. They can be arranged as entries in the transition matrix P

$$P = \begin{bmatrix} P_{11} & P_{12} & \dots & P_{18} \\ P_{21} & P_{22} & \dots & P_{28} \\ \cdot & \cdot & \dots & \cdot \\ \cdot & \cdot & \dots & \cdot \\ \cdot & \cdot & \dots & \cdot \\ P_{81} & P_{82} & \dots & P_{88} \end{bmatrix} = \frac{1}{4} \begin{bmatrix} 11 & 0000 & 11 \\ 11 & 0000 & 11 \\ 00 & 1111 & 00 \\ 00 & 1111 & 00 \\ 11 & 0000 & 11 \\ 11 & 0000 & 00 \\ 00 & 1111 & 00 \\ 00 & 1111 & 00 \end{bmatrix} \quad (7.1.18b)$$

In each symbol interval, $h(t_n)$ is chosen from the set $\{v_i(t_n), i = 1, 2, \dots, 8\}$. The waveshape of $h(t_n)$ is dependent on the waveshape of the previous $h(t_{n-1})$ and the waveshapes of $y_I(t_n)$ and $y_Q(t_n)$. The stationary probabilities

$p_i = P \{h(t_n) = v_i(t_n)\}$, $i=1, 2, 3, \dots, 8$
and transition probabilities

$$p_{ik} = P \{h(t_n) = v_k(t_n) \mid h(t_{n-1}) = v_i(t_{n-2})\},$$

$$i, k = 1, 2, \dots, 8$$

can be obtained by investigating the encoding law of $y_I(t)$ and $y_Q(t)$ and construction of $v_i(t)$, $i = 1, 2, \dots, 8$,

$$\begin{aligned} p_1 &= P \{h(t_n) = v_1(t_n)\} = P \{y_I(t_n) = s_1(t_n), y_Q(t_n) = s_1(t_n) \text{ or } s_2(t_n)\} \\ &= P \{y_I(t_n) = s_1(t_n)\} \cdot [P \{y_Q(t_n) = s_1(t_n)\} + P \{y_Q(t_n) = s_2(t_n)\}] \\ &= \frac{1}{4} \cdot (\frac{1}{4} + \frac{1}{4}) = 1/8 \end{aligned}$$

since $y_I(t_n)$ and $y_Q(t_n)$ are statistically independent.

Similarly, it can be shown that:

$$p_i = 1/8, \quad i = 1, 2, \dots, 8$$

(7.1.18a)

The statistical properties of $y'_I(t)$ can be represented by an 8-state Markov chain model as shown in Fig.7.1.13. The states represent the basic waveshapes $v_i(t)$ for $i = 2, 3, \dots, 8$. The arrows denote the possible transitions from a state i to another state k . From this statistical description, the power spectral density of $y'_I(t)$ or $(y'_Q(t))$ is given by [7].

$$\begin{aligned}
 Y(f) = & \frac{1}{T_s} \sum_{n=-\infty}^{+\infty} \left| \sum_{i=1}^8 p_i v_i\left(\frac{n}{T_s}\right) \right|^2 \delta\left(f - \frac{n}{T_s}\right) \\
 & + \frac{1}{T_s} \sum_{i=1}^8 p_i |v_i(f)|^2 \\
 & + \frac{2}{T_s} \operatorname{Re} \left\{ \sum_{i=1}^8 \sum_{k=1}^8 p_i v_i^*(f) v_k(f) v_{ik} \right\} \quad (7.1.19)
 \end{aligned}$$

where $V_i(f)$ is the Fourier transform of $v_i(t)$, $i=1, \dots, 8$,

$V_i^*(f)$ is the complex conjugate of $V_i(f)$,

$$V_{ik} = \sum_{n=1}^{+\infty} p_{ik}^{(n)} e^{-j2\pi f T_s},$$

$P_{ik}(n)$ is the ik th entry of the n -step transition matrix

$$P^n = \underbrace{P \times P \times \dots \times P}_{n \text{ times}},$$

and $\operatorname{Re}\{\dots\}$ is the real part of $\{\dots\}$

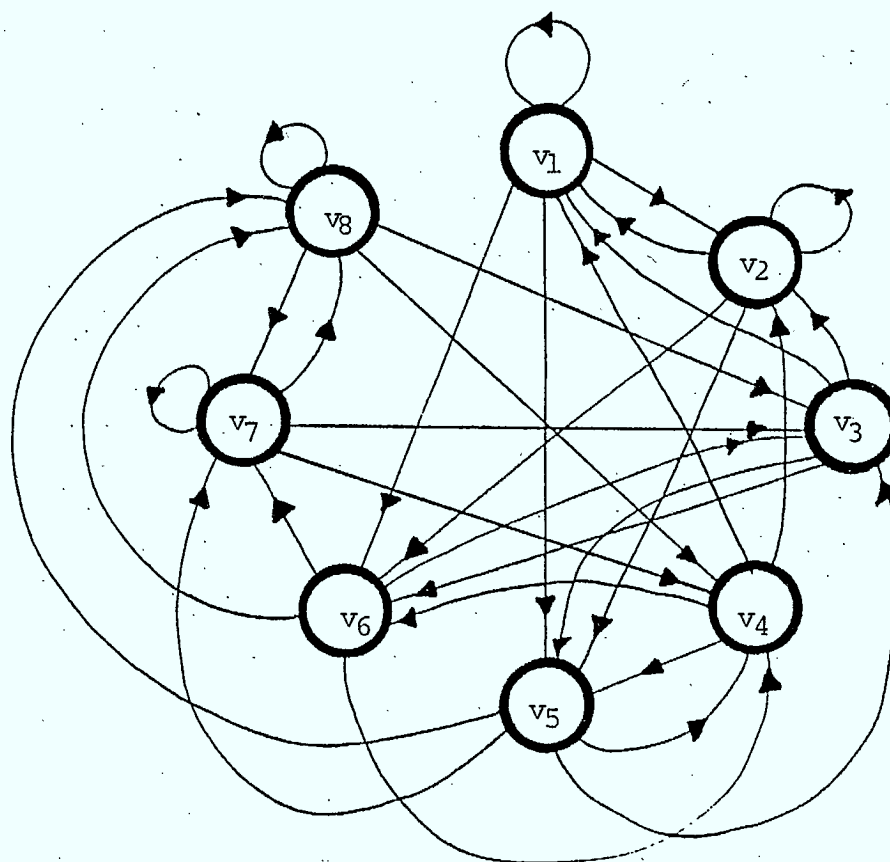


Fig. 7.1.13 8-state transition diagram of the baseband component of the hardlimited IJF-QPSK

Since

$$P^n = \frac{1}{8} \begin{bmatrix} 11111111 \\ 11111111 \\ 11111111 \\ 11111111 \\ 11111111 \\ 11111111 \\ 11111111 \\ 11111111 \end{bmatrix} \quad \text{for } n=2, \dots, +\infty,$$

it follows that

$$V_{ik} = P_{ik} e^{-j2\pi f T_s} + \frac{1}{8} \sum_{n=2}^{\infty} e^{-j2\pi f T_s} \quad (7.1.20a)$$

The Fourier transforms of $v_i(t)$, $i=1,2,\dots,8$ are

$$\begin{aligned} V_1(f) &= -V_8(f) \\ V_2(f) &= -V_7(f) \\ V_3(f) &= -V_6(f) \\ V_4(f) &= -V_5(f) \end{aligned} \quad (7.1.20b)$$

Substituting (7.1.18a,b) and (7.1.20a,b,c,d) into Eq. (7.1.19) yields

$$Y(f) = \frac{1}{4T_s} \left[2 \sum_{i=1}^4 |V_i(f)|^2 + \operatorname{Re} \{ (V_1(f) + V_2(f) + V_3(f) + V_4(f))^* \cdot (V_1(f) + V_2(f) - V_3(f) - V_4(f)) e^{-j2\pi f T_s} \} \right]$$

Based on Eq.(7.1.11) the normalized PSD function of the hardlimited IJF-QPSK signal is:

$$z_{IJF-QPSK}^h(x) \approx z_0 \left[2 \sum_{i=1}^4 |V_i(x)|^2 + \operatorname{Re} \left\{ (V_1(x) + V_2(x) + V_3(x) + V_4(x))^* (V_1(x) + V_2(x) - V_3(x) - V_4(x)) e^{-j2\pi x} \right\} \right] \quad (7.1.21b)$$

where z_0 is the normalized coefficient so that

$$z_{IJF-QPSK}^h(0) = 1$$

and x is the normalized frequency

$$x = (f - f_c) T_s$$

b. Properties of Hardlimited IJF-Offset-Keyed OQPSK Signals

Figures 7.1.14 a,b illustrate the inphase and quadrature equivalent baseband components of the hardlimited IJF-OQPSK signal. Since the transition in $y_I(t)$ or $y_Q(t)$ occurs at the maximum eye opening point of $y_Q(t)$ or $y_I(t)$, the inphase to quadrature crosstalk introduces intersymbol interference (ISI). As shown in Figs.7.1.14a,b the ISI is 3 dB peak-to-peak.

The PSD of the hardlimited IJF-OQPSK signal is derived using the approach given in Section a.

In each symbol interval $((n-\frac{1}{2})T_s, (n+\frac{1}{2})T_s)$, the inphase baseband signal, $y_I(t)$, has four possible waveshapes $s_i(t)$, $i=1, 2, 3, 4$ defined by Eq.(7.1.2b). Since the $y_Q(t)$ is delayed by $\frac{T_s}{2}$ with respect to $y_I(t)$ it has 8 possible waveshapes $s'_i(t)$, $i=1, 2, \dots, 8$ in each symbol interval of $y_I(t)$:

(a) Inphase baseband component

(b) Quadrature baseband component

Eye diagrams



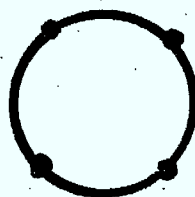
I channel



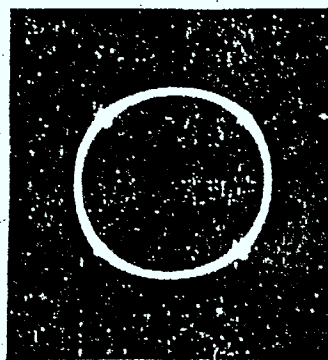
Q channel

measured results

carrier frequency: 512 kHz
bit rate: 64 kb/s



(i) computed



(ii) measured

(c) Hardlimited IJF-OQPSK signal space diagrams

Fig.7.1.14 Effects of hardlimiting on I and Q equivalent baseband components of the IJF-OQPSK signal (dotted lines show $y_I(t)$, $y_Q(t)$)

$$s'_1(t_n) = -s'_8(t_n) = \begin{cases} s_e(t_n + \frac{T_s}{2}) & \text{for } -\frac{T_s}{2} \leq t_n < 0 \\ +s_e(t_n - \frac{T_s}{2}) & \text{for } 0 \leq t_n \leq \frac{T_s}{2} \end{cases} \quad (7.1.22a)$$

$$s'_2(t_n) = -s'_7(t_n) = \begin{cases} s_o(t_n + \frac{T_s}{2}), & -\frac{T_s}{2} \leq t_n < 0 \\ -s_o(t_n - \frac{T_s}{2}), & 0 \leq t_n \leq \frac{T_s}{2} \end{cases} \quad (7.1.22b)$$

$$s'_3(t_n) = -s'_6(t_n) = \begin{cases} s_e(t_n + \frac{T_s}{2}), & -\frac{T_s}{2} \leq t_n < 0 \\ s_e(t_n - \frac{T_s}{2}), & 0 \leq t_n \leq \frac{T_s}{2} \end{cases} \quad (7.1.22c)$$

$$s'_4(t_n) = -s'_5(t_n) = \begin{cases} s_e(t_n + \frac{T_s}{2}), & -\frac{T_s}{2} \leq t_n < 0 \\ -s_o(t_n - \frac{T_s}{2}), & 0 \leq t_n \leq \frac{T_s}{2} \end{cases} \quad (7.1.22d)$$

where $t_n = t - nT_s$

In other words the quadrature baseband signal $y_Q(t)$ can be represented by

$$y_Q(t) = \sum_{n=-\infty}^{+\infty} w(t_n) \quad (7.1.23a)$$

where $w(t_n)$ is the waveshape of $y_Q(t)$ in the n^{th} symbol interval of $y_I(t)$. It is one of 8 waveshapes $s'_i(t_n)$, $i=1,2,\dots,8$ defined by Eqs.(7.1.22a to d). Based on Eq.(7.1.2b) the statistical properties of $y_Q(t)$ can be described by an 8-state Markov chain model shown in Fig.7.1.15 where the states represent waveshapes $s'_i(t)$, $i=1,2,\dots,8$. The stationary probabilities are

$$p_i = P\{w(t_n) = s'_i(t_n)\} = \frac{1}{8}, \quad i=1,2,\dots,8, \quad (7.1.23b)$$

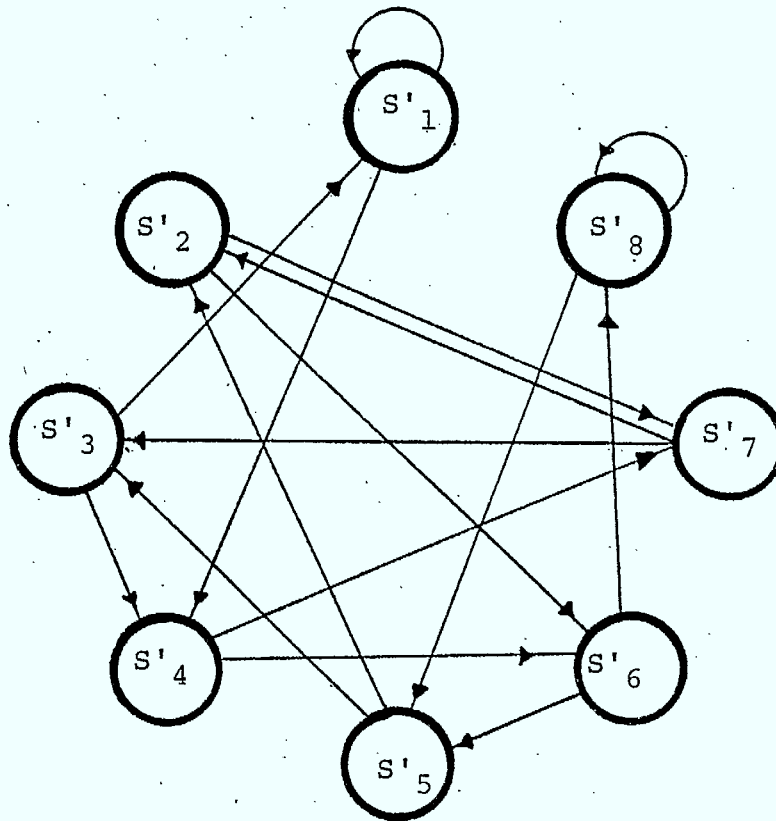


Fig.7.1.15 8-state transition diagram
of the waveshapes $s'_i(t_n)$, $i=1, 2, \dots, 8$

and the transition probabilities

$$P_{ik} = P \{ w(t_n) = s'_k(t_n) \mid w(t_{n-1}) = s'_i(t_{n-1}) \}$$

are obtained by investigating Fig. 7.1.15. They can be arranged as the entries in the transition matrix:

$$P = \begin{bmatrix} P_{11} & P_{12} & \dots & P_{18} \\ P_{21} & P_{22} & \dots & P_{28} \\ . & . & \dots & . \\ . & . & \dots & . \\ . & . & \dots & . \\ P_{81} & P_{82} & \dots & P_{88} \end{bmatrix} = \frac{1}{2} \begin{bmatrix} 1001 & 0000 \\ 0000 & 0110 \\ 1001 & 0000 \\ 0000 & 0110 \\ 0110 & 0000 \\ 0000 & 1001 \\ 0110 & 0000 \\ 0000 & 1001 \end{bmatrix} \quad (7.1.23c)$$

Let the equivalent baseband component $y'_I(t)$ (or $y'_Q(t)$) be represented by

$$y'_I(t) = \sum_{n=-\infty}^{+\infty} q(t_n) \quad (7.1.24)$$

where $q(t_n)$ is the waveshape of $y'_I(t_n)$ in each symbol interval $-\frac{T_s}{2} \leq t_n \leq \frac{T_s}{2}$. Based on Eqs. (7.1.2b), (7.1.15a) and (7.1.22a,b,c,d) the possible waveshapes of (t_n) are

$$v_1(t_n) = -v_{16}(t_n) = \frac{C' s_e(t_n)}{\sqrt{s_e^2(t_n) + s_1'^2(t_n)}} \quad (7.1.25a)$$

$$v_2(t_n) = -v_{15}(t_n) = \frac{C s_e(t_n)}{\sqrt{s_e^2(t_n) + s_2'^2(t_n)}} \quad (7.1.25b)$$

$$v_3(t_n) = -v_{14}(t_n) = \frac{C s_e(t_n)}{\sqrt{s_e^2(t_n) + s_3'^2(t_n)}} \quad (7.1.25c)$$

$$v_4(t_n) = v_{13}(t_n) = \frac{C s_e(t_n)}{\sqrt{s_e^2(t_n) + s_3'^2(t_n)}} \quad (7.1.25d)$$

$$v_5(t_n) = v_{12}(t_n) = \frac{C s_o(t_n)}{\sqrt{s_o^2(t_n) + s_1'^2(t_n)}} \quad (7.1.25e)$$

$$v_6(t_n) = -v_{11}(t_n) = \frac{C s_o(t_n)}{\sqrt{s_o^2(t_n) + s_2'^2(t_n)}} \quad (7.1.25f)$$

$$v_7(t_n) = -v_{10}(t_n) = \frac{s_o(t_n)}{\sqrt{s_o^2(t_n) + s_3'^2(t_n)}} \quad (7.1.25g)$$

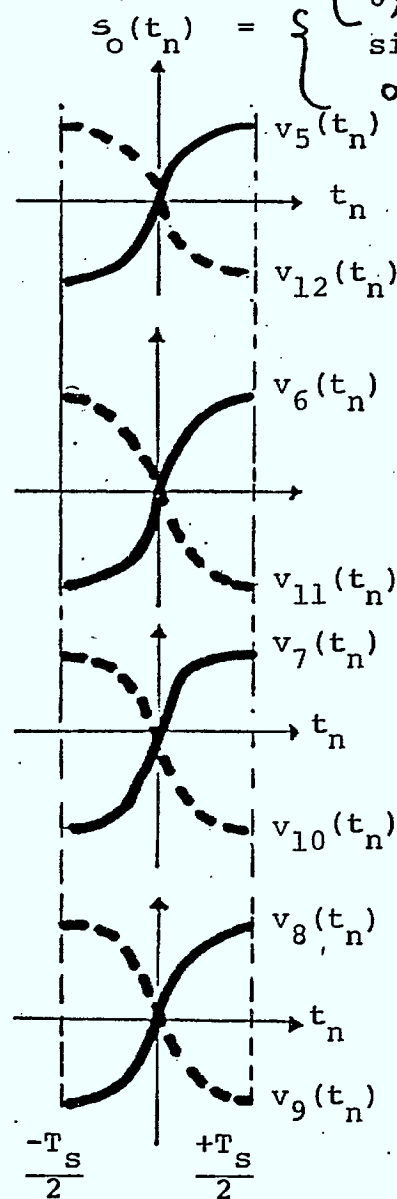
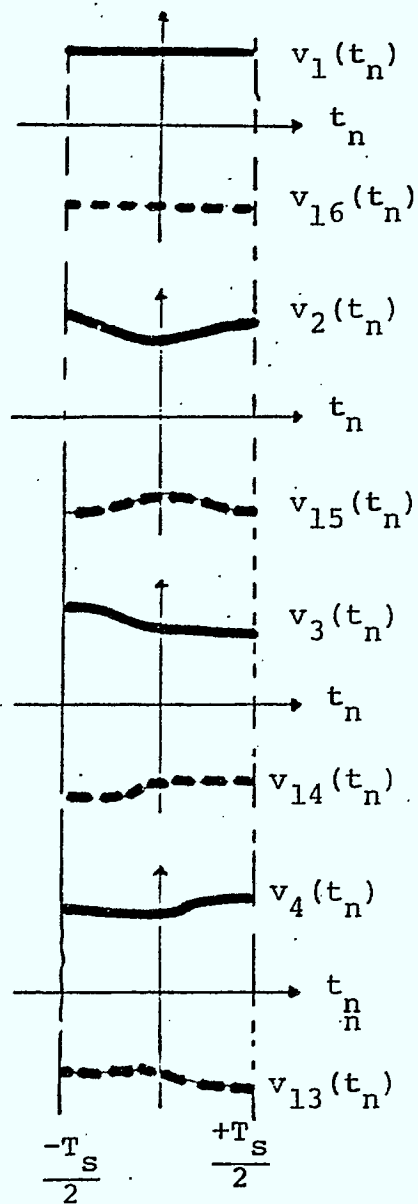
$$v_8(t_n) = -v_9(t_n) = \frac{s_o(t_n)}{\sqrt{s_o^2(t_n) + s_4'^2(t_n)}} \quad (7.1.25h)$$

An example of a waveshape $v_i(t_n)$'s, $i=1,2,\dots,16$ is illustrated in Fig. 7.1.16.

Fig.7.1.16 An example of the waveshapes $v_i(t_n)$, $i=1, 2, \dots, 16$

$$\text{with } s_e(t_n) = \begin{cases} 1, & -T_s/2 \leq t_n \leq +T_s/2 \\ 0, & \text{elsewhere} \end{cases}$$

$$s_o(t_n) = \begin{cases} \sin \frac{\pi t_n}{T_s}, & -T_s/2 \leq t_n \leq +T_s/2 \\ 0, & \text{elsewhere} \end{cases}$$



In each symbol interval, $q(t_n)$ is chosen from the set $\{v_i(t_n), i=1,2,\dots,16\}$. The waveshape of $q(t_n)$ is dependent on the waveshape of the previous $q(t_{n-1})$ and $y_I(t_n)$ and $y_Q(t_n)$. The stationary probabilities

$$p_i = P \{q(t_n) = v_i(t_n)\}, \quad i=1, 2, \dots, 16$$

and transition probabilities

$$p_{ik} = P \{q(t_n) = v_k(t_n) \mid q(t_{n-1}) = v_i(t_{n-1})\}, \\ i, k = 1, 2, \dots, 16,$$

can be obtained by investigating the encoding law of $y_I(t)$, $y_Q(t)$ and the construction of $v_i(t_n)$, $i=1, 2, \dots, 16$.

$$\begin{aligned} p_1 &= P \{q(t_n) = v_1(t_n)\} = P \{y_I(t_n) = s_1(t_n), y_Q(t_n) = \\ &\quad s'_1(t_n) \text{ or } s'_8(t_n)\} \\ &= P \{y_I(t_n) = s_1(t_n)\} \cdot [P \{y_Q(t_n) = s_1(t_n)\} + P \{y_Q(t_n) = \\ &\quad s'_8(t_n)\}] \\ &= \frac{1}{4} \cdot \left(\frac{1}{8} + \frac{1}{8}\right) = \frac{1}{16} \end{aligned}$$

since $y_I(t_n)$ and $y_Q(t_n)$ are statistically independent.

Other p_i , $i=1, 2, \dots, 16$ can be obtained in the similar manner and

$$p_i = \frac{1}{16}, \quad i = 1, 2, \dots, 16 \quad (7.1.26a)$$

$$P_{11} = P\{q(t_n) = v_1(t_n) \mid q(t_{n-1}) = v_1(t_{n-1})\}$$

$$P\{y_I(t_n) = s_1(t_n), y_Q(t_n) = s'_1(t_n) \text{ or } s'_8(t_n) \mid y_I(t_{n-1}) = s_1(t_{n-1}), y_Q(t_{n-1}) = s'_1(t_{n-1})$$

$$\text{or } s'_8(t_{n-1})\}$$

$$= P\{y_I(t_n) = s_1(t_n) \mid y_I(t_{n-1}) = s_1(t_{n-1})\}$$

$$\cdot [P\{y_Q(t_n) = s'_1(t_n) \text{ or } s'_8(t_n) \mid y_Q(t_{n-1}) = s'_1(t_{n-1})$$

$$\text{or } s'_8(t_{n-1})\}]$$

$$= \frac{1}{2} \cdot \left[\frac{1}{2}\right] = \frac{1}{4}$$

Other P_{ik} 's, $i, k=1, 2, \dots, 16$ are obtained in the same manner. They are arranged as entries of the transition matrix P

$$P = \begin{bmatrix} P_{11} & P_{12} & \dots & P_{1,16} \\ P_{21} & P_{22} & \dots & P_{2,16} \\ \cdot & \cdot & \dots & \cdot \\ \cdot & \cdot & \dots & \cdot \\ P_{16,1} & P_{16,2} & \dots & P_{16,16} \end{bmatrix} = \frac{1}{4} \begin{bmatrix} 1001 & 0000 & 0000 & 1001 \\ 0110 & 0000 & 0000 & 0110 \\ 1001 & 0000 & 0000 & 1001 \\ 0110 & 0000 & 0000 & 0110 \\ 0000 & 1001 & 1001 & 0000 \\ 0000 & 0110 & 0110 & 0000 \\ 0000 & 1001 & 1001 & 0000 \\ 0000 & 0110 & 0110 & 0000 \\ 1001 & 0000 & 0000 & 1001 \\ 0110 & 0000 & 0000 & 0110 \\ 1001 & 0000 & 0000 & 1001 \\ 0110 & 0000 & 0000 & 0110 \\ 0000 & 1001 & 1001 & 0000 \\ 0000 & 0110 & 0110 & 0000 \\ 0000 & 1000 & 1001 & 0000 \\ 0000 & 0110 & 0110 & 0000 \end{bmatrix} \quad (7.1.26b)$$

The statistical description of the signal $y_1'(t)$ can be represented by a 16-state Markov chain model as shown in Fig. 7.1.17. Its PSD function is given by [7].

$$Y(f) = \frac{1}{T_s^2} \sum_{n=-\infty}^{+\infty} \left| \sum_{i=1}^{16} p_i v_i \left(\frac{n}{T_s} \right) \right|^2 \delta \left(f - \frac{n}{T_s} \right) + \frac{1}{T_s} \sum_{i=1}^{16} p_i \left| v_i(f) \right|^2$$

$$+ \frac{2}{T_s} \operatorname{Re} \left\{ \sum_{i=1}^{16} \sum_{k=1}^{16} p_i V_i^*(f) V_k(f) V_{ik} \right\} \quad (7.1.27)$$

where $V_i(f)$ is the Fourier transform of $v_i(t)$, $i=1,2,\dots,16$
 $V_i^*(f)$ is the complex conjugate of $V_i(f)$,

$$V_{ik} = \sum_{n=1}^{\infty} P_{ik}^{(n)} e^{-j2\pi n f T_s},$$

$P_{ik}^{(h)}$ is the ik^{th} entry in the matrix P^n ,

$$P^n = \underbrace{P \times P \times \dots \times P}_{n \text{ times}}$$

and

$\operatorname{Re}\{\dots\}$ is the real part of $\{\dots\}$

Note that

$$P^n = \frac{1}{16} \begin{bmatrix} 1111 & 1111 & 1111 & 1111 \\ 1111 & 1111 & 1111 & 1111 \\ 1111 & 1111 & 1111 & 1111 \\ . & . & . & . \\ . & . & . & . \\ . & . & . & . \\ 1111 & 1111 & 1111 & 1111 \end{bmatrix} \quad \text{for } n=2,3,\dots$$

$$V_{ik} = P_{ik} e^{-j2\pi f T_s} + \frac{1}{16} \sum_{n=2}^{+\infty} e^{-j2\pi n f T_s} \quad (7.1.28a)$$

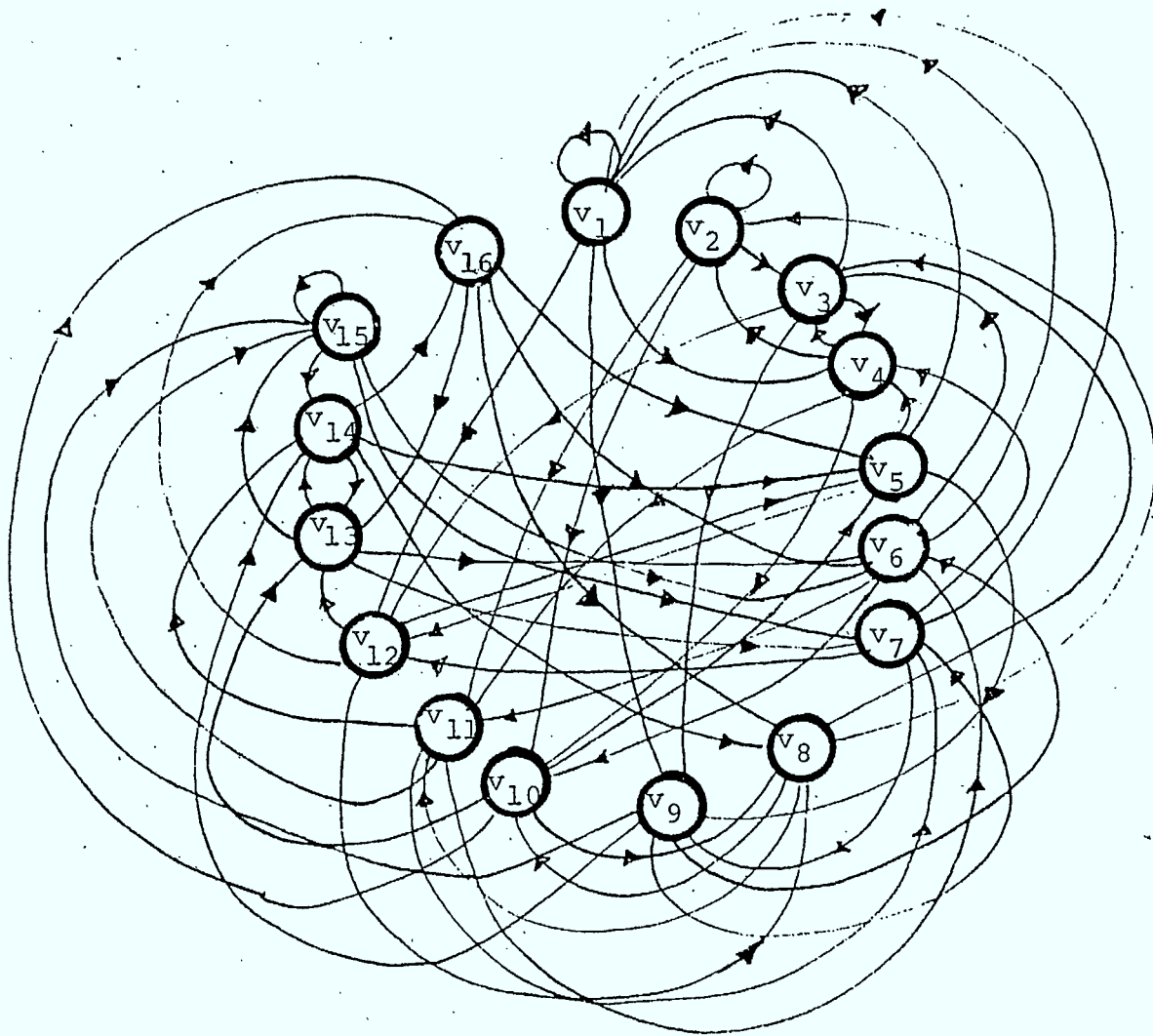


Fig. 7.1.17 16-state transition diagram
of the baseband component
of the hardlimited IJF-QPSK
signal

and

$$V_1(f) = -V_{16}(f) \quad (7.1.28b)$$

$$V_2(f) = -V_{15}(f) \quad (7.1.28c)$$

$$V_3(f) = -V_{14}(f) \quad (7.1.28d)$$

$$V_4(f) = -V_{13}(f) \quad (7.1.28e)$$

$$V_5(f) = -V_{12}(f) \quad (7.1.28f)$$

$$V_6(f) = -V_{11}(f) \quad (7.1.28g)$$

$$V_7(f) = -V_{10}(f) \quad (7.1.28h)$$

$$V_8(f) = -V_9(f) \quad (7.1.28i)$$

Substituting Eqs. (7.1.26a,b) and (7.1.28a to i) into Eq.(7.1.27) yields

$$\begin{aligned} Y(f) = \frac{1}{8T_s} \sum_{i=1}^8 |V_i(f)|^2 + \frac{1}{32} \operatorname{Re} \{ & [(V_1(f) + V_3(f) + V_5(f) + V_7(f))^* \\ & \cdot (V_1(f) + V_4(f) - V_5(f) - V_8(f)) + (V_2(f) + V_4(f) + V_6(f) + V_8(f))^* \\ & \cdot (V_2(f) + V_3(f) - V_6(f) - V_7(f))] e^{-j2\pi f T_s} \} \end{aligned} \quad (7.1.29a)$$

Based on Eq.(7.1.11) the normalized PSD function of the hardlimited IJF-OQPSK signal is

$$\begin{aligned} Z_{IJF-OQPSK}^h(x) \approx Z_0 \{ & 4 \sum_{i=1}^8 |V_i(x)|^2 \\ & + \operatorname{Re} \{ [(V_1(x) + V_3(x) + V_5(x) + V_7(x))^* \\ & \cdot (V_1(x) + V_4(x) - V_5(x) - V_8(x)) \\ & + (V_2(x) + V_4(x) + V_6(x) + V_8(x))^* \\ & \cdot (V_2(x) + V_3(x) - V_6(x) - V_7(x))] e^{-j2\pi x} \} \} \end{aligned} \quad (7.1.29b)$$

where Z_0 is a normalizing coefficient chosen such that

$$Z_{\text{IJF-QOSPK}}^h(0) = 1$$

and

$$x = (f - f_c) T_s$$

Equations (7.1.21b) and (7.1.29b) represent the power spectral density functions of the hardlimited IJF-QPSK and IJF-OQPSK signals respectively. Figures 7.1.18 and 7.1.19 illustrate the power spectrum spreading of hardlimited IJF-QPSK and IJF-OQPSK signals respectively. It is shown that the spectrum spreading of the hardlimited OQPSK signal is much less than that of the hardlimited QPSK. Measured spectrum spreading of the hardlimited IJF quadrature modulated signals are shown in Fig. 7.1.20. They are in agreement with the theoretical prediction (Figs. 7.1.18 and 7.1.19). As indicated in Fig. 7.1.21 the IJF-OQPSK modulation technique has significant spectral advantages over QPSK, OQPSK and MSK in nonlinear channels.

Figure 7.1.22a shows a computer simulation model which is used to evaluate the performance of the hardlimited IJF-OQPSK modems with $s(t) = \frac{1}{2}(1 + \cos \frac{\pi t}{T_s})$. The P_e performance degradation versus the values of α of the receive filter is shown in Figure 7.1.22b.

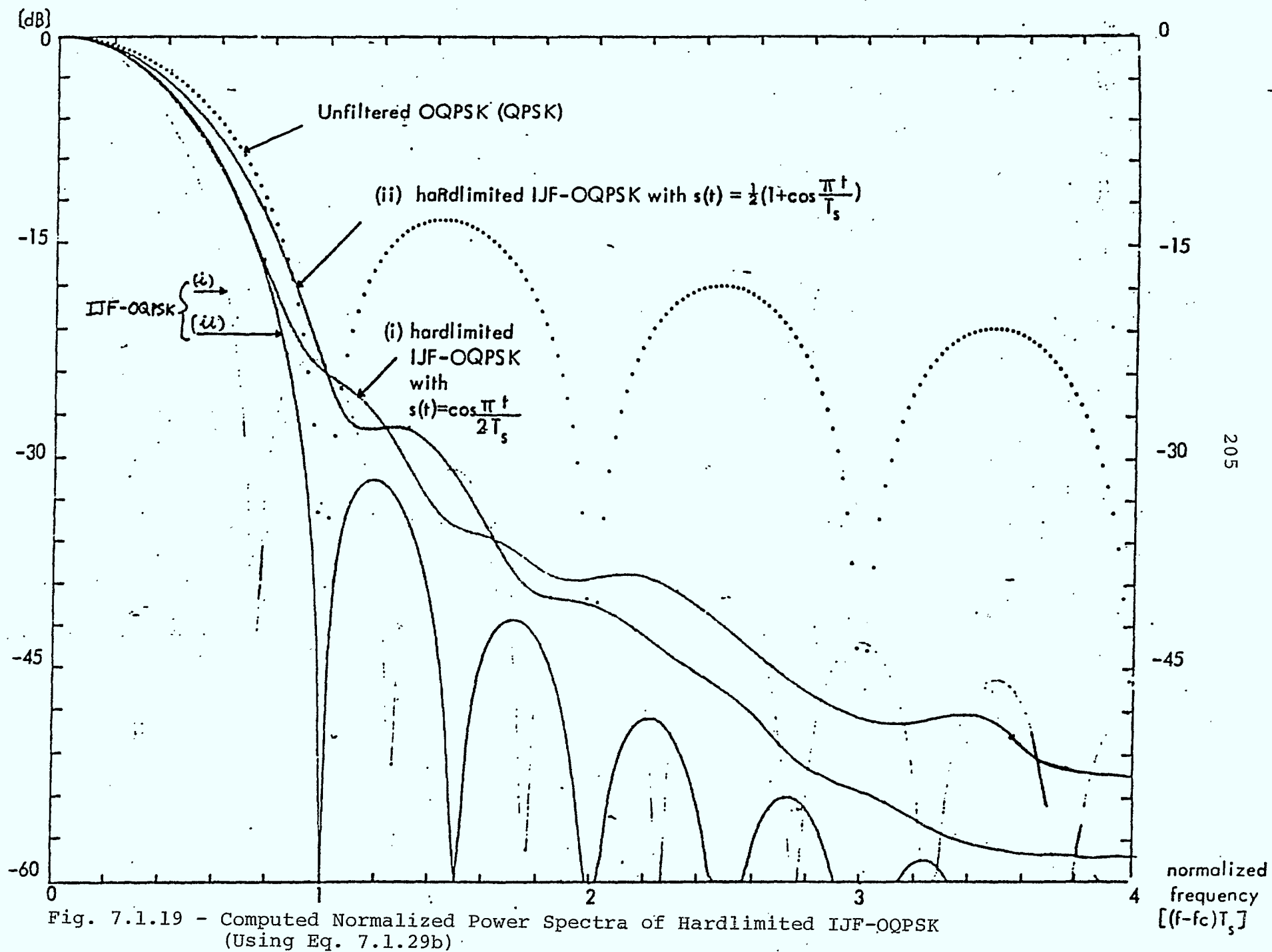
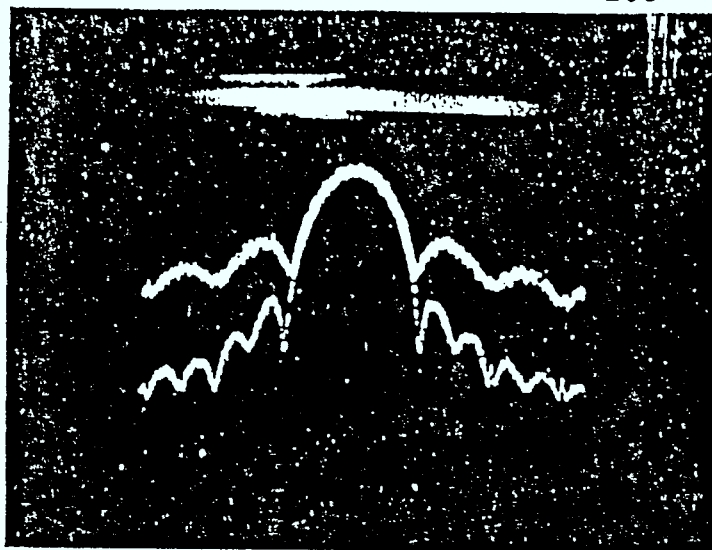


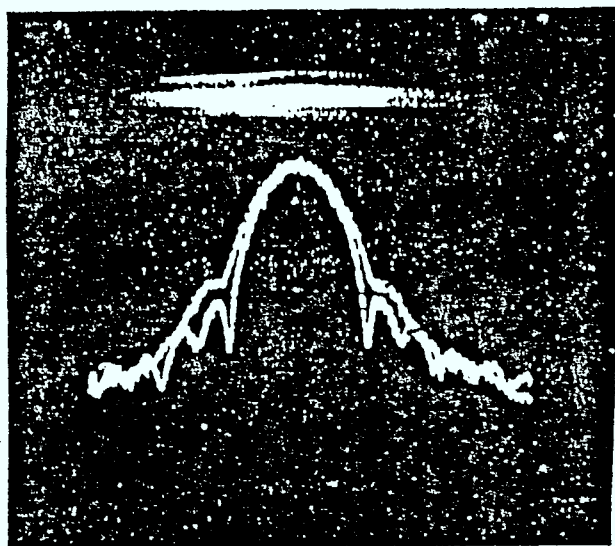
Fig. 7.1.19 - Computed Normalized Power Spectra of Hardlimited IJF-OQPSK
 (Using Eq. 7.1.29b)



Hardlimited IJF-QPSK

IJF-QPSK

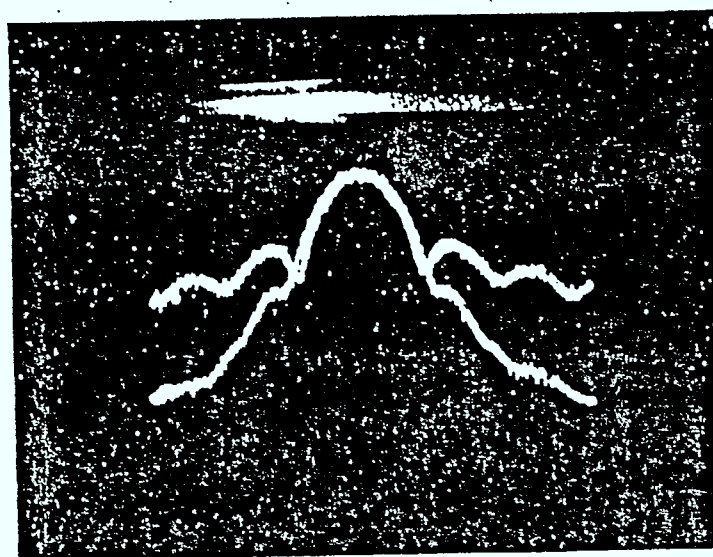
(a) IJF-QPSK



Hardlimited IJF-OQPSK

IJF-OQPSK

(b) IJF-OQPSK



Hardlimited IJF-QPSK

Hardlimited IJF-OQPSK

(c) Comparison of hardlimited
IJF-QPSK and IJF-OQPSK
signals

Fig.7.1.20 Measured power spectra of the
hardlimited IJF-QPSK and IJF-OQPSK
signals (bit rate: 64 kb/s, carrier: 512 kHz)

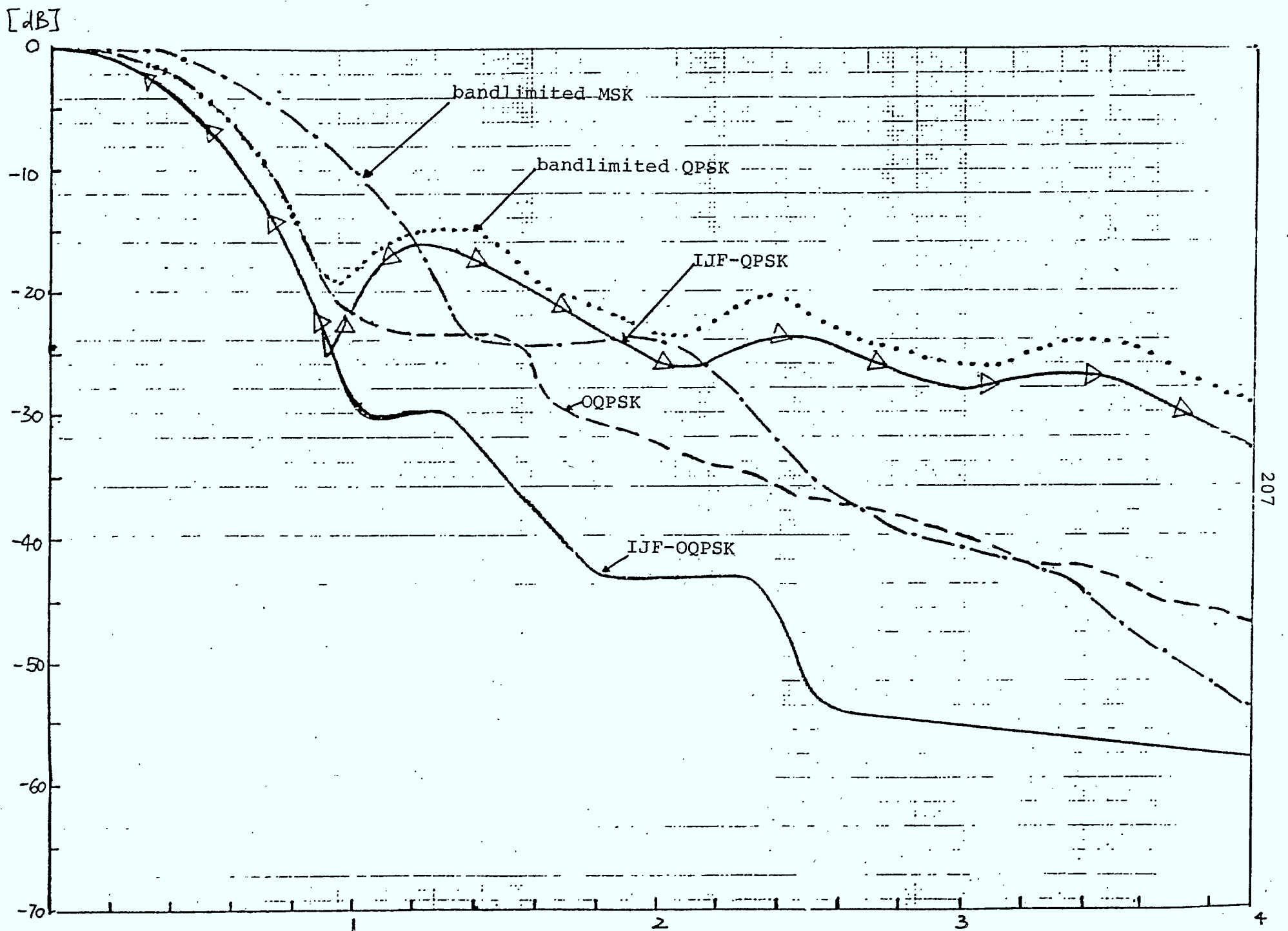
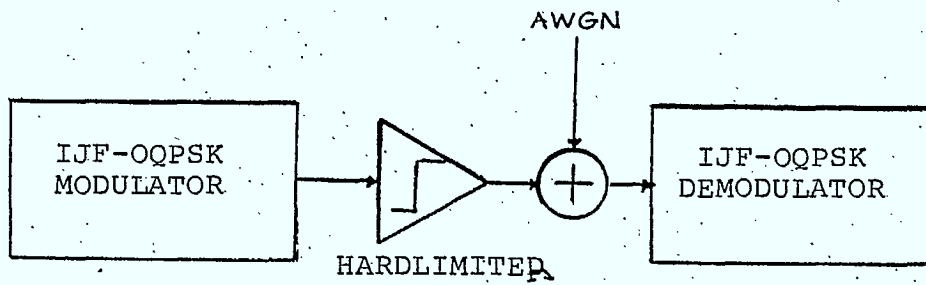
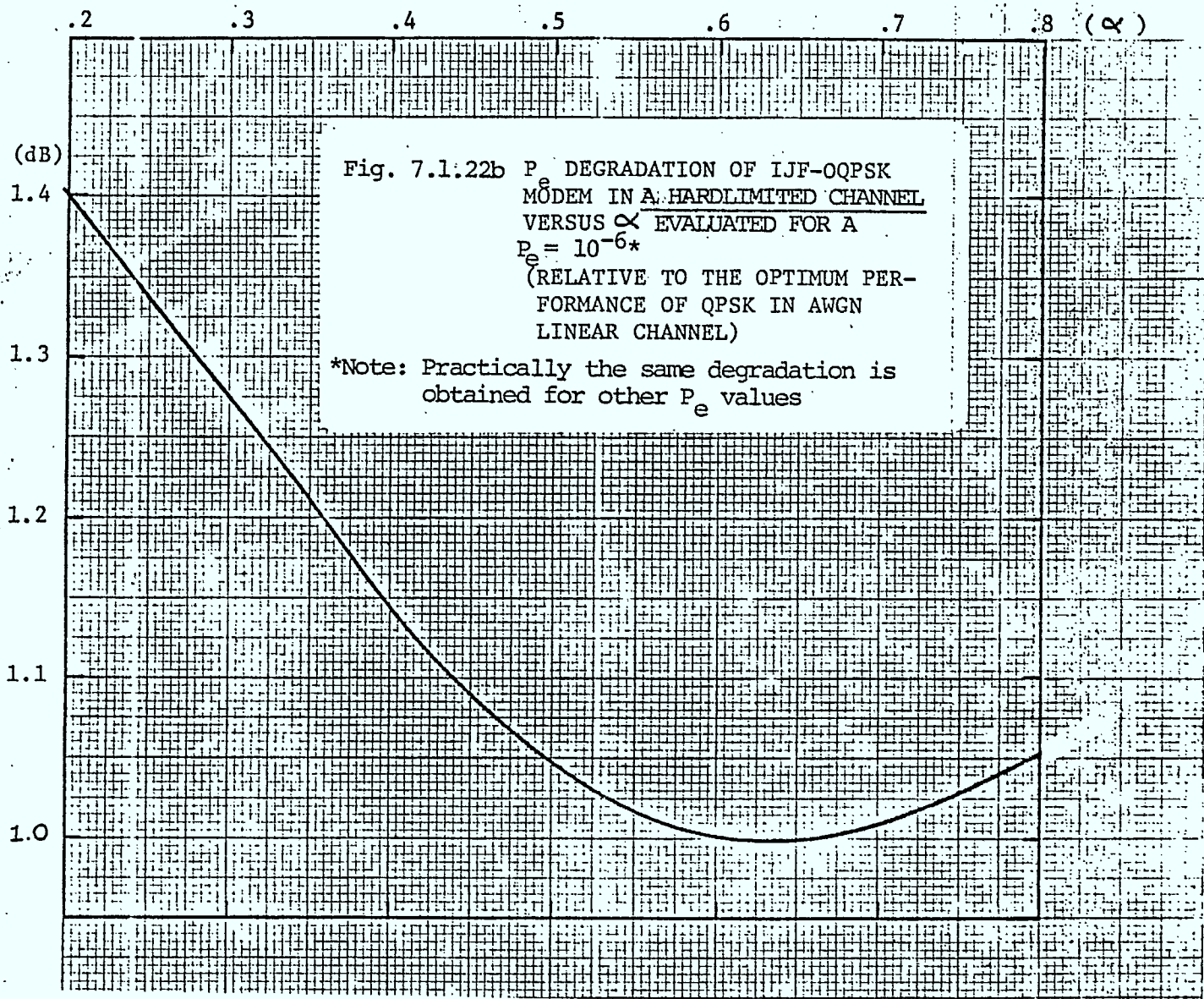


Fig. 7.1.21 Measured power spectra of hardlimited IJF-QPSK, IJF-OQPSK, and bandlimited QPSK, OQPSK, MSK



(a) A Hardlimited Channel

Fig. 7.1.22a. Model of IJF-QPSK modem in a bandlimited AWGN channel.



7.1.5 Potential Applications of the IJF-OQPSK Modulation Technique to Onboard Regenerative Satellite Systems

The low spectral spreading advantage and almost negligible P_e degradation results presented in the previous section encourage the applications of the IJF-OQPSK modulation techniques to regenerative satellite systems. In this section, the spectral spreading and P_e performance of the IJF-OQPSK modems in conventional cascaded nonlinear channels and in regenerative satellite links are studied and compared to those of the conventional QPSK, using a computer simulation.

a. Spectral Spreading and P_e Performance of the IJF-OQPSK Modem in Conventional Cascaded Nonlinear Channels

Figures 7.1.23 a and b illustrate the simulation models of a conventional satellite link using IJF-OQPSK and QPSK modems respectively.

The characteristics of the earth-station HPA, transponder TWTA, input and output MUX filters recommended in the INTELSAT V-TDMA system specifications [8] are used in the simulation. The AM/AM and AM/PM conversion characteristics of the HPA and TWTA are illustrated in Fig. 7.1.24. In accordance with the recommended INTELSAT-V satellite simulator model we assume a negligible uplink noise.

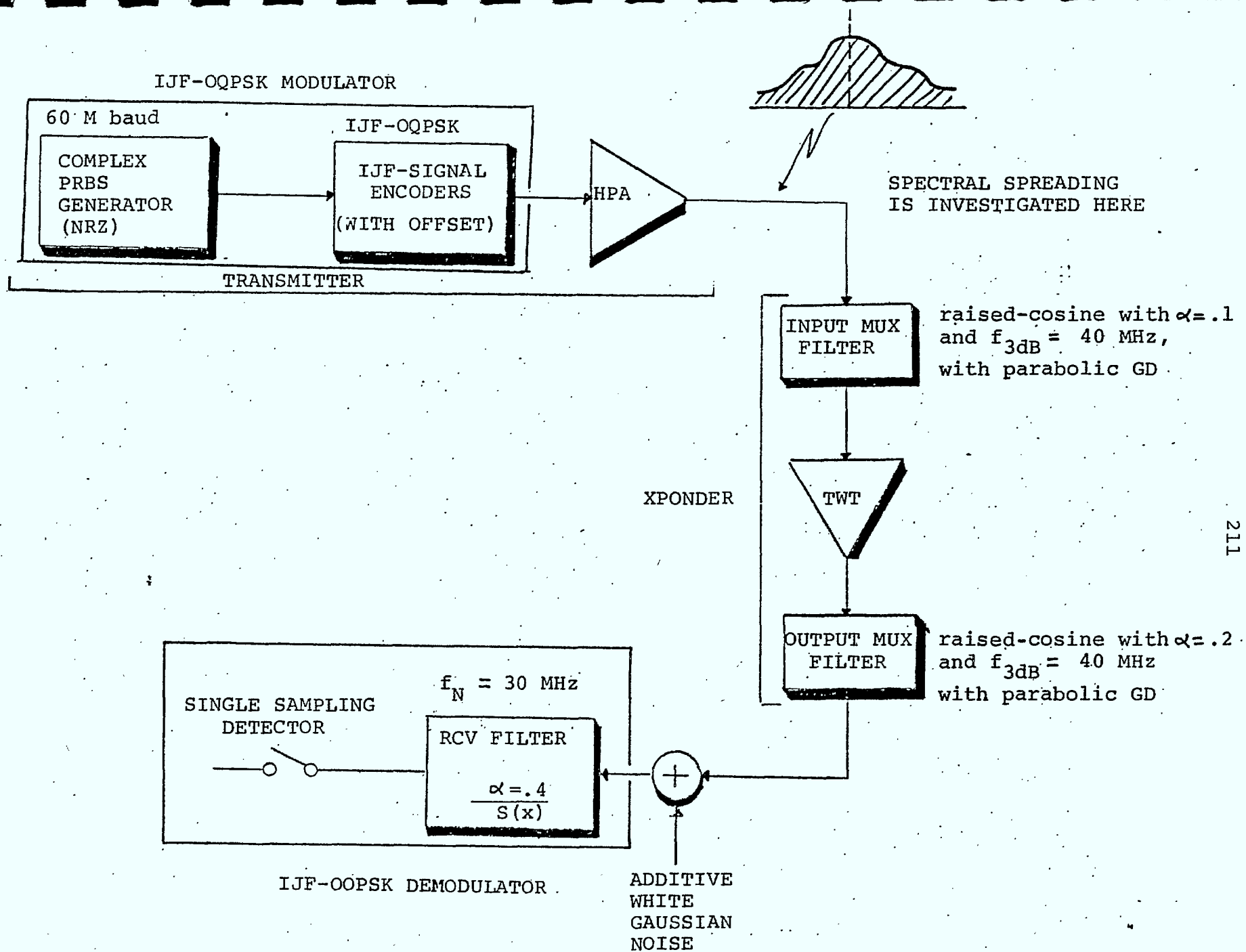


Fig. 7.1.23a COMPUTER SIMULATION MODEL OF A CONVENTIONAL SATELLITE LINK USING IJF-OQPSK MODEMS

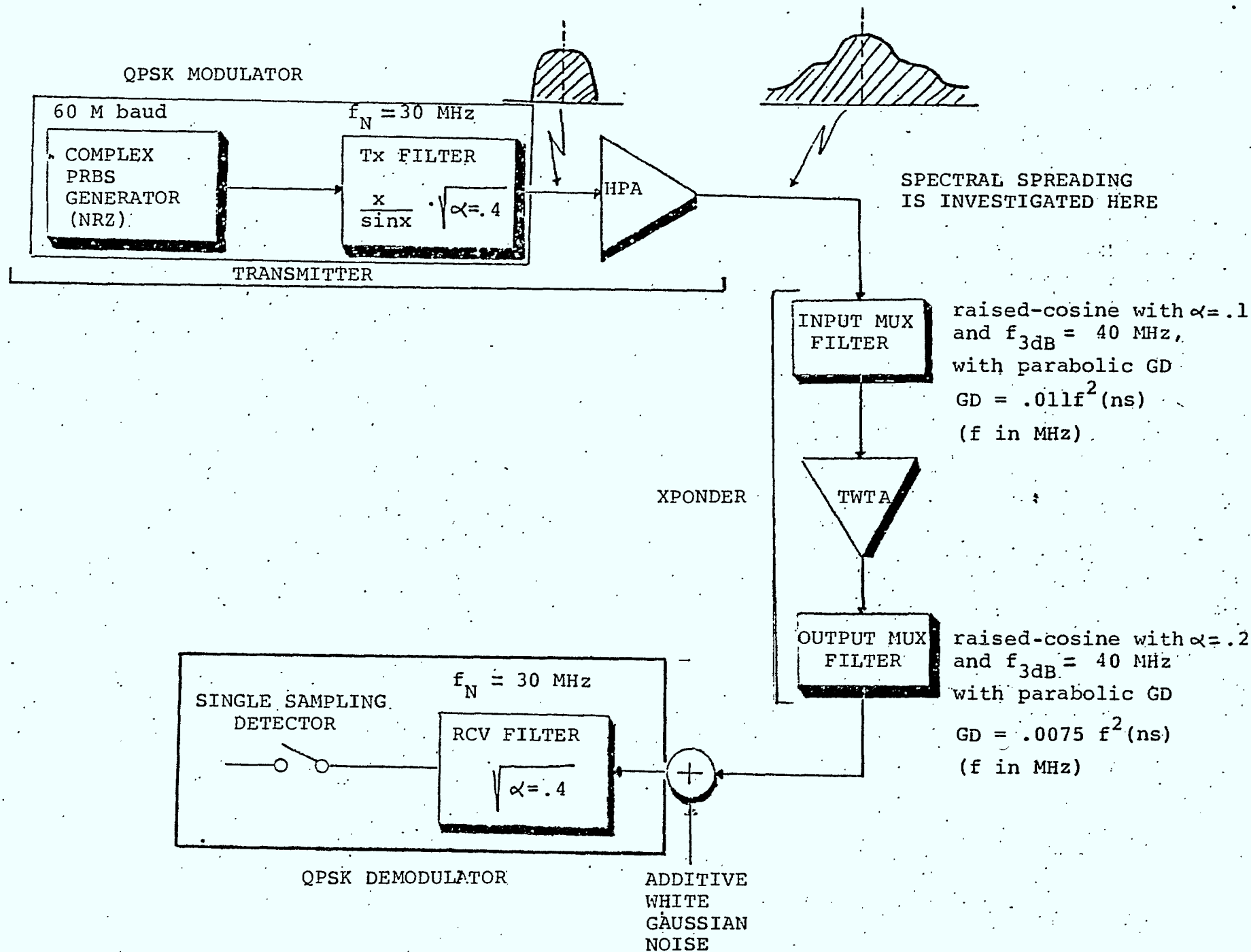


Fig. 7.1.23b Computer Simulation Model of a Conventional Satellite Link With QPSK Modem

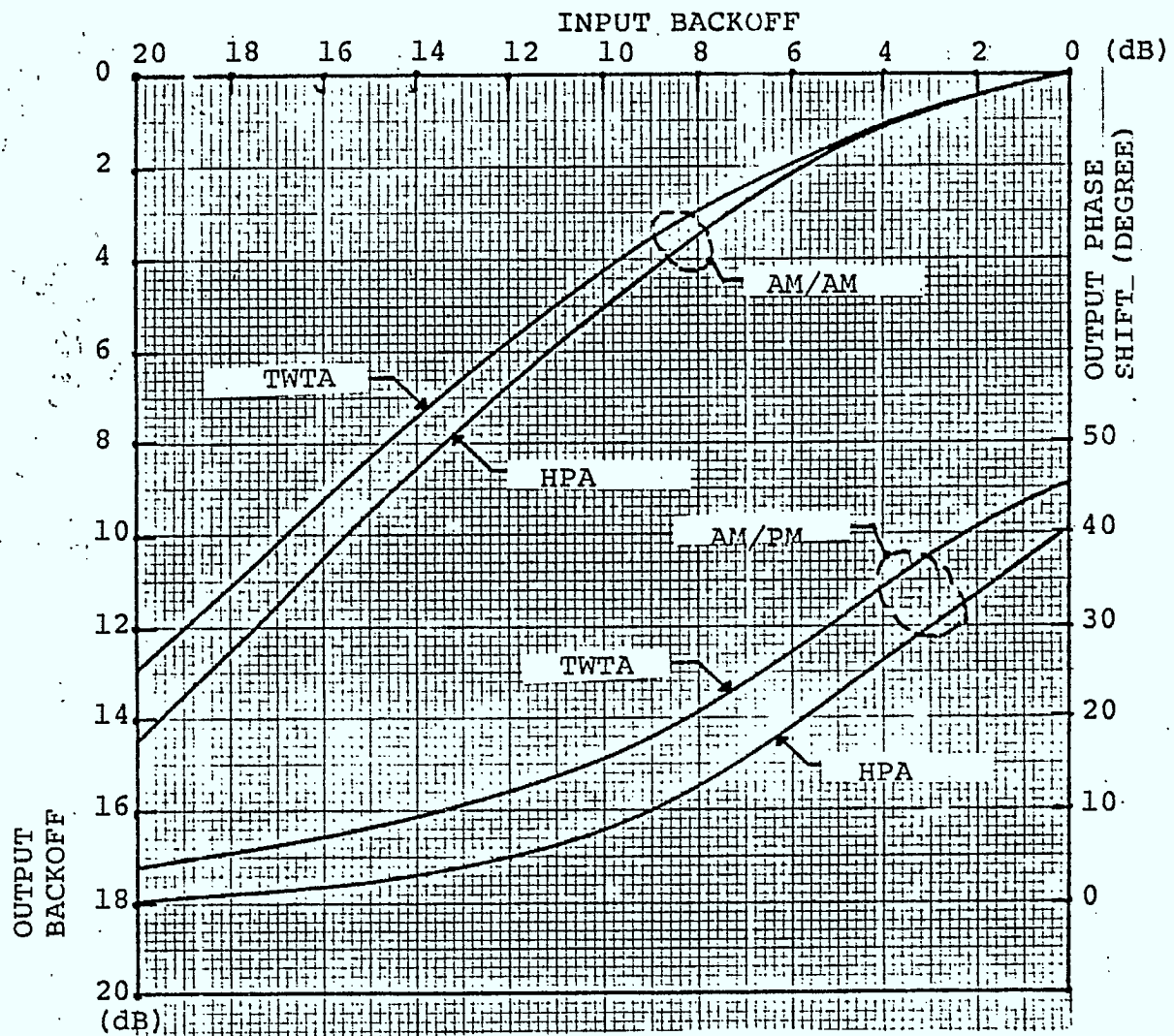


Fig. 7.1.24 NONLINEAR CHARACTERISTICS OF HPA AND TWTA

In the simulation of the conventional satellite link using IJF-OQPSK modems, the IJF baseband double-interval pulse is

$$s(t) = \frac{1}{2}(1 + \cos \frac{\pi t}{T_s}), \quad -T_s \leq t \leq T_s$$

and the receive filter used in the IJF-OQPSK demodulator is

$$F_R(f) = \frac{R(f)}{S(f)}$$

where $S(f)$ is the Fourier transform of $s(t)$ and $R(f)$ is raised-cosine filter with $\alpha=0.4$

In the simulation of the conventional satellite link using QPSK modems, the transmit filter is

$$T_X(f) = \frac{\pi f T_s}{\sin[\pi f T_s]} \cdot \sqrt{R(f)}$$

and the receive filter is

$$R_X(f) = \sqrt{R(f)}$$

where $T_s = \frac{1}{60 \text{ MHz}}$

(i) Spectral spreading

Prior to the earth station HPA, the QPSK signal is bandlimited while the IJF-OQPSK signal has an infinite bandwidth. The envelope of the QPSK signal has

much more fluctuation than that of IJF-OQPSK, hence the bandlimited QPSK signal is more sensitive to the AM/AM and AM/PM effects of the HPA than the IJF-QPSK.

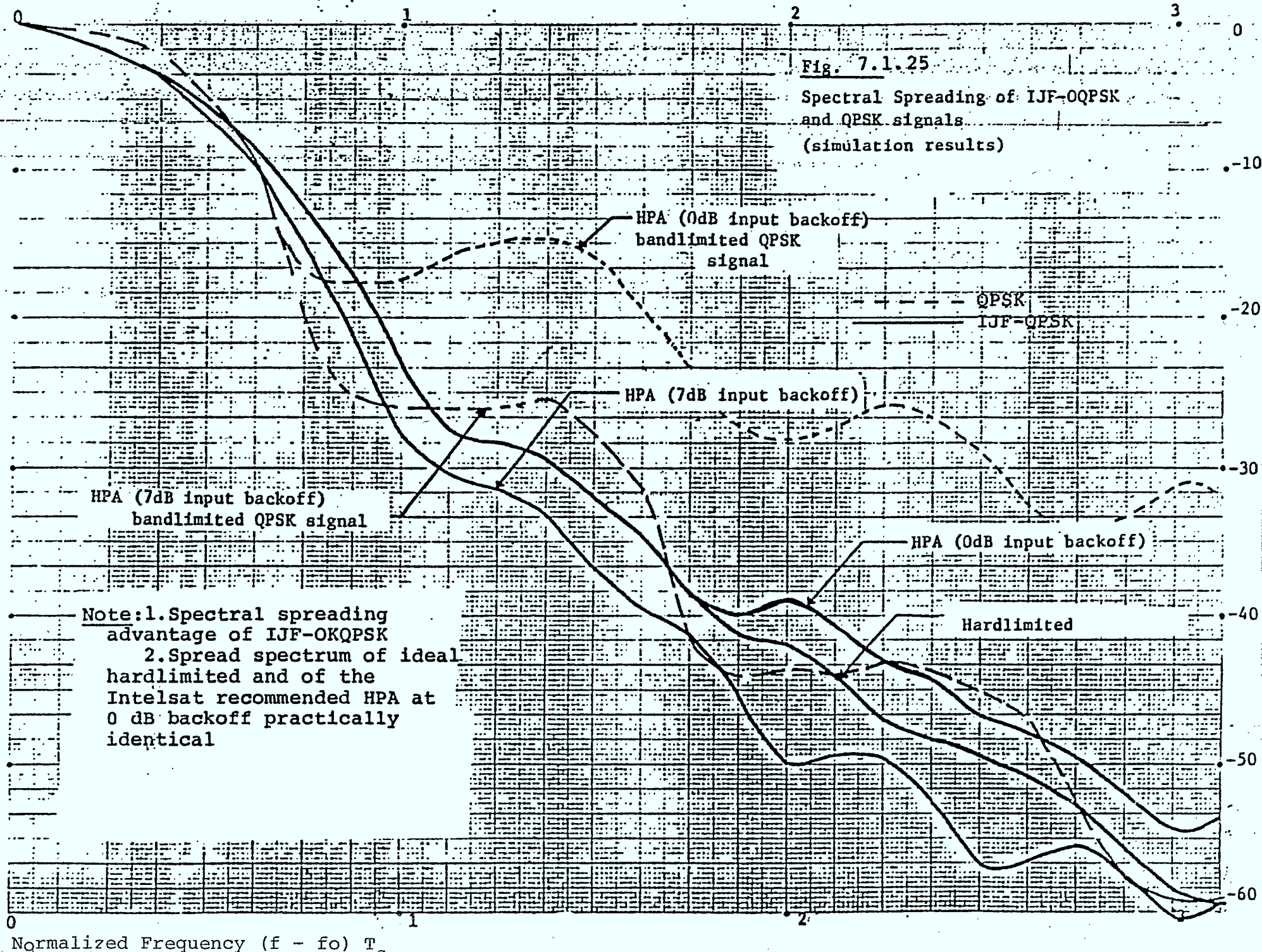
Consequently the spectral regrowth of the bandlimited QPSK at the output of the HPA is higher than that of IJF-OQPSK when the HPA operates in a nonlinear region. Figure 7.1.25 shows the spectral spreading of the transmitted IJF-OQPSK and QPSK signals at the output of the HPA with different HPA input backoffs. It is clearly shown that the IJF-OQPSK signal has much less spectral spreading than the bandlimited QPSK, specially when the HPA operates in saturation mode (0 dB backoff). It is also noted that the power spectra of the hardlimited and saturated (i.e. amplified by an HPA having 0 dB backoff) IJF-OQPSK signals are approximately equal.

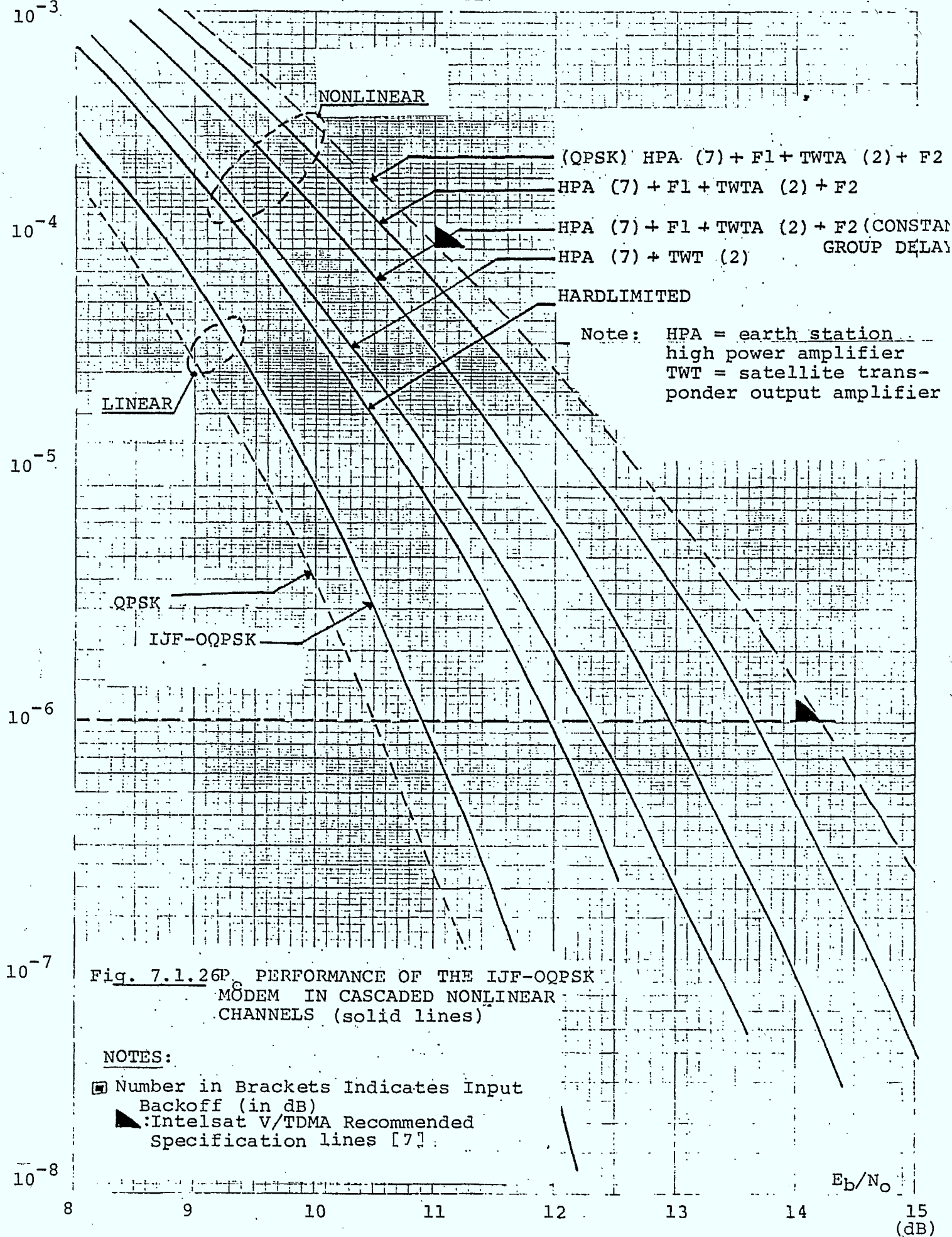
(ii) P_e performance:

The combined effect of the AM/AM and AM/PM nonlinearities with the imperfect amplitude and group delay characteristics of the input/output transponder MUX filters introduce a degradation in the P_e performance of the IJF-OQPSK. Figure 7.1.26 illustrates the simulation results on the P_e performance of the IJF-OQPSK modem with different combinations of the satellite transmission link. The degradation due to AM/AM and AM/PM conversion effects of the HPA and TWTA (curve HPA(7)-TWT(2)) is about 0.35 dB (at $P_e = 10^{-6}$) more than that due to an ideal hardlimiter, since the latter has no AM/PM effects. By introducing input and output transponder filters, the IJF-OQPSK signal

Fig. 7.1.25

Spectral Spreading of IJF-QPSK
and QPSK signals
(simulation results)



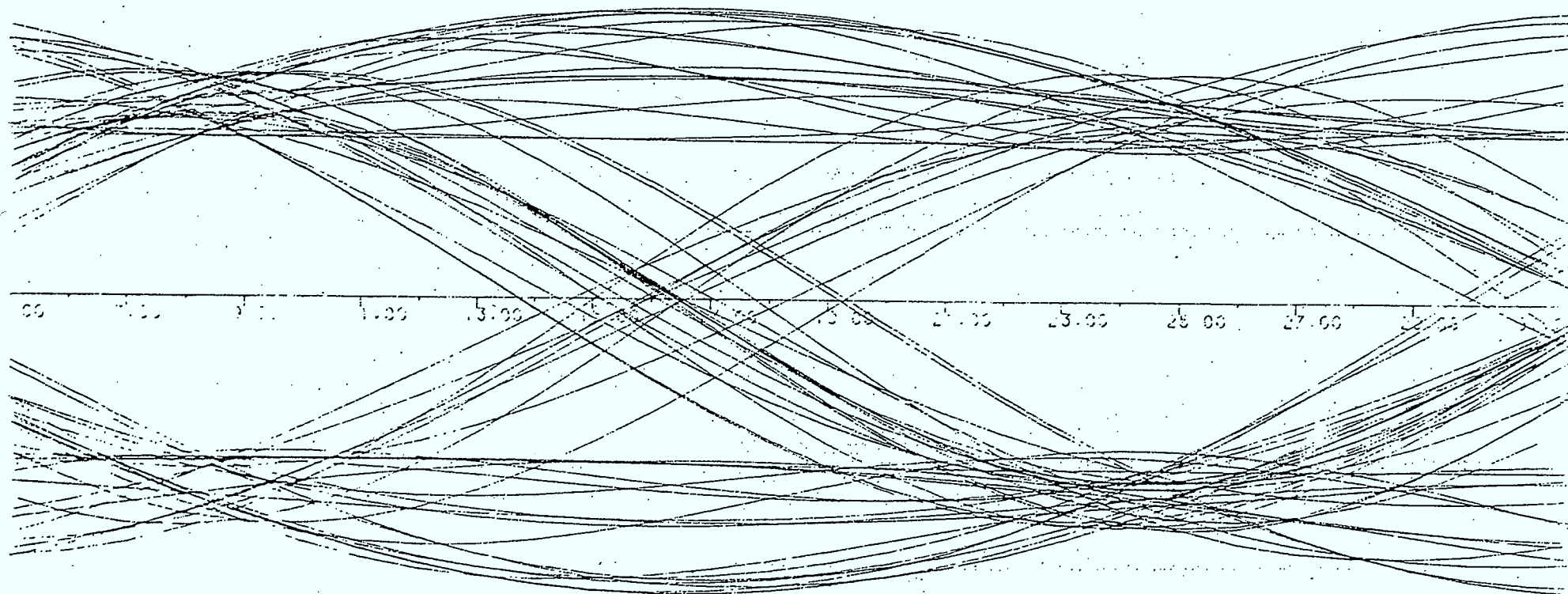


prior to the transponder TWTA exhibits and increased amplitude fluctuation. Therefore, it suffers more degradation due to AM/AM and AM/PM conversion effects of the TWTA. If constant group delay characteristics of MUX filters are assumed the P_e performance of the IJF-OQPSK is degraded by 0.65 dB (at $P_e = 10^{-6}$) relative to the case of no MUX filtering. If parabolic group delay characteristics of MUX filters are assumed, the P_e performance is degraded by 1.35 dB (at $P_e = 10^{-6}$) relative to the case of no MUX filtering. Since a negligible uplink noise is assumed the degradation in P_e performance is related to the increase of intersymbol interference in the received IJF-OQPSK signals prior to the single sampling detector as shown in Fig. 7.1.27. The P_e performance of the IJF-OQPSK modem is also compared to that of the QPSK in the same transmission link as illustrated in Fig. 7.1.26 (dotted lines). While in the linear channel the P_e performance of the IJF-OQPSK is 0.4 dB worse than that of the QPSK, the IJF-OQPSK shows a "gain" of 0.5 dB (at $P_e = 10^{-6}$) compared to QPSK in the bandlimited and cascaded nonlinear channel.

b. P_e performance of the IJF-OQPSK modem in a regenerative satellite link.

Figures 7.1.28 a and b show the simulation model of a regenerative satellite link using IJF-OQPSK or QPSK modem.

The HPA, TWTA, and filters have the same characteristics as in the simulation of conventional cascaded nonlinear channels. (i.e. specifications of



(B) NONLINEAR CHANNEL: HPA (7) + F1 + TWTA (2) + F2

Fig. 7.1.27 EYE DIAGRAMS OF RECEIVED IJF-QQPSK SIGNALS
IN LINEAR AND CASCADED NONLINEAR CHANNELS

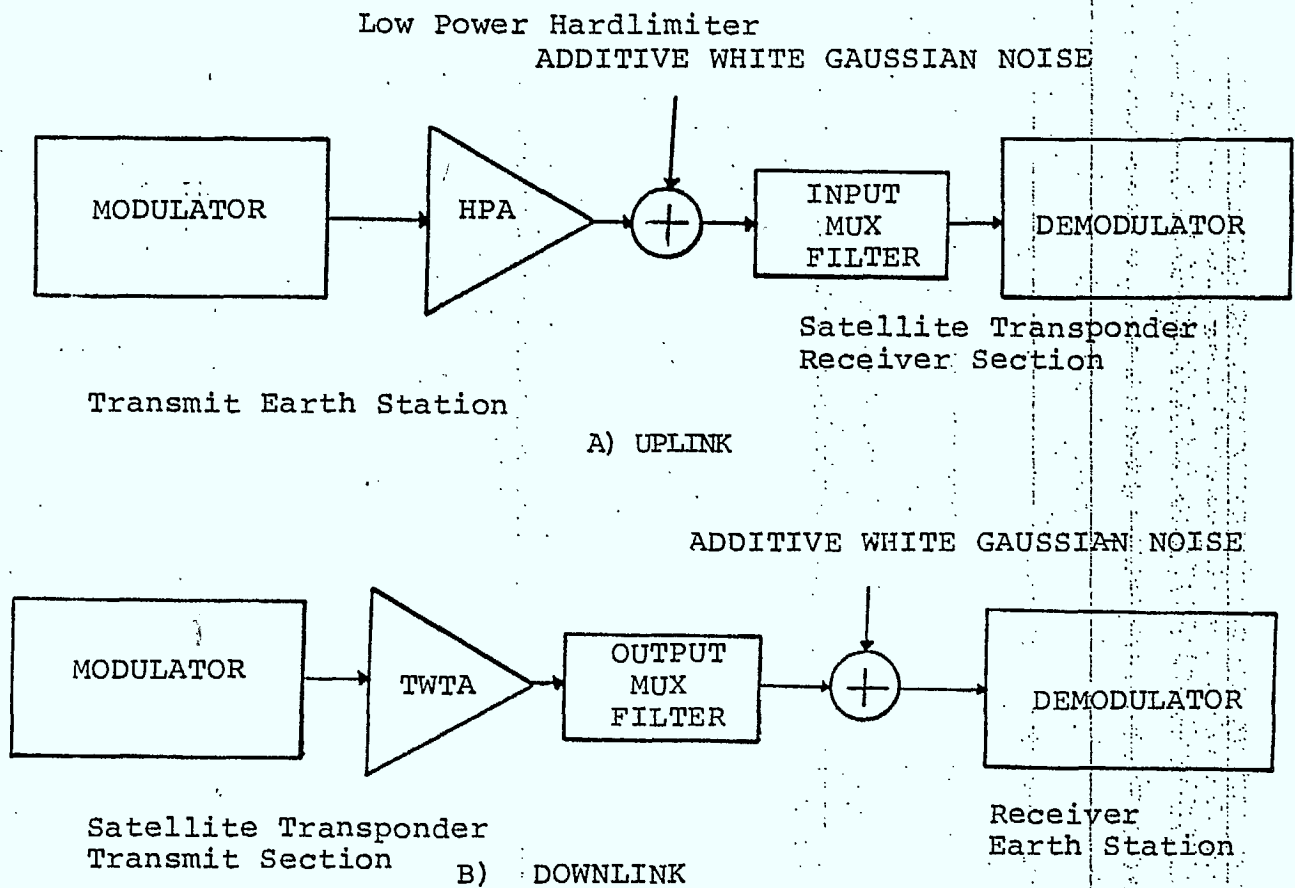


Fig. 7.1.28

MODEL OF A REGENERATIVE SATELLITE LINK

$P(e)$
 10^{-3}

221

10^{-4}

REGENERATIVE
SATELLITE
LINK

CONVENTIONAL SATELLITE
LINK

HPA (7) + TWTA (2)

(UPLINK NOISE IS
NEGLIGIBLE)

10^{-5}

DOWNLINK:
TWTA (0)

UPLINK:
HPA (0)

10^{-6}

2.15 dB

10^{-7}

FIG. 7.1.29a

P_e PERFORMANCE OF CONVENTIONAL AND
REGENERATIVE SATELLITE LINKS USING
IJF-OQPSK MODEMS

10^{-8}

E_b/N_o

8

9

10

11

12

13

14

15
(dB)

P(e)

 10^{-3} 10^{-4} 10^{-5} 10^{-6} 10^{-7} 10^{-8} REGENERATIVE
SATELLITE
LINKJJF-OQPSK
DOWNLINK only

TWT

JJF-OQPSK
UPLINK only
HPAQPSK WITH
HPA (0) - F1 - TWTA (2) - F2
Conventional linkIFF-QPSK
conventional
link

2.3 dB

FIG. 7.1.29b

PERFORMANCE OF HARDLIMITEDLJF-OQPSK MODEMS IN CONVENTIONAL
AND REGENERATIVE SATELLITE SYSTEMSLegend:

HPA: Earth Station HPA

TWT: Transponder TWT

F1: Input Mux Xponder Filter

F2: Output Mux Xponder Filter

Number in brackets indicates input
backoff [dB]▲: Intelsat V/TDMA Recommended
Specification E_b/N_0

(dB)

8 9 10 11 12 13 14 15

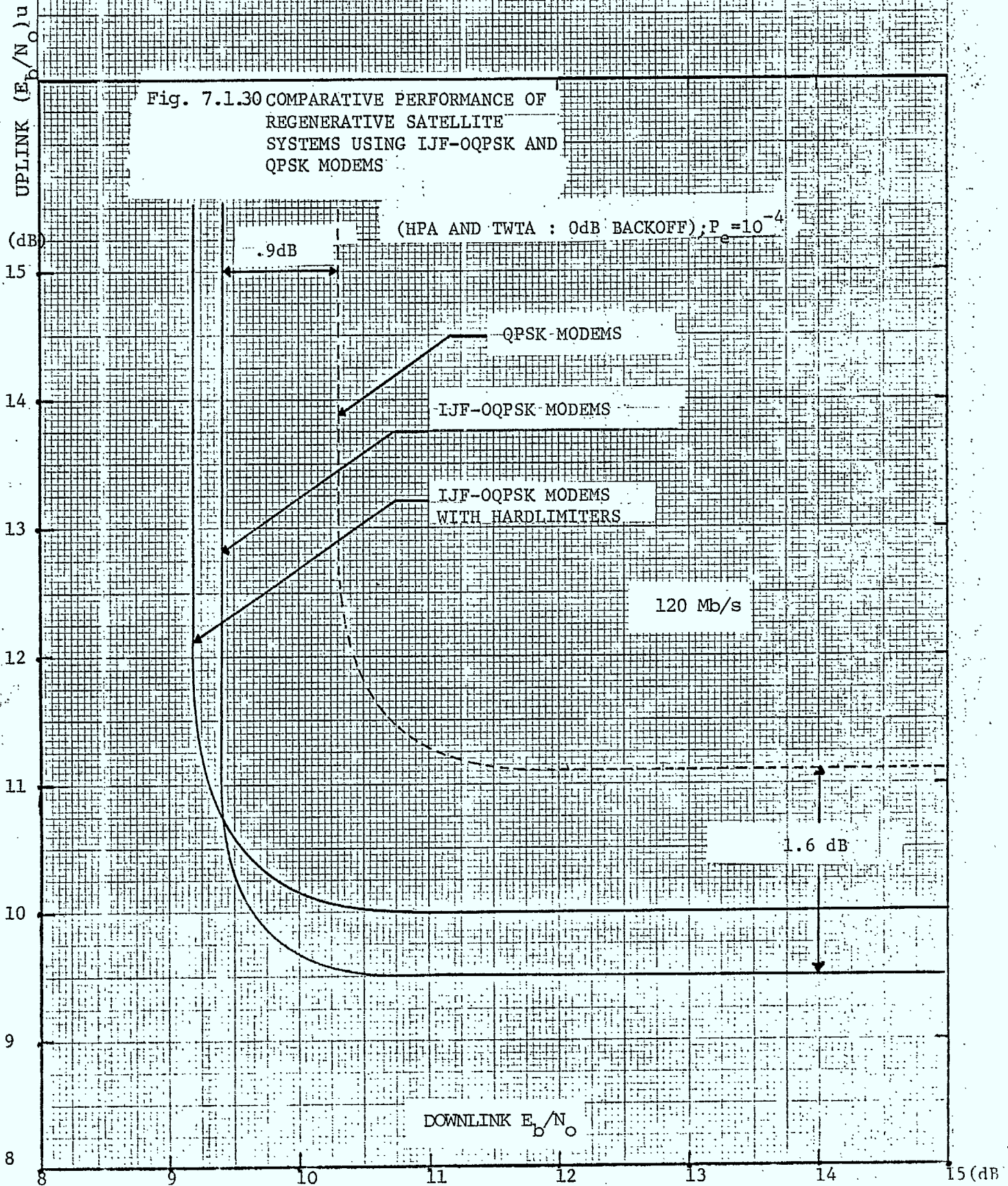
Intelsat V). The simulation results on the uplink and downlink P_e performance of the IJF-OQPSK modulation scheme are shown in Figs. 7.1.29 a and b. The regenerative satellite system introduces a P_e performance gain of 2.15 dB (at $P_e = 10^{-6}$) relative to the conventional satellite systems having the same IJF-OQPSK modem.

In regenerative satellite systems the total P_e performance is given by [3]

$$P_{etotal} = P_{ev} + P_{ed}$$

where P_{ev} and P_{ed} are uplink and downlink P_e performances respectively. This equation is used to plot "the Iso-Probability of error performance" curves for $P_{etotal} = 10^{-4}$ of the regenerative link using IJF-OQPSK modems, as shown in Fig. 7.1.30. The IJF-OQPSK modulators may be equipped with ideal hardlimiters prior to the conventional output amplifiers. When the IJF-OQPSK modulators are used in conjunction with the hardlimiters the IJF-OQPSK signal, prior to the HPA (or TWTA), has a constant envelope. Therefore, the spectral and P_e performances of the IJF-OQPSK modems with hardlimiter are independent of HPA and TWTA backoffs. This implies that the HPA and TWTA can operate at saturation mode (i.e. 0 dB backoff). Consequently the system power efficiency of the transmitter is increased

and the cost and the weight of the HPA or TWTA in use is reduced. The simulation results shown in Fig. 7.1.30 indicate that the regenerative satellite system using IJF-OQPSK modems with hardlimiter is the best choice when the HPA and TWTA operate at 0 dB backoffs. The results (Fig. 7.1.30) also show that the regenerative system using IJF-OQPSK modems introduces a gain of 1 dB at $P_e = 10^{-4}$ in both uplink and downlink performances, compared to the regenerative system using QPSK modems.



7.1.6 Conclusions

The properties of IJF-QPSK and IJF-OQPSK signals in linear and nonlinear channels were presented. It was shown that finite-state Markov chain models can be used to calculate power spectra of hardlimited IJF-QPSK and IJF-OQPSK signals. The analysis provides insight into the spectrum spreading action of the ideal hardlimiter on the IJF-QPSK and IJF-OQPSK signals. Experimental results are in agreement with theoretical predictions. The experimental results also indicated that the IJF-OQPSK signal has much less spectrum spreading than QPSK, OQPSK, and MSK.

The spectral spreading and probability of error, P_e , performances of the IJF-OQPSK modems in conventional cascaded nonlinear channels and regenerative satellite links were presented. It was shown that a gain of more than 2 dB can be obtained with the regenerative satellite link using an IJF-OQPSK modem relative to the conventional nonlinear channel using the same modem. In a regenerative satellite link, the IJF-OQPSK modem has better spectral spreading and P_e performances than the conventional QPSK. A gain of 1 dB is attained on both uplink and downlink with the IJF-OQPSK modem. This excellent P_e performance, combined with the spectral efficient characteristic of the IJF-OQPSK modulation technique makes it attractive for applications in regenerative satellite systems.

REFERENCES

- [1] K. Feher, Digital modulation techniques in an interference environment, Don White Consultants, Inc., Maryland, 1977.
- [2] K. Feher, Filter, Canadian Patent Disclosure 372, 365, filed May 10, 1979, Ottawa, Canada.
- [3] S.J. Campanella, F. Assal, A. Berman, Onboard Regenerative Repeater, ICC'77 Conference Record, pp. 6.2 121-125.
- [4] K. Feher, Digital Communications: Satellite Applications, Prentice-Hall, a forthcoming book, 1982.
- [5] T. Le-Ngoc, K. Feher, Power and bandwidth efficient ISI and Jitter-Free (IJF) Transmission Techniques, ICC-81, Denver, Colorado, June 14-17, 81.
- [6] T. Le-Ngoc and K. Feher, Power and Bandwidth Efficient ISI and Jitter-Free (IJF) Transmission Techniques for Linear and Nonlinear Channels, submitted to IEEE Trans. on Comm.
- [7] W.C. Lindsey and M.K. Simon, Telecommunication Systems Engineering, Prentice-Hall, Inc., New Jersey, 1973.
- [8] Intelsat TDMA/DSI Specification, BG-42-65E, June 26, 1980.

7.2.0 NLA-16-QAM: A New Method for Generating High Power 16-QAM Signals Through Nonlinear Amplification

7.2.1 Introduction

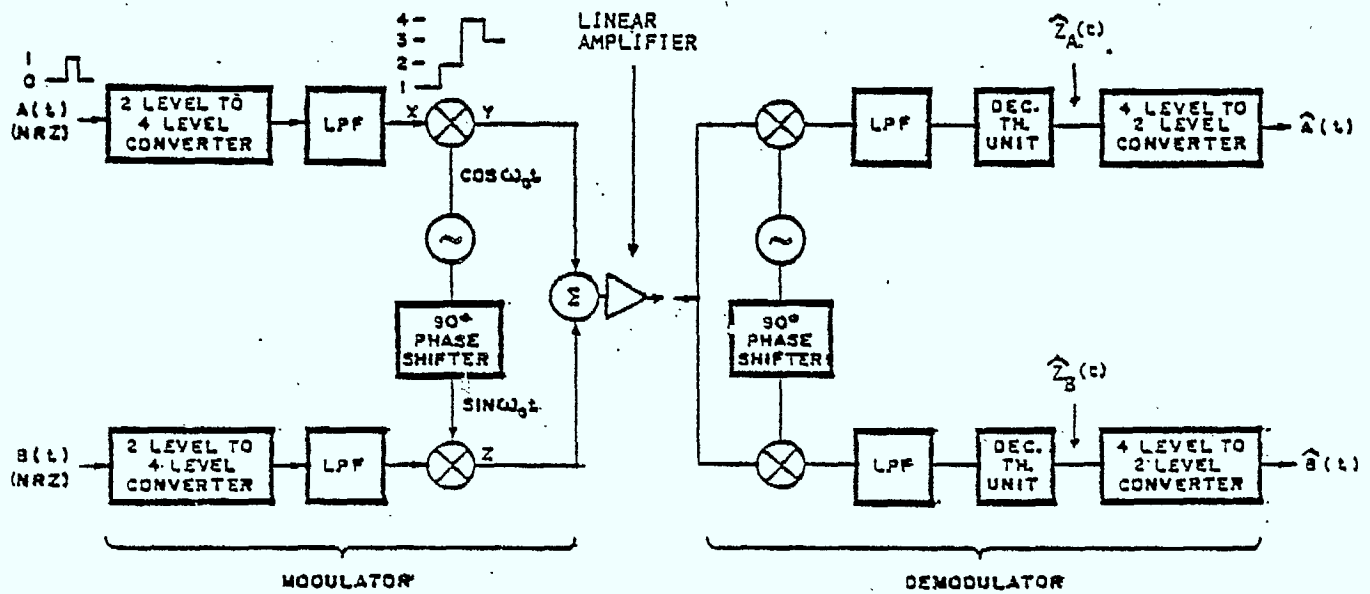
From the spectral efficiency point of view, 16-QAM with a theoretical maximum efficiency of 4 b/s/Hz is a very attractive modulation technique [1,2,3,8,9]. Figure 7.1.1 shows a conventional system block diagram for the generation and detection of a 16-QAM signal. The system shown assumes two asynchronous input data streams. One important and limiting feature of this realization, however, is that it requires extremely linear transmitter power amplification with minimal Amplitude Modulation to Phase Modulation (AM-PM) conversion. This is due to the strong amplitude and phase modulated components of the 16-QAM signal. Although some nonlinearity can be compensated for by using predistortion techniques [1,2], an essentially linear transmission environment is nonetheless required.

In transmission systems, in order to overcome poor detection due to signal loss as a result of long path length or fading, the generation of high transmitter output power is often desirable. In general, output power is most easily maximized by using as a power amplifying element an amplitude-limiting device. Examples of such devices are Travelling Wave Tubes (TWT's) in saturation, Class C operated transistorized amplifiers, and Gunn and Impatt diode Injection Locked Amplifiers (ILA's).

The purpose of this paper is to outline a new method of generating a 16-state QAM signal that permits nonlinear transmitter output power amplification and hence higher output power

than in methods considered to date. One attractive feature of this new modulation method is that despite significant differences with conventional 16-QAM in the method of generating a modulated signal, the same straightforward demodulation techniques apply to both. As this new method permits nonlinear amplification, it has been designated *Nonlinear Amplified 16-State Quadrature Amplitude Modulation*, or NLA-16-QAM for short. NLA-16-QAM has the same flexibility with regards to input data as conventionally realized 16-QAM. That is, it can accept either two asynchronous input data streams or, with additional hardware, one single input stream. In the single input stream version, the timing of the data transitions on the quadrature channel can be coincident with respect to the data transitions on the in-phase channel. Alternately, it can be offset by a unit bit duration resulting in Offset Keyed NLA-16-QAM.

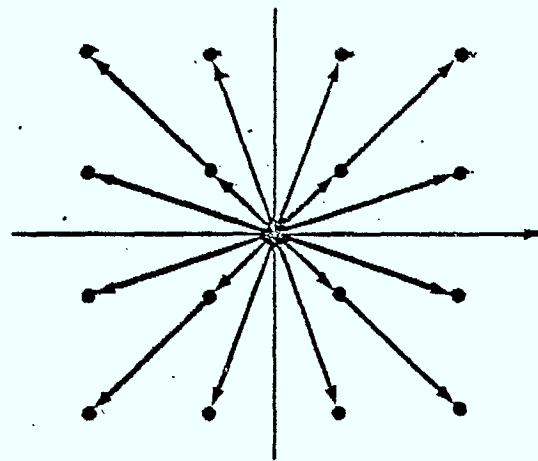
The principles applied to the realization of NLA-16-QAM are not limited to the creation of 16-state signals only. This study shows that NLA-16-QAM is only one of a class of QAM signal realization techniques, where the number of states realizable is 2^{2n} , n being any positive integer.



a) MODULATOR AND DEMODULATOR

| IN | | OUT |
|----|---|-----|
| 0 | 0 | 1 |
| 0 | 1 | 2 |
| 1 | 1 | 3 |
| 1 | 0 | 4 |

b) 2 LEVEL - 4 LEVEL CODING TABLE



c) SIGNAL SPACE DIAGRAM

FIGURE 7.2.116 QAM SYSTEM REPRESENTATION

7.2.2 Modulation Method for NLA-16-QAM

A. Modulator

A block diagram of the modulator is shown in Figure 7.2.2. It is basically a parallel type as outlined in Reference 3. However, there are significant differences in the manner in which data is fed to the modulators and the location of filtering as will be described in the following paragraphs. It is these differences that give the NLA-16-QAM technique its unique characteristics.

Figure 7.2.2 shows two asynchronous Non-Return-to-Zero (NRZ) data streams $A(t)$ and $B(t)$, of the same nominal bit rate, present at input points 1 and 2. Each stream is converted into two synchronous streams by a serial-to-parallel converter. The outputs from the converter accepting the A stream are labelled I_1 and I_2 ; the outputs from the second converter labelled Q_1 and Q_2 . I_1 and Q_1 feed "QPSK Modulator 1" and I_2 and Q_2 feed "QPSK Modulator 2", these being standard Quaternary Phase Shift Keying (QPSK) modulators. Note, however, that they are both driven by the same carrier source. This method of input data distribution to the QPSK modulators differs to that outlined in Reference 3. There, an input data stream is converted into two synchronous streams which form the I and Q inputs to one modulator, and the other input data stream is similarly converted into two synchronous streams which form the I and Q inputs to the other modulator. It will be shown later that this difference significantly simplifies the demodulation process required for NLA-16-QAM generated signals.

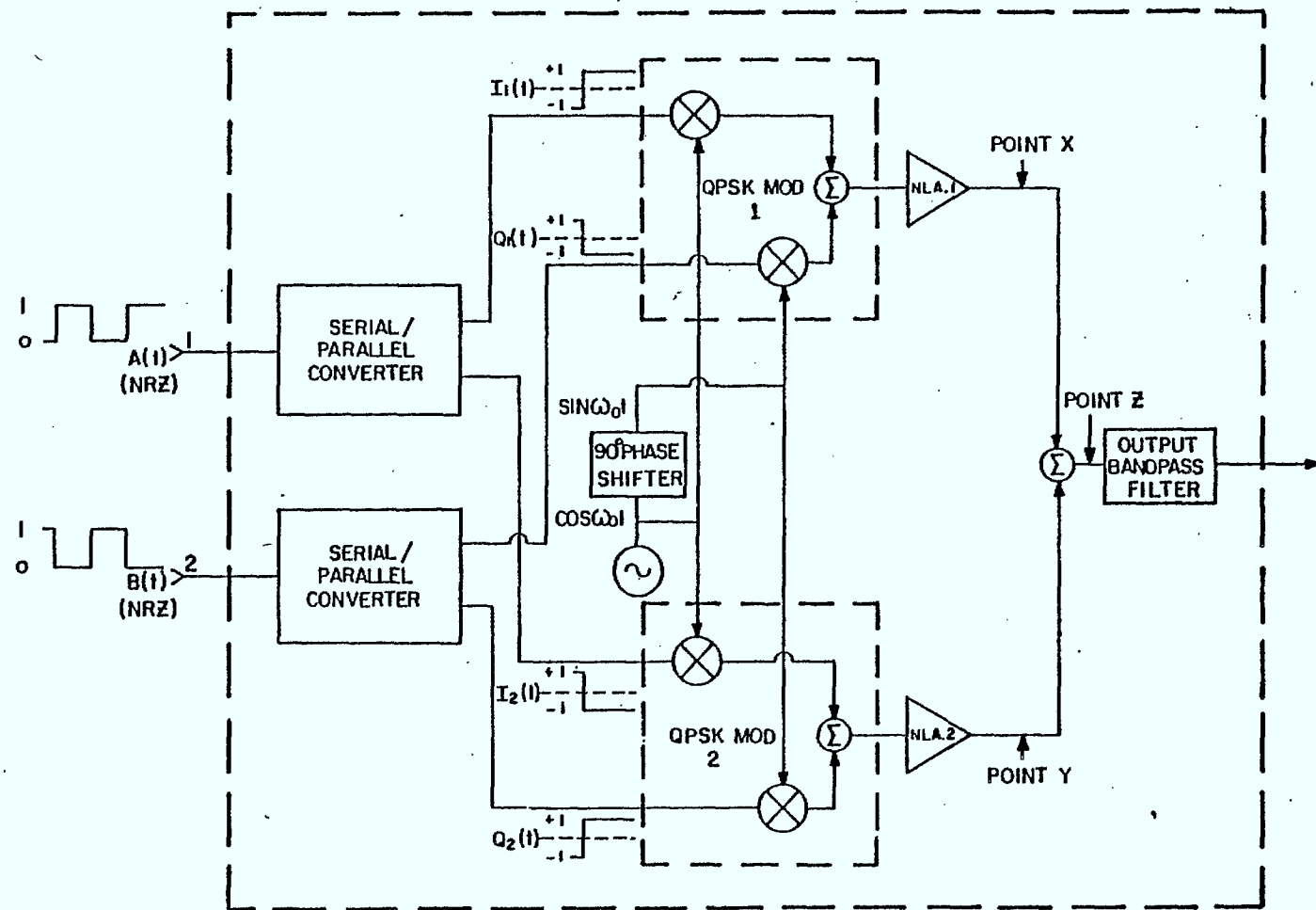


Figure 7.2.2 NLA-16-QAM MODULATOR

As shown in Figure 2, the outputs of the QPSK modulators are amplified by nonlinear amplifiers. Because the QPSK modulated signals are unfiltered, they contain no AM, and thus suffer no degradation from the nonlinear amplification. The output voltage level of amplifier NLA 1 is arranged to be twice that of the voltage level out of amplifier NLA 2. The reason for this will become evident in discussions to follow. The outputs of the two amplifiers are linearly combined in a 3 dB hybrid, and then filtered through the output bandpass filter to limit the radiated spectrum. We note, therefore, that with NLA-16-QAM, the only transmitter filtering that affects the modulated signal is that beyond the nonlinear amplifiers. This is in contrast with conventional 16-QAM where significant transmitter baseband filtering is common [1,2,7,10].

B. Principle of Operation

The principle of operation is most easily seen by following the path of one input signal only as the second input path is operationally identical. Due to linear combining, this method of analysis is applicable as the superposition principle applies. Following the path of input signal $A(t)$, we see that at point X of the modulator the signal present can be given by

$$S_{XA} = 2G I_1(t) \cos \omega_0 t \quad (7.2.1)$$

where $2G$ is the gain of amplifier NLA 1.

Similarly, at point Y,

$$S_{YA} = G I_2(t) \cos \omega_0 t \quad (7.2.2)$$

where G is the gain of amplifier NLA 2.

Thus, at point Z we have

$$\begin{aligned} S_{ZA} &= [2I_1(t) + I_2(t)] \cdot G \cdot \cos \omega_0 t \\ &= Z_A(t) \cdot G \cdot \cos \omega_0 t \end{aligned} \quad (7.2.3)$$

where ω_0 is the carrier frequency in radians/second.

$I_1(t)$ and $I_2(t)$ are synchronous NRZ streams. We have shown them in Fig. 7.2.2 to have values of $+1$ and -1 for logic levels of 1 and 0, respectively. Thus, the possible amplitude and code levels of $Z_A(t)$ for various combinations of amplitudes or logic states of $I_1(t)$ are as shown in Table 7.2.1

Table 7.2.1

CODE LEVELS AND AMPLITUDES OF MODULATED SIGNAL $Z_A(t)$
FOR VARIOUS COMBINATIONS OF VALUES OF $I_1(t)$ AND $I_2(t)$

| $2I_1(t)$ | | $I_2(t)$ | | $Z_A(t)$ | |
|-------------|-----------|-------------|-----------|------------|-----------|
| Logic State | Amplitude | Logic State | Amplitude | Code Level | Amplitude |
| 0 | -2 | 0 | -1 | 1 | -3 |
| 0 | -2 | 1 | 1 | 2 | -1 |
| 1 | 2 | 0 | -1 | 3 | 1 |
| 1 | 2 | 1 | 1 | 4 | 3 |

Analyzing Table 7.2.1, we see that as a result of having set the output voltage of NLA 1 to be twice that of NLA 2, amplitude values of $Z_A(t)$ are equally spaced and symmetrical about zero. Also, when the logic levels of data stream $A(t)$, and hence of $I_1(t)$ and $I_2(t)$, are equiprobable, then all the levels of $Z_A(t)$ are in turn equiprobable. Thus, $S_{ZA}(t)$ is a standard Double Sideband Suppressed Carrier (DSBSC) 4-level AM modulated signal, with amplitude levels optimum for P_e versus S/N performance [4].

A similar analysis of the modulation of input signal, $B(t)$, leads to a signal at point Z given by

$$\begin{aligned} S_{ZB} &= [2Q_1(t) + Q_2(t)] \cdot G \cdot \sin \omega_0 t \\ &= Z_B(t) \cdot G \cdot \sin \omega_0 t \end{aligned} \quad (7.2.4)$$

where S_{ZB} is also a standard DSBSC 4-level AM signal, but importantly, in quadrature with S_{ZA} .

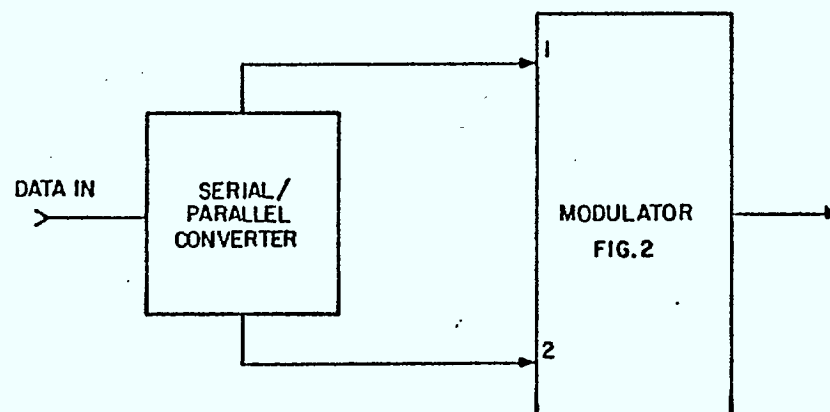
The relationship between the possible amplitudes of $S_{ZB}(t)$ and those of $Q_1(t)$ and $Q_2(t)$ is identical to that between $S_{ZA}(t)$ and those of $I_1(t)$ and $I_2(t)$ as given in Table 7.2.1. Given the above, it is obvious that when input signals $A(t)$ and $B(t)$ are present, we have at point Z two DSBSC 4-level AM signals in quadrature. These signals form a standard 16-state QAM signal [5, 10] as shown in Figure 7.2.1c and given by

$$S_Z = G[Z_A(t) \cos \omega_0 t + Z_B(t) \sin \omega_0 t] \quad (7.2.5)$$

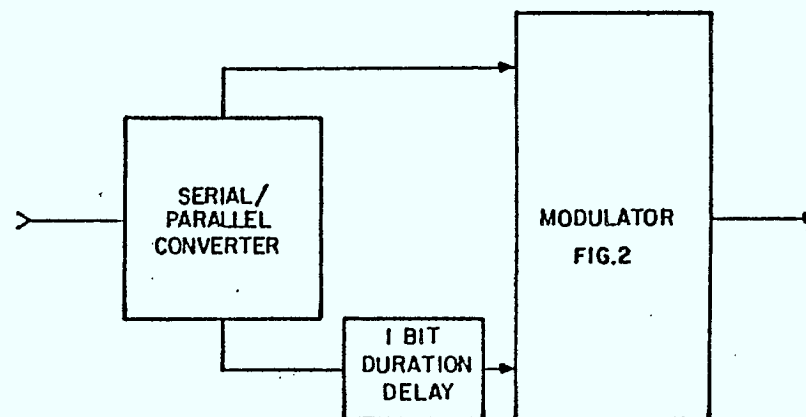
Figure 7.2.3 shows how the modulator can be modified if it is intended to handle only one data stream. The single input stream is simply divided into two by a serial-to-parallel converter and the outputs fed to inputs 1 and 2. This results in a modulated signal with coincident transitions on the in-phase quadrature channels. On the other hand, if an Offset Keyed 16-QAM modulated signal [6] is desired, a delay of a unit bit duration is introduced to one of the outputs of the serial-to-parallel converter.

C. Transmitter Output Power Comparison Between
NLA-16-QAM and Conventional 16-QAM

It will now be shown that NLA-16-QAM results in a transmitter output power advantage that is in the order of 10 dB when compared to conventional 16-QAM. In Reference 3 an analysis of parallel type modulation with the amplified



(A) SINGLE INPUT MODULATOR WITH COINCIDENT TRANSITIONS ON QUADRATURE CHANNELS



(B) SINGLE INPUT MODULATOR WITH OFFSET TRANSITIONS ON QUADRATURE CHANNELS.

Figure 7.2.3 SINGLE INPUT MODULATOR

QPSK modulated signal levels adjusted as in the modulator given in Figure 7.2.2 shows that the power at the modulator output is 1.8 times or 2.5 dB greater than that generated by the conventional method. The analysis assumes that amplifiers with the same maximum linear output power are used in both modulators. However, with nonlinear amplifiers as in NLA-16-QAM, higher output power is available than with linear amplifiers. For example, when using TWT's as the amplifying elements and the NLA-16-QAM modulation, the amplifiers can be run at saturation. With conventional modulation, however, the TWT output power must be backed-off typically 8 dB from saturation, even when predistortion techniques are used [7, 8]. In Reference 2, a standard modulator is described that uses predistortion techniques and a GaAsFET amplifier. The amplifier, designed to be operated in a linear fashion, had a saturated output power of 5 watts. Results indicated that the amplifier had to be operated with output power backed-off 5 dB from saturation for satisfactory performance. Had the amplifier been designed to operate in the Class C mode, it would probably have had a saturated output power at least 3 dB higher than the linear design. It thus seems a fair assumption that using either transistorized amplifiers or TWT's, additional output power of approximately 8 dB is available when using nonlinear amplification in NLA-16-QAM as opposed to linear

amplification. When we compare NLA-16-QAM to conventional 16-QAM modulation the additional available power is 10.5 dB, comprising the 2.5 dB advantage of parallel modulation and the 8 dB advantage of nonlinear amplification.

With conventional 16-QAM modulation, filtering for spectrum limiting is normally done at baseband. If the output amplifier is followed by a filter, this filter would be for branching purposes and harmonic rejection and be relatively wideband. It thus normally results in insignificant loss to the transmitted signal. With NLA-16-QAM, however, filtering for spectrum limiting must be done beyond the amplifiers. Thus, measurable signal loss occurs. Typically, the transmitted signals from 16-QAM modulators are filtered so as to be contained within about 50% excess Nyquist bandwidth. The power loss due to the attenuation of signal power outside of the 50% excess bandwidth is in the order of 0.5 dB. In addition, there is inband signal attenuation which is a function of the filter percentage bandwidth and method of realization. Output filter design is normally such as to limit this loss to within about 1 dB. Since a fair comparison of transmitter output power between modulation methods should be made at the transmitter output filter, the loss through the NLA-16-QAM output filter should be taken into account. It is, however, small compared to the pre-output filter power advantage which, as shown above, is in the order of 10 dB.

7.2.3 Demodulation and Probability of Error Performance

The demodulator block diagram shown in Figure 7.2.1 for conventionally-generated 16-QAM signals is directly applicable to NLA-16-QAM-generated signals. For both systems the receiver filtering is such that, in conjunction with the transmitter filtering, it results in signals with raised cosine spectral densities at the decision threshold inputs.

The only difference between the systems is that for NLA-16-QAM, the 4-level to 2-level decoding is the converse to the coding scheme shown in Table 7.2.1 which is standard binary coding; whereas for conventional 16-QAM the decoding is the converse to that shown in Fig. 7.2.1, which is Gray binary coding [9].

The P_e versus S/N of NLA-16-QAM system can be determined from the P_e versus S/N of a 4-level Pulse Amplitude Modulation (PAM) system as follows:

The optimum $P_e(S/N)$ performance of a 4-level PAM baseband system is found from Eq. (4.46) of Reference 4 to be

$$P_e = \frac{3}{4} \operatorname{erfc} \left[\left(\frac{1}{5} \cdot \frac{S}{P_N} \right)^{\frac{1}{2}} \right] \quad (7.2.6)$$

where P_e = probability that a symbol of the 4-level signal is in error,

S = average input power to receiver,

P_N = input noise power in the baud rate bandwidth of the 4-level signal.

The $P_e \left(\frac{S}{P_N} \right)$ relationship of a DSBSC system is the same as that of a baseband system when the baseband signal for both systems are the same [9]. But as shown previously, the NLA-16-QAM signal can be considered as two DSBSC 4-level AM signals operating in quadrature. Thus, were the input signal $B(t)$ to be absent, the system would be a single DSBSC system and the P_e of signal $A(t)$ would be given by Eq. (7.2.6). Similarly, were $A(t)$ to be absent, the P_e of $B(t)$ would be given by Eq. (7.2.6). With both $A(t)$ and $B(t)$ present, demodulation of each signal continues independently of the other. However, compared to the single DSBSC system, only one half of the total received signal S , but the same noise power, is now demodulated by each DSBSC demodulator. Thus, the $P_e \left(\frac{S}{P_N} \right)$ performance of each data signal $A(t)$ and $B(t)$ is now degraded by 3 dB.

Expressed mathematically, we have for the regenerated 4-level signals $\hat{Z}_A(t)$ and $\hat{Z}_B(t)$ at the output of the decision

$$P_{e(4L)} = \frac{3}{4} \operatorname{erfc} \left[\left(\frac{1}{5} \cdot \frac{1}{2} \frac{S}{P_N} \right)^{\frac{1}{2}} \right] \quad (7.2.7)$$

where P_N is the input noise power in the baud rate bandwidth of the 4-level signals $Z_A(t)$ and $Z_B(t)$.

Defining

T_{4L} as the baud duration of $Z_A(t)$ and $Z_B(t)$,

T_I as the bit duration of $I_1(t)$ and $I_2(t)$,

T_i as the bit duration of the input signals $A(t)$ and $B(t)$,

N_0 as the noise spectral density,

and N_i as the noise power in the bit rate bandwidth of $A(t)$ and $B(t)$,

$$\text{then, } P_N = \frac{N_0}{T_{4L}}$$

$$T_{4L} = T_I \text{ (see Eq. 7.2.3)}$$

$$T_I = 2T_i$$

$$N_i = \frac{N_0}{T_i}$$

Therefore,

$$P_N = \frac{N_0}{2T_i} = \frac{N_i}{2} \quad (7.2.8)$$

Substituting Eq. (7.2.8) into Eq. (7.2.7) we get:

$$P_{e(4L)} = \frac{3}{4} \operatorname{erfc} \left[\left(\frac{1}{5} \cdot \frac{S}{N_i} \right)^{\frac{1}{2}} \right] \quad (7.2.9)$$

It can be easily shown that with standard binary coding, 4-level to 2-level decoding results in the P_e of the bits in the 2-level signal being approximately $\frac{2}{3}$ that of the P_e of the symbols in the 4-level signal. Thus, the $P_{e(\text{NLA-16-QAM})}$ of the receiver output signals $\hat{A}(t)$ and $\hat{B}(t)$ is given by

$$P_{e(\text{NLA-16-QAM})} = \frac{1}{2} \operatorname{erfc} \left[\left(\frac{1}{5} \cdot \frac{S}{N_i} \right)^{\frac{1}{2}} \right] \quad (7.2.10)$$

The P_e of the 4-level signals, $\hat{Z}_A(t)$ and $\hat{B}(t)$, in a conventional 16-QAM can be shown to be identical to the P_e

for NLA-16-QAM. However, because its coding is Gray binary, 4-level to 2-level decoding results in the P_e of the 2-level signal being approximately $\frac{1}{2}$ that of the 4-level signal [9]. The net result is that for the same S/N, NLA-16-QAM generates 33% more errors than conventional 16-QAM. This is equivalent to a difference in $P_e(S/N)$ performance between the two systems of about 0.1 dB in the practical P_e range of interest of approximately 10^{-4} to 10^{-10} . The difference in performance is thus negligible.

For single input systems with NLA-16-QAM modulators as shown in Fig. 7.2.3, the demodulators are the same as described above, but with an extra parallel-to-serial converter added, and in the offset case, an additional unit bit duration delay to the data output signal $\hat{A}(t)$. In the offset modulator signal $\hat{B}(t)$ is delayed. Thus, delaying signal $\hat{A}(t)$ in the demodulator allows the signals $\hat{A}(t)$ in and $\hat{B}(t)$ to be recombined in the proper time phase.

Finally, we note that, because of differences in the NLA-16-QAM modulator structure in comparison to those proposed in Reference 3, the demodulator required for NLA-16-QAM is much simpler than that proposed in Reference 3, which requires the regeneration of a 4-PSK modulated signal.

7.2.4 A Generalized Technique for Nonlinear Amplifier QAM Signal Generation

NLA-16-QAM is one of a class of techniques for generating nonlinear amplified QAM signals. In this class

the number of states realizable is 2^{2n} , n being any positive integer. NLA-16-QAM thus represents the case where $n=2$.

For all realizations the modulator accepts two asynchronous data streams, $A(t)$ and $B(t)$. It splits $A(t)$ into n parallel I streams and $B(t)$ into n parallel Q streams. Each I stream is paired with a Q stream and fed to a QPSK modulator. Thus, n QPSK modulators are required. All modulators are fed with in-phase and quadrature carriers derived from the same source.

The outputs of the n QPSK modulators are amplified and combined to give a 2^{2n} state QAM signal. The relative levels of the amplifier output signals are adjusted so that the sum of the signals of a given phase (in-phase or quadrature) represents a DSBSC amplitude modulated signal, of 2^n equally spaced levels, symmetrical about zero. To achieve this, the relative output levels of the n amplifiers are set at $\pm 2^{x-1}$, for $x=1, n$.

For the simplest case where $n=1$, the technique is designated NLA-4-QAM and results in a modulator that generates a 4-state signal. The block diagram of such a modulator is shown in Figure 4 and is seen to be very similar to a standard 4-state QAM. The only difference is that the output amplifier is nonlinear and all filtering that affects the modulated signal is done after the amplifier.

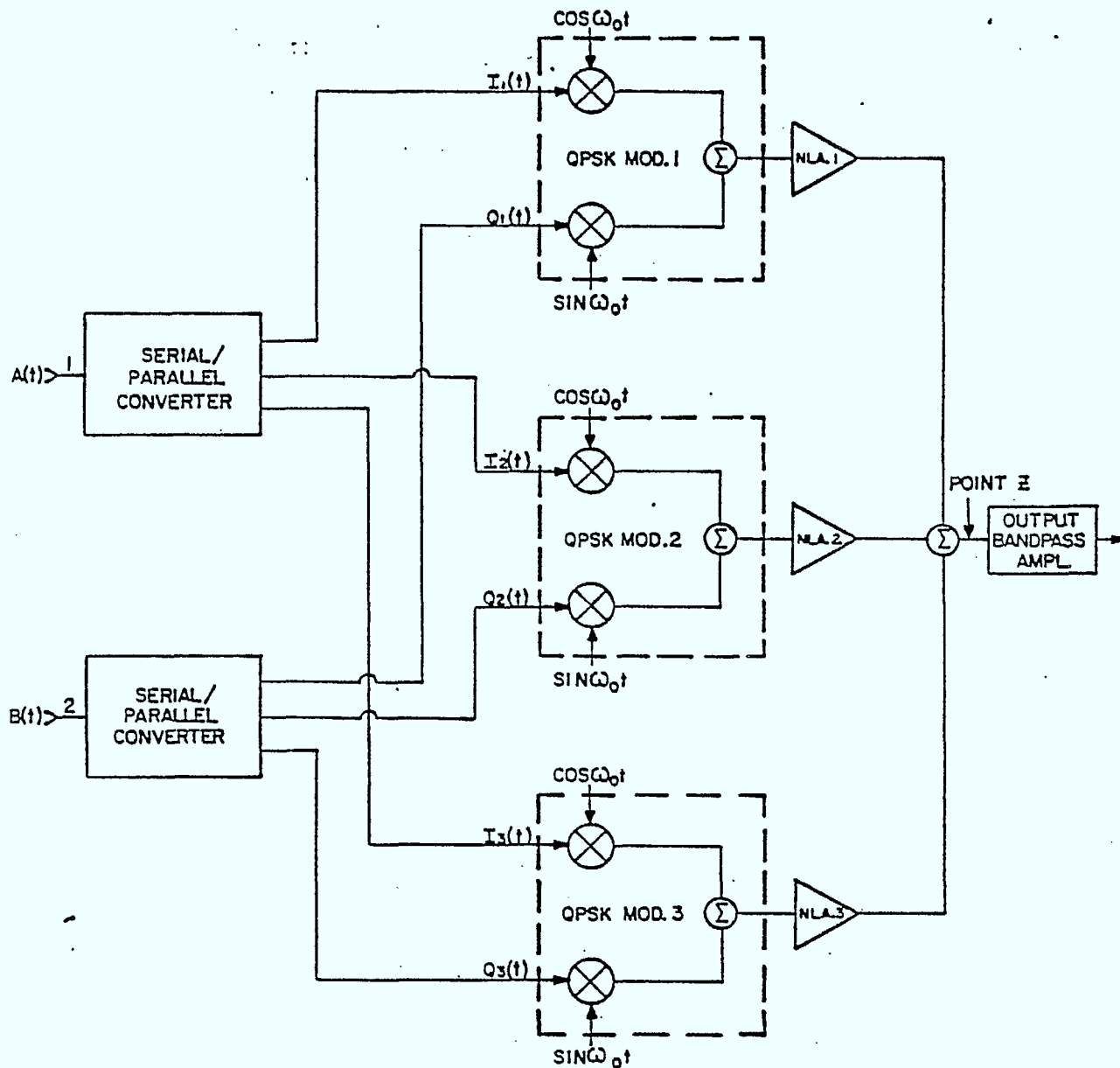
For the case where $n=3$, the technique is designated NLA-64-QAM and results in a modulator that generates a

64-state signal by combining in quadrature two DSPSC, 8-level AM signals. The block diagram of such a modulator is shown in Fig. 7.2.5. The demodulator required for signals generated by such a modulator would be the same as that shown in Fig. (7.2.1a) but with 8-level to 2-level standard binary coded converters in place of the 4-level to 2-level converters shown.

We note that the maximum spectral efficiency of a 64-state QAM system is 6 b/s/Hz, a very high efficiency when compared to most systems in use to date. Reluctance to use such high spectrally efficient systems has in part been due to lower P_e versus S/N performance compared to that of less spectrally efficient methods, as well as to low output power capability imposed by the requirement for linear generation. Nothing can be done about the relative P_e versus S/N performance. However, with nonlinear amplification, output power can be increased to the extent that 64-state QAM systems should be given serious consideration for use in situations requiring extremely high utilization of the available spectrum.

7.2.5 Conclusion

A new modem technique for generating high power 16-QAM signals through nonlinear amplification was presented. The technique used was designated NLA-16-QAM and has been shown to result in a transmitter output power advantage of

NOTES:

- 1) GAIN OF NLA.1 = 4G
 " " NLA.2 = 2G
 " " NLA.3 = G
- 2) $S_z = [Z_A(t) \cos \omega_0 t + Z_B(t) \sin \omega_0 t]$
 Where $Z_A(t) = [4I_1(t) + 2I_2(t) + I_3(t)]$
 & $Z_B(t) = [4Q_1(t) + 2Q_2(t) + Q_3(t)]$

Figure 7.2.5 NLA-64-QAM MODULATOR

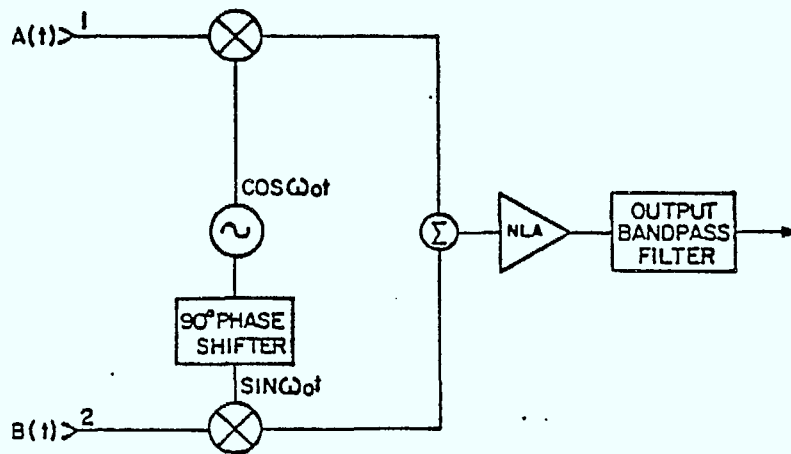


Figure 7.2.4. NLA-4-QAM MODULATOR

approximately 10 dB over conventional 16-QAM.

Demodulation techniques and P_e versus S/N performance of NLA-16-QAM have been shown to be essentially identical to those of conventional 16-QAM. Furthermore, NLA-16-QAM has been shown to be a member of a general class of modulation techniques capable of generating QAM signals through non-linear amplification.

REFERENCES

- [1] M. Byington and C. Pallemartz, "Design and Performance of 16-State Digital Modem," International Conference on Communications, Boston, June 1979, pp. 5.4.1-5.4.6.
- [2] Y. Yashida, Y. Kitahara and S. Yokoyana, "6G-90 Mb/s Digital Radio System with 16-QAM Modulation," International Conference on Communications, Seattle, June 1980, pp. 52.4.1-52.4.5.
- [3] K. Miyauchi, S. Seki and H. Ishio, "New Technique for Generating Multi-level Signal Formats", IEEE Trans. on Communications, COM-24, No. 2, Feb. 1976, pp. 263-267.
- [4] R. Lucky, J. Salz, E. Weldon, Jr., Principles of Data Communication, (New York, N.Y.: McGraw-Hill Book Co.) 1968.
- [5] D. Morais and K. Feher, "Modulation Methods for Point-to-Point Digital Radio Systems," International Telecommunications Exposition, Rio de Janeiro, Brazil, May 1980.
- [6] M. Simon and J. Smith, "Offset Quadrature Communications with Maximum Likelihood Phase Estimation," IEEE Trans. on Communications, Vol. COM-22, No. , Nov. 1974, pp. 1859-1862.
- [7] I. Horikawa, Y. Okamoto and K. Morita, "Characteristics of a High Capacity 16-QAM Digital Radio System on a Multipath Fading Channel," International Conference on Communications, Boston, June 1979, pp. 48.4.1-48.4.6.
- [8] D. Doherty and C. Pallemartz, "Spectral Compatibility of 16-State QAM," International Conference on Communications, Seattle, June 1980, pp. 34.4.1-34.4.6.
- [9] W. Bennett and J. Davey, Data Communications, (New York, N.Y.: McGraw-Hill Book Co.), 1965.
- [10] K. Feher, Digital Communications by Microwave, a forthcoming book, (Englewood Cliffs, N.J.: Prentice-Hall, Inc.), 1980.
- [11] K. Feher, "Digital Modulation Techniques in an Interference Environment," Vol. 9 of the EMC Encyclopedia (Germantown, MD: Don White Consultants, Inc.), 1977.

7.3.0 State NLA QAM: A Method for Generating 64-State QAM Signals Using Nonlinear Amplification

7.3.1 Introduction

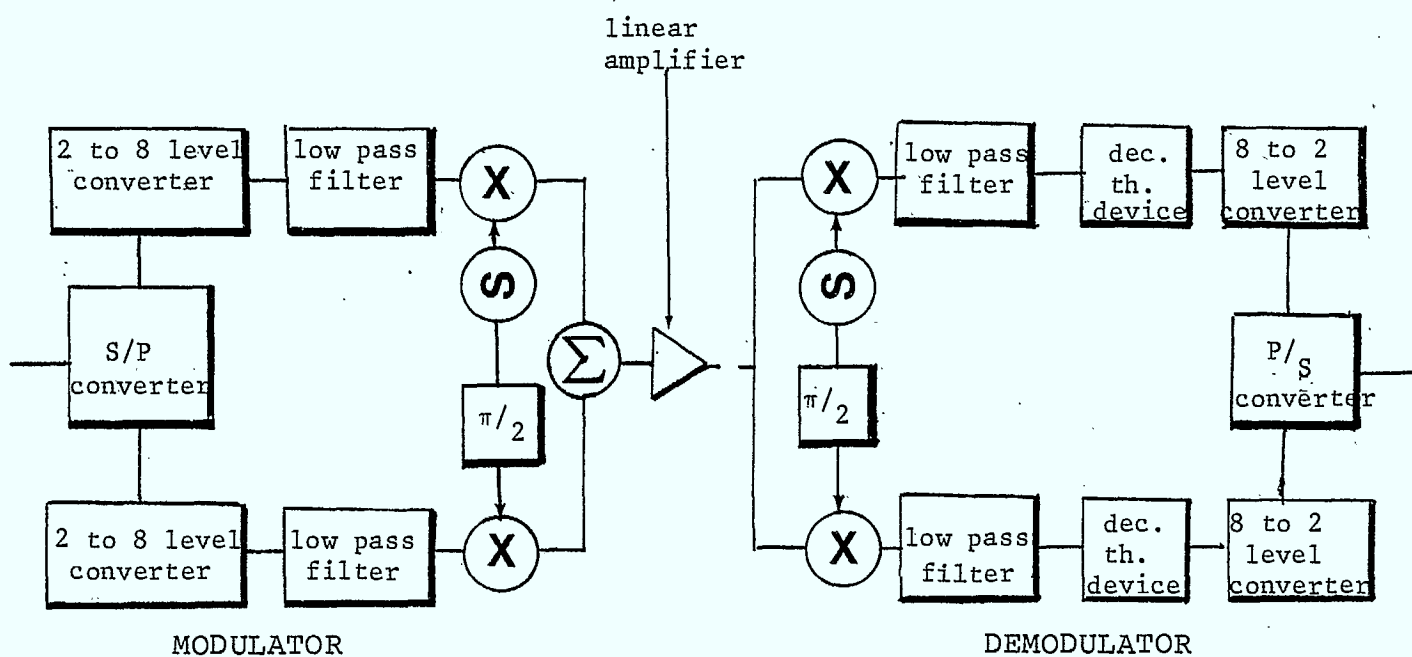
As a continuation of the previous section (7.2.0) [2], the specific case of 64-state NLA QAM is considered.

The method of generating this 64-state QAM signal, which permits nonlinear transmitter output power amplification, is presented. In addition, the generation of this modulation scheme using an Intersymbol Interference & Jitter Free (IJF) filtering technique is considered.

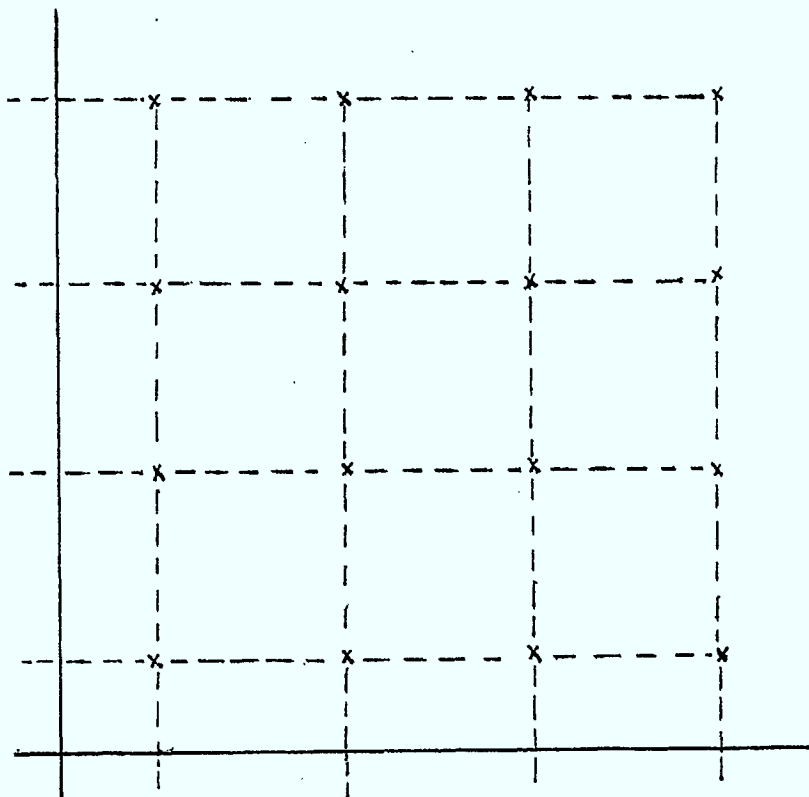
7.3.2 Modulation Design

With the increase in satellite communication traffic it will become necessary to implement more power and spectral efficient communication systems. With this in mind, 64-state NLA QAM with its theoretical maximum spectral efficiency of 6 b/s/Hz and nonlinear amplification possibilities becomes a very attractive modulation technique.

Figure 7.3.1 shows a system block diagram of a conventional 64-state APK modulator and demodulator, and the associated 64-ary rectangular signal set design [1]. Using this system configuration one is constrained to using linear transmitter power amplification. This is because AM/AM and AM/PM conversions resulting from nonlinear amplification would cause significant distortion to the signal space configuration of Figure 7.3.1.



a) modulator and demodulator



b) Signal set design with only the basic symmetry region shown [1].

Figure 7.3.1. Conventional 64-state APSK system.

To accomplish linear amplification, the power amplifying element, typically an HPA or TWT, must be operated below saturation in the linear region. However, there is a price to be paid for this luxury: an HPA or TWT designed for higher power must be used. This amplifier, in turn, costs more than one specified for lower power that can be operated in the nonlinear region.

The 64-state NLA QAM modulator and demodulator is shown in Figure 7.3.2[4]. For synchronous operation the NRZ input signal $X(t)$ is serial-to-parallel converted into two NRZ streams, $X_I(t)$ and $X_Q(t)$. Each stream is converted into 3 synchronous streams labelled I_1 , I_2 & I_3 and Q_1 , Q_2 & Q_3 by a serial-to-parallel converter. For asynchronous operation the two asynchronous NRZ signals are each fed directly into the second serial-to-parallel converter. As in the synchronous case each signal is converted into 3 synchronous NRZ streams. I_1 and Q_1 feed the QPSK modulator 1, I_2 and Q_2 feed the QPSK modulator 2, and I_3 and Q_3 feed the QPSK modulator 3. This method of data allocation simplifies the demodulation process for asynchronous operation.

The output signal of each of the three QPSK modulators is amplified by a nonlinear amplifier, the output voltage level of NLA 1 being 3 dB higher than that of NLA 2 which, in turn, is 3 dB higher than the output voltage level of NLA 3. The output of the three amplifiers are linearly combined and then bandpass filtered to limit the transmitted spectrum.

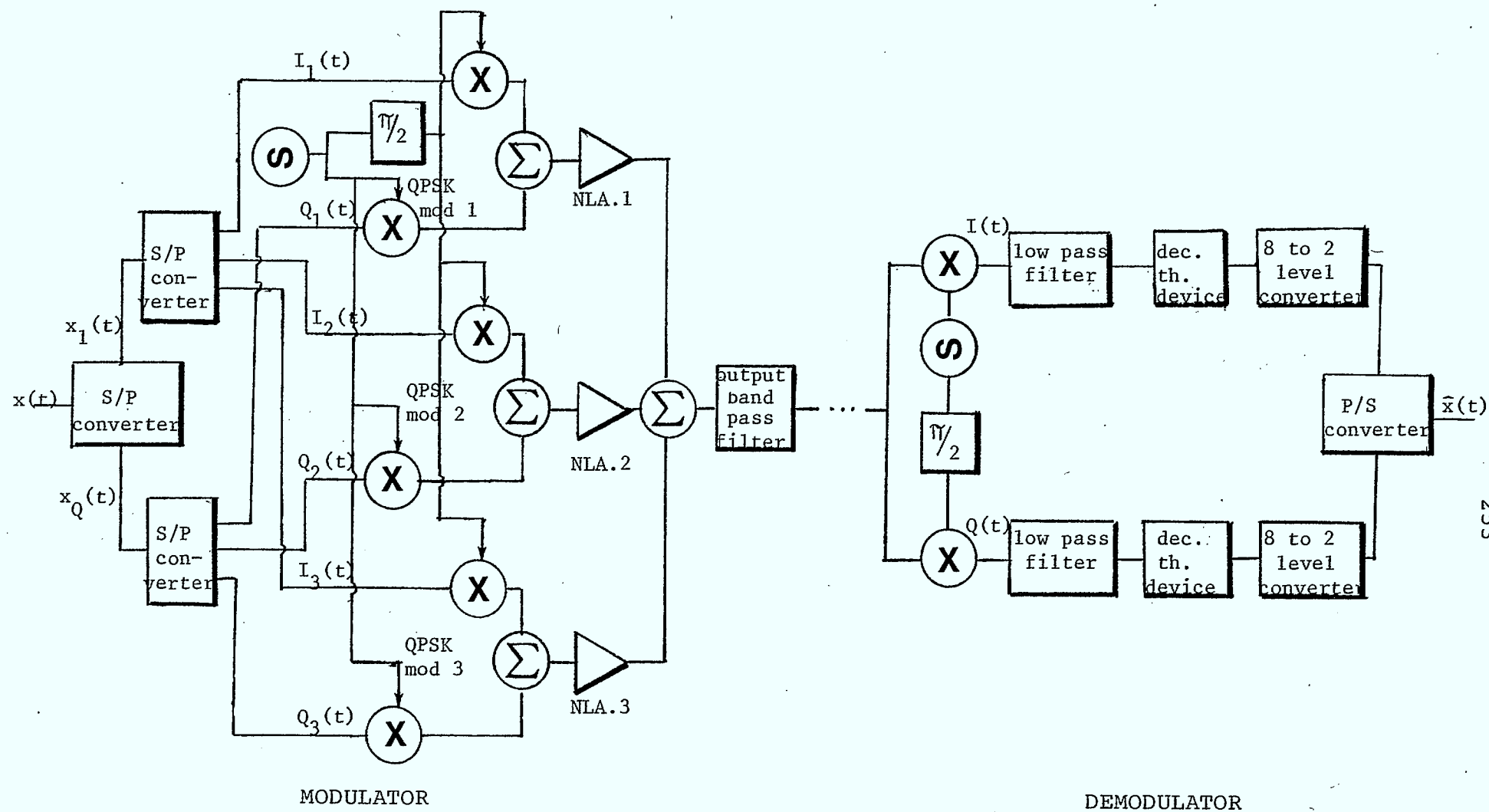


Figure 7.3.2. 64-state NLA QAM modulator and demodulator [2].

The principal advantage of this modulation scheme is that it permits nonlinear transmitter output power amplification. The QPSK modulated signals are unfiltered prior to nonlinear amplification so that they contain no AM, thus no degradation should result from their nonlinear amplification.

7.3.3 Demodulation

The demodulation block diagram shown in Figure 7.3.2 is the same as that shown in Figure 7.3.1 for the conventional case. The receiver filtering in combination with the transmit filter results in the signals having raised-cosine spectral densities. The incoming modulated signals are bandpass filtered to remove out-of-band interference. The filtered signals are demodulated, using a conventional QPSK demodulator, into two synchronous or asynchronous streams, $I(t)$ and $Q(t)$. Each stream is then eight-to-two level converted into an NRZ data signal. The demodulation process is completed for asynchronous operation. For synchronous operation these two streams are parallel-to-serial converted into the single NRZ data signal $\hat{X}(t)$.

7.3.4 Principle of Operation

The principle of operation is explained only for the case of synchronous operation because the same principles also apply for asynchronous operation. Following the path of the NRZ input signal, $X(t)$, it is converted into six NRZ data streams $I_1(t)$, $I_2(t)$, $I_3(t)$, $Q_1(t)$, $Q_2(t)$ and $Q_3(t)$. The symbol interval, T_s , of each of these streams is six times

the bit interval, T_b , of $X(t)$, i.e. $T_s = 6 T_b$. For each of the QPSK modulators the two signals, $I_i(t)$ and $Q_i(t)$, modulate the quadrature carriers, $\cos w_c t$ and $\sin w_c t$, and are summed to produce the quadrature modulated signal, $S_i(t)$.

$$S_i(t) = I_i(t) \cos w_c t + Q_i(t) \sin w_c t \quad (7.3.1)$$

where $i = 1, 2, 3$.

After amplification, at the output of the summing device the signal is given by

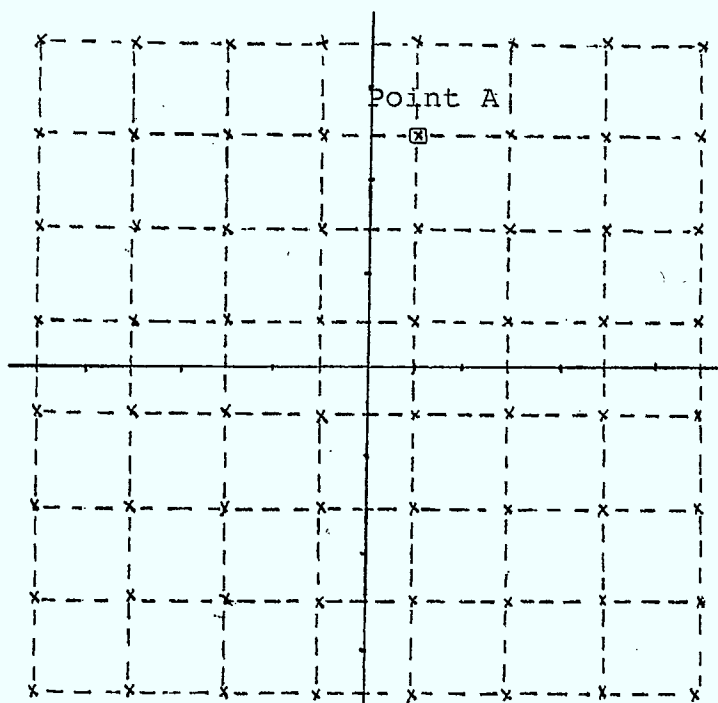
$$\begin{aligned} S(t) &= G.[4S_1(t) + 2S_2(t) + S_3(t)] \\ &= G.[(4I_1(t) + 2I_2(t) + I_3(t)) \cos w_c t + (4Q_1(t) \\ &\quad + 2Q_2(t) + Q_3(t)) \sin w_c t] \\ &= G.[I(t) \cos w_c t + Q(t) \sin w_c t] \end{aligned} \quad (7.3.2)$$

where $4G$, $2G$ and G are the gains of amplifiers NLA 1, NLA 2 and NLA 3 respectively.

The table in Figure 7.3.3a shows the possible relative amplitudes of $I(t)$ for all the possible combinations of $I_1(t)$, $I_2(t)$ and $I_3(t)$. The same table could also be reproduced for $Q(t)$ where the same relationship exists between the amplitude of $Q(t)$ and $Q_1(t)$, $Q_2(t)$ and $Q_3(t)$ as exists between $I(t)$ and $I_1(t)$, $I_2(t)$ and $I_3(t)$. The table shows that having set the output voltage of NLA 1 to be twice that of NLA 2 and four times that of NLA 3 the amplitude values of $I(t)$ (and similarly $Q(t)$) are equally spaced and symmetrical about zero. This is illustrated in the system's signal set design shown in Figure 7.3.3b. From the signal set design we see that, for example, the signal marked point A is produced as a result of

| $4I_1(t)$ | | $2I_2(t)$ | | $I_3(t)$ | | $I(t)$ |
|----------------|-----------|----------------|-----------|----------------|-----------|-----------|
| $I_1(t)$ state | Amplitude | $I_2(t)$ state | Amplitude | $I_3(t)$ state | Amplitude | Amplitude |
| 1 | 4 | 1 | 2 | 1 | 1 | 7 |
| 1 | 4 | 1 | 2 | -1 | -1 | 5 |
| 1 | 4 | -1 | -2 | 1 | 1 | 3 |
| 1 | 4 | -1 | -2 | -1 | -1 | 1 |
| -1 | -4 | 1 | 2 | 1 | 1 | -1 |
| -1 | -4 | 1 | 2 | -1 | -1 | -3 |
| -1 | -4 | -1 | -2 | 1 | 1 | -5 |
| -1 | -4 | -1 | -2 | -1 | -1 | -7 |

a) Table of amplitudes of $I(t)$ for combinations of values of $I_1(t)$, $I_2(t)$ and $I_3(t)$



b) 64-state QAM signal set design

Figure 7.3.3 Table of relative amplitudes of $I(t)$ and 64-ary signal set design.

$$I_1(t) = 1$$

$$Q_1(t) = 1$$

$$I_2(t) = 1$$

$$Q_2(t) = -1$$

$$I_3(t) = -1$$

$$Q_3(t) = -1$$

Similarly, all the points on the state-space diagram can be represented as combinations of the input data stream(s) but for brevity are not given here.

In the case of linear channel applications the signal when perturbed by additive white Gaussian noise can be expected to give a symbol probability of error performance as a function average symbol SNR as shown in Figure 7.3.4 [1]. This figure shows that a triangular signal set design yields the optimum performance for average SNR with the 64-state QAM requiring about 0.5 dB greater SNR. In turn, 64-state PSK is shown to require about 10 dB greater SNR than 64-state QAM. Although the triangular set yields the optimum performance its complex implementation makes it undesirable. Due to the significantly higher power required by 64-state PSK the 64-state QAM is the most desirable configuration at this spectral efficiency.

As yet only preliminary work has been done on NLA 64-state QAM. For this reason, no results on the performance of this modulation technique are available at present. In the following section we will take a brief look at IJF 64-state NLA QAM.

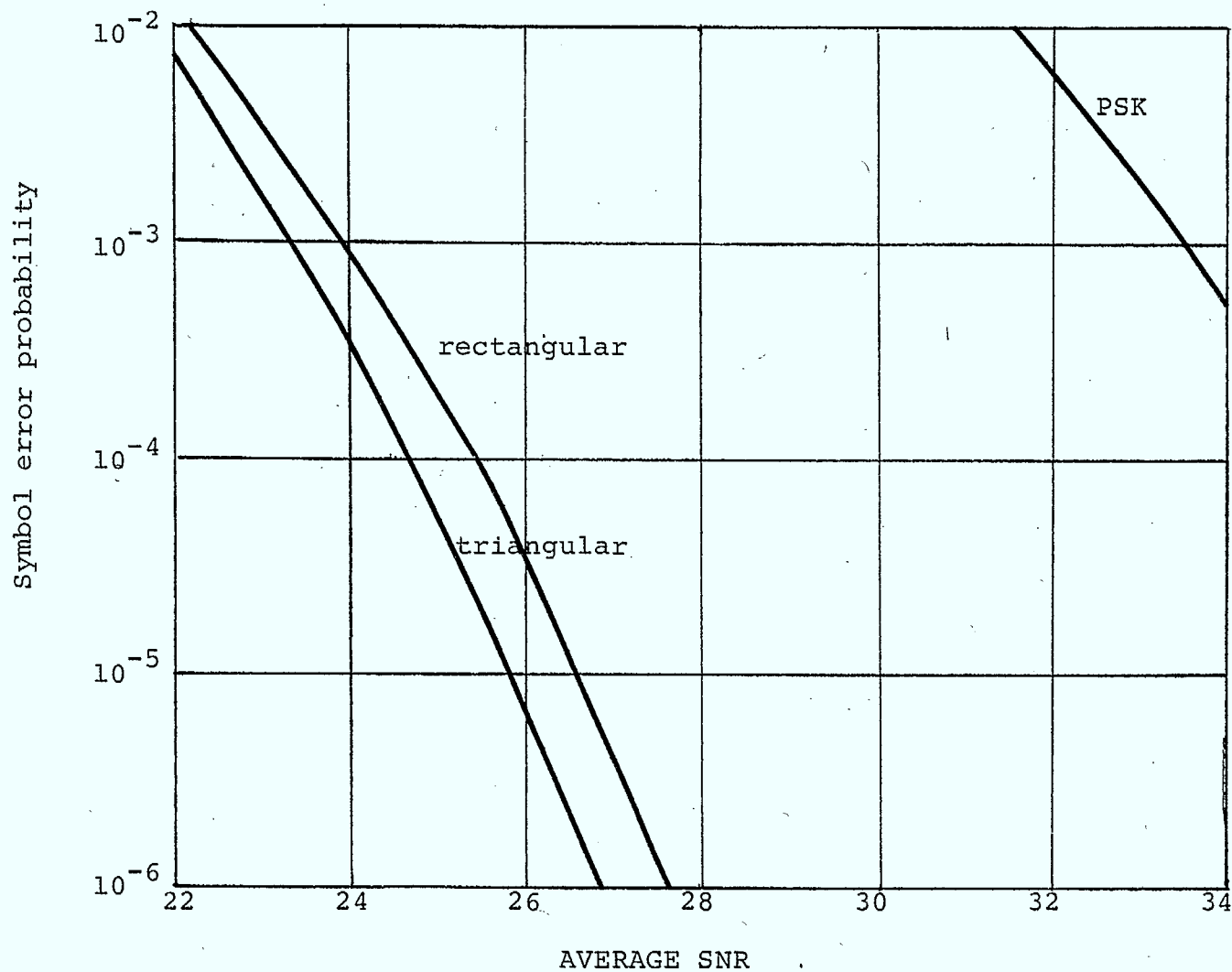


Figure 7.3.4. Symbol error probability versus average SNR for 64-ary alphabets [1].

7.3.5 IJF 64-State QAM: An Extension of 64-State QAM

7.3.6 Introduction

At high radio frequency-to-bit rate ratios post HPA filtering may become impractical, as well as its use being discouraged in cases where transponder hopping is of interest. By filtering prior to the HPA, the nonlinear effects of the HPA tend to regenerate the spectral sidelobes previously removed through filtering. One solution to this problem of spectrum spreading is to choose a modulation technique which keeps the restored sidelobes due to nonlinear amplification as low as possible. An acceptable solution is to use baseband IJF filtering. Recent theoretical and experimental results for IJF-OQPSK in a nonlinear channel indicate IJF-OQPSK exhibits significantly less spectrum spreading than QPSK, OQPSK or MSK [3]. As an extension to this work the baseband IJF filtering technique is proposed for use in the generation of 64-state NLA QAM.

7.3.7 Principle of Operation

The block diagram of the IJF 64-state QAM modulator is the same as shown in Figure 7.3.2 with the exception that IJF filters are located prior to the QPSK modulator in both the I and Q channels. Similarly the principle of operation for this IJF modulator is the same as for the previous modulator with the only difference being that prior to the input of each of the QPSK modulators the NRZ signals are encoded into IJF signals. The principles of this IJF encoding technique are given from reference [3].

The NRZ signal is encoded into a signal represented by

$$Y(t) = \sum_{n=-\infty}^{\infty} y_n(t) \quad (7.3.3)$$

where

$$y_n(t) = \begin{cases} S_e(t-n T_s) & \text{if } x_n = x_{n-1} = 1 \\ -S_e(t-n T_s) & \text{if } x_n = x_{n-1} = -1 \\ S_o(t-n T_s) & \text{if } x_n = 1, x_{n-1} = -1 \\ -S_o(t-n T_s) & \text{if } x_n = -1, x_{n-1} = 1 \end{cases} \quad (7.3.4)$$

if

$$x(t) = \sum_{n=-\infty}^{\infty} x_n g(t-nT_s)$$

is the NRZ input to the encoder. For one example of IJF encoding the pulses $S_e(t-nT_s)$ and $S_o(t-nT_s)$ can be defined as

$$S_e(t_n) = \begin{cases} B & \text{for } |t_n| \leq T_s/2 \\ 0 & \text{elsewhere} \end{cases} \quad (7.3.5a)$$

$$S_o(t_n) = \begin{cases} B \sin \frac{\pi t_n}{T_s} & \text{for } |t_n| \leq T_s/2 \\ 0 & \text{elsewhere} \end{cases} \quad (7.3.5b)$$

The IJF quadrature modulated signal, $S'_i(t)$, with IJF encoded signal inputs, $I'_i(t)$ and $Q'_i(t)$, is given by

$$S'_i(t) = Q'_i(t) \sin w_c t + I'_i(t) \cos w_c t \quad (7.3.6)$$

Results on this extension of the 64-state NLA QAM are pending further analytic work and experimental verification.

7.3.8 Conclusion

A technique for generating 64-state QAM that permits nonlinear output power amplification has been presented. With this technique 64-state QAM signals are generated by combining three unfiltered, nonlinear amplified QPSK signals.

The probability of error performance curves of various 64-ary signal set designs indicated that the rectangular signal set of 64-QAM would be the optimal choice for physically realizable 64-ary alphabets.

REFERENCES

- [1] C.M. Thomas, M.Y. Weidner and S.H. Durrani, "Digital Amplitude-phase Keying with m-ary Alphabets", IEEE Trans. on Communications, Com-22, No. 2, Feb. 1974, pp. 168-178.
- [2] D.H. Morais, K. Feher, "NLA-QAM: A New Method for Generating High Power QAM Signals Through Nonlinear Amplification", submitted to IEEE Trans. on Comm.
- [3] T. Le-Ngoc, H. Pham Van and K. Feher, "Power and Bandwidth Efficient Intersymbol Interference and Jitter-free Quadrature Modulation Techniques for Linear and Nonlinear Channels", submitted to IEEE Trans. on Comm.
- [4] W.J. Weber, P.H. Stanton and J.T. Sumida, "A Bandwidth Compressive Modulation System Using Multi-amplitude Minimum Shift Keying (MAMSK)", IEEE Trans. on Communication, Com-26, No. 5, May 1978.

CHAPTER 8

CONCLUSIONS AND RECOMMENDATIONS

The results obtained in this study indicate that on-board satellite regeneration may be used to meet (and exceed) system performance specifications, vis-a-vis INTELSAT V, which would not be otherwise met in a conventional system unless the earth station HPA is operated at large input back-offs. Hence regeneration might lead to more cost-efficient satellite systems. Gains of from 2.0 dB to 5.7 dB in E_b/N_o requirements for a P_e of 10^{-4} are achievable depending on the modulation method used. QPSK is seen to have better performance, in both regenerative and conventional systems, than offset QPSK and MSK. Results for DPSK and DQPSK are close enough to those of QPSK to merit serious consideration especially since it reduces on-board satellite complexity. The new modulation method, IJF-OKQPSK shows considerable promise for use in regenerative satellite systems because of its excellent out-of-band emission characteristics after nonlinear amplification.

The results obtained herein lead us to conclude that the Department of Communications should carry out further research in this area and address problems such as:

- 1) the modulation techniques preferable for the uplink and downlink,

- 2) the effect of up-link and down-link capacities on the configuration and parameters of the overall system,
- 3) analysis of recently discovered power/bandwidth efficient modulations in the complex regenerative satellite environment,
- 4) Spectral operating evaluation aimed at assessing interference effects on adjacent transponders and an investigation of uplink noise,
- 5) and finally digital synchronization schemes should be analyzed with the aim of finding novel methods.

DATE DUE
DATE DE RETOUR

~~JAN 10 1987~~

~~FEB 10 1987~~

~~MAR 13 1987~~

~~JUL 17 1982~~

LKC
P91 .C654 F43 1981
Report on regenerative
transponders for more
efficient digital satellite
systems : phase II

INDUSTRY CANADA / INDUSTRIE CANADA



208052

